



Università degli Studi *Mediterranea* di Reggio Calabria

Dipartimento di Agraria

Corso di Dottorato di ricerca

Scienze Agrarie Alimentari e Forestali XXXIII ciclo

SSD AGR/10 – Costruzioni Rurali e Territorio Agroforestale

Development and application of innovative remote sensing techniques for early-season monitoring of crop vigor and vegetative stress in Mediterranean agro-ecosystems

PhD Thesis

Candidato (PhD Candidate):

Dr. Gaetano Messina

Tutor (Supervisor): **Prof. Giuseppe Modica**

Co-Tutor (Co-Supervisor): **Dr. José Manuel Peña Barragán**

PhD Coordinator: **Prof. Marco Poiana**

Anno 2021

Index

Abstract

Riassunto

1	General introduction and thesis organization	10
1.1	Crops surveyed.....	12
2	Remote Sensing of Vegetation.....	22
2.1	Thermal Remote Sensing.....	25
2.2	Remote Sensing of Vegetation and Soil.....	28
2.3	Remote Sensing Aerial Platforms: a brief introduction	36
3	Monitoring the vegetation vigor in heterogeneous citrus and olive orchards. Extraction of tree crowns from multispectral UAV images	39
3.1	Materials and Methods.....	43
3.1.1	Study sites and workflow	43
3.1.2	Surveys Equipment.....	45
3.1.3	Data acquisition and pre-processing	47
3.1.4	Radiometric analyzes and statistics.....	49
3.1.5	Image segmentation.....	49
3.1.6	Vegetation indices and topographic elevation layers	52
3.1.7	Image Classification and trees' crowns extraction	53
3.1.8	Accuracy assessment	55
3.2	Results and discussions.....	57
3.2.1	Geometric and radiometric characteristics	57
3.2.2	Image classification, tree crown extraction and accuracy assessment.....	61
3.2.3	Vegetation indices (VIs) and vigor maps.....	67
3.3	Conclusions.....	70

4	Object-based classification using machine learning algorithms and UAVs multispectral imagery precision agriculture: case studies on bergamot and “Cipolla Rossa di Tropea”	72
4.1	Materials and Methods.....	74
4.1.1	Study site.....	74
4.1.2	UAV surveys and data acquisition.....	75
4.1.3	Pre-processing and datasets	77
4.1.4	eCognition Multi-Resolution Segmentation (MRS).....	77
4.1.5	Image Classification.....	78
4.2	Accuracy Assessment	81
4.3	Results.....	82
4.3.1	Image Segmentation	82
4.3.2	Image Classification.....	84
4.4	Discussion.....	94
4.4.1	Image Segmentation	94
4.4.2	Image Classification and Accuracy Assessment.....	95
4.5	Conclusions.....	98
5	Thermal UAV Remote Sensing in precision agriculture	100
5.1	Thermal cameras types, structure and Unmanned Aerial Vehicles.....	102
5.2	Camera calibration and data collection.....	104
5.3	Data processing	110
5.4	Thermal UAV imagery applications in precision agriculture.....	111
5.4.1	Crop water stress monitoring.....	111
5.4.2	Plant disease detection, phenotyping, yield estimation, and vegetation status monitoring.....	116
5.5	Future Research Outlook.....	119
5.6	A case study on monitoring onion crops using UAV multispectral and thermal imagery	121

5.6.1	Materials and methods.....	122
5.6.2	Results.....	126
6	Comparison of UAV and satellites multispectral imagery: a case study in monitoring onion “Cipolla Rossa di Tropea”	128
6.1	Materials and methods.....	132
6.1.1	Study site.....	132
6.1.2	Platforms and data acquisition.....	133
6.1.3	Vegetation indices.....	137
6.1.4	Comparison of vegetation indices (VIs) from the three platforms.....	139
6.1.5	Image Segmentation and Classification.....	140
6.2	Results and discussions.....	142
6.3	Conclusions.....	161
7	General conclusions.....	163
	Acknowledgements.....	165
8	LIST OF FIGURES.....	166
9	LIST OF TABLES.....	173
10	ACRONYMS	175
11	References.....	177

Abstract

Precision agriculture (PA) is defined as “a management strategy that gathers, processes and analyzes temporal, spatial and individual data and combines it with other information to support management decisions according to estimated variability for improved resource use efficiency, productivity, quality, profitability and sustainability of agricultural production”. In order to achieve effective and sustainable environmental management of agricultural production, and an improvement in the competitiveness of the agricultural sector, PA methodologies and technologies are currently a reliable and cost-effective approach. PA represents also one of the most important applications of remote sensing (RS). While satellite observation has guided many information-based advances in agricultural management and practice, critical technological developments and steep rise have affected unmanned aerial vehicles (UAVs) in the last decade, which represent a potential game-changer in PA applications. In comparison with other RS platforms, UAVs are generally more independent of climatic variables. Furthermore, being able to provide data with higher temporal and spatial resolution, the UAVs today represent a significant source of RS imagery in PA considering that the knowledge of the within-field spatial variation of edaphic factors and the state of crops constitute an essential prerequisite.

Many multispectral (MS) UAV cameras permit to obtain spectral information in the Red, Red edge, and NIR wavebands for vegetation applications with a very high spatial resolution. Based on the combination of these three wavebands, many vegetation indices (VIs) were developed with the aim to monitor, analyze, and map temporal and spatial variations of vegetation in both herbaceous and tree crops. Furthermore the geographic object-based image analysis (GEOBIA) techniques have demonstrated higher effectiveness for extracting reliable and reusable information from the images in comparison to traditional pixel-based procedures.

In the framework of this PhD thesis, crops of great interest in the Mediterranean agro-ecosystems and specifically, in Calabria region, were monitored by using a combination of innovative technologies, i.e, UAV and satellite images, vegetation indices, and GEOBIA procedures, with the primary aims of producing vigor maps and assessing the uses of these maps for PA applications. The studied crops were olive (*Olea europaea* L. subsp. *sativa*), bergamot (*Citrus bergamia*, Risso), clementine (*Citrus clementina* Hort. ex Tan.), and onions (*Allium cepa*, “Cipolla Rossa di Tropea”).

The novelty of the proposed procedures relies on their replicability, reliability, and speed, which proved promising results in different datasets characterized by heterogeneous agricultural

contexts. The heterogeneity and spatial variability of the surveyed scenarios showed that the proposed approaches can be applied to a wide range of both herbaceous and tree vegetation types. Furthermore, the results obtained in the several case studies demonstrated the potential of the approaches adopted in providing useful information to manage farm operations and guide farmers' decisions in PA, even in agricultural scenarios that are not necessarily characterized by crop parcels of very large dimensions.

Keywords: precision agriculture (PA); unmanned aerial vehicles (UAVs); satellite multispectral imagery; multispectral and thermal UAV imagery; vegetation indices (VIs); geographical object-based image classification (GEOBIA); vigor maps

RIASSUNTO

L'agricoltura di precisione (PA) è definita "una strategia di gestione che raccoglie, elabora e analizza dati temporali, spaziali e individuali e li combina con altre informazioni per supportare le decisioni gestionali in base alla variabilità stimata per migliorare l'efficienza dell'uso delle risorse, la produttività, la qualità, la redditività e la sostenibilità della produzione agricola". Al fine di ottenere una gestione ambientale efficace e sostenibile della produzione agricola e un miglioramento della competitività del settore agricolo, le metodologie e le tecnologie della PA sono attualmente un approccio affidabile ed economico. La PA rappresenta anche uno dei più importanti campi di applicazione del telerilevamento (o Remote Sensing, RS). Mentre la raccolta di dati da satellite ha guidato molti progressi basati sull'informazione nella gestione e nella pratica agricola, nell'ultimo decennio diversi sviluppi tecnologici importanti hanno riguardato i veicoli aeromobili a pilotaggio remoto (droni, UAV), che oggi rappresentano un potenziale fattore di cambiamento nelle applicazioni della PA. Rispetto ad altre piattaforme di RS, gli UAV sono generalmente più indipendenti dalle variabili climatiche. Inoltre, essendo in grado di fornire dati con una maggiore risoluzione temporale e spaziale, rappresentano oggi una fonte significativa di immagini nella PA, considerando che la conoscenza della variabilità spaziale all'interno del campo dei fattori edafici e dello stato delle colture costituisce un prerequisito essenziale. Ad esempio, molte fotocamere multispettrali UAV permettono di ottenere informazioni spettrali nelle bande del rosso, Red edge e del vicino infrarosso con una risoluzione spaziale molto elevata. Sulla base della combinazione di queste tre bande, molti indici di vegetazione (VI) sono stati sviluppati con l'obiettivo di monitorare, analizzare e mappare le variazioni temporali e spaziali della vegetazione sia nei campi che nelle colture arboree. Nell'ambito delle applicazioni della PA, tra le tecniche in grado di estrarre informazioni affidabili e riutilizzabili, le tecniche di analisi delle immagini basate su oggetti geografici (GEOBIA) hanno dimostrato la loro efficacia.

Nell'ambito della presente tesi di dottorato, attraverso l'utilizzo di immagini UAV e satellitari, utilizzando GEOBIA e indici di vegetazione per la produzione di mappe della vigoria, è stato effettuato un monitoraggio di colture che rivestono un grande interesse dal punto di vista socio-economico nella regione Calabria: Olivo (*Olea europaea* L. subsp. *sativa*), Bergamotto (*Citrus bergamia*, Risso), Clementina (*Citrus clementina* Hort. ex Tan.), e Cipolla (*Allium cepa* L., "Cipolla Rossa di Tropea").

I risultati ottenuti nei diversi casi studio hanno dimostrato le potenzialità degli approcci adottati nel fornire informazioni utili a orientare la gestione e le decisioni degli agricoltori e delle aziende, anche in contesti agricoli non necessariamente caratterizzati da superfici coltivate molto estese.

1 General introduction and thesis organization

Agriculture constitutes one of the most important fields for Remote Sensing (RS) applications, particularly, in the aspects related to precision agriculture (PA). PA is defined as “a management strategy that gathers, processes and analyzes temporal, spatial and individual data and combines it with other information to support management decisions according to estimated variability for improved resource use efficiency, productivity, quality, profitability and sustainability of agricultural production” (ISPAG, 2019). Increasing the sustainability of the Italian agricultural model through innovation is one of the most important challenges for agriculture in order to increase quality agricultural production while maintaining agrobiodiversity. From a European point of view, the future Common Agricultural Policy (CAP) should promote greater synergies with research and innovation policies to foster innovation. Technological development and digitization make possible major advances in efficiency, and can reduce the environmental/climatic impact of agriculture as well as reduce costs for farmers. The use of new technologies in agriculture remains inadequate and limited at EU level, with insufficient or too slow uptake of new knowledge and innovative solutions in agriculture by small and medium-sized farms. This hinders a gradual transition to a more sustainable agriculture and to farm sector competitiveness and sustainable development. These considerations give rise to a crucial objective of the new CAP for supporting knowledge, innovation and technology through Agricultural Knowledge and Innovation System (AKIS). AKIS is a set of organisations and/or persons, including the links and interactions between them, involved in the generation, transformation, transmission, storage, retrieval, integration, dissemination and use of knowledge and information, with the aim of working synergistically to support decision-making, problem-solving and innovation in agriculture (OCSE).

In this context, PA plays a leading role in optimizing production efficiency and reducing environmental impact. The objectives of the PA include the increase of agricultural production efficiency, product quality and profitability, benefiting at the same time the climatic, environmental, economic sustainability of agricultural practices. In particular, these objectives can be achieved through:

- Optimization of inputs used through a controlled distribution of fertilizers and pesticides according to the real needs of the crop and with a consequent reduction in the infiltration of chemical substances into the ground water;
- Reduction of irrigation water volumes;

- Efficiency intended as reduction in cultivation operations per unit of time and area, and increase in units yields, thanks to improved logistics of pre- and post-harvest operations, and rationalization of data;
- Use of sensors for real-time monitoring of crop health, control of the onset of phytopathogens or environmental conditions.

In the framework of this PhD thesis, the present research aims at defining specific vegetation indices for the early estimation and monitoring of abnormalities of vegetative vigor provoked by biotic and abiotic factors. For this purpose, RS techniques will be implemented with the integration of satellite and UAV data. A particular emphasis will be placed on the management of multiplatform and multitemporal datasets for the obtaining of prescriptive maps. The objective is also to give an overview of RS-based approaches for mapping of agricultural systems, applicable even in a context of PA, and to illustrate these approaches through case studies focused on monitoring carried out on herbaceous and tree crops of great socio-economic interest in Mediterranean agroecosystems and specifically, in Calabria region. To do this, the introductory part in Chapters 1 and 2 includes a description of the crops that have been monitored and the basic notions about RS, and in particular its applications to vegetation characterization. The next chapters illustrate several case studies which have provided for the use of different RS platforms and sensors. The Chapter 3 was devoted to show a quick and reliable semi-automatic workflow, using GEOBIA, to process MS UAV imagery, and aiming at the detection and extraction of olive and citrus trees' crowns in the framework of PA. Finally, the production of vigor maps show the vegetative state of the tree crowns. In the Chapter 4, the main objective was to compare the performances of different GEOBIA algorithms in terms of outputs quality and of processing resources, focusing to PA applicability. In particular, a complete supervised classification of UAV imagery, applied to a bergamot orchard and an onion field was done. The Chapter 5 was partly devoted to the description of the state of the art in PA applications. Finally, a case study was presented about the potentiality of coupling multispectral and thermal imagery acquired by UAVs in monitoring onion crops. In the Chapter 6 a case study was aimed at comparing data acquired by fixed-wing UAV and the PlanetScope and Sentinel-2 satellites in onion crop monitoring. In particular, RS techniques applied to onion crops could help to monitor crop growth and to guide localized fertilization, phytosanitary treatments, and harvest, i.e., to generally support the implementation of PA strategies.

1.1 Crops surveyed

The surveys of RS carried out in this thesis concern herbaceous and tree crops, among those of greatest importance in Calabria region, as they can provide products recognized for their quality outside regional and national borders: olive, clementine, bergamot and onion.

Olive

Olea europaea L. subsp. *sativa* is an evergreen tree species (Figure 1.1); the height of the olive tree can vary from 3 to 15 meters, depending on the cultivar, the pedoclimatic conditions and the environment. A peculiar characteristic of this plant is its ability to regenerate, in fact if the trunk is damaged, the base called stump (or pedal) is able to produce new shoots (Fiorino, 2018). The leaves are lance-shaped and leathery, the flowers are hermaphrodite and white, and the fruit is a drupe, oval and purple to green and is the only fruit from which an oil is extracted, being the other vegetable oils extracted from seeds.



Figure 1.1 Olive orchard.

The olive tree is one of the most important cultivated tree species in the Mediterranean basin. The diffusion of the two subspecies *Olea europaea* L. subsp. *oleaster* (oleaster) and *Olea europaea* L. subsp. *sativa* (cultivated olive tree) from the areas of origin (Asia Minor and Middle East) dates back to at least 5000 BC (Zohary et al., 2015). From the original area of the first crops, corresponding to the eastern Mediterranean, its use was spread to all the countries of the Mediterranean basin in parallel

with the progress of human movements and trade that have marked much of the history of these countries. From the primary areas, secondary areas of diversification (Aegean region) and tertiary areas (southern Italy, Tunisia) would have formed. Under the pressure of the Camito-Semitic populations first, and later by the Phoenicians, Greeks, Romans and lastly by the Arabs, the history of the olive tree is increasingly intertwined with that of the peoples who learn to use and appreciate it, first only as an industrial product for lighting and as an ointment, and later also as a food product (Fiorino, 2018). Today the world area invested in olive trees is about 12 million hectares, on which there are about one billion plants. With regard to the average production of olive oil, this amounts to over 2 million tons. The main producer countries in the European Community are Spain, Italy, Greece and Portugal followed by France, the Balkan countries, Algeria, Morocco, Tunisia etc. Among the emerging ones, Argentina, Chile and Australia are particularly noteworthy. In Italy, about 80% of olive production is widespread in the southern and island regions, with Puglia, Calabria and Sicily being the most productive regions. Calabria, with its 184 thousand hectares of olive groves (Table 1.1) (ISTAT, 2019), covers almost 14% of the entire Italian olive-growing area (Figure 1.2). The olive groves (about 76%) are located in hilly areas while 16% are in mountain areas; only 8% of these are located on the plain. The province of Cosenza has the largest area in production (53,678 ha), followed by Reggio Calabria (49,700 ha), Catanzaro (40,240 ha) Crotona (23,437 ha) and Vibo Valentia (17,509 ha) (Table 1.2) (ISTAT, 2019).

Table 1.1 Total area cultivated and total production (quintals of olives) in Italy and Calabria.

	Total area (ha)	Total production (q)
ITALY	1,180,912	28,979,352
Calabria	184,564	7,224,071

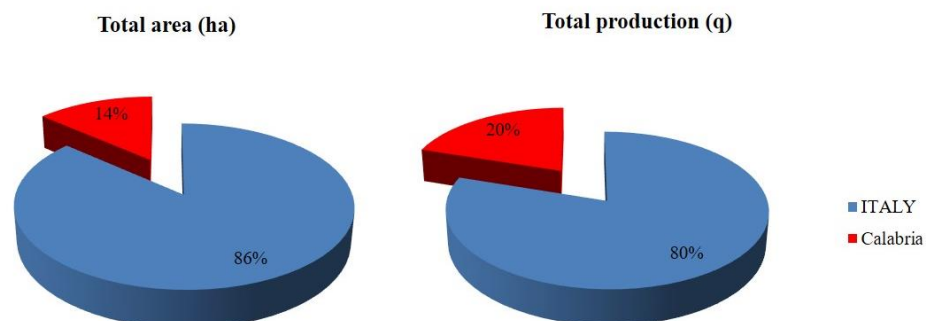


Figure 1.2 Total area and production in Italy and Calabria and related percentages.

Table 1.2 Total area cultivated and total production in Calabria’s provinces.

Province	Total area (ha)	Total production (q)
Cosenza	53,678	1,908,391
Catanzaro	40,240	1,600,000
Reggio Calabria	49,700	2,485,000
Crotone	23,437	465,500
Vibo Valentia	17,509	765,180

As far as production is concerned, Reggio Calabria is the province with the highest production, 2,485,000 quintals of olives, equal to 29% of regional production followed by the province of Cosenza (1,908,391 quintals), Catanzaro (1,600,000 quintals), Vibo Valentia and Crotone (Table 1.2) (Figure 1.3).

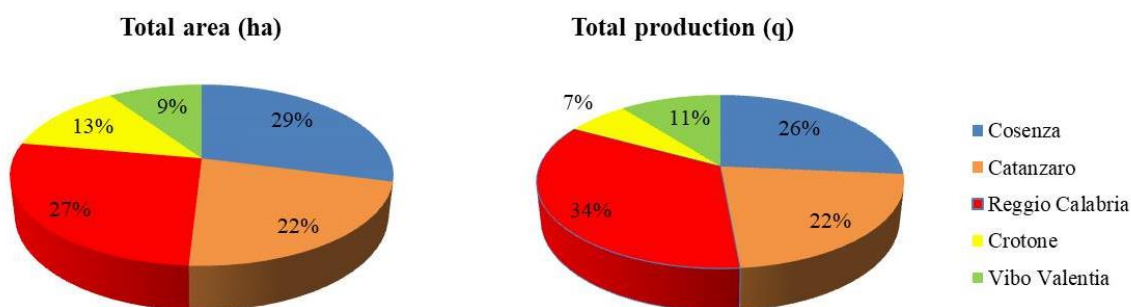


Figure 1.3 Total area and production in Italy and Calabria’s provinces expressed in percentage.

Bergamot

Bergamot (*Citrus bergamia*, Risso) crops (Figure 1.4) are mainly located on the Ionian sea coast in the province of Reggio Calabria (South Italy), its place of election and perhaps even of origin, where this crop has been known since the 17th century. The introduction of this citrus fruit plant in Italy took place in that period first in the region of Tuscany, where the use of the plant was limited only to ornamental purposes, and then in the South, in the province of Reggio Calabria (Vacante and Calabrese, 2009). Here this plant spread mainly thanks to a favorable climate, in the Tyrrhenian coast between Reggio and Cannitello di Villa S. Giovanni and in the Ionian coast between Reggio and Palizzi. Subsequently its cultivation, both because of the competition with other citrus fruits grown and because of the low yield in essential oil, was located exclusively on the Ionian coast (Vacante and Calabrese, 2009).

Citrus bergamia is an evergreen tree, with a cylindrical stem and thin irregular branches (Rapisarda and Paula Germano, 2014). This plant can reach 12 m in height. Flowering takes place between April and May while the fruit ripens, depending on the cultivar, between November and March. There are three varieties, selected by the farmers, which have established themselves in the territory of Reggio Calabria: Femminello, Castagnaro and Fantastico. The fruit (Figure 1.4) is primarily cultivated for the extraction of essential oil from the peel to use it in the cosmetic, perfumery (Jin et al., 2016) and food industries (Pernice et al., 2009). Since 2001, these productions awarded the European protected designation of origin (PDO) label Bergamotto di Reggio Calabria – olio essenziale (“Bergamot of Reggio Calabria – essential oil”). In the food industry, an increasing interest has focused on the use of bergamot’s juice as a beverage and in a blend with other fruit juices (Giuffrè, 2019). This interest is related to the antioxidant properties of juice, beneficial for health (Da Pozzo et al., 2018). From the dried and processed waste is obtained the so-called pastazzo, which can be used as animal feed (Nesci and Sapone, 2014). Over 90% of the world’s bergamot production comes from Calabria while the remaining 10% from Africa (Côte d’Ivoire, Mali, Cameroon, Guinea) and South America (Argentina and Brazil) (Nesci and Sapone, 2014). This is because the climate, the soil characteristics, the cultivation techniques, the rootstock, the degree of ripeness and harvesting, and the extraction method influence the composition and quality of the essence (Vacante and Calabrese, 2009). The surface area cultivated with bergamot is 1500 ha with a production of 300,000 quintals (ISTAT, 2018).



Figure 1.4 Bergamot orchard (top) and fruits at different degrees of ripeness (below).

Clementine

Clementine (*Citrus clementina* Hort. ex Tan.) is one of the essential cultivated varieties of citrus mandarins in the Mediterranean Basin (Benabdelkamel et al., 2012) where it found great popularity thanks to the early ripening of the fruit. This citrus fruit (Figure 1.5), found at the beginning of the 20th century in the garden of an orphanage in Algeria, comes from a natural (or man-made) cross between *Citrus reticulata* and *Citrus sinensis* (Vacante and Calabrese, 2009). From cultivar-population with different clones, different cultivated varieties have been obtained, distinguished by name and for different ripening times, from the month of October to the beginning of February (Vacante and Calabrese, 2009). Italy is one of the largest producers in Europe, and its crops are located in the southern part of the country. Cultivated in Italy since the 1930s, they have found one of their ideal habitats in Calabria. Productions made in the Calabria region are labeled with the European protected geographical indication label “Clementine di Calabria” (Benabdelkamel et al., 2012). This label was awarded because of clementine’s high organoleptic properties. As far as production is concerned, a large part is consumed as fresh fruit and used in the preparation of sorbets, juices, syrups and marmalades (Falcone et al., 2020).

Calabria is the most important Italian region for the production of clementines since the more than 16,000 hectares cultivated represent about 62% of the Italian surface dedicated to its cultivation and with more than 440,000 tons almost 60% of the national production (Table 1.3) (Figure 1.6). The areas of greatest production are concentrated in the plain areas existing in the region and are: Piana di Sibari and Corigliano in the Cosentino area, Piana di Lamezia in Catanzaro, Piana di Gioia Tauro-Rosarno and Locride in the province of Reggio Calabria. In only 58 municipalities in Calabria is concentrated almost half of the regional citrus fruit area, divided as follows (Figure 1.7): Province of Reggio Calabria 20 municipalities (Ardore, Benestare, Bianco, Bovalino, Brancaleone, Casignana, Caulonia, Ferruzzano, Locri, Marina di Gioiosa Jónica, Monasterace, Portigliola, Roccella Jónica, Sant’Ilario dello Jonio, Siderno, Rizziconi, Gioia Tauro, Palmi, Rosarno, S.Ferdinando); Province of Catanzaro 14 municipalities (Borgia, Botricello, Curinga, Lamezia Terme, Maida, Montauro, Montepaone, San Floro, San Pietro a Maida, Sant’Andrea Apostolo dello Jonio, Selliä Marina, Simeri Crichi, Soverato, Squillace, Catanzaro); Province of Cosenza 16 municipalities (Cassano Jonio, Castrovillari, Corigliano Calabro, Crosia, Francavilla Marittima, San Lorenzo del Vallo, Spezzano Albanese, Terranova da Sibari, Trebisacce, Vaccarizzo Albanese, Rossano, Saracena, Cariati, Calopezzati, S. Demetrio C, S. Giorgio A.); Province of Vibo 5 municipalities (Briatico, Francavilla, Angitola, Limbadi, Nicotera, Pizzo); Province of Crotona 3

municipalities (Ciro Marina, Crucoli Torretta, Rocca di Neto) (www.igpclementinedicalabria.it). The clementines are harvested from October to early February, depending on the varieties (Spinoso, SRA 63, Comune, Hernandina, Fedele, Tardivo, Hernandina, Marisol and Nules). The Calabrian surface area cultivated with clementines is divided as follows (Table 1.4) (Figure 1.8): the province of Cosenza has the largest area in production, about 12,250 ha (76%), followed by Reggio Calabria with about 2,350 ha (14%), Catanzaro (752 ha), Vibo Valentia (635 ha) and Crotona (110 ha) (ISTAT, 2019). The production data (Table 1.4) show, of course, Cosenza as the leading province in regional production, with 3,572,414 quintals of clementines produced in 2019, followed by the province of Reggio Calabria (540,500 q), Catanzaro (225,000 q), Vibo Valentia (90,803 q) and Crotona (13,750 q) (ISTAT, 2019).



Figure 1.5 Trees and clementine fruits.

Table 1.3 Total area cultivated and total production (quintals) in Italy and Calabria.

	Total area (ha)	Total production (q)
ITALY	25,759	6,432,096
Calabria	16,097	4,442,467

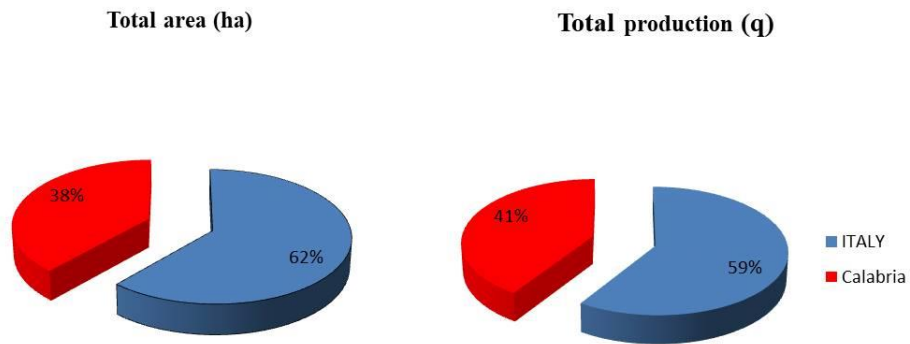


Figure 1.6 Total area and production in Italy and Calabria and related percentages.

Table 1.4 Total area cultivated and total production (quintals) in Calabria's provinces.

Province	Total area (ha)	Total production (q)
Cosenza	12,250	3,572,414
Catanzaro	752	225,000
Reggio Calabria	2,350	540,500
Crotone	110	13,750
Vibo Valentia	635	90,803

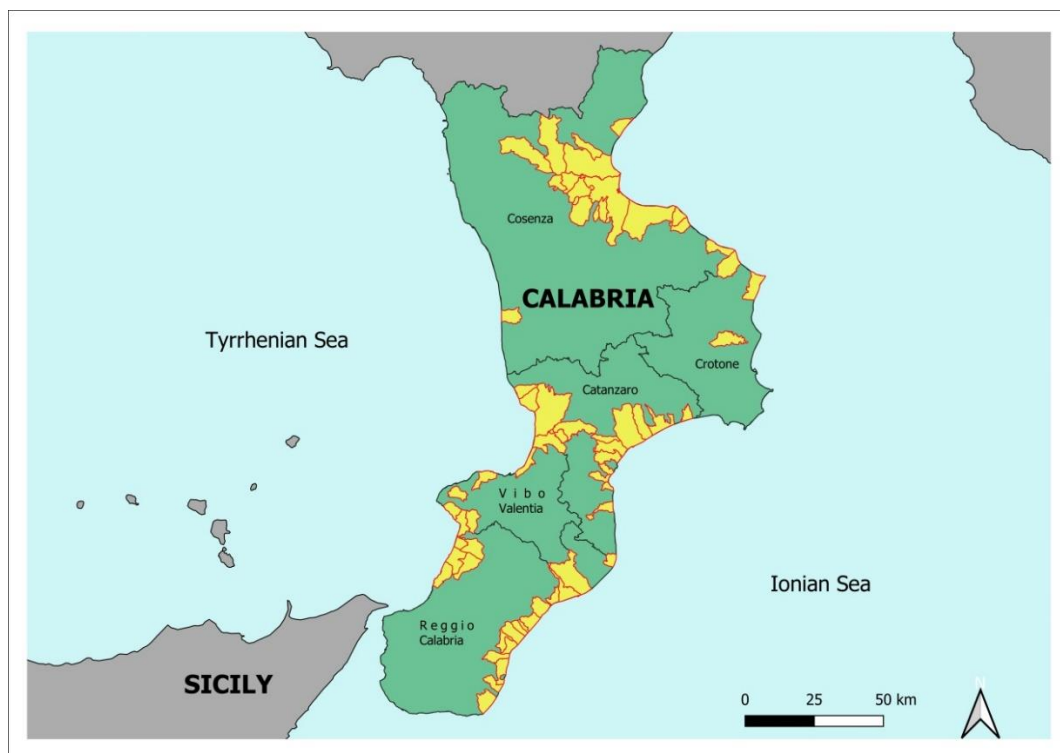


Figure 1.7 Map of Calabria with the municipalities belonging to the production area of "Clementine di Calabria IGP" highlighted in yellow.

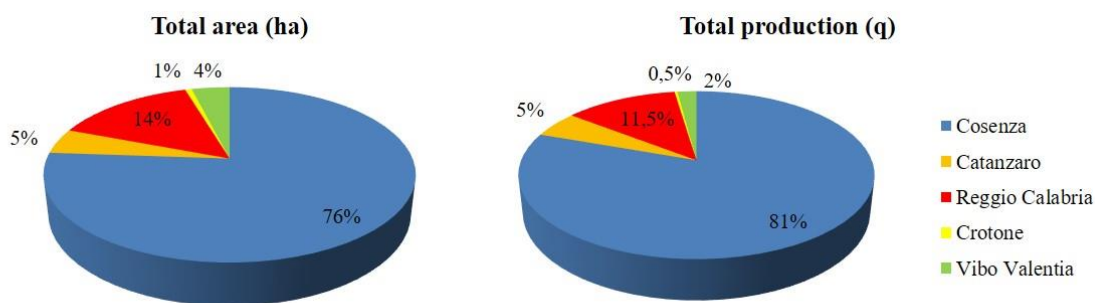


Figure 1.8 Total area and production in Italy and Calabria's provinces expressed in percentage.

Onion

Onion (*Allium cepa* L.) is a vegetable bulb crop (Figure 1.9) widely cultivated and known to most cultures (Ballesteros et al., 2018; Córcoles et al., 2013). For economic importance among vegetables, the onion ranks second after the tomato (Aboukhadrach et al., 2017; Mallor et al., 2011). This plant belongs to the family of Amaryllidaceae and is biannual or perennial (depending on the cultivar). The plant has shallow adventitious fibrous roots (Ranjitkar, 2003), which grow, usually in the first 20-25 cm of soil. The umbrella-shaped inflorescence develops from an apical ring meristem and is formed by the aggregation of small single flowers (from 200 to 600). As for the bulb, it has variable shapes (flat to globular to oblong) and colors (red, white, or yellow). The bulb, the edible part, comes from the enlargement of the basal part of the leaves that are inserted, superimposed on a central cauline axis. The thick outer leaves of the bulb lose moisture and become scaly until harvest, while the inner leaves thicken as the bulb develops (Pareek et al., 2017).

The onions "Cipolla Rossa di Tropea" produced in Calabria are an essential crop that, as a typical product, plays a crucial role in the economic and rural development of the territory (Bernardi et al., 2013). This particular pink-red colored onion type, since 2008, is labeled with the European Protected Geographical Indication label "Cipolla Rossa di Tropea IGP". It is well-known worldwide for its sweet flavor and for its high content of nutraceuticals that make it an upcoming "functional food" (Tiberini et al., 2019). The production area of "Cipolla Rossa di Tropea IGP" includes suitable land in the following municipalities in Calabria (Figure 1.10): Fiumefreddo, Longobardi, Serra d'Aiello, Belmonte, Amantea (Province of Cosenza), Nocera Terinese, Falerna, Gizzeria, Lamezia Terme, Curinga (Province of Catanzaro), Pizzo, Vibo Valentia, Briatico, Parghelia, Zambrone, Zaccanopoli, Zungri, Drapia, Tropea, Ricadi, Spilinga, Joppolo, Nicotera (Province of Vibo Valentia).

The Calabrian surface area cultivated with onions is divided as follows (Table 1.5) (Figure 1.11): in the provinces of Catanzaro and Vibo Valentia there are the largest production areas, 320 ha and 400 ha respectively, with productions between about 160,000 and 180,000 quintals followed by from the other three provinces where areas cultivated with onions and production are lower.



Figure 1.9 Onions on the field (left) and onions "Cipolla Rossa di Tropea" (right).

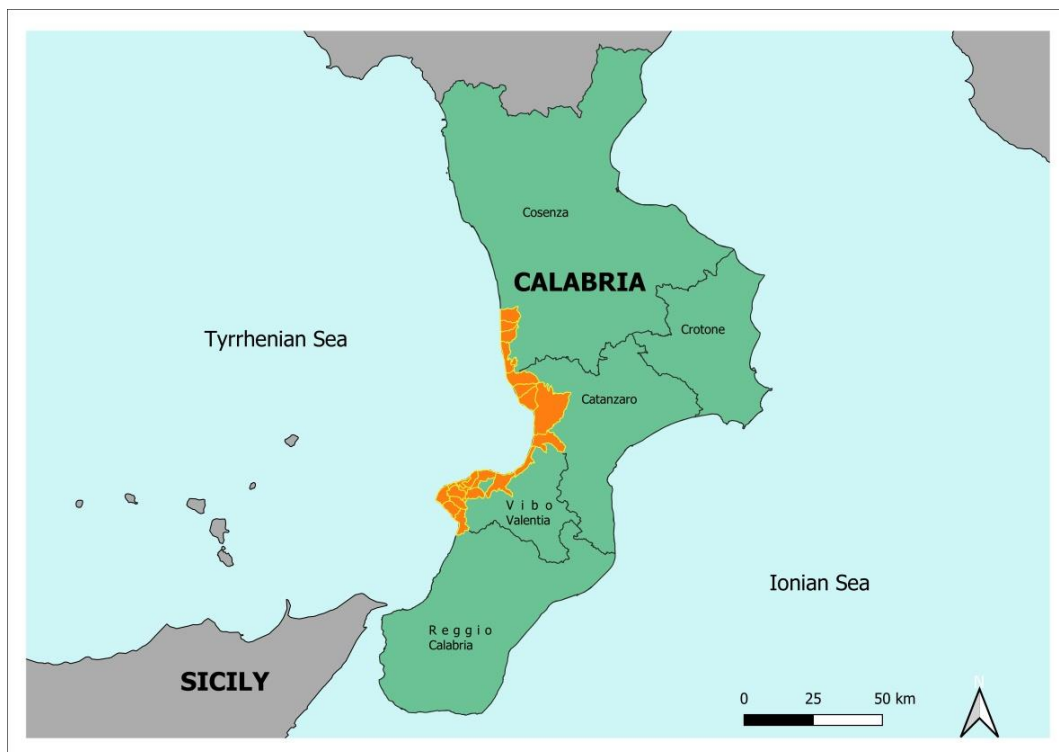


Figure 1.10 Map of Calabria with the municipalities belonging to the production area of "Cipolla di Tropea IGP" highlighted in orange.

Table 1.5 Total area cultivated and total production (quintals) in Calabria's provinces.

Province	Total area (ha)	Total production (q)
Cosenza	139	26,140
Catanzaro	320	180,000
Reggio Calabria	50	7,750
Croton	40	8,800
Vibo Valentia	400	164,400

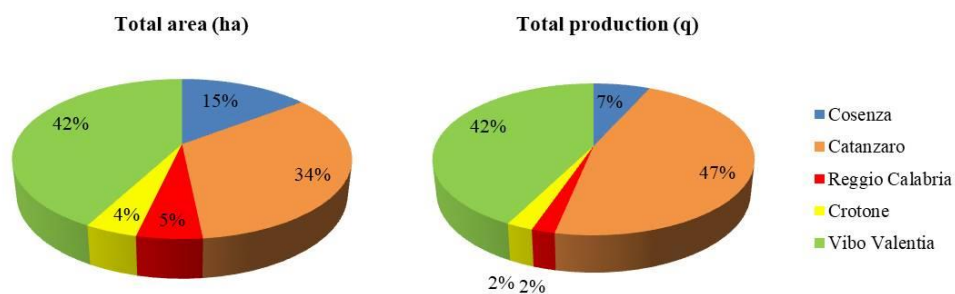


Figure 1.11 Total area and production in Italy and Calabria's provinces expressed in percentage.

2 Remote Sensing of Vegetation

Remote sensing (RS) is the practice of obtaining information about an object, an area, or a phenomenon through the analysis of images acquired by a device, not in touch with them (Lillesand et al., 2015). RS investigations are mostly based on the analysis of a deterministic relationship between the amount of electromagnetic (EM) energy reflected, emitted or backscattered, in specific bands or frequencies and the chemical, biological, and physical characteristics of the studied phenomena. In RS, three ways are considered to sense information about an object: reflection, emission, and combination of emission and reflection (Chuvieco, 2016). The first exploits sunlight, which is the primary source of energy on Earth. In particular, sunlight illuminates the surface, which reflects some of this energy, causing it to turn back, based on the composition of the reflective surface cover (Campbell e Wynne, 2017). The second way is provided by reflected EM energy detected by a satellite sensor, which records and transmits the signal to a receiving station (Chuvieco, 2016).

Furthermore, RS observations can be based on the emitted energy from the surface, as all objects with a temperature higher than absolute zero (0 K) emit energy (Kuenzer et al., 2013). Finally, active sensors, which have their energy source, can send pulses to the objects recording reflections to characterize objects themselves (Chuvieco, 2016). Historically, RS has been mainly based on the passive reflection of radiation in the visible and broader optical-reflective region. On the other hand, thermal RS and microwaves' use is growing (Jones and Vaughan, 2010). The present thesis will deal with the first three ways to sense objects' information dealing with issues that have involved the use of imagery derived by optical and thermal RS sensors.

In RS, it is common to categorize EM waves by their wavelength location inside the EM spectrum (Figure 2.1). EM radiation consists of a series of wavelengths that form the EM spectrum and define specific regions called spectral bands. However, there is no clear dividing line between one nominal spectral region and the next. The portion of the EM spectrum visible to the human eye is called visible light or VIS region. The VIS region, which ranges from 0.4 to 0.7 μm , covers the spectral wavelengths that our eyes can sense. This region can be further divided into the three primary colors: blue (0.4–0.5 μm), green (0.5–0.6 μm), and red (0.6–0.7 μm); in this region, the change in reflectance behavior of an object results in its "color". Before the blue band is located the

ultraviolet (UV) energy, while the infrared region lies beyond the red band, the spectrum's microwave portion is beyond the infrared region (Lillesand et al., 2015).

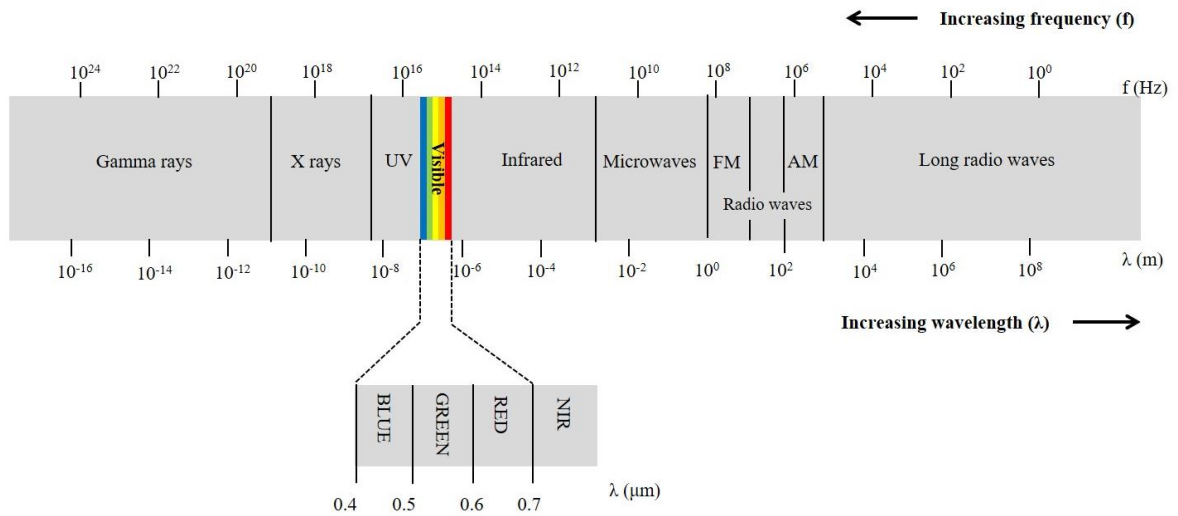


Figure 2.1 The electromagnetic spectrum. In evidence, the visible region, in which the three bands blue, green and red (0.4 – 0.7 μm) are further detailed.

Some physical laws, in particular, the laws of Planck, Wien and Stefan–Boltzmann make it possible to understand the behavior of EM radiation better. First of all, from basic physics, waves follow this general equation (2.1):

$$c = \lambda \nu \quad (2.1)$$

where c represents the "speed of light", one of the forms with which EM energy propagates according to this theory. EM energy travels harmoniously and sinusoidally at the velocity of light. λ is the distance between two consecutive wave peaks while the frequency ν represents the number of wave peaks that pass from a point in a second (Figure 2.2).

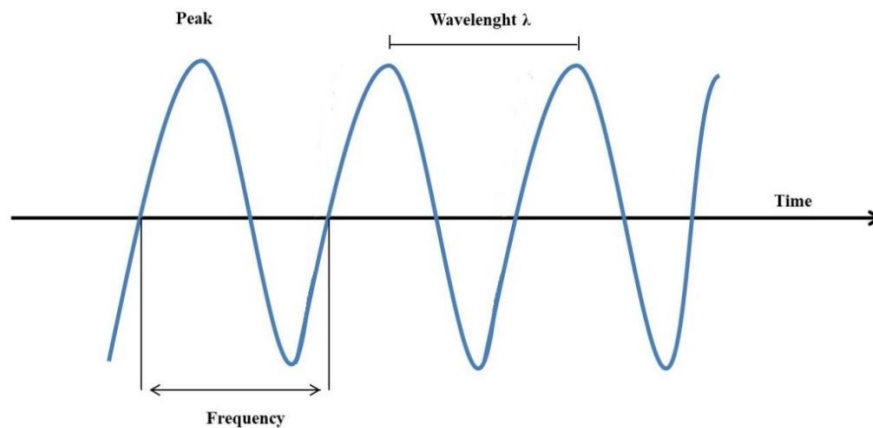


Figure 2.2 The electromagnetic radiation's components according to the wave theory of light.

According to Planck's theory, EM radiation is composed of discrete packets of energy called *photons* or *quanta*. The energy of a quantum (defined Q and expressed in Joule, J) is proportional to its frequency ν (expressed in Hertz, Hz), while the Planck's constant h (6.626×10^{-34} J sec) is used to adjust this relationship (Equation 2.2):

$$Q = h\nu \quad (2.2)$$

When considering that the frequency of the wave (ν) is directly proportional to the speed of light (c) and inversely proportional to its length (λ), equation 2.2 can be rewritten as follows (Equation 2.3):

$$Q = \frac{hc}{\lambda} \quad (2.3)$$

In other words, the energy of a quantum is inversely proportional to its wavelength. Thus, the longer the wave (larger wavelength), the lower its energy.

Wien's and Boltzmann's laws describe the relationship of a black body's radiations (i.e., an ideal object that absorbs and re-emits all of the incident energy) and the wavelength of the maximum emission with a black body's temperature (Walker et al., 2015). Wien's displacement law explains the relationship between a black body's true temperature, being expressed in degrees Kelvin, and its peak spectral exitance or dominant wavelength. As the temperature increases, its maximum exitance shifts towards shorter wavelengths (Equation 2.4):

$$\lambda_{\max} = \frac{A}{T} \quad (2.4)$$

Given that the Wien's constant b is equal to $2898 \mu\text{m K}$, this formula indicates the wavelength at which the maximum radiant spectral exitance can be obtained. It is possible to observe such effects in nature. For example, a body with a very high absolute temperature like the sun (about 6000 K) has a λ_{\max} and, thus, a peak of emission in the visible part of the spectrum (Kuenzer et al., 2013). The above formula results are useful to indicate the measurement range of the sensor used to measure the radiation emitted by a given body (Jensen, 2014). The Stefan-Boltzmann law states that the emittance of a black body is proportional to the fourth power of its absolute temperature (Equation 2.5):

$$E = \sigma T^4 \quad (2.5)$$

where E represents the spectral radiant exitance expressed in $\text{W}\cdot\text{m}^{-2}$, σ is the Stefan-Boltzmann constant, and T is the absolute temperature [K]. The formula clearly shows that the total EM

radiation that is emitted by a black body is a function of its absolute temperature. Therefore, the radiation emitted by a body increases as its temperature increases.

2.1 Thermal Remote Sensing

Thermal RS uses the information at the emitted radiation in the thermal infrared (TIR) range (Figure 2.3) of the EM spectrum (Prakash, 2000). This information is converted into temperature (Khanal et al., 2017). Two categories can be distinguished within the IR region (0.7–100 μm), namely, the reflected-IR (0.7–3.0 μm) and TIR (3.0–100 μm). Generally, all of the landscape elements, such as vegetation, soil, water, and people, emit TIR radiation in the 3.0–14 μm portion of the EM spectrum (Jensen, 2014).

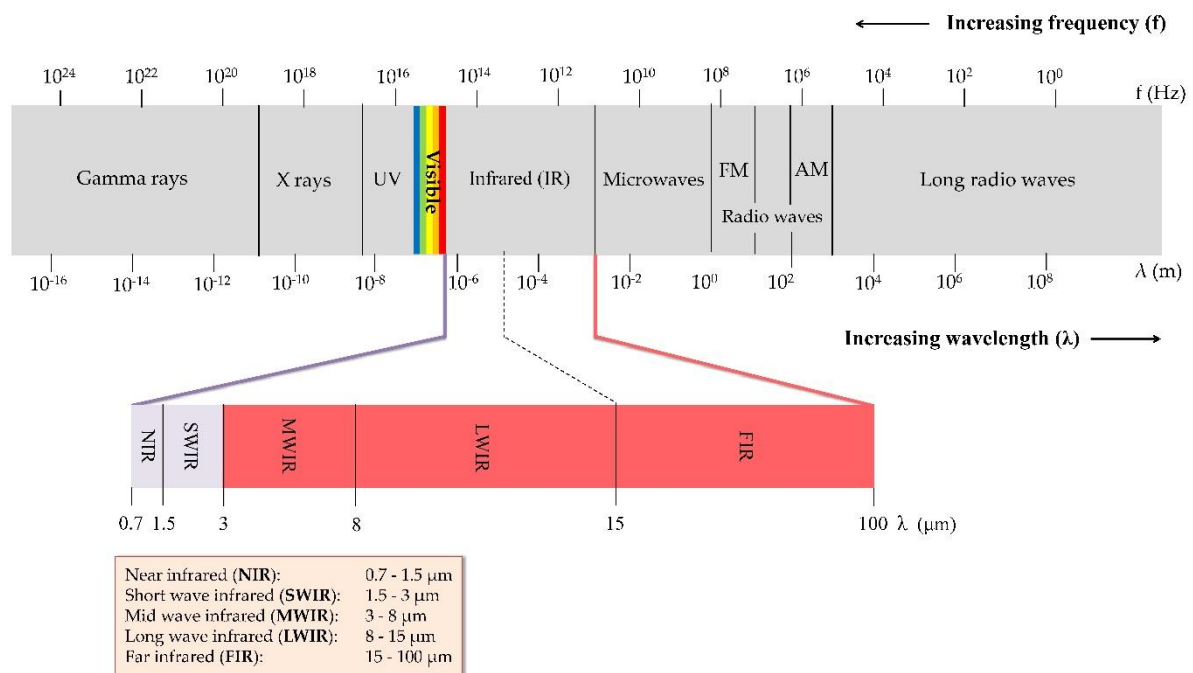


Figure 2.3 The electromagnetic spectrum. In evidence, the infrared region (IR), in which the reflected-IR (0.7–3.0 μm) and the emitted-IR (3.0–100 μm) are further detailed (source, Messina and Modica, 2020b).

In this range of the EM spectrum, part of the IR energy is transmitted to the Earth’s surface through two so-called *atmospheric windows*, ranging from 3 to 5 μm and from 8 to 14 μm (Vinet and Zhedanov, 2010) (Figure 2.4). Atmospheric gases absorb almost all of the radiation between 5 and 8 μm as water, carbon dioxide (CO_2), and ozone (O_3) molecules, as indicated in Figure 2.4 (Jensen, 2014), which are the most efficient absorbers of solar radiation (Lillesand et al., 2015). These gases impede the transmission of EM radiation. EM spectrum’s regions where radiations’ transmission

is allowed are defined atmospheric windows. These are of fundamental importance in RS as they define the wavelengths used for image production (Campbell e Wynne, 2017). Obviously, the wavelengths that are not inside the windows are not usable.

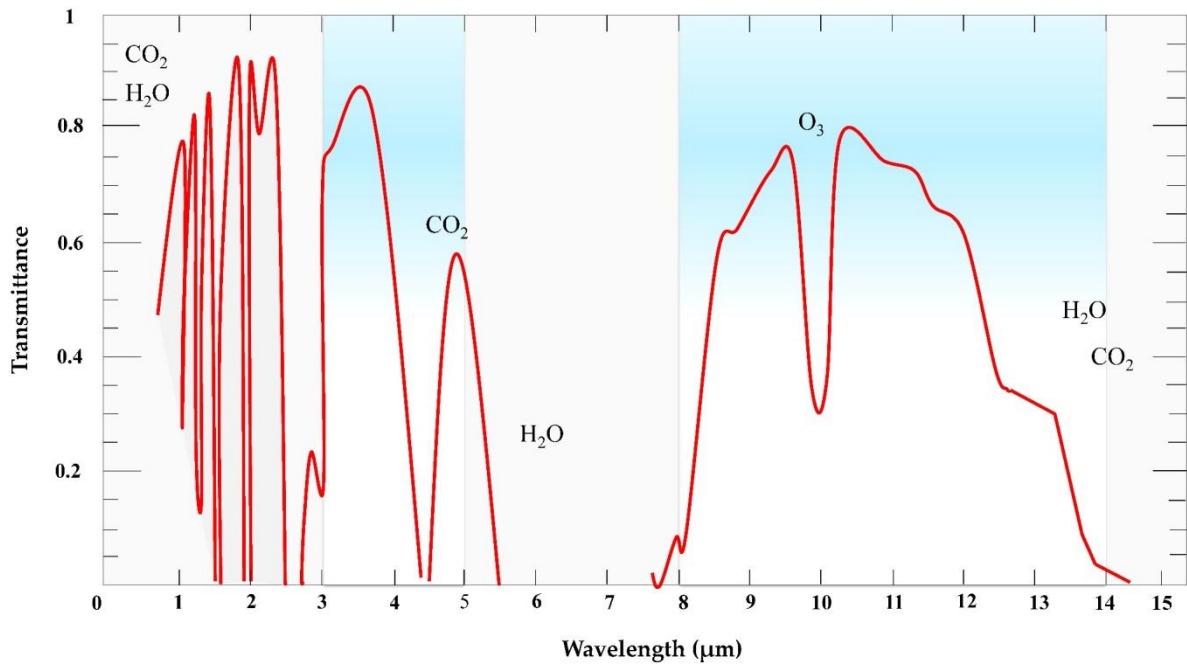


Figure 2.4 Atmospheric transmittance in the thermal region with typical absorption bands induced by gases and water (*source*, Messina and Modica, 2020b) modified from (Richter and Schlapfer, 2019)).

Radiation can interact differently with matter depending on both the wavelength and the nature of the matter. For example, in the optical region, specific wavelengths can cause electronic transitions from one energy level to another, in atoms and molecules, when the energy of the quantum involved is equal to the energy difference between the two levels of electronic energy. The wavelengths are emitted if the atoms are excited or are absorbed because the same electronic transitions are involved. Therefore, spectral emissivity ϵ is equal to spectral absorptivity α (Equation 2.6). Equation 2.6 states that, at a given wavelength, the emittance of a body is equal to its absorption capacity, which is:

$$\epsilon = \alpha \quad (2.6)$$

This is frequently formulated as “good absorbers are good emitters and good reflectors are poor emitters” (Jensen, 2014).

In the thermal region, the interaction of radiation with solid matter occurs mostly by means of molecular vibrations and rotations (Jones and Vaughan, 2010). Thermal radiation (and optical) interactions occur primarily through the electric field vector in the EM radiation, leading to

electronic and vibrational transitions in the material (Jones and Vaughan, 2010). The energy involved in the interaction between radiation and matter is stored so that the total amount of energy dissipated by reflection, transmission and absorption, corresponds precisely to the incident energy. The principle of energy conservation is defined by the following equation (Equation 2.7):

$$\varepsilon + \rho + \tau = 1 \quad (2.7)$$

where ρ is the reflection and τ is the transmission. When considering that most objects are opaque to thermal radiation, the above equation becomes (Equation 2.8):

$$\varepsilon + \rho = 1 \quad (2.8)$$

Materials with a high ε absorb a large quantity of incident energy and radiate large quantities of energy, while materials with low ε absorb and radiate less energy (Kirchhoff, 1860) (Sabin, 1997). All bodies with a temperature above absolute zero are characterized by random movement—i.e., the kinetic heat, whose measure is the kinetic temperature T_{kin} (Jensen, 2014). Besides, an object emits energy as a function of temperature, and the emitted energy is used in order to determine its radiant temperature T_{rad} (Vinet and Zhedanov, 2010). Although there is a strong positive linear correlation between T_{kin} and T_{rad} , T_{rad} is lower than T_{kin} due to emissivity (ε) (Schmugge et al., 2002). For this reason, the temperature that is measured by a sensor (T_{rad}) will always be lower than the real temperature (T_{kin}) (Equation 2.9) (Kuenzer et al., 2013). It follows from this, as explained by Kirchhoff's law (Equation 2.9), that:

$$T_{rad} = \varepsilon^{\frac{1}{4}} T^{kin} \quad (2.9)$$

The emissivity is the ratio between the radiation that is emitted by the surface and the radiation emitted by a black body at the same temperature (Jacob et al., 2004). Because the radiance of any real body, at the same temperature, is always lower than that of a black body (equal to 1), its emissivity has a value between 0 and 1 (Jensen, 2014). Planck's law explains that any physical body absorbs and emits radiation less effectively at a given temperature than a black body. Practically, the sensed temperatures of materials with low emissivity appear to be much lower than those of nearby objects with the same temperatures, making the T_{kin} assessment less precise (Kuenzer et al., 2013). Many factors influence emissivity: color, chemical composition, surface roughness, moisture content, field of view, viewing angle, spectral wavelength, etc. (Campbell e Wynne, 2017; Jacob et al., 2004; Jensen, 2014). The emissivity of materials is difficult to measure, although it is more or less constant in the region of the EM that ranges from 8 to 14 μm . The emissivity of vegetation

ranges from 0.96 to 0.99, while that of soil is around 0.89, and the emissivity of the water is 0.99 (Table 2.1).

Table 2.1 The emissivity of different surfaces over the range of 8–14 μm (Campbell e Wynne, 2017; Lillesand et al., 2015).

Material	Average emissivity (ϵ)
Healthy vegetation	0.96–0.99
Dry vegetation	0.88–0.94
Wood	0.93–0.94
Sand	0.90
Dry soil	0.92
Wet soil	0.95–0.98
Water	0.98–0.99
Snow	0.98–0.99

Regarding the intrinsic characteristics of a body, which affect its emissivity, thermal capacity (or heat capacity, measured in $\text{J kg}^{-1}\text{K}^{-1}$) measures the quantity of heat energy necessary for a body to increase its temperature by one degree—the lower the heat capacity, the less energy required. Another important parameter is the thermal conductivity (measured in $\text{W m}^{-1}\text{K}^{-1}$), which measures the rate at which heat passes through a material. This capacity is greater the higher the value of such a parameter in a material. These parameters can be integrated into the thermal inertia (expressed in $\text{J m}^{-2} \text{K}^{-1} \text{s}^{-1/2}$), which measures a body's tendency to change in temperature or the rate of heat transfer between two substances put in contact. This concept is of great importance in the field of TIR because the capacity of a body to change its temperature quickly (if the thermal inertia is low) depends on this parameter.

2.2 Remote Sensing of Vegetation and Soil

A key element of the application of RS in agriculture is the knowledge of plant leaves and canopy's spectral properties. For example, a leaf appears green because its reflectance at green wavelengths is higher than its reflectance in the other two portions of the VIS spectrum. In particular, there is a region of less intensely absorbed radiation about 0.55 μm , between blue and red spectral regions, where there is green reflectance peak. This peak defines the green color of healthy leaves (Figure 2.5) (Chuvieco, 2016). The characteristic reflectance behavior of an object over various wavelengths of the EM spectrum is called spectral reflectance signature or spectral signature (Campbell e Wynne, 2017). The spectral signatures of vegetation can be differentiated according to leaf type and

morphology, leaf physiology, chlorophyll content, plant stress, and senescence (Chuvienco, 2016). In particular, vegetation's spectral signature is characterized by low reflectance in the VIS and high reflectance in the near-infrared (NIR) region. As for reflectance in the VIS, chlorophyll plays an essential role in controlling the leaf's spectral response, giving it a green color.

Indeed, chlorophyll does not absorb all light in the same way but mainly blue and red light while reflects green light (Figure 2.5). Chlorophyll a, in particular, contained in chloroplasts, absorbs sunlight as a form of energy by creating carbohydrates from CO₂ and water. The photosynthetic process of food-making determines how a leaf and a plant appear radiometrically on RS imagery (Jensen, 2014). In addition to chlorophyll, the action of other pigments, such as carotene and xanthophylls (which give orange and yellow colors) and anthocyanins (which give predominantly red colors), that absorb primarily in the blue and green, become more evident in autumn in the case of deciduous species. Therefore, the behavior of pigments is a powerful tool for species discrimination based on leaf color. Of course, the color of the leaves can be due to the action of biotic and abiotic stress factors in addition to senescence. In these cases, the red and green reflectance will be higher, making the leaves appear yellowish and chlorotic (Jensen, 2014). Senescent or stressed leaves are characterized by a reduced chlorophyll activity, absorbing less in the red and blue bands (carotenes remain in the leaf absorbing in the blue). This causes an increasing reflectance in red and blue bands and alters leaf's color. This behavior explains why leaves show a yellowish color in senescence or stress conditions. Besides, stress may also reduce leaf reflectance in the NIR because of the deterioration of the leaf's cellular structure (Chuvienco, 2016).

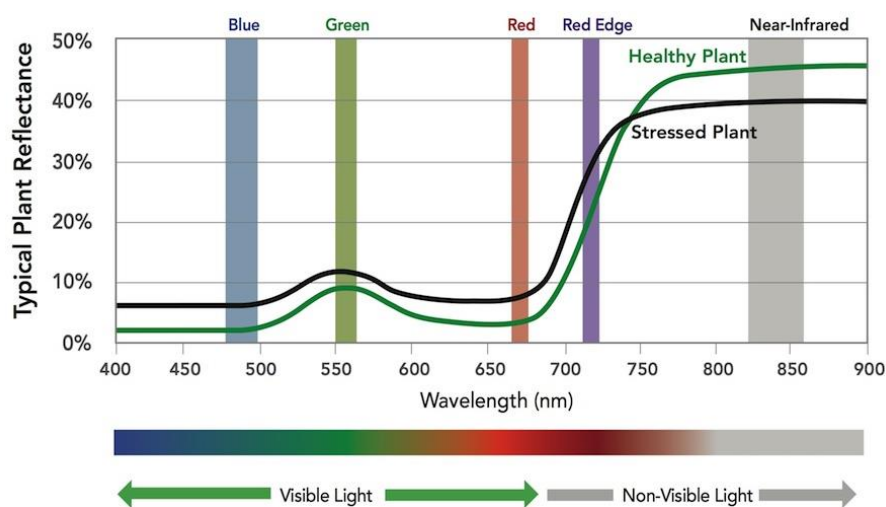


Figure 2.5 Typical spectral signatures of a healthy and stressed plant (*source*, www.micasense.com).

As far as the NIR region (0.7–1.2 μm), it is a portion of the EM which lies beyond the human eye's perception capability and it is of particular interest because of its usefulness in the RS of vegetation being its sensitivity useful to determine plant health status (Chuvieco, 2016). A small part of NIR radiation is absorbed inside the leaf (5 – 10 percent) while the rest is reflected upwards or transmitted downwards (40 – 60 percent) (Jensen, 2014). It is not the pigments that regulate the reflection by the leaf but the mesophyll's spongy tissue (Figure 2.6). That is because the cuticle and the epidermis are mostly completely traversed by NIR radiation. This condition occurs throughout the NIR range, where direct incident sunlight has most of its energy. If plants absorb all this energy as efficiently as possible in VIS, leaves could heat up and cause irreversible protein denaturation. For this reason, plants have adapted not to use this massive amount of energy in NIR but rather reflect it or transmit it to the leaves below or to the ground (Jensen, 2014). In a healthy leaf, the reflectance in NIR increases between 0.7 and 1.2 μm . This increase corresponds to a drastic lowering of absorption ("red shift", Collins, 1978) in a portion of the EM spectrum called Red edge (Figure 2.6), between red and NIR. Red edge is precisely between 0.68 and 0.75 μm , with the exact position depending on the species and condition (Lillesand et al., 2015). The reflection by vegetation in the NIR is more significant than in the visible region. For this reason, the differences in the reflection of NIR by different plant species allow their discrimination from non-vegetation.

Different structural characteristics of the leaves as well as different pigment compositions, determine their radiative properties in each species. These characteristics allow a distinction to be made on the basis of reflected radiation behavior. The same applies to those changes in physical and chemical structural characteristics caused by plant growth and development. In a tree's canopy, in addition to the angle of incidence of radiation to the leaf, the foliage's arrangement influences the way the canopy reflects the radiation. This results from both radiation dispersion and secondary and tertiary interactions between the leaves of the canopy and between the leaves and the soil below the tree (Jones and Vaughan, 2010). It must be considered that only part of the radiation is reflected from the leaf's upper page while the pigments, including chlorophyll, absorb the rest, dispersed and transmitted. Therefore some of the possible trajectories of radiation penetration and scattering and inside the tree's canopy may foresee the reflection of incident sunlight by the leaf towards the sky. At the same time, a small percentage is transmitted through the leaf and/or involved in secondary and tertiary reflections by the leaves below the first and then reflected towards the sky (Jones and Vaughan, 2010). Since energy is absorbed in each dispersion, the greater the number of interactions, the lower the intensity of radiation. The light that penetrates

inside foliage is subject to numerous interactions, greater in particularly dense foliage. From this, it is clear that dense foliage's overall reflectance is much lower than that found on a single leaf (Jones and Vaughan, 2010). Besides, in trees, foliar vegetation's behavior due to the shadow conditions, generated by overlapping leaf layers, attenuates the spectral behavior typical of a single leaf by reducing the reflectance percentages in the various portions of the EM (Campbell e Wynne, 2017).

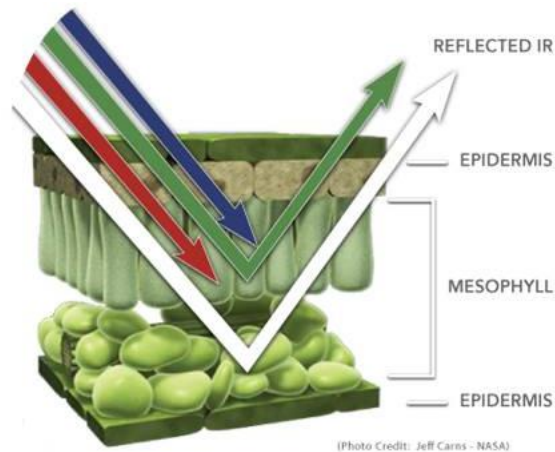


Figure 2.6 Interaction of electromagnetic energy in the different leaf layers (source NASA).

In summary, the spectral signatures of vegetation can be differentiated according to leaf type and morphology, leaf physiology, chlorophyll content, leaf arrangement, plant stress, and senescence (Chuvieco, 2016). In the same way, soils have spectral reflectance signatures (Figure 2.7), which increases with increasing wavelengths depending on its content in organic matter, water, minerals and salt (Chuvieco, 2016). In addition, the spectral signature of soil varies in consequence of its structural and morphologic properties (e.g., roughness). The high moisture content of the soil reduces reflectance, as well as the increase in organic matter and/or iron oxide content, making moist soils appear darker and, therefore, less reflective than dry soils. Coarse and sandy soils, being well-drained, have high reflectance (Lillesand et al., 2015). The same happens in soils with low surface roughness (Eshel et al., 2004). The increased iron oxide content in the soil results in a greater reflection in red and less reflection in green (Ben-Dor, 2002). Finally, because soils are nearly opaque to visible and infrared radiation, it should be noted that soil reflectance comes from the uppermost layer of the soil and may not indicate the properties of the bulk of the soil (Lillesand et al., 2015).

Water on the other hand, unlike vegetation and soil, it is almost completely transparent at shorter wavelengths than visible radiation, while it has high absorption at wavelengths above 1.1 μm .

Another aspect to be taken into account during measurements is that the sensor's area is often a surface made up of different materials (e.g., a mixture of soil and vegetation) in varying proportions. In these cases, the sensor will detect mixed signals that are the result of multiple spectral signatures. The spectral signatures are useful for interpreting images and selecting the optimal combination of bands to better discriminate between different surfaces.

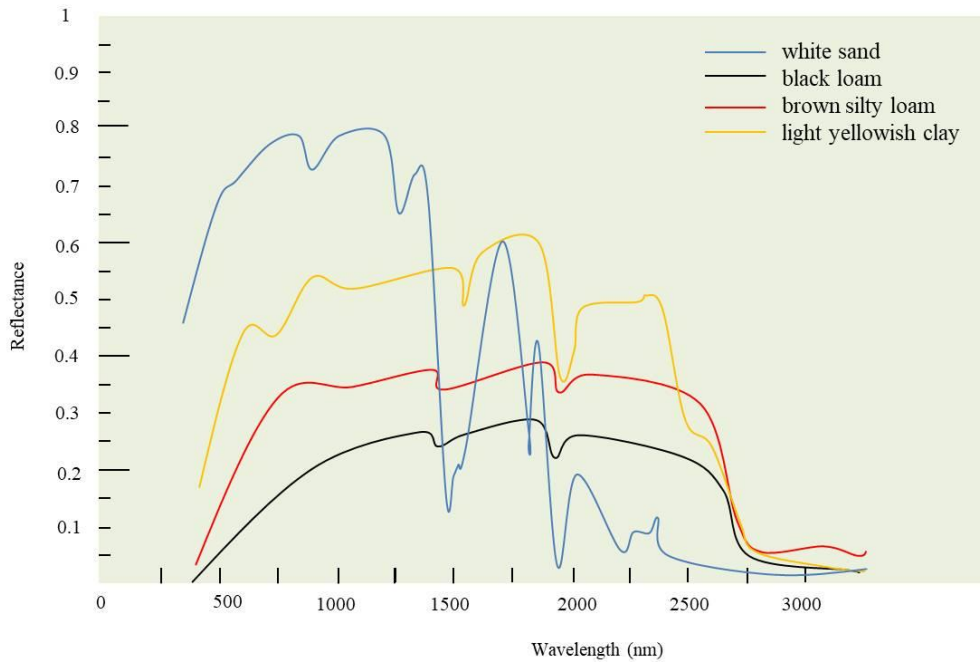


Figure 2.7 Typical spectral signature of different types of soil (*modified after Jones and Vaughan, 2010*).

Spectral signatures are not constant for each cover, being the radiance flux detected by RS dependent not only by the observed surface's intrinsic properties (Chuvienco, 2016). Indeed, it depends also on the external conditions of the measurement, the main ones being follows:

- Atmospheric components;
- Land cover changes that cause variations in physical or chemical composition, such as moisture or roughness. In agriculture, these changes can be determined by crop phenology or agricultural practices;
- Soil and geologic substrate;
- Solar illumination depending on the latitude, hour of the day, season;
- Terrain slope;
- Terrain aspect, affecting the illumination conditions of a surface.

Geometric conditions of the observation as incidence, viewing angles relative to the reflecting surface and their relationship with the surface properties determine how the incoming radiation is scattered (Chuvienco, 2016). In this regard, three types of surface scattering can be distinguished. The first kind of scattering is the specular reflection (Figure 2.8): the sun's incident energy is reflected at the same angle as the incident solar angle, so no energy is dispersed in other directions. In the second kind of surface scattering, the incident energy is reflected and diffused equally in all directions. Finally, when a surface is perfectly diffuse and exhibits the same reflected radiance for any angle of reflection, that is, independent of viewing angle to the surface normal, it is known as a Lambertian surface (Figure 2.8). Most surfaces exhibit a third type of scattering behavior, known as anisotropic (non-Lambertian) reflectance, in which both diffuse and specular scattering dependent on the sun and view angle (Chuvienco, 2016).

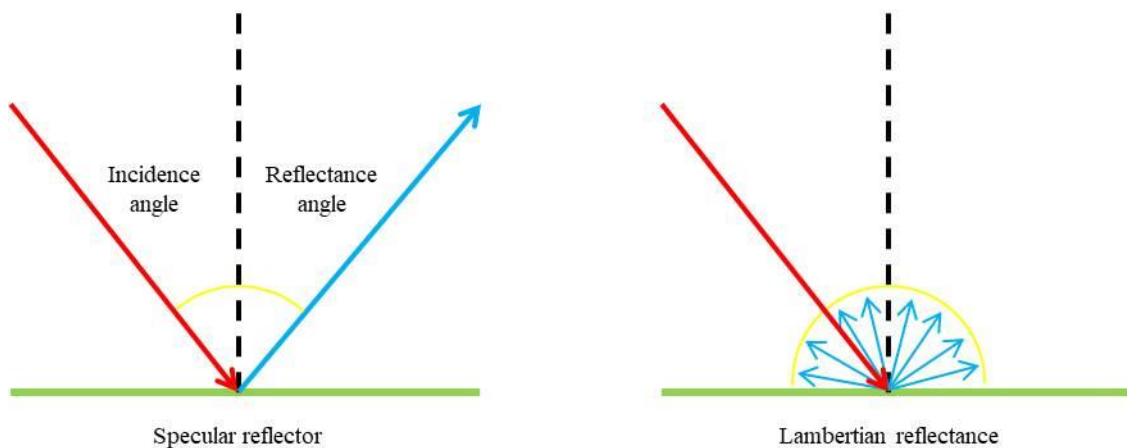


Figure 2.8 Types of surface reflection.

Vegetation Indices

As seen in the previous section, materials have characteristic spectra, with maximum or minimum absorption at precise wavelengths. Therefore, the vegetation indices (VIs) are essential in RS to determine vegetation's biophysical parameters (Jones and Vaughan, 2010). The vegetation indices are dimensional and radiometric combinations that measure the relative abundance and activity of vegetation, biomass, or vegetative vigor (Campbell e Wynne, 2017; Jensen, 2014). Indeed a VI is calculated using a formula containing several spectral values that are summed, multiplied, or divided to obtain a value that measures vegetative vigor within a pixel (Campbell e Wynne, 2017). The most common formula is the one that provides for a relationship between bands. The ratios can improve or reveal latent information if there is an inverse relationship between two spectral

responses to the same biophysical phenomenon (Campbell e Wynne, 2017). The ratio gives little information when two objects have the same spectral behavior. In contrast, the ratio gives a value representing the contrast between the bands' reflectances at the numerator and denominator if their spectral responses are different (Campbell e Wynne, 2017). The use of the ratio between bands can exploit, for example, an inverse relationship between the reflectance of the red band and the NIR in the vegetation, known in this particular case as Simple Ratio (SR) (Equation 2.10):

$$SR = \frac{(\rho_{NIR})}{(\rho_{Red})} \quad (2.10)$$

Where, ρ_{NIR} and ρ_{Red} represent the reflectances of a pixel in the NIR and Red bands.

Generally a significant contrast between these two regions involves more vegetation's vigor (Chuvieco, 2016). The development of VIs is based on this theoretical spectral behavior of vegetation in the red and NIR. Many VIs are constructed by combining these bands. These indices were created to isolate and enhance the signal coming from the vegetation allowing easier discrimination and information extraction (Asrar et al., 1992; Huete et al., 1994, 1997). This is because there is a strong absorption in red and a high reflection in NIR in vegetation. Therefore the ratio between NIR and red in growing plants will be of high value. For the same reason, when the same ratio is applied to stressed or dead plants, unplanted surfaces, bare soil, surfaces of anthropic origin, and water, the value provided is low (Campbell e Wynne, 2017; Chuvieco, 2016). Therefore, the SR allows one to separate healthy vegetation and other surfaces into an image (Chuvieco, 2016). Also, SR can indicate a lower amount of vegetation in the pixel or vegetation under stress or senescence if it assumes a low value.

Ratios permit a reduction of several forms of multiplicative noise, which influence multiple bands similarly. These noise forms include illumination differences resulting from the angle of the Sun, atmospheric effects, shadows cast by clouds, and topographic variations due to differences in slope and aspect (Jensen, 2014). The most common and well-known index with these features is the Normalized Difference Vegetation Index (NDVI), which was developed by Rouse (1974) and whose formula is as follows (Equations 2.11-2.12):

$$NDVI = \frac{(\rho_{NIR} - \rho_{Red})}{(\rho_{NIR} + \rho_{Red})} \quad (2.11)$$

or

$$NDVI = \frac{SR - 1}{SR + 1} \quad (2.12)$$

NDVI is a functional variant of SR, which differs from SR in that the latter does not have an upper limit. NDVI has a range between -1 and 1. NDVI allows the monitoring of seasonal changes in vegetation growth. The advantage of NDVI over SR is that the former is very sensitive to low vegetation amounts and the presence of sparse vegetation (Chuvieco, 2016). In addition, this index is highly correlated with leaf area index (LAI). However, this relationship is not strong in relatively dense vegetation, i.e., when the LAI value is higher than 2, likely due to saturation problems (Wang et al., 2005). Other limitations regard the attenuation of atmospheric effects, sensitivity to soil background effects, and signal saturation problems from moderate to high-density vegetation (Huete et al., 2002). As regards the negative influence of the background soil on the index values, this happens both in dark soils, which amplify the vegetal component of the signal, and in lighter soils that tend to suppress it (Huete, 1988; Rondeaux et al., 1996). For this reason, an optimized VI was developed by Huete (1988). He conceived Soil-Adjusted Vegetation Index (SAVI) using the same NDVI's formula but incorporating an L correction factor (Equation 2.13). In particular, this factor permits removing the influence of the backscattered soil signal. $L = 0.5$ is taken as a default value while $L = 1$ and $L = 0$ are used in case absence or very high vegetative cover. SAVI' range is equal to NDVI (from -1 to 1), and when L is equal to 0, the SAVI is equal to NDVI (Xue and Su, 2017).

$$SAVI = \frac{(\rho_{NIR} - \rho_{Red})}{(\rho_{NIR} + \rho_{Red} + L)} (1 + L) \quad (2.13)$$

Two other indexes have a similar formula to NDVI. Normalized Difference Red edge Index (NDRE) has a range of values and formula similar to those of NDVI. However, it takes advantage of the vegetation's sensitivity to the Red edge wavelengths by replacing the Red band (Equation 2.14). The Green Normalized Difference Vegetation Index (GNDVI) (Gitelson et al., 1996) was developed to estimate leaf chlorophyll concentration and uses a Green band rather than a Red band (Equation 2.15). The GNDVI is more sensitive to chlorophyll concentration than NDVI and its range is from 0 to 1 (Candiago et al., 2015).

$$NDRE = \frac{(\rho_{NIR} - \rho_{Red\ Edge})}{(\rho_{NIR} + \rho_{Red\ Edge})} \quad (2.14)$$

and

$$GNDVI = \frac{(\rho_{NIR} - \rho_{Green})}{(\rho_{NIR} + \rho_{Green})} \quad (2.15)$$

2.3 Remote Sensing Aerial Platforms: a brief introduction

The traditional RS was based on the use of photographic instruments mounted on airplanes to capture Earth's characteristics (Thenkabail, 2015). Instead, the satellites have been used for RS imagery in agriculture since the early 1970s (Mulla, 2013), using sensors mounted on the satellite Landsat 1 launched in 1972. As regards the third type of platform, the unmanned aerial vehicle (UAV) (Figure 2.9), was invented for military applications and has become a common tool for use in geomatics for data acquisition in various research and operational fields: regional security, monitoring of structures and infrastructures, monitoring of archaeological sites, environmental monitoring, application in agriculture, etc. (Nex and Remondino, 2014; Pajares, 2015; Shakhathreh et al., 2018). Its spread in the agricultural sector has taken place over the last decade (Maes and Steppe, 2019).



Figure 2.9 UAV quadcopter DJI Phantom 4 Pro.

The RS platforms and their imaging systems are distinguished based on platform altitude, temporal and spatial resolution. Regarding the height of the surveys, the three platforms operate at different altitudes. UAV flies at heights of the order of tens of meters; aircraft flies at the height of between 300 and 3000 meters (Thenkabail, 2015) while satellites are in space at hundreds of kilometers of altitude. Just being in space, following precise orbits, affects the temporal resolution of satellites. The temporal resolution can be defined as the observation frequency or revisiting period of a sensor (Chuvieco, 2016). More specifically, in satellites, it represents the time it takes for them to complete their entire orbit around the earth by "revisiting" the same area. The revisiting

period of a satellite is influenced by speed, height, and declination. Its duration ranges from 15-30 minutes of geostationary satellites to several hours of polar-orbiting satellites (as the European METOP) to over 20 days for the completion of the orbit of other satellites. This, of course, affects the periods of availability of images for a given area. Moreover, it must be considered that the actual temporal resolution of a satellite for the acquisition of useful images can be further extended depending on climatic conditions and image acquisition plans (Chuvieco, 2016). The first aspect mainly refers to atmospheric events that may hinder the acquisition of an image. Cloud coverage interposed between the sensor and the area of interest is a classic example. As for the image acquisition planes, not all satellites automatically store historical image series or images of specific areas. Therefore, individual images are only available upon request and not free of charge. In aircraft and UAVs, the operators choose the time resolution according to the need and type of survey. From this point of view, UAVs are advantaged, theoretically allowing the operator to survey the same area every day.

Regarding the spatial resolution, it defines the smallest element detectable in an image by a sensor. The spatial resolution of the image depends mainly on the sensor aperture and the platform's altitude. Satellite sensors can cover a wide range of spatial resolutions, from the coarsest with pixels (minimum unit of a digital image) "containing" areas of 200-1000 m, to those less than or equal to 10 m as in the images provided by the Sentinel-2 and PlanetScope satellites. Spatial resolution plays an important role because the image's level of detail depends on it, allowing those who interpret the image to recognize only those elements/objects whose size is greater than a single pixel. Until a few years ago, before the advent of nanosatellites, the highest resolution, sub-metric, could only be achieved using sensors mounted on UAVs. Currently, the UAV surveys, taking into account the flight altitude and the quality and characteristics of the mounted sensor, allow to obtain levels of detail equal and below 5 cm.

Sensors measure radiations in different regions of the EM spectrum. The spectral resolution is the number of bands provided by the sensor and their spectral bandwidths. The discrimination capability increases as the number of used bands increases (Chuvieco, 2016). Among the optical sensors used in RS are those able to "see" in the visible spectrum (RGB sensors, from the initials of Red, Green and Blue), in NIR, or other EM spectrum regions with a longer wavelength. Therefore optical RS sensors can be classified into several types depending on the number of spectral bands used in the imaging process (Thenkabail, 2015): panchromatic sensors are single band (or single channel) detectors, multispectral (MS) RS sensors are multiband detectors with some spectral

bands including Blue, Green, Red, NIR (and also Red edge sometimes) while hyperspectral RS sensor records data in hundreds of bands etc. (Jensen, 2014).



Figure 2.10 An example of a multispectral UAV camera, the Parrot Sequoia, capable of taking pictures in 4 different bands: Green, Red, Red edge and NIR.

3 Monitoring the vegetation vigor in heterogeneous citrus and olive orchards. Extraction of tree crowns from multispectral UAV images

Adapted from

Monitoring the vegetation vigor in heterogeneous citrus and olive orchards. A multiscale object-based approach to extract trees' crowns from UAV multispectral imagery. Comput. Electron. Agric. 175, 105500. <https://doi.org/10.1016/j.compag.2020.105500>

Computers and Electronics in Agriculture 175 (2020) 105500



Contents lists available at ScienceDirect

Computers and Electronics in Agriculture

journal homepage: www.elsevier.com/locate/compag



Original papers

Monitoring the vegetation vigor in heterogeneous citrus and olive orchards. A multiscale object-based approach to extract trees' crowns from UAV multispectral imagery



Giuseppe Modica*, Gaetano Messina, Giandomenico De Luca, Vincenzo Fiozzo, Salvatore Praticò

Dipartimento di Agraria, Università degli Studi Mediterranea di Reggio Calabria, Località Feo di Vito, I-89122 Reggio Calabria, Italy

ARTICLE INFO

Keywords:

Multispectral unmanned aerial vehicles (UAVs) imagery
Multiresolution segmentation
Precision Agriculture (PA)
Spectral Vegetation Indices (VIs)
Geographic object-based image analysis (GEOBIA)
Vigor maps

ABSTRACT

Precision agriculture (PA) constitutes one of the most critical sectors of remote sensing applications that allow obtaining spatial segmentation and within-field variability information from field crops. In the last decade, an increasing source of information is provided by unmanned aerial vehicle (UAVs) platforms, mainly equipped with optical multispectral cameras, to map, monitor, and analyze, temporal and spatial variations of vegetation using ad hoc spectral vegetation indices (VIs). Considering the centimeter or sub-centimeter spatial resolution of UAV imagery, the geographic object-based image analysis (GEOBIA) approach, is becoming prevalent in UAV remote sensing applications. In the present paper, we propose a quick and reliable semi-automatic workflow implemented to process multispectral UAV imagery and aimed at the detection and extraction of olive and citrus trees' crowns to obtain vigor maps in the framework of PA. We focused our attention on the choice of GEOBIA data input and parameters, taking into consideration its replicability and reliability in the case of heterogeneous tree orchards. The heterogeneity concerns the different tree plantation distances and composition, different crop management (irrigation, pruning, weeding), and different tree age, height, and crown diameters. The proposed GEOBIA workflow was implemented in the eCognition Developer 9.5, coupling the use of multispectral and topographic information surveyed using the Tetracam μ -MCA06 snap multispectral camera at 4 cm of ground sample distance (GSD). Three different study sites in heterogeneous citrus (Bergamot and Clementine) and olive orchards located in the Calabria region (Italy) were provided. Multiresolution segmentation was implemented using spectral and topographic band layers and optimized by applying a trial-and-error approach. The classification step was implemented as process-tree and based on a rule set algorithm, therefore easily adaptable and replicable to other datasets. Decision variables for image classification were spectral vegetation indices (NDVI, SAVI, CVI) and topographic layers (DSM and CHM). Vigor maps were based on NDVI and NDRE and allowed to highlight those areas with low vegetative vigor. The accuracy assessment was based on a per-pixel approach and computed through the F-score (F). The obtained results are promising, considering that the resulting accuracy was high, with F-score ranging from 0.85 to 0.91 for olive and bergamot, respectively. Our proposed workflow, which has proved effective in datasets of different complexity, finds its strong point is the speed of execution and on its repeatability to other different crops with few adjustments. It appears worth of interest to highlights that it requests a working day of two good skilled operators in geomatics and computer image processing, from the on-field data collection to the obtaining of vigor maps.

To achieve effective and sustainable environmental management of agricultural production and an improvement in the competitiveness of the agricultural sector, precision agriculture (PA) methodologies and technologies are currently a reliable and cost-effective approach (Solano et al., 2019). PA can be considered a management strategy aiming to implement agronomic applications according to crop needs and the soil's physical and biochemical characteristics and represent one of the most important sectors of remote sensing (RS) applications (De Montis et al., 2019). As reported by several scholars, PA permits to increase crop productivity and farm profitability by means of better management of farm inputs (Larson and Robert, 1991; Zhang et al., 2002) and exploiting intensive data and information collection. In PA, RS techniques permit obtaining spatial segmentation and within-field variability information from field crops (Sepulcre-Canto et al., 2005). Generally, RS has been associated with satellite platforms or manned aircrafts equipped with several sensors (Pajares, 2015) while, since the last decade, the advent of unmanned aerial vehicles (UAVs) platforms constitutes one of the primary sources of RS imagery in PA. Moreover, continuous technological improvement regards UAV platforms and the type of sensors in terms of radiometric resolution, weight and optical characteristics (Romero-Trigueros et al., 2017). Compared to satellites, UAVs can provide images with very high spatial and temporal resolution. Moreover, these characteristics combined with an increasingly high radiometric resolution, which leads to cost efficiency. As reported by Benincasa et al. (2017), UAV surveys are better suited than satellite RS in cloudy conditions, in the monitoring of small surfaces, and in case of need of centimeter resolution.

UAV applications in PA have mostly dealt with the following research topics: weed and disease detection (Abdulridha et al., 2019a; Albetis et al., 2018; De Castro et al., 2018, 2015; Maes and Steppe, 2019; Pérez-Ortiz et al., 2016; Torres-Sánchez et al., 2015), assessment of vegetation coverage (Ampatzidis and Partel, 2019; Candiago et al., 2015; Senthilnath et al., 2017), analysis, monitoring and assessment of biomass and vegetation vigor (Bendig, 2015; Díaz-Varela et al., 2015; W. Li et al., 2016; Malambo et al., 2018; Panagiotidis et al., 2017; Roth and Streit, 2018; Zarco-Tejada et al., 2014). Moreover, several scholars focused on the trees' crown extraction from UAV imagery in the context of PA applications (Caruso et al., 2019; Díaz-Varela et al., 2015; Koc-San et al., 2018; Ok and Ozdarici-Ok, 2018; Solano et al., 2019).

Currently, UAVs equipped with multispectral (MS) cameras are the most commonly exploited RS systems in agriculture (Khanal et al., 2017). These systems allow obtaining spectral information in the red and NIR regions of electromagnetic (EM) spectrum, which allows deriving vegetation

indices (VIs) useful for applications in PA (Yao and Qin, 2019), in order to map, monitor, and analyze, spatial and temporal variations of vegetation. Most of the VIs currently available for PA applications are obtained by combining information in the red and NIR regions of the EM spectrum. VIs have a high correlation with the biophysical parameters of the plants and a reduced sensitivity to all the factors that hinder the interpretation of RS data, such as atmosphere and soil bed (Wójtowicz et al., 2016).

In the last two decades, RS technologies have been improved to use more effective techniques for the extraction of more reliable and reusable information in PA applications (Solano et al., 2019). Among these techniques, the geographic object-based image analysis (GEOBIA) permits detecting geographical entities through the definition and the analysis of object-images rather than single pixels (Blaschke, 2010; Hay and Castilla, 2008). GEOBIA is becoming prevalent in UAV RS (W. Li et al., 2016). Furthermore, the GEOBIA approach permits to detect of the rapid change of geographic objects in VHR UAV imagery, including the shadow effect of trees, generally higher than in satellite or aerial imagery, caused by a larger parallax effect taking into account the lower distance between the surveyed objects and the sensor.

Image objects are objects visually distinguished in the scene and consisting of groups (or clusters) of neighboring pixels which share a common context (or meaning), such as pixels joining together to form the canopy of a tree or crops in a field (Chen et al., 2018). GEOBIA proved its effectiveness in classifying weeds, herbaceous (De Castro et al., 2018, 2017, Peña et al., 2015, 2013, 2012, Pérez-Ortiz et al., 2016, 2015), and tree species (Csillik et al., 2018; Díaz-Varela et al., 2015; Koc-San et al., 2018; Ozdarici-Ok, 2015; Solano et al., 2019).

Within the scientific and technological framework briefly outlined, the present chapter has a twofold research objective. The first one is devoted to showing a quick and reliable semi-automatic workflow implemented to process MS UAV imagery and aimed at the detection and extraction of olive and citrus trees' crowns in PA's framework with the final production of vigor maps showing the vegetative state of the tree crowns. The second one focuses on the choice of GEOBIA data input and parameters reliable in heterogeneous tree orchards. The heterogeneity regards the different tree plantation distances, the different crop management among which irrigation, pruning, weeding, and the different crop composition, also taking into account the different tree age, height, and crown diameters. The proposed GEOBIA workflow was implemented in the software eCognition Developer 9.5 (Trimble Inc., 2019) using both MS and topographic information. The

workflow was tested on three different study sites in heterogeneous citrus (Bergamot and Clementine) and olive orchards, all located in the Calabria region (Italy).

3.1 Materials and Methods

3.1.1 Study sites and workflow

The three-study sites are located in the province of Reggio Calabria (Calabria, Italy) (Figure 3.1).

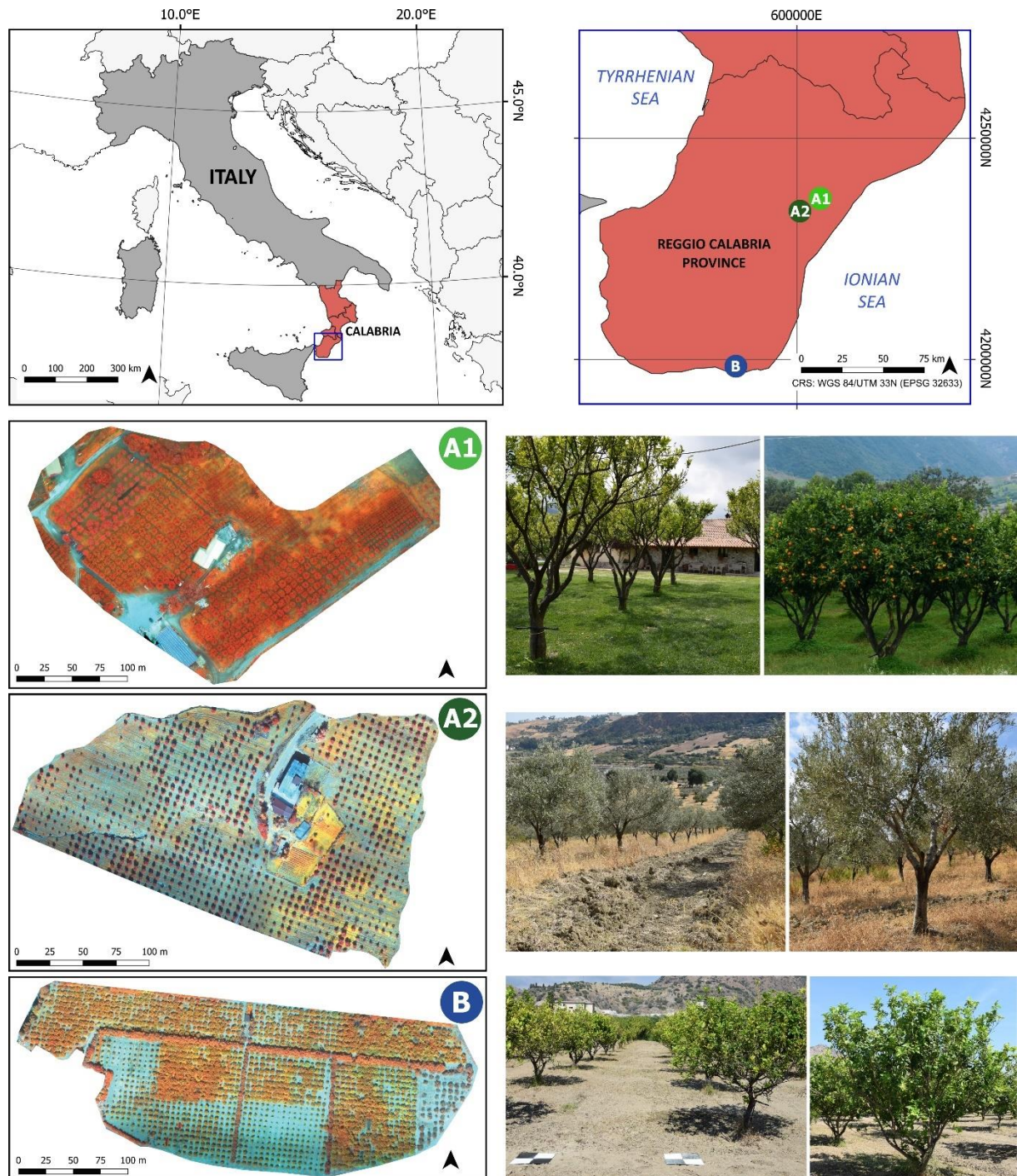


Figure 3.1 Geographic location and photographic description of the study sites A1 (Clementine), A2 (Olive), and B (Bergamot and olive) orchard (*source*, Modica et al., 2020).

Study sites A1 and A2 fall in the municipality of Antonimina (38°15'52'' N, 16°11'12'' E, 111 m a.s.l., and 38°16'12'' N, 16°11' 04'' E, 193 m a.s.l., respectively); study site B in the municipality of Palizzi (37° 55' 06'' N, 15° 58' 54'' E, 4 m a.s.l.).

In the study site A1, there is a 20-year even-aged citrus orchard (clementine, *Citrus x clementina*) with a 5 m x 5 m single-tree planting distance covering an area of 4.6 ha. In the study site A2, there is a 20-year even-aged specialized olive orchard with a 6 m x 6 m single-tree planting distance covering 7.12 ha.

The orchards are managed according to organic farming methods. Study site B covers an area of 5.13 ha. There is an uneven-aged citrus orchard (Bergamot, *Citrus bergamia*) characterized by long windbreak barriers made up of olive trees. The orchard is remarkably heterogeneous, composed of trees 5 years (1.5 m height) to 20 years old (4 m height).

The workflow followed in this work can be synthesized according to these methodological steps: UAV data acquisition; pre-processing (photogrammetric reconstruction, orthorectification, and mosaicking, radiometric and statistical analysis of UAV imagery, derivation of topographic layers); processing (object-based image segmentation, derivation of VIs, image classification and tree crowns extraction, accuracy assessment) (Figure 3.2).

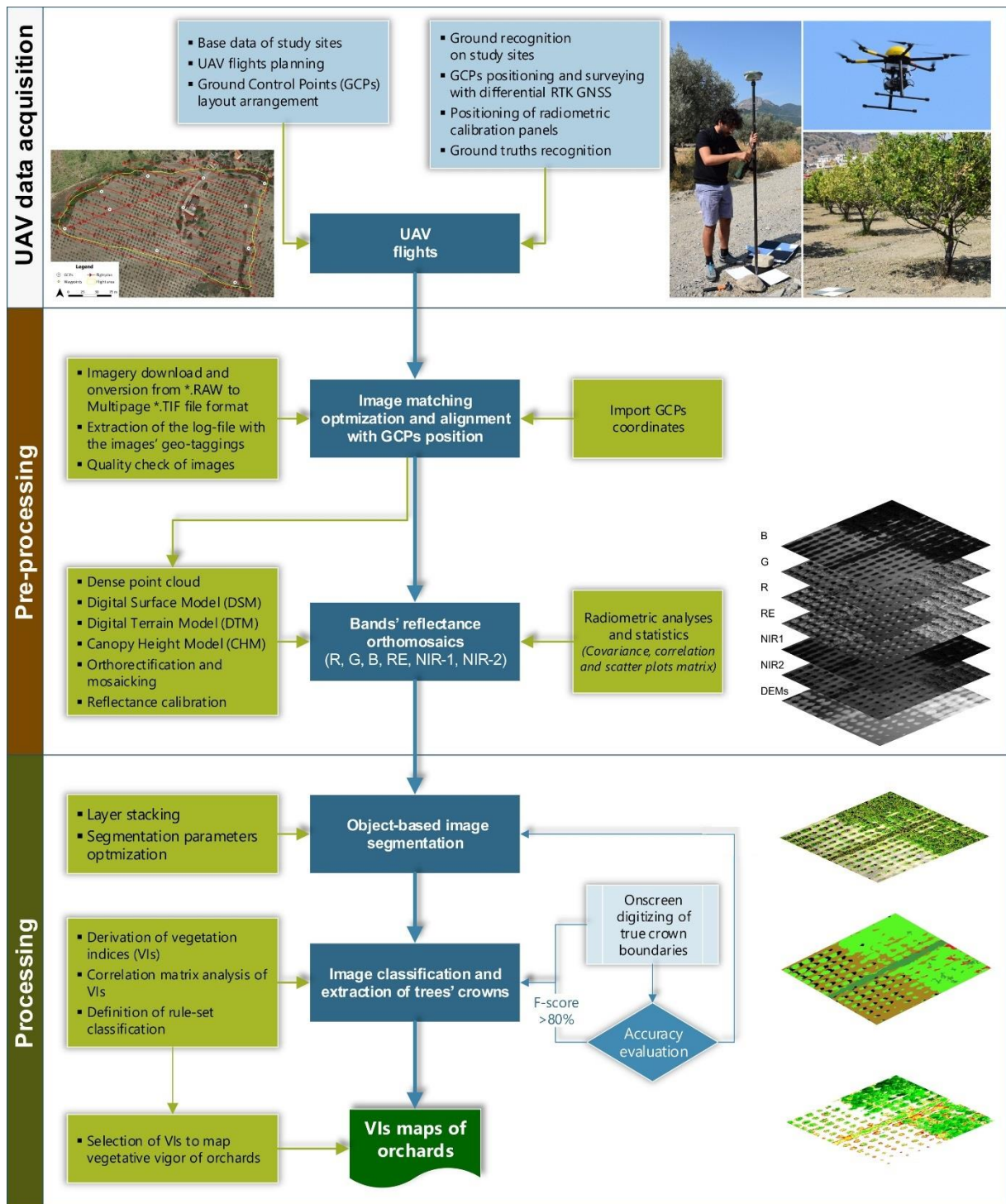


Figure 3.2 Workflow followed for the vegetation monitoring using UAV multispectral imagery in heterogeneous citrus and olive orchards (source, Modica et al., 2020).

3.1.2 Surveys Equipment

UAV surveys were carried out, as showed in Modica et al., (2020). In particular, aerial surveys were performed using a Multirotor G4 Surveying-Robot (Service Drone GmbH) equipped with six electric brushless motors, gimbal and flight control (Figure 3.3). This UAV was equipped with a

multispectral camera, μ -MCA06 snap, with a global shutter sensor produced by Tetracam Inc. (Chatsworth, USA). The camera consists of 6 individual 1.3 megapixel CMOS sensors (4:3 format, 1280 x 1024 pixels) equipped with interchangeable bandpass filter housed in one unit, one called “master,” responsible for synchronizing the other called “slaves” (Table 3.1).

Table 3.1. Tetracam μ -MCA06 snap (Global shutter) sensor characteristics bands specification (wavelength and bandwidth).

Geometry of lens	Sensors	Bands	Central band wavelength [nm]	Bandwidth [nm]
Focal Length (fixed lens) 9.6 mm Horizontal Angle of View 38.26° Vertical Angle of View 30.97° Ground sample distance (GSD) 40.0 mm and field of view (FOV) 51.5 m x 41.25 m at 80 m of flight height	Master (0)	Near-Infrared (NIR1)	800	10
	1	Blue	490	10
	2	Green	550	10
	3	Red	680	10
	4	Red edge	720	10
	5	Near-Infrared (NIR2)	900	20

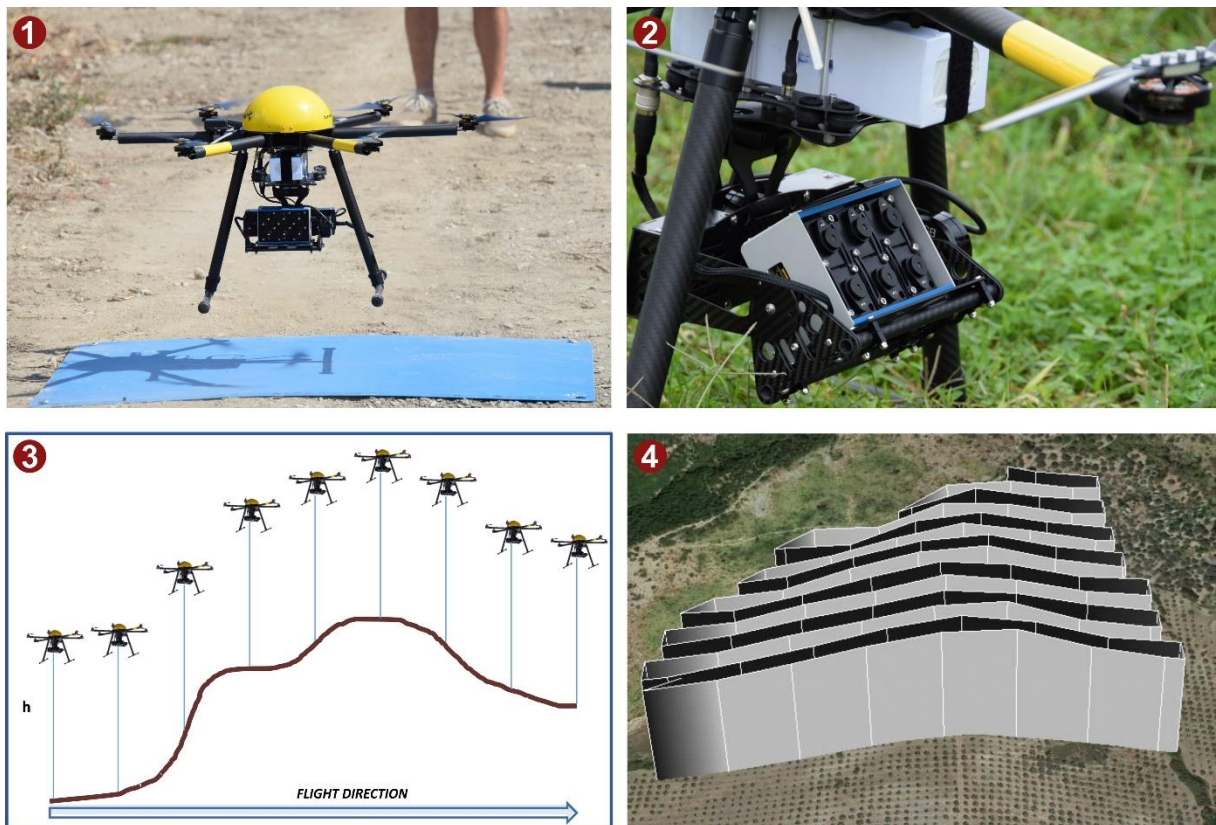


Figure 3.3 Top left (1), the UAV Multirotor G4 Surveying-Robot (Service Drone GmbH) equipped with Tetracam μ -MCA06 snap multispectral camera; top right (2), camera mounted on UAV gimbal and ready to capture images. Bottom left (3), a graphical scheme shows how the UAV takes into account the 3D morphology of the surveyed area, guaranteeing a constant height of flight and (4) a 3D view of a flight plan (source, Modica et al., 2020).

Every sensor has a size of 6.66 mm x 5.32 mm with a pixel of 4.8 microns and a focal length of 9.6 mm (fixed lens). Images are stored as single shots of 1.3 megapixels per bands, exposing the entire image at the same instant in time, at 8 or 10 bit, giving a total of 7.8 megapixels across the six bands. Furthermore, the camera was equipped with its own global navigation satellite system (GNSS) (the FirePoint 100 GPS).

3.1.3 Data acquisition and pre-processing

Data acquisition and pre-processing were performed, as explained in Modica et al., (2020). In particular, flight missions were planned using the UAV Planner 3D (www.alto-drones.com), which is a commercial plugin available for version 2 of QGIS, and that allows to take into account the 3D morphology of the study site. The flights were carried out at 80 m of flight height, with a field of view (FoV) of 51.5 x 41.25 m, ground sample distance (GSD) of 4 cm, and with 2.5 m s⁻¹ of cruise speed (Table 3.2). To obtain a high quality of the imagery, overlap and side lap were set at 80% and 75%, respectively. All over the study sites, 50 cm x 50 cm white polypropylene panels were placed. Each ground control point (GCP) was made using two black cardboard quadrants in order to locate the point (Figure 3.4), georeferencing with the Leica GS12 RTK-GNSS in the coordinate system WGS84/ETRF1989 UTM33N (EPSG 32633) with a planimetric accuracy ± 2.5 cm and altimetric accuracy ± 5 cm.

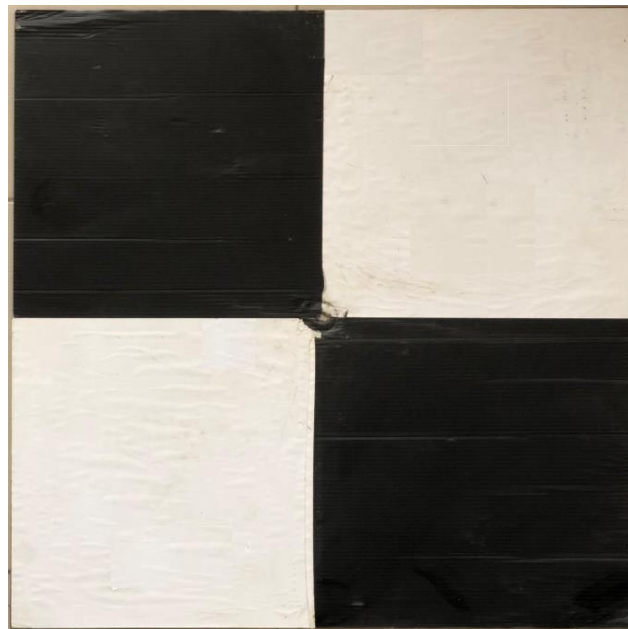


Figure 3.4 Ground control point (GCP) made by attaching two black cards to a polypropylene panel.

Table 3.2 Flight and UAV dataset characteristics.

ID	Date	Flight height [a.g.l.]	Take-off time [UTC+1]	Speed [m s ⁻¹]	N° of flights	Total duration [min]	Surveyed area [ha]	Photos [n°]	Sidelap [%]	Overlap [%]	RMSE [m]		
											X	Y	Z
A1	2016/11/16	80 m	12:00	2.5	2	38	4.6	1026	80	75	0.05	0.05	0.08
A2	2017/02/15	80 m	12:00	2.5	2	40	7.12	1878	80	75	0.07	0.07	0.1
B	2018/09/17	80 m	11:00	2.5	2	49	7.9	2825	80	75	0.03	0.03	0.09

To calibrate the conversion of the original digital numbers (DN) to band reflectance, three polypropylene calibration panels (in white, black, and grey) were placed on the field. During the flight, their reflectance was measured using the Apogee Ps-300 spectroradiometer. The reflectance of the grey panel in correspondence of each central band was extracted. These values were used, taking into account the radiometric correction parameters written in the EXIF metadata of the images to compute each pixel's radiometric calibration, generating reflectance maps. UAV images were acquired in the *.RAW native format subsequently converted to 10-bit TIFF format through PixelWrench II (version 1.2.4, Tetracam, Inc., Chatsworth, USA). The data pre-processing step was implemented in Pix4Dmapper Pro 4.3 (Pix4D SA, Switzerland), which permits managing the alignment, stacking and performing radiometric calibration of the single-band images as camera rigs systems. The camera's internal orientation was executed based on the camera specification and the alignment parameters provided by Tetracam (i.e. X and Y translation, rotation, and scaling). External orientation was initially based on the GNSS geotags recorded for each shot and then improved by using the GCPs positions. After, classical digital photogrammetry processes based on structure from motion (SfM) and aerial triangulation were performed producing sparse and dense 3D clouds, digital surface model (DSM), digital terrain model (DTM) and canopy height model (CHM). After the radiometric calibration, a reflectance orthomosaic for each of the six-layer bands (Blue, Green, Red, Red edge, NIR1, NIR2) was produced and finally stacked to obtain a single six-band orthomosaic.

3.1.4 Radiometric analyses and statistics

Before the image processing, the radiometric characterization of datasets and correlation analysis of bands were performed using pairwise scatter plots based on Pearson's correlation coefficient (r_{ij}) according to Equation 3.1 and organized as scatter plots matrix.

$$r_{ij} = \frac{Cov_{ij}}{\sigma_i \sigma_j} \quad (3.1)$$

$$Cov_{ij} = \frac{\sum_{k=1}^N (DN_{ik} - \overline{DN}_i)(DN_{jk} - \overline{DN}_j)}{N-1} \quad (3.2)$$

where

Cov_{ij} (Equation 3.2) represents the covariance of layer bands i and j , DN_{ik} the digital numbers (i.e., the cell value of each pixel) while \overline{DN}_j represents the mean of the DNs in the specific band (i and j). σ_i and σ_j represent bands' standard deviations calculated in Equation 3.3.

$$\sigma_{i(j)} = \sqrt{\frac{\sum_{k=1}^N (DN_{i(j)} - \overline{DN}_{i(j)})^2}{N-1}} \quad (3.3)$$

The dataset was analyzed in Python using the pandas library and the rasterio toolbox to read and implement the data array of input data. As far as the input data is concerned (i.e., the layer bands), the six spectral bands Blue, Green, Red, Red edge, NIR1, NIR2 plus DSM, and CHM were used. This input data was concatenated in a unique data frame using *NumPy* library. Scipy and numpy libraries were used to perform correlation analysis. The implementation of the scatter plots and the final correlation matrix were based on the matplotlib and seaborn libraries. Kernel density estimation (KDE) with a Gaussian kernel was used to represent graphically scatter plots.

3.1.5 Image segmentation

The first step of a GEOBIA procedure foresaw the segmentation of the image into separate, non-overlapping regions (Aguilar et al., 2016) and extracted as vectorial objects. Segmentation is a fundamental pre-requisite for classification/feature extraction (Drăguț et al., 2014). This process consists of the partitioning of objects into smaller entities creating new ones, and altering the existing ones' morphology following precise rules. Regarding the approaches adopted in performing the segmentation, two different strategies are possible: a top-down strategy that involves cutting large objects into small objects. The bottom-up strategy merges small objects to create larger ones. In this work, a bottom-up strategy, the multiresolution segmentation (MRS) (Baatz and Schäpe, 2000), implemented in eCognition Developer 9.5, was adopted. MRS is an

optimization process that minimizes the average heterogeneity for a certain number of image objects while maximizes their respective homogeneity (Trimble Inc., 2019). The algorithm initially identifies single objects of a pixel's size and subsequently merges them with other neighboring objects following a criterion of relative homogeneity. This criterion measures the level of homogeneity within each object. The process continues selecting another image object's best neighbor and works until no further image object mergers can be created without infringing the maximum allowed homogeneity of an image object (Trimble Inc., 2019). The final result of a good image classification process is influenced mainly by the quality of segmentation, which in turn depends on the choice of segmentation parameter values (El-naggar, 2018).

Several criteria should be accurately evaluated to produce good segmentation (El-naggar, 2018). The homogeneity criterion results from the combination of the spectral and shape properties of the initial object and of that generated by the merging process. Color homogeneity derived from standard deviation of spectral colors while the shape homogeneity results from the deviation of a compact (or smooth) shape. Homogeneity criteria is adjusted through two parameters: shape and compactness. Shape parameter influences the importance of the segmentation of the segmented objects' shape concerning the color and its value ranges from 0 to 0.9. Shape and color are two interrelated parameters. The user can choose their weight: the greater the first parameter's weight, the lower the weight of the second parameter in the segmentation, and vice versa (Drăguț et al., 2010). Compactness determines the influence of shape with respect to smoothness. Compactness can be defined by the product of width and length calculated on numbers of pixels (El-naggar, 2018).

Some scholars proved the importance of the scale parameter in determining the final size and dimension of the resulting objects (Drăguț et al., 2014; Ma et al., 2017). Using higher values or smaller values of scale parameter, larger or smaller objects are produced, respectively. This parameter defines the maximum allowed heterogeneity with regard in the weighted image layers for the obtained image objects (Trimble Inc., 2019). Therefore, datasets containing images of homogeneous environments will lead to larger segments and vice versa (El-naggar, 2018). In implementing the segmentation algorithm, different weights can be assigned to each of the several input data (i.e., band layers). In the workflow, images were segmented adopting a MRS algorithm and using an equal weight for all band layers. Layers used were the spectral bands provided by the multispectral camera, Blue, Green, Red, Red edge, NIR1, NIR2, and the DSM generated during pre-processing in study site A1. Regarding the study sites A2 and B, the NIR2 band was instead

excluded, since it was highly correlated with the NIR1 band (0.99). The MRS parameters used in this work were chosen by applying a trial-and-error approach (Aguilar et al., 2016). Indeed, as reported both in Prošek et al. (2019) and Kaufman et al. (1994), the visual interpretation of segmentation can be considered an effective method to assess the results' quality. Specifically, in the study site A1 (Figure 3.5), segmentation settings were the following: weight 1 for all layers, scale parameter 60, shape 0.1, and compactness 0.5. In the study site A2 (Figure 3.6), displaying the image in the different band combinations and based on a better distinction from the scene of canopies and their shadows, a different weight was assigned to the different layers bands. In particular, higher (band weight = 2), for the layers NIR1, Red edge, DSM and DTM, lesser (band weight = 1) for Blue, Green and Red bands/layers. The scale parameter was set to 200 and the shape and compactness parameters were set to to 0.7. Instead, in the study site B (Figure 3.7), the segmentation settings were 1, 85, 0.5 and 0.1 for band weights, scale, shape and compactness, respectively.

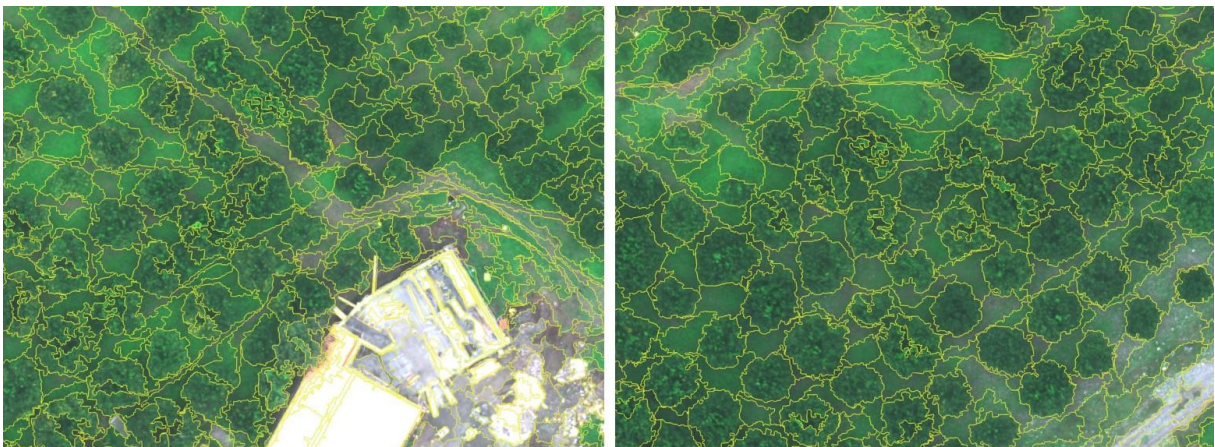


Figure 3.5 Segmentation in the study site A1.

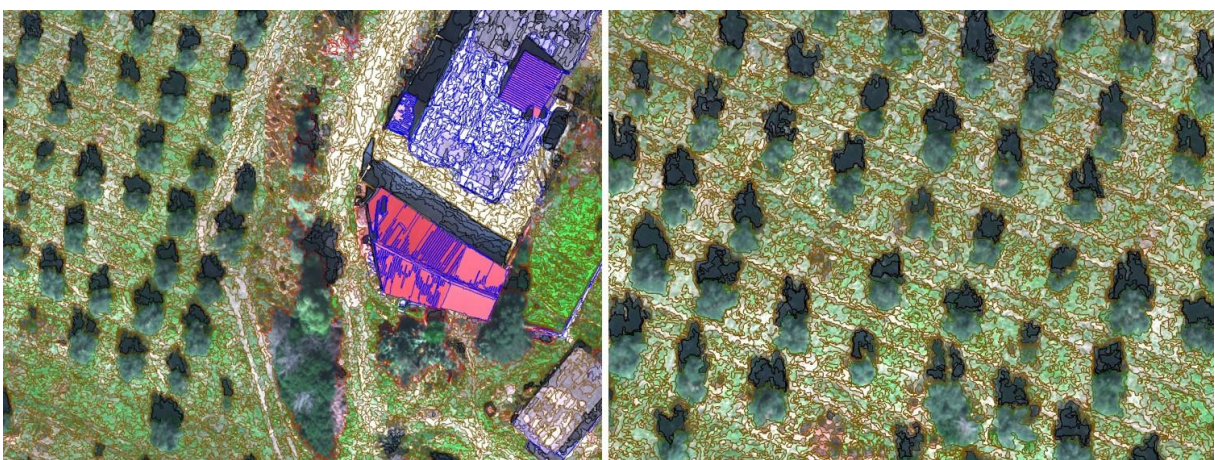


Figure 3.6 Segmentation in the study site A2.

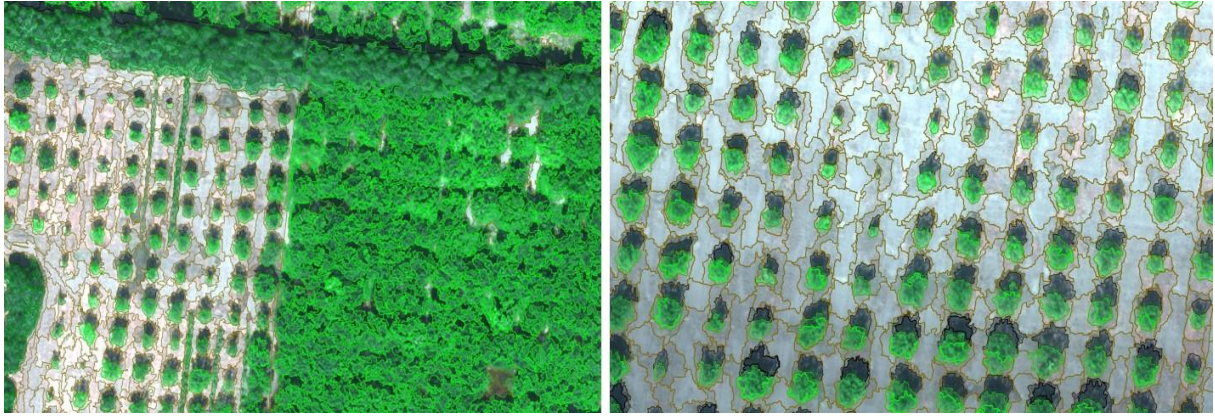


Figure 3.7 Segmentation in the study site B.

3.1.6 Vegetation indices and topographic elevation layers

A reliable radiometric measurement of vegetation vigor can be obtained by combining the information provided by specific regions of the EM, such as those characterizing the curve between the maximum absorption of photosynthetic pigments (Jones and Vaughan, 2010).

In this work, six VIs were derived (Table 3.3): Normalized Difference Vegetation Index (NDVI), Normalized Difference Red edge Vegetation Index (NDRE), Soil-Adjusted Vegetation Index (SAVI), Green Normalized Difference Vegetation Index (GNDVI), Green and Red Normalized Difference Vegetation Index (GRNDVI), Chlorophyll Vegetation Index (CVI). Furthermore, two topographic elevation layers were generated, the DSM (Digital Surface Model) entered as input layer while the DTM (Digital Terrain Model) was used to calculate the CHM (Canopy Height Model) (Popescu, 2007).

As regards VIs used (Table 3.3), NDVI is one of the most widely used indices derived from the multispectral information and is calculated by the normalized ratio between the Red and NIR bands (Rouse et al., 1974). This index, which can assume values ranging from -1 to 1, measures healthy vegetation exploiting the highest chlorophyll absorption and reflectance regions and it is useful to characterize canopy growth or vigor (Xue and Su, 2017). However, NDVI is very sensitive to background factors, such as the shade and the vegetation canopies and soil backgrounds' brightness. Therefore, Huete (1988) developed the SAVI index in order to minimize the effects of soil background on the vegetation signal by inserting a constant soil adjustment factor L in the original formula of NDVI (Taylor and Silleos, 2006). L , which is a function of vegetation density, can assume values between 0 and 1, depending on the vegetation amounts. L factor works as follows: in the presence of shallow vegetation, the value of L recommended is 1, while a value of

0.5 is suggested for intermediate levels of vegetation. Naturally, given the index formula, when the value of L is equal to 0, SAVI corresponds precisely to the NDVI. NDRE has a range of values from -1 to 1 and its formula is very similar to that of NDVI but the former exploits the sensitivity of the vegetation to the Red edge by replacing the Red. GNDVI (Gitelson et al., 1996) has a formula also very similar to that of NDVI but exploits the Green band rather than the Red band and has been developed to estimate the leaf chlorophyll concentration. CVI (Vincini et al., 2007) was initially proposed as a broad-band VI sensitive to leaf chlorophyll content and insensitive to LAI variation. Its formula was obtained from that of Green SR multiplying the Green/NIR ratio by Red/Green ratio. Red/Green ratio, developed by Gamon and Surfus (1999), has been exploited to estimate foliage development in canopies. GRNDVI was developed together with other indices in whose formulas the Red band of NDVI formula was substituted with several combinations of Blue, Green and Red bands to verify the response and capability to estimate LAI of these indices (Wang et al., 2007).

Table 3.3 Formulation of the six vegetation indices (VIs) used in the present work.

Index denomination	Index formula	References
Normalized Difference Vegetation Index (NDVI)	$\frac{(\rho_{NIR1} - \rho_{Red})}{(\rho_{NIR1} + \rho_{Red})}$	(Rouse et al., 1974)
Normalized Difference Red edge Vegetation Index (NDRE)	$\frac{(\rho_{NIR1} - \rho_{RedEdge})}{(\rho_{NIR1} + \rho_{RedEdge})}$	(Barnes et al., 2000)
Soil-Adjusted Vegetation Index (SAVI)	$\frac{(\rho_{NIR1} - \rho_{Red})}{(\rho_{NIR1} + \rho_{Red} + L)}(1 + L)$	(Huete, 1988)
Green Normalized Difference Vegetation Index (GNDVI)	$\frac{(\rho_{NIR1} - \rho_{Green})}{(\rho_{NIR1} + \rho_{Green})}$	(Gitelson et al., 1996)
Chlorophyll Vegetation Index (CVI)	$\rho_{NIR1} \frac{\rho_{Red}}{(\rho_{Green} * \rho_{Green})}$	(Vincini et al., 2007)
Green and Red Normalized Difference Vegetation Index (GRNDVI)	$\frac{\rho_{NIR1} - (\rho_{NIR1} + \rho_{Red})}{\rho_{NIR1} + (\rho_{Green} + \rho_{Red})}$	(Wang et al., 2007)

* ρ is the reflectance at the given wavelength.

3.1.7 Image Classification and trees' crowns extraction

The classification was performed based on a rule set implemented in eCognition as an automated process-tree, so it is adaptable and replicable to other datasets. The classification was based on the algorithm *Assign Class* which permits assigning a class to an object which falls within one or more

selected conditions (or rules), based on values attributed to features (in this work, for example, threshold values VIs and topographic layers), operating as a masking-approach as reported both in De Castro et al. (2018) and in Peña-Barragán et al. (2012). In this work, the classification was implemented by assigning, to each target land-use class, different threshold values for each of the different input layers and VIs (Table 3.4). In case study A1, the classification was performed for four classes: "Citrus", "Buildings and roads", "Other vegetation", and "Bare soil". This dataset was derived from UAV flights performed at midday in November, so shadows were considered irrelevant. For this reason, it was decided not to create a dedicated class for shadows.

The classification algorithm was set starting to classify "Buildings and roads" using SAVI values ≤ 0.1 . "Citrus" class was created using SAVI ≥ 0.7 and CHM ≥ 1.6 , while "Other vegetation" was created using CHM values higher than 6. All unclassified objects were inserted in the class "Bare soil". In the case study A2, five classes were implemented: "Olive", "Shadows" (due to the different sun position with respect to the horizon line in the month of February), "Buildings and roads", "Other vegetation" and "Bare soil". "Olive trees" were detected using CVI values ≥ 1.5 and CHM ≥ 1.5 , while "Shadows" were classified exploiting the NIR1 band. The class "Building and roads" was created using SAVI values ≤ 0.1 and CHM ≥ 1.1 . The class "Other vegetation" was created taking into consideration their larger canopy size ($\geq 30 \text{ m}^2$) than olive trees, therefore using a feature related to dimensions. All unclassified objects were inserted in the class "Bare soil".

In case study B, five classes were used: "Citrus", "Olive", "Shadows", "Other vegetation" and "Bare soil". Since the citrus orchard is uneven-aged, being significant differences in the size of the trees' canopies, the image was subdivided into parcels (Figure 3.8). This choice can be further justified by the presence of many olive trees forming long windbreak barriers in the citrus orchard. According to the irrigation scheme, the orthomosaic was divided into ten parcels that roughly divided the orchard according to the different plantation age of bergamot trees. In detail, in sectors 4-6 and 7, trees are 5 years old. This division was performed using the open-source software QGIS, creating a thematic layer then imported in eCognition. In this study site, using threshold values of SAVI between - 0.16 and 0.45, the vegetation, without distinguishing between the two species present (olive and bergamot), was classified as a temporary class called "Vegetation". Then, olive trees in sectors 1 to 5 and 7 were classified using DSM and NDVI ≥ 0 and CVI ≥ 1.3 , reclassifying the class "Vegetation". Therefore, remaining objects belonging to the class "Vegetation" were reclassified as "Citrus". All the objects not belonging to the class "Vegetation" were classified as

“Bare soil”. The objects attributable to the “Shadows” class were extrapolated from the classes “Citrus”, “Olive” and “Bare soil” using a threshold value in the band NIR1.



Figure 3.8 Map showing the study site B with, highlighted in red, the ten parcels identified according to the irrigation scheme (*source*, Modica et al., 2020).

3.1.8 Accuracy assessment

The approach of accuracy assessment used in this study case was based on the comparison of the total number of correctly detected crown pixels by classification algorithm with a reference vector data. The reference segments for each image have been manually digitized based on a visual interpretation of UAV images. All the trees' crowns following in the three analyzed study sites were digitized to obtain a comprehensive picture of the implemented approach. With the aim to cope with the heterogeneity of the tree crowns structure in some parts of the images, a pixel-based accuracy assessment was executed. Superimposing trees' crowns with the reference vector data, each pixel was labeled as belonging to one of these accuracy categories (Goutte and Gaussier, 2005; Ok et al., 2013; Shufelt, 1999; Sokolova et al., 2006): True Positive (TP), False Negative (FN) and False Positive (FP).

TP includes those pixels labeled as a *tree* by the classification algorithm, which corresponds to a *tree* in the reference vector data. In this case, TP includes the pixels are correctly classified.

FN includes those pixels not labeled as a *tree* by the classification algorithm but labeled in the reference vector data as a *tree*. In this case, FN includes the pixels not detected.

FP includes those pixels labeled as a *tree* by the classification algorithm, which does not correspond to any of the pixels labeled by the reference vector data. In this case, FN includes the pixels erroneously detected.

The number of TP, FP, and FN pixels was counted in every image to evaluate the accuracy. After this, *Recall* (r), *Precision* (p), *F-score* (F) and *Branching Factor* (BF) metrics were computed through the equations 3.4-3.7 (Goutte and Gaussier, 2005; Li et al., 2012; Ok et al., 2013; Shufelt, 1999; Sokolova et al., 2006):

$$r = \frac{\| TP \|}{\| TP + FN \|} \quad (3.4)$$

$$p = \frac{\| TP \|}{\| TP + FP \|} \quad (3.5)$$

$$F = 2 \cdot \frac{r \cdot p}{r + p} \quad (3.6)$$

$$BF = \frac{\| FP \|}{\| TP \|} \quad (3.7)$$

The r parameter, measuring the fraction of pixels that were correctly denoted as object pixels by the algorithm, permits representing the omission error (derived from $1-r$). The parameter p indicates the correctness of detected crowns, and in the same way, it is also representative of the commission error ($1-p$). F measures the overall accuracy through the harmonic mean of commission and omission errors. The values of r , p , and F range from 0 to 1. If r e p corresponds to high values, the F value is also high. For example, if all trees are correctly segmented, r e p values are equal to 1 and F will be equal to 1 (Goutte and Gaussier, 2005; Li et al., 2012; Shufelt, 1999; Sokolova et al., 2006). The BF measures the degree to which an algorithm over classifies background pixels with the target label (i.e., tree crown in this study case). If the classifier wrongly labels every pixel in the scene, the BF is equal to 1, while if the classifier never “over-delineates” the extent of any reference segment, BF 's value is equal to 0 (Shufelt, 1999). All the above measures, taken together, allow the classification algorithm's performance to be evaluated (Shufelt, 1999).

3.2 Results and discussions

3.2.1 Geometric and radiometric characteristics

All three datasets' consecutive images were processed via aerial image triangulation with the geo-tagged flight log and the GCPs' coordinates using the software Pix4D Mapper. 3D densified point clouds, DSM, DTM, and for each spectral band, reflectance orthomosaics were generated. In DSM and orthomosaics, the GSD range between 4.1 and 4.3 cm pixel⁻¹. Regarding the approach used in the three datasets, being the scenario different, before proceeding with the classification, for each study site, a correlation analysis between all input layers was performed through the Pearson's correlation coefficient (r_{ij}) and implemented in a scatter plots matrix (Figures 3.10, 3.12 and 3.14). Besides, to have a comprehensive view of the spectral correlation between the six derived VIs, the latter were analyzed on the whole image of each dataset as a correlation matrix (Figure 3.9-3.11-3.13).

Study site A1	NDVI	NDRE	SAVI	GNDVI	CVI	GRNDVI
NDVI	1.00	0.77	1.00	0.95	0.46	0.99
NDRE	0.77	1.00	0.77	0.89	0.78	0.73
SAVI	1.00	0.77	1.00	0.95	0.46	0.99
GNDVI	0.95	0.89	0.95	1.00	0.69	0.92
CVI	0.46	0.78	0.46	0.69	1.00	0.40
GRNDVI	0.99	0.73	0.99	0.92	0.40	1.00

Figure 3.9 Correlation matrix between the six selected vegetation indices (VIs) implemented on the whole image of the study site A1.

Referring to the whole datasets, in the study site A1 (Figure 3.9), high correlations of SAVI with NDVI (1), GNDVI (0.95), and GRNDVI (0.99) were evident. SAVI was essential in defining the class "Buildings and roads" and then for the creation of the class "Citrus", coupled with the CHM, and using a threshold value ≥ 0.7 . NDRE showed to be highly correlated with GNDVI (0.89) and lowly correlated with NDVI (0.77), SAVI (0.77), and CVI (0.78).

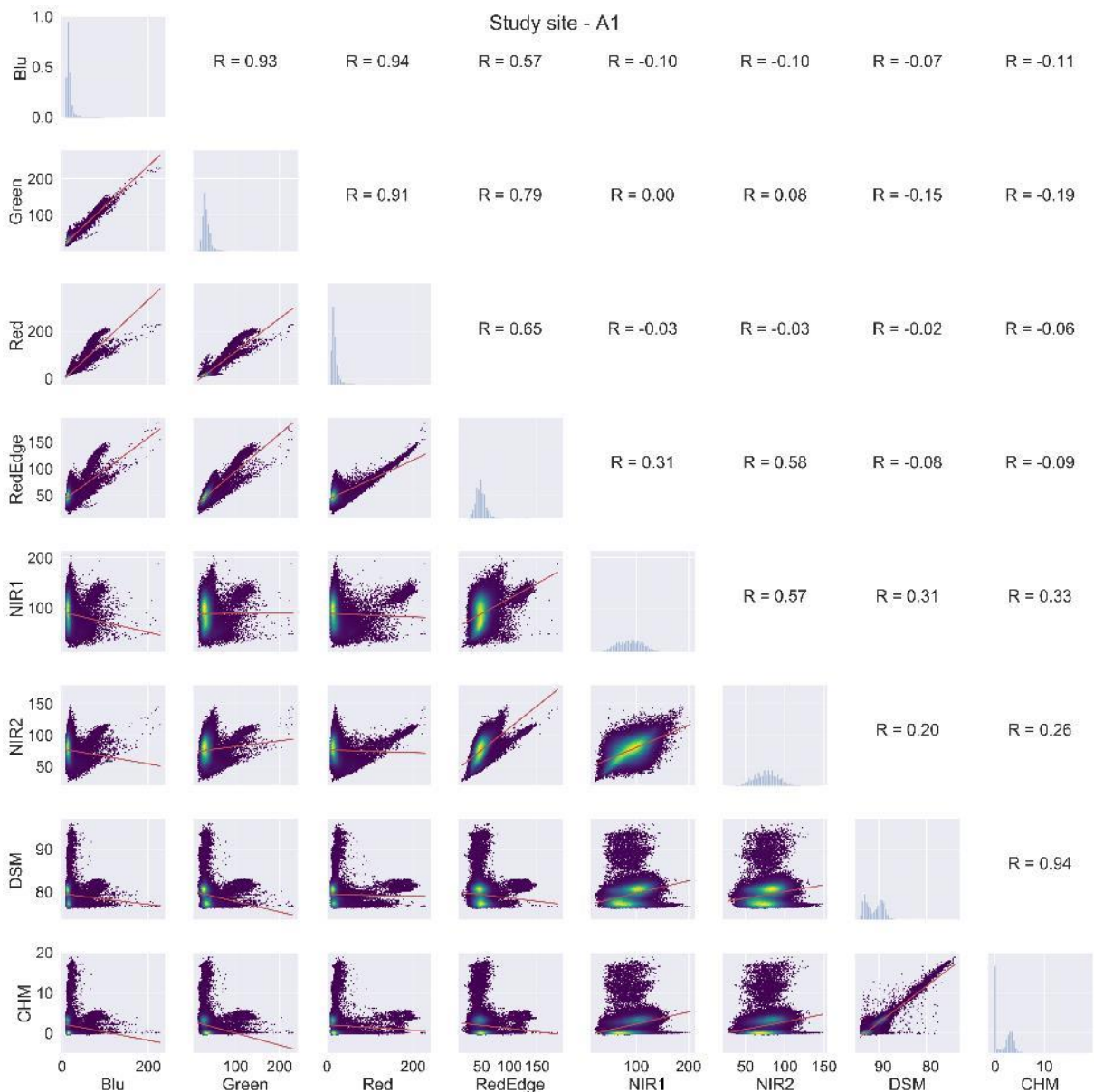


Figure 3.10 Study site A1. Scatter plot matrix showing all bivariate relationships between the input layer bands. For each scatterplot, implemented using the 2D kernel density estimate (KDE) with a Gaussian function, the correlation line (in red), was provided. The main diagonal reports the histograms showing the frequency distribution of pixel values. Pearson's correlation (R) coefficients for all pairwise combinations of variables are reported in the upper half-matrix (source, Modica et al., 2020).

Observing Figure 3.12 showing correlation matrices on input data of the study site A2, there were evident high correlations between the NIR bands and the Red edge (0.88) and between the two NIR bands (0.99). Given this last significant correlation, it was decided to exclude the NIR2 band as an input layer from the segmentation phase onwards.

Study site A2	NDVI	NDRE	SAVI	GNDVI	CVI	GRNDVI
NDVI	1.00	0.79	0.68	0.91	0.17	0.99
NDRE	0.79	1.00	0.54	0.88	0.50	0.76
SAVI	0.68	0.54	1.00	0.62	0.12	0.68
GNDVI	0.91	0.88	0.62	1.00	0.54	0.85
CVI	0.17	0.50	0.12	0.54	1.00	0.06
GRNDVI	0.99	0.76	0.68	0.85	0.06	1.00

Figure 3.11 Correlation matrix between the six selected vegetation indices (VIs) implemented on the whole image of the study site A2.

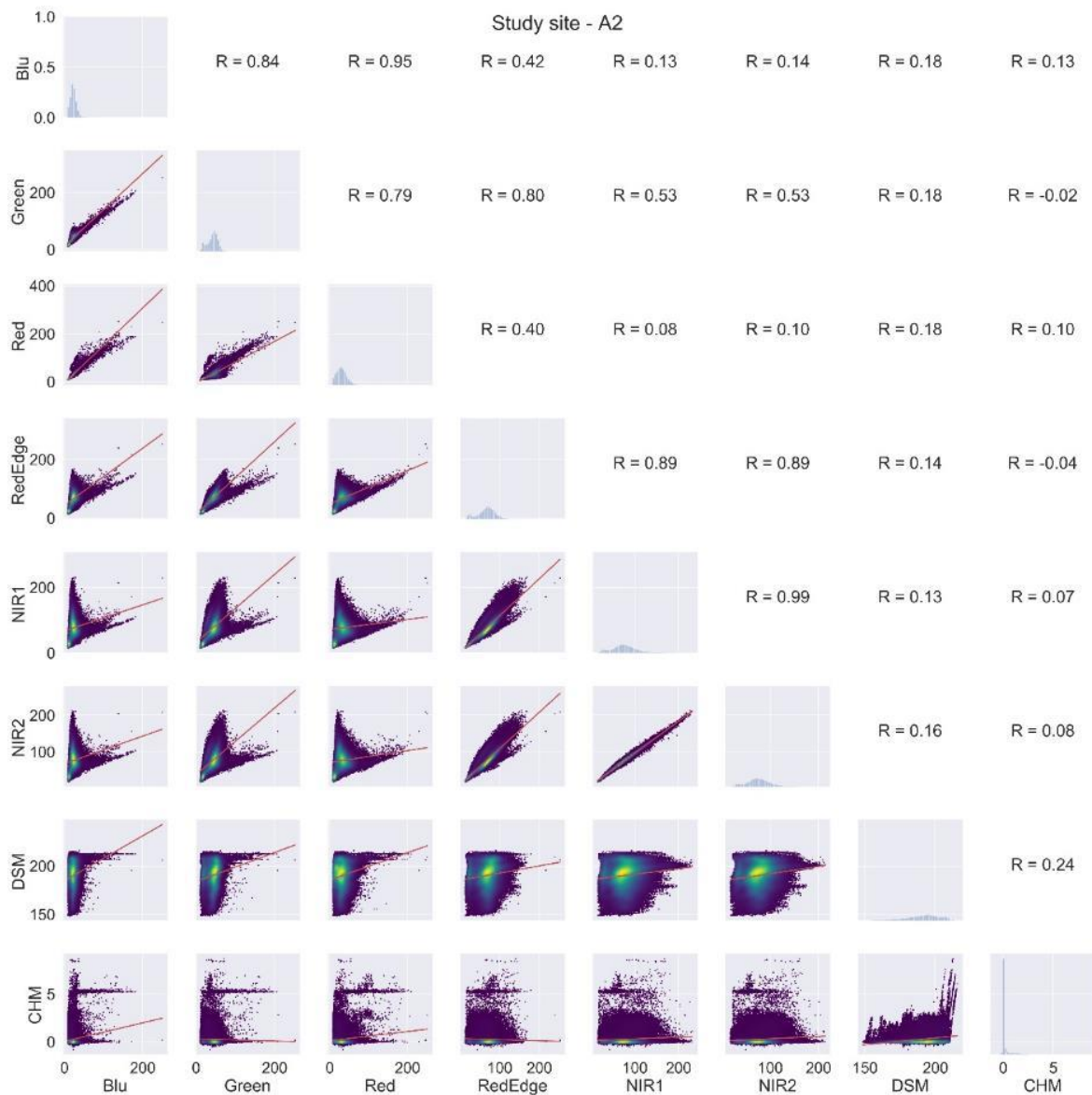


Figure 3.12 Study site A2. Scatter plot matrix showing all bivariate relationships between the input layer bands. For each scatterplot implemented using the 2D kernel density estimate (KDE) with a Gaussian function, the correlation line (in red), was reported. The main diagonal reports the histograms showing the frequency distribution of pixel values. In the upper half-matrix, Pearson's correlation (R) coefficients for all pairwise combinations of variables are reported (*source*, Modica et al., 2020).

Regarding the study site B, observing Figure 3.14 showing the correlations of the input data, it is possible to observe a high correlation between NIR and Red edge bands (0.88) and between the two NIR bands (0.99). Also, in this case, the NIR 2 band was excluded as an input layer from the segmentation phase onwards. Regarding the VIs (Figure 3.13), the correlation of SAVI was very high with GRNDVI (0.99) and NDVI (1.00), while there was no significant correlation of CVI with no other index. CVI and SAVI were crucial for the correct classification of the olive and bergamot species. NDRE is highly correlated with GNDVI (0.93), NDVI (0.87), and SAVI (0.86).

Study site B	NDVI	NDRE	SAVI	GNDVI	CVI	GRNDVI
NDVI	1.00	0.87	1.00	0.96	0.11	1.00
NDRE	0.87	1.00	0.86	0.93	0.43	0.85
SAVI	1.00	0.86	1.00	0.96	0.10	0.99
GNDVI	0.96	0.93	0.96	1.00	0.37	0.94
CVI	0.11	0.43	0.10	0.37	1.00	0.05
GRNDVI	1.00	0.85	0.99	0.94	0.05	1.00

Figure 3.13 Correlation matrix between the six selected vegetation indices (VIs) implemented on the whole image of the study site B.

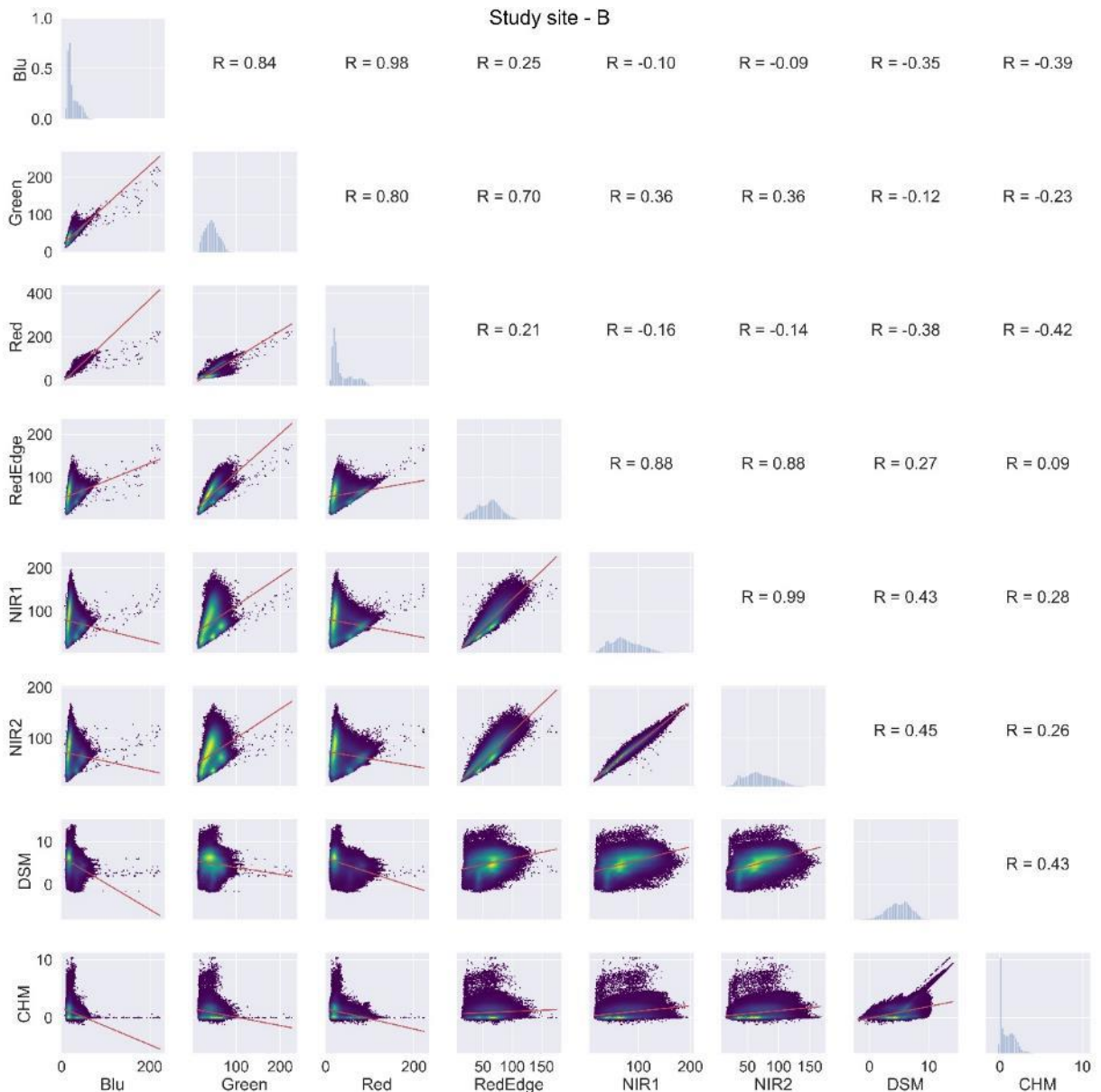


Figure 3.14 Study site B. Scatter plot matrix showing all bivariate relationships between the input layer bands. For each scatterplot implemented using the 2D kernel density estimate (KDE) with a Gaussian function, the correlation line (in red), was reported. The main diagonal reports the histograms showing the frequency distribution of pixel values. Pearson's correlation (R) coefficients for all pairwise combinations of variables are reported in the upper half-matrix (source, Modica et al., 2020).

3.2.2 Image classification, tree crown extraction and accuracy assessment

The image classification was based on six land use classes, "Citrus", "Olive", "Buildings and roads", "Other vegetation", "Bare soil" and "Shadows" (Figure 3.15).

In the study site A1, the detection of the class "Buildings and roads" permitted to isolate from the rest of the image objects of no interest using SAVI. Regarding trees' classification, the objects' minimum height was detected through verification of CHM's values. All trees were inserted in the

class “Citrus” by coupling the SAVI with CHM. The class “Other vegetation”, included different tree species, distinguishable from citrus trees, having larger canopies. Therefore, “Other vegetation” was identified using CHM values higher than those used for the class “Citrus trees”. The objects of the image excluded from the first three classes were assigned to the class “Bare soil”.

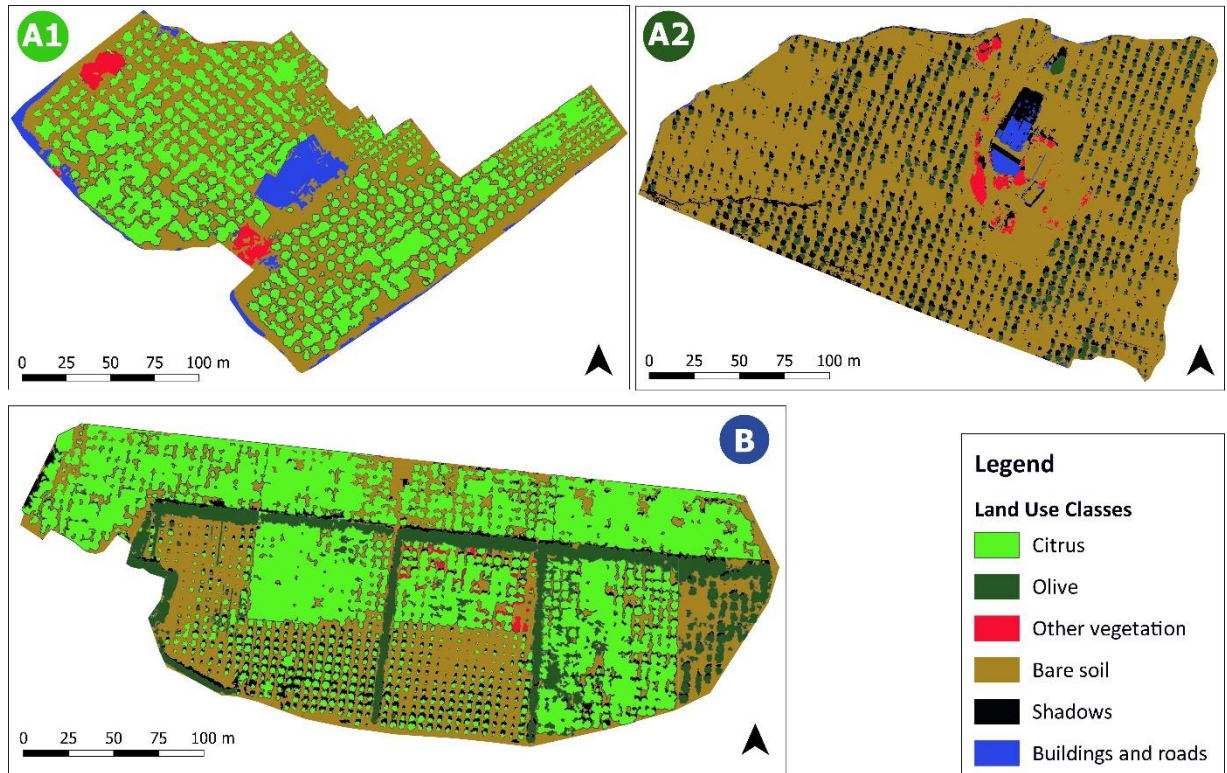


Figure 3.15 Land use maps of the three study sites obtained applying the implemented image object classification workflow: A1(Clementine), A2 (Olive), and B (Bergamot and Olive) (source, Modica et al., 2020).

For what concerns the study site A2, the classification of “Olive trees” was performed using CVI coupled with CHM in order to avoid the attribution of the class to specific regions of grass sensitive to the used VI. The class “Shadows” was generated using NIR1 band while the objects of the class “Building and roads” were isolated from the rest of the image by combining the SAVI with the CHM. In the case of “Other vegetation”, this class was identified based on a larger canopy size respect to the elements inserted in the class “Olive trees”. Unclassified objects were included in the class “Bare soil”.

Dataset B was considered the most complex. It is the largest study site and is occupied by two species (bergamot and olive) that coexist in several orchard parts. As can be seen in Figure 3.15, olive trees can be found separately from the bergamot orchard at the right end of the image, while in other parts of the image, they act as a windbreak. The latter are not of the same age and so have

different heights and sizes of the canopies. The same trees were not properly pruned, and, consequently, most of the canopies of the larger trees touch each other on one or more sides. On the other hand, there are small trees (mainly in sectors 4-6 and 7) whose canopies allow discerning significant portions of bare soil from above. Given this heterogeneity characterizing the entire image in different aspects, it was chosen to subdivide it into 10 sectors by grouping the bergamot trees based on the irrigation sectors' layout scheme, roughly corresponding to the different plantation age. Similarly, given the differences in height between the trees within the individual sectors, it was chosen to classify only using VIs. Initially, the entire tree vegetation was classified without making distinctions between species, using a temporary class called "Vegetation class", proceeding by sectors in which different SAVI threshold values were used. Given the presence of bare soil or grass, a value of 1 or 0, respectively, was used as factor L in SAVI's formula. The isolation of the olive trees from the rest of the orchard was done using the SAVI in the sector (1) having olive trees a regular plantation scheme while the CVI was used to classify olive trees which had the function of windbreak barrier (2-5, and 7).

The method tested on the three datasets was based mainly on the use of spectral response that permits enhancing the detection and classification of the objects of interest: citrus trees in dataset A1, olive trees in dataset A2, and both species in dataset B. Other measures could provide useful information on the classification phase but were not considered, as reported, for example, in Laliberte and Rango (2009), which is very time-consuming to compute several features during the object-based analysis. The proposed method proved to be effective in datasets of different complexity finding its strong point in the speed of execution and on its repeatability to other different crops with few adjustments. Regarding the processing speed and the time needed to obtain the orthomosaics, this was taken in total for the three datasets and was 4 hours. In particular, one hour was used for each of the first two datasets, A1 and A2, including visual analysis of images, segmentation and classification. The remaining time was necessary for dataset B. The time taken for the manual digitizing of the reference canopies (described below) and the verification of the results' accuracy was not added to the total computation time of the entire process performed. As far as the method's repeatability is used in other contexts, it is worthy of interest to take into account the obtained accuracy on the three datasets in the crown extraction phase. Indeed, results proved that most bergamot and olive trees were correctly classified and extracted in all the analyzed study sites.

About the accuracy, Figure 3.16 shows the extracted trees when they were overlaid on the reference data, and provided for each dataset. The green color (TP) defines the correctly detected trees' crowns according to the manual digitization representing the reference data. The yellow color (FP) indicates crowns that were found by the algorithm, where there was no tree in the reference data. The red color (FN) indicates missing crowns, i.e., where the algorithm did not detect tree canopies or parts of trees and included in the reference data. As can be seen by analyzing the results showed in Table 3.4, in the study site A1, the value of r (omission error) is 0.80 and the p value (commission error) is 0.94. The F takes into account both r and p and is 0.86. In the study site A2, where the classification regarded only olive trees, r is 0.81, and p is 0.89, while the value of F is 0.85. In the study site B, the values of r , p , and F are 0.96, 0.84 and 0.90 (F -score of bergamot trees is 0.91 and that of olive trees 0.85), respectively.

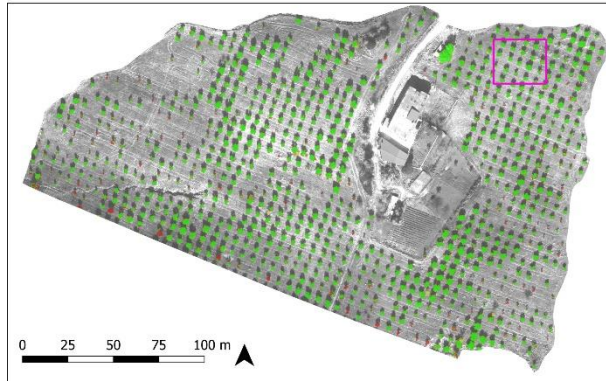
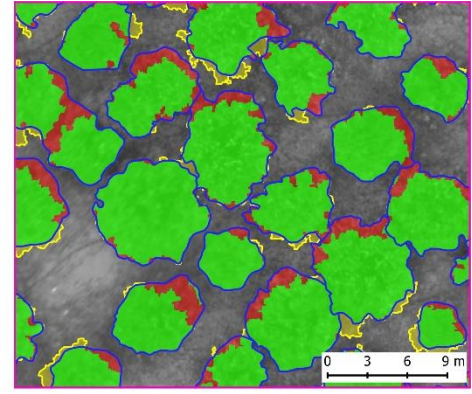
Analyzing the precision in identifying and extracting the trees' canopies, the best results in terms of percentage of TP pixels and F , among all the three analyzed datasets, were obtained in the study site B (81.66% and 0.90, respectively). The percentage of FP was also the highest of the three datasets (15.22%) and is mostly found in zones where the canopies were closer to each other and there was, at the same time, a thick layer of grass. The percentage of FN was the lowest (3.12%) concerning the failure of the classifier in identifying parts of canopies and some trees on edge the image, in the top of the image, where there is, of course, a distorting effect, and some trees in sector 3, where some tiny trees can be found.

FN pixels represent 18.5% and 16.65% in the study sites A1 and A2, respectively. These percentages were due both to the sporadic presence of foliage identified by the classifier and the error caused by the surrounding background grass that hinders the detection of the canopies along the edges. As reported in Koc-San (2018), classification, when the background's spectral values are similar to those of trees (e.g. grass), is difficult. In the study site A2, considering the parameters exploited for the classification ($CHM > 1.5$ and $CVI > 1.5$), tiny olive trees with a low vegetation vigor, were not correctly identified and classified.

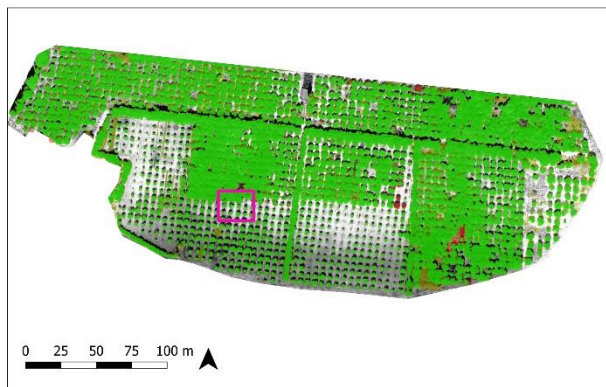
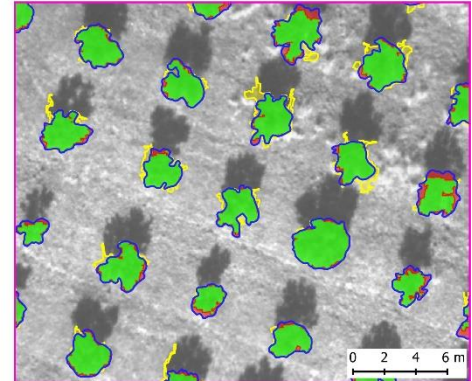
Considering the complexity and heterogeneity of the classified orchards and taking into account that a pixel-based accuracy assessment was adopted, the obtained results can certainly be considered very satisfactory.



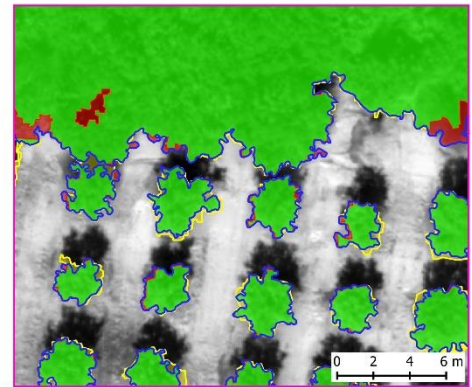
A1



A2



B



Legend

- Reference canopy boundaries
- False Positives (FP)
- False Negatives (FN)
- True Positives (TP)

Figure 3.16 Maps showing a visual picture of the obtained accuracy in the analyzed three study sites [A1 (Clementine), A2 (Olive) and B (Bergamot and Olive)], using the onscreen digitized canopy boundaries as reference data. Reference crowns (Rc) are in blue, true positives (TP) are in green, false negatives (FN) in red, and false positives (FP) in yellow (source, Modica et al., 2020).

Table 3.4 Results and accuracy indicators of the trees' crowns extraction (TP, true positives; FP, false positives; FN, false negatives; r, recall; p, precision; branching factor, BF).

Study site	*TP	*FP	*FN	r	p	BF	F-score
A1	5,600,825 (76.75%)	345,273 (4.75%)	1,350,538 (18.5%)	0.80	0.94	0.06	0.86
A2	2,093,729 (74.25%)	256,891 (9.10%)	470,206 (16.65%)	0.81	0.89	0.12	0.85
B (Bergamot)	10,018,331 (83.3%)	1,612,542 (13.4%)	397,518 (3.3%)	0.96	0.86	0.16	0.91
B (olive)	2,021,941 (74.47%)	631,225 (23.25%)	61,879 (2.28%)	0.97	0.76	0.31	0.85
<i>B (overall)</i>	12,040,272 (81.66%)	2,243,767 (15.22%)	459,397 (3.12%)	0.96	0.84	0.18	0.90

* TP, FP, and FN are expressed in numbers of pixels.

Moreover, it is worth of interest to highlight that the TP category (crowns correctly detected and extracted), includes only pixels correctly classified, differently from an object-based accuracy assessment. If this last accuracy assessment had been chosen, all polygons, whose overlap area with the reference area is higher than a minimum threshold value (Ok and Ozdarici-Ok, 2018; Rutzinger et al., 2009), would have been classified as TP, therefore also containing incorrectly classified pixels. Moreover, also observing the F-score obtained in the study site A2 (0.85), and comparing these results with those reported in other works (Ok and Ozdarici-Ok, 2018; Ozdarici-Ok, 2015), performed in more regular and well-managed orchards, the results of this case study can be considered very promising. The same consideration can be reached by comparing the results of this work with those obtained by using other methods among which convolutional neural networks, LiDAR's data and other algorithms based on the use of DSMs (Csillik et al., 2018; Mohan et al., 2017; Ok and Ozdarici-Ok, 2018).

Also, the results obtained in study site B (the more complex among the three analyzed), with an overall F-score of 0.90 and with an FN ranging between 2.28% and 3.3%, decisively corroborated the methodology here proposed. The results obtained suggest that the proposed workflow allows to classify and extract trees' crowns more efficiently, faster, and more effectively in cases of well-managed orchards.

3.2.3 Vegetation indices (VIs) and vigor maps

Vigor maps were produced after a correlation analysis of the six VIs and only referring to olive and citrus trees shown in Figure 3.17.

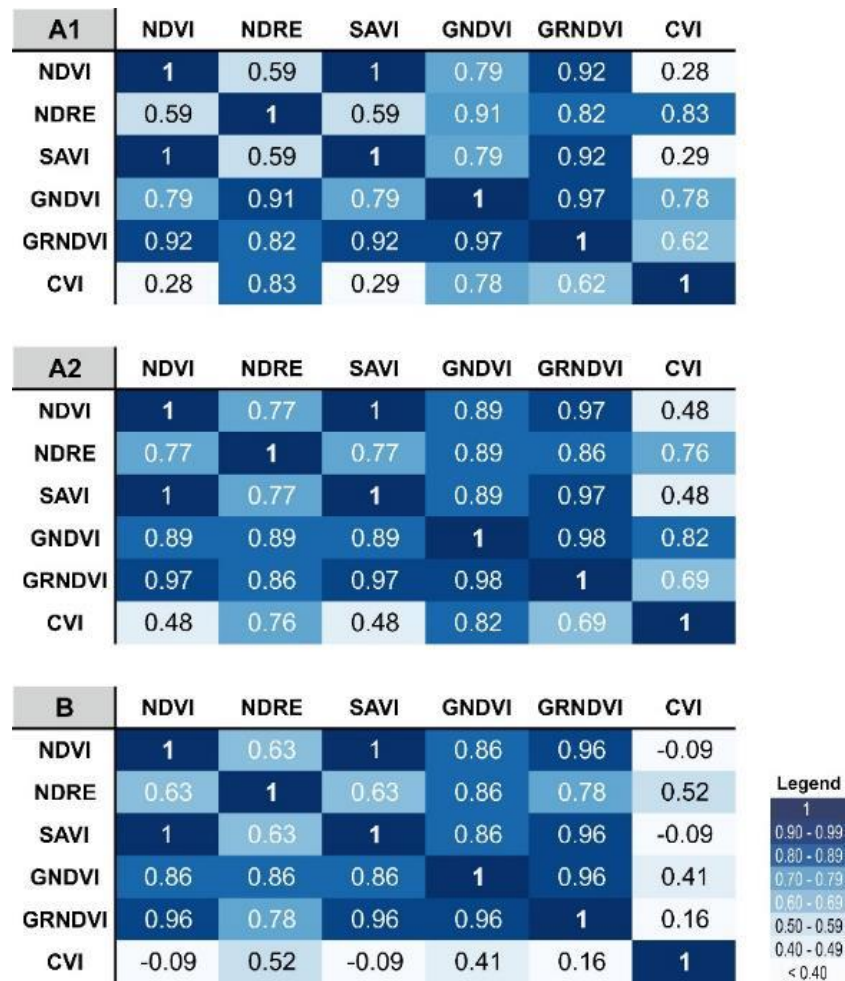


Figure 3.17 Correlation matrix between the six selected vegetation indices (VIs) implemented only using the class of trees (bergamot, clementine, and olive) as input data (source, Modica et al., 2020).

For each study site, two vigor maps were produced (Figures 3.18 and 3.19). Analyzing correlation matrices on VIs applied on trees' crowns in the study case A1, can be observed a high correlation between GNDVI and GRNDVI (0.97), GNDVI and NDRE (0.91) while there is not a very high correlation between GNDVI and NDVI (0.79). NDVI is equal to SAVI (1) and is low correlated with NDRE (0.59). For these reasons, NDRE and NDVI were used for the production of vigor maps of the orchards.

In the study-site A1, the NDVI map, shown in Figure 3.18, highlights two different zones of the citrus orchard. In one, the clementine trees showed a reduced vegetative vigor, and index values range between 0.4 and 0.65, while in the other zone, NDVI values, comprised between 0.7 and 0.9,

showed a better trees' condition. NDRE (Figure 3.19) has average vigor values comprised between 0.2 and 0.3 in most parts of the citrus orchard. The lowest values, were found where, being the foliage less dense, the background soil is visible.

The study site A2, observing correlation matrices on VIs applied on trees' crowns (Figure 3.17), observed high correlations between the NDVI, GNDVI, and GRNDVI. SAVI and CVI had no significant correlations with the other VIs. The olive orchard was detected using the CVI combined with CHM, similar to what was done in the study site A1, while shadows and buildings were classified using the NIR band and the SAVI combined with the CHM. GNDVI has a good correlation with NDRE (0.89), NDVI (0.89), SAVI (0.89) and a very high correlation with GRNDVI (0.98). SAVI shows a high correlation with GNDVI (0.89) and GRNDVI (0.97) and NDVI (1). NDRE has a high correlation with GNDVI (0.89) and low correlations with NDVI (0.77), SAVI (0.77) and CVI (0.76). As in dataset A1, NDRE and NDVI were selected to map vigor.

The NDVI vigor map (Figure 3.18) showed that the olive orchard's vegetative status is not good, ranging its values from 0.15 to 0.7, highlighting this orchard's vegetative stress planted in unsuitable land characterized by a very clayey and compact soil. The NDRE vigor map (Figure 3.19), on the other hand, assumes low to medium values, ranging between 0.2 and 0.3, and confirms what has already been highlighted by the NDVI index.

Looking at correlation matrices on VIs applied on trees' crowns in the case study B (Figure 3.17), similar correlations to those regarding the indices applied on the entire scene were observed with regard to the NDVI while there is a low correlation between NDRE and NDVI (0.63). For this reason, these two indices were chosen to map vigor. The NDVI (Figure 3.18) still proves to be suitable for monitoring vegetation's health status. In detail, in the lower part of the image and on the right, where both bergamot and olive trees are closer to the sea, and where the vegetative vigor is lower, the index' values range between 0.2 and 0.5. As can be easily observed on the map, the highest values are in sector 5, comprised between 0.8 and 1.

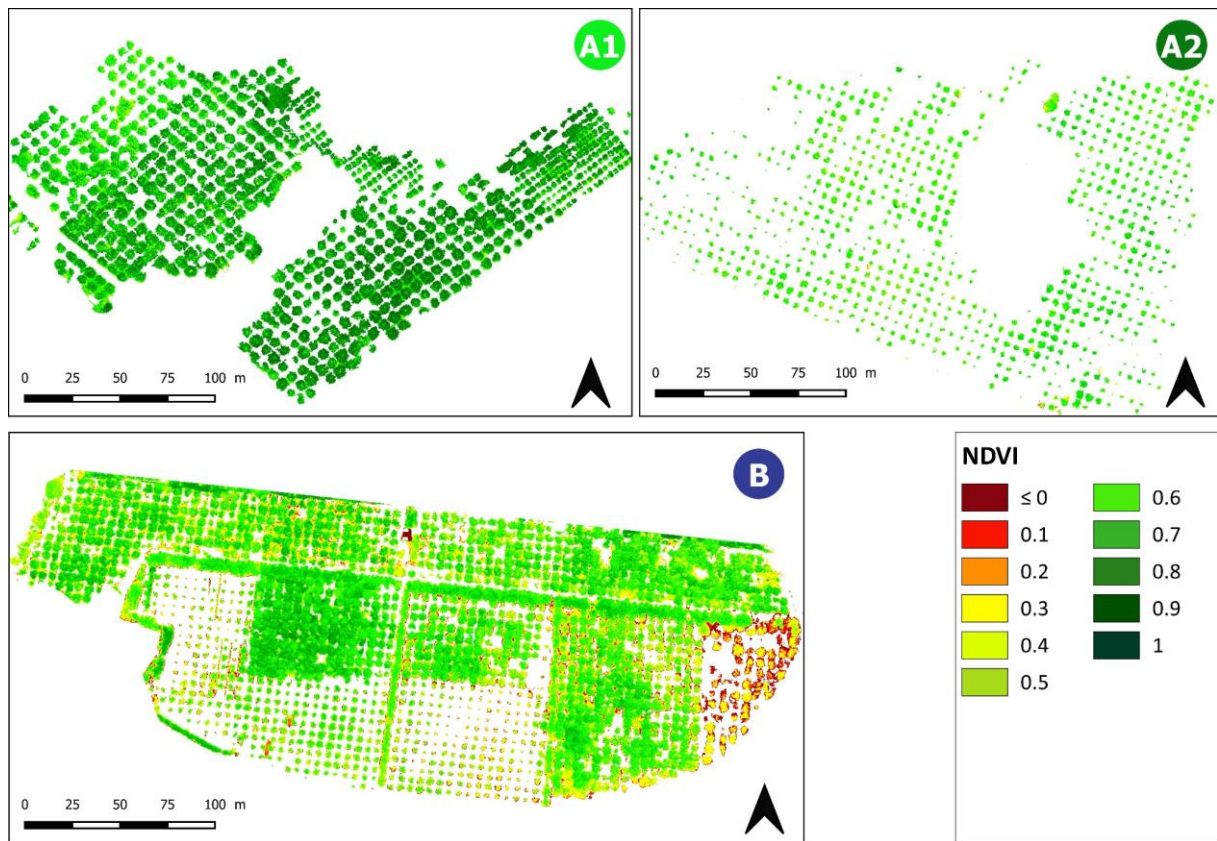


Figure 3.18 Vegetative vigor maps of the three analyzed study site [A1 (Clementine), A2 (Olive) and B (Bergamot and Olive)] based on the Normalized Difference Vegetation Index (NDVI) values (*source*, Modica et al., 2020).

Observing NDRE (Figure 3.19) map, the contrast between the vegetative vigor of bergamot trees and olives trees is evident. In particular, olive trees are characterized by NDRE values from 0.25 and up, while the highest value (0.25) concerns bergamot trees and can be found only in sectors 5 and 8. As also highlighted by the NDVI the lowest values of NDRE can be found in the lower part of sector 4 and in the middle between sectors 2 and 1, which are the areas closest to the sea.

Furthermore, two aspects cannot be overlooked. The first regards the size of the analyzed study sites, comprised from 4.6 to 7.9 ha, whose surface is comparable to operational conditions and the second aspect also concerns an operational issue. The time needed for the complete implementation of the proposed workflow, from the on-field data collection to obtaining vigor maps, can be estimated in one working day of two good skilled operators in geomatics and computer image processing. All data processing was implemented using a workstation with these characteristics: OS MS Windows 10 Pro, CPU Intel Xeon E5-2687W v2, 64 GB RAM DDR3 1866 MHz, GPU NVIDIA K5000.

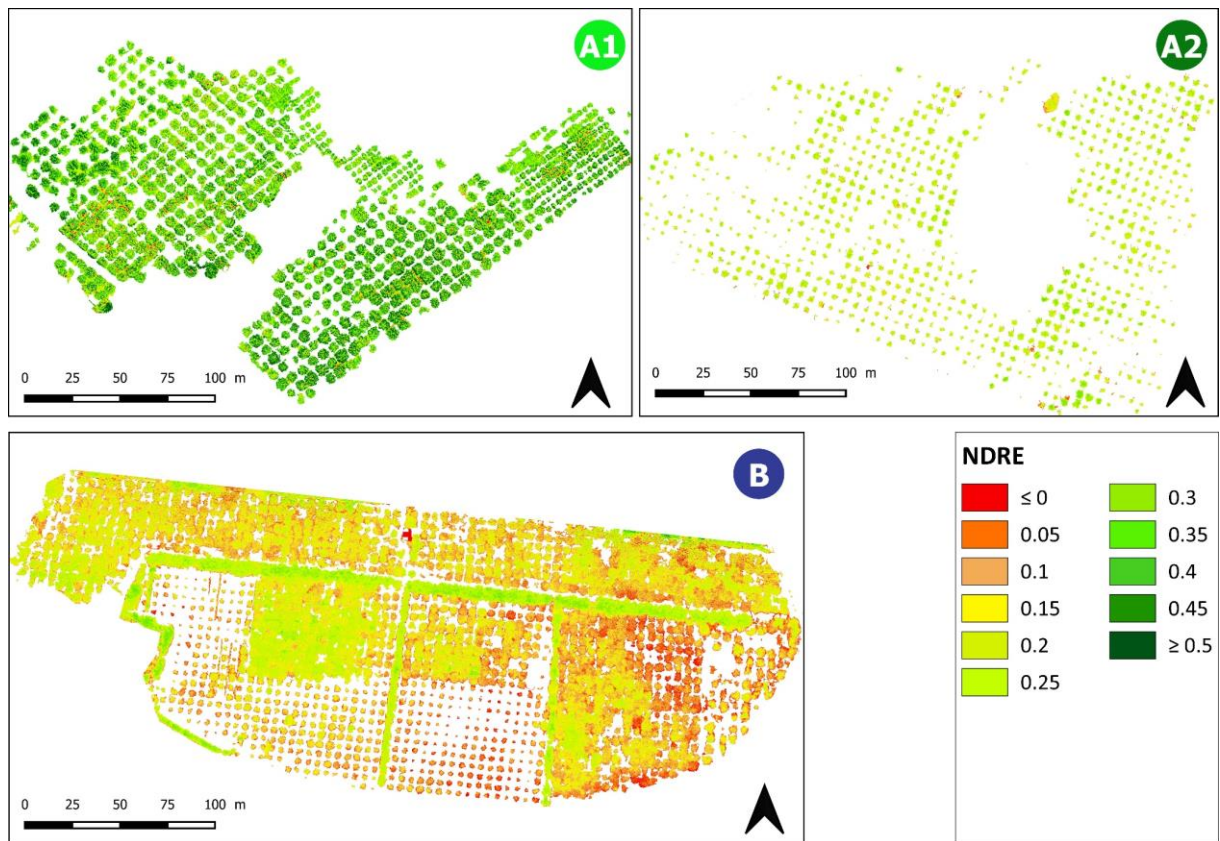


Figure 3.19 Vegetative vigor maps of the three analyzed study site [A1 (Clementine), A2 (Olive) and B (Bergamot and Olive)] based on the Normalized Difference Red edge Vegetation Index (NDRE) values (source, Modica et al., 2020).

3.3 Conclusions

In the present research work, a quick and reliable semi-automatic workflow implemented to process MS UAV imagery and aimed at detecting and extracting olive and citrus trees' crowns in PA was proposed. As reported by Solano et al. (2019), in the GEOBIA approach, the extraction of the trees' crowns benefits from orchards arranged according to regular planting patterns with minimal overlap between the canopies. In this work, it was demonstrated that the high spatial resolution of UAV permits overcoming these issues. Furthermore, the use of the UAV platform, mounting an MS camera such as Tetracam μ -MCA06 Snap, has demonstrated flexibility and reliability in photogrammetric reconstruction at the farming scale. Using UAV high-resolution images, more focused analyzes were carried out only on the cultivated areas, excluding shadows and ground, with the aim to obtain a reasonable reconstruction of the orchards and monitoring of the crop conditions. For obtaining good results, good quality UAV field surveys are needed. As stated in discussing the obtained accuracy, the correct UAV flight planning has a key-role in obtaining good results, and the same can be said about the measures taken in the field, such as the

laying of GCP. In this work, referring to study sites A2 and B, a wider buffer beyond the orchard boundary could have improved the accuracy in the extraction of trees' crowns. This can be suggested by providing a buffer distance of at least 20 m outside the surveyed area. In the presented workflow, great attention was also paid to simplifying the classification step and the procedure's speed. Firstly, visual interpretation was applied to UAV imagery to acquire prior knowledge of the imagery (Ma et al., 2015). Concerning image segmentation, scale parameters were selected to generate segmented objects representing real objects (Blaschke, 2010), single canopies in this case.

Regarding the classification, an unsupervised approach that has the advantage not to provide a training phase was proposed. Thus, there is not the need for the selection of training samples set for training the classifier (Ma et al., 2015). The novelty of the proposed procedure relies upon, thus, on its replicability, reliability and speed proved with promising results in three different datasets. It is important to consider that agricultural environments may be more uniform than natural ones (Csillik et al., 2018). The present work has, among other things, concerning the application of the proposed approach on a case (study site B) of heterogeneous tree orchards. The heterogeneity regards several tree plantation distances and composition, different crop management, and different tree age, height, and crown diameters, thus, resulting in the high spatial variability of the scene.

Therefore, in implementing the proposed workflow, its operational application has been taken into account. It appears worth of interest to highlight that this workflow needs a working day of two good skilled operators in geomatics, starting from the on-field data collection to obtaining vigor maps. In this respect, for its application in different conditions of those analyzed in the present work, the time needed for its complete implementation can be estimated in one working day of two good skilled operators in geomatics and image processing. These characteristics are in line with the need of the PA to provide information, in a short time, useful to guide farmers' decisions.

4 Object-based classification using machine learning algorithms and UAVs multispectral imagery precision agriculture: case studies on bergamot and “Cipolla Rossa di Tropea”

Adapted from

Comparison and assessment of different object-based classifications using machine learning algorithms and UAVs multispectral imagery in the framework of precision agriculture

Submitted and under revision

Giuseppe Modica, Giandomenico De Luca*, Gaetano Messina*, Vincenzo Fiozzo, Salvatore Praticò**

** Dipartimento di Agraria, Università degli Studi Mediterranea di Reggio Calabria, Località Feo di Vito, I-89122 Reggio Calabria, Italy*

Precision agriculture (PA) is defined as “a management strategy that gathers, processes and analyzes temporal, spatial and individual data and combines it with other information to support management decisions according to estimated variability for improved resource use efficiency, productivity, quality, profitability and sustainability of agricultural production (www.ispag.org/about/definition, last access 15 May 2020). Commonly PA’s implementation phases are data collection, field variability mapping, decision making, and management practice (Zhang and Kovacs, 2012). Remote sensing (RS) intervenes in the first three phases (Lamb and Brown, 2001; Mulla, 2013; Seelan et al., 2003; Stafford, 2000), i.e., in collecting and analyzing information about crops and soil characteristics using sensors mounted on satellites and aircraft (Gago et al., 2015; Khanal et al., 2017; Senthilnath et al., 2017; Wójtowicz et al., 2016). Over the last decade, the increasing use of unmanned aerial vehicles (UAVs) platforms has offered a new solution for crop management and monitoring, as it enables very-high-resolution (VHR) images (Maes and Steppe, 2019; Pádua et al., 2017; Tsouros et al., 2019). UAV data has also been characterized to be obtained with high time-frequency, especially in monitoring small production areas (Primicerio et al., 2012; Zhang and Kovacs, 2012). Besides, UAVs have low maintenance costs (Shakhathreh et al., 2018) and are easy to manipulate (Sheng et al., 2010). Furthermore, UAVs have the unique ability to mount onboard and use several sensors simultaneously (Maes and Steppe,

2019). However, it is important to know how to apply effective and automatic image analysis methods with a large calculation capacity to obtain maps useful for crop monitoring (Brocks and Bareth, 2018; Jiménez-Brenes et al., 2017; Schirrmann et al., 2016). The availability of a large amount of VHR data created new possibilities for vegetation classification and monitoring with very high spatial detail levels (De Luca et al., 2019; Teodoro and Araujo, 2016). This also represents a challenge for RS, because of the greater intraclass spectral variability (Aplin, 2006; Torres-Sánchez et al., 2015). Geographic Object-Based Image Analysis (GEOBIA) (Blaschke, 2010; Blaschke et al., 2014) approach allows addressing these issues. GEOBIA is a classification method that divides RS images into significant image objects and evaluates their characteristics on a spatial, spectral, and temporal scale (Hay and Castilla, 2006; Solano et al., 2019). GEOBIA generates image objects using different segmentation methods rather than analyze and classify individual pixels (Hofmann et al., 2011). In the last decade, machine learning (ML) algorithms have attracted a great deal of attention in RS (Crabbe et al., 2020; Liakos et al., 2018; Noi and Kappas, 2018), offering new opportunities for agricultural mapping (M. Li et al., 2016; Liakos et al., 2018; Ma et al., 2017; Perez-Ortiz et al., 2017; Rehman et al., 2019). ML algorithms demonstrated effectiveness in classifying weeds (De Castro et al., 2018; Pérez-Ortiz et al., 2016), disease detection (Abdulridha et al., 2019a, 2019b), and land cover mapping and assessment (De Luca et al., 2019; M. Li et al., 2016; Ma et al., 2017; Noi and Kappas, 2018; Qian et al., 2015). Among the object-based classification algorithms, Random Forest (RF) and Support Vector Machine (SVM) were considered, as reported in Li et al. (2016) and Ma et al. (2017), the most suitable supervised classifiers for GEOBIA having been their classification performances very satisfying (Mountrakis et al., 2011). On the other hand, in recent years, the K-Nearest Neighbour (KNN) algorithm has been widely used for object-based land classification (Crabbe et al., 2020; Griffith and Hay, 2018; Huang et al., 2016; Maxwell et al., 2018; Noi and Kappas, 2018; Sun et al., 2018). Normal Bayes (NB) is another algorithm that differs from the three already mentioned because it does not need the setting of any parameter which, besides being time-consuming, could be subjective (Qian et al., 2015).

This study's main objective is to compare the performances of different GEOBIA algorithms (KNN, SVM, RF, and NB) in terms of quality of obtained results and requested processing time and to assess them in terms of their applicability in the framework of PA. A complete supervised classification of VHR UAV imagery was done, one for each of the above mentioned four algorithms implemented in eCognition software (Trimble Inc., 2019). This software allows an easy implementation of several different and numerous decision-making rules (made available by the

software or customizable and implementable by the user) based on distinctive features derived from objects (Drăguț et al., 2014).

Study sites are two and are characterized by two different crops, both socioeconomically relevant for the investigated areas. Bergamot (*Citrus bergamia*, Risso), labeled with the protected designation of origin (PDO) label *Bergamotto di Reggio Calabria – olio essenziale* (“Bergamot of Reggio Calabria - essential oil”), and onion (*Allium cepa* L.), labeled with the protected geographical indication label “Cipolla Rossa di Tropea IGP” (“Tropea’s Red Onion PGI”). Therefore the comparison between different classification algorithms was provided in two different crops. The first one is a citrus orchard, and the second one is an onion crop.

4.1 Materials and Methods

4.1.1 Study site

The study site 1 (Figure 4.1) is a citrus orchard (bergamot, *Citrus bergamia*) located in Palizzi (Province of Reggio Calabria, Calabria, Italy) (37°55'06"N, 15°58'54"E, 4 m a.s.l.). Inside the orchard, there are long windbreak barriers made up of olive trees. The area where the orchard lies is 5.13 ha. The citrus orchard is uneven-aged, with trees aged from 5 to 25 years and which height is comprised between 1.5 to 4.0 m.

The study site 2 is an onion crop located in Campora S. Giovanni, in the municipality of Amantea (Cosenza, Italy, 37°55'06" N, 15°58' 54" E, and 4 m a.s.l.). The farm is part of a consortium that includes other producers whose total cultivated area under onion crop is more than 500 ha. The onions produced are a relevant typical product for the economic and rural development of this area (Bernardi et al., 2013; Messina et al., 2019). The study area examined is a field of 1.00 ha. The field is crossed by 4 paths of 2.5 m each, used for the passage of agricultural vehicles. Inside the field, visible in the images used, it is evident the presence of weeds whose removal, manually, is carried out periodically. Typically, the onions transplant took place in early September while the harvest occurs from mid to the end of January.

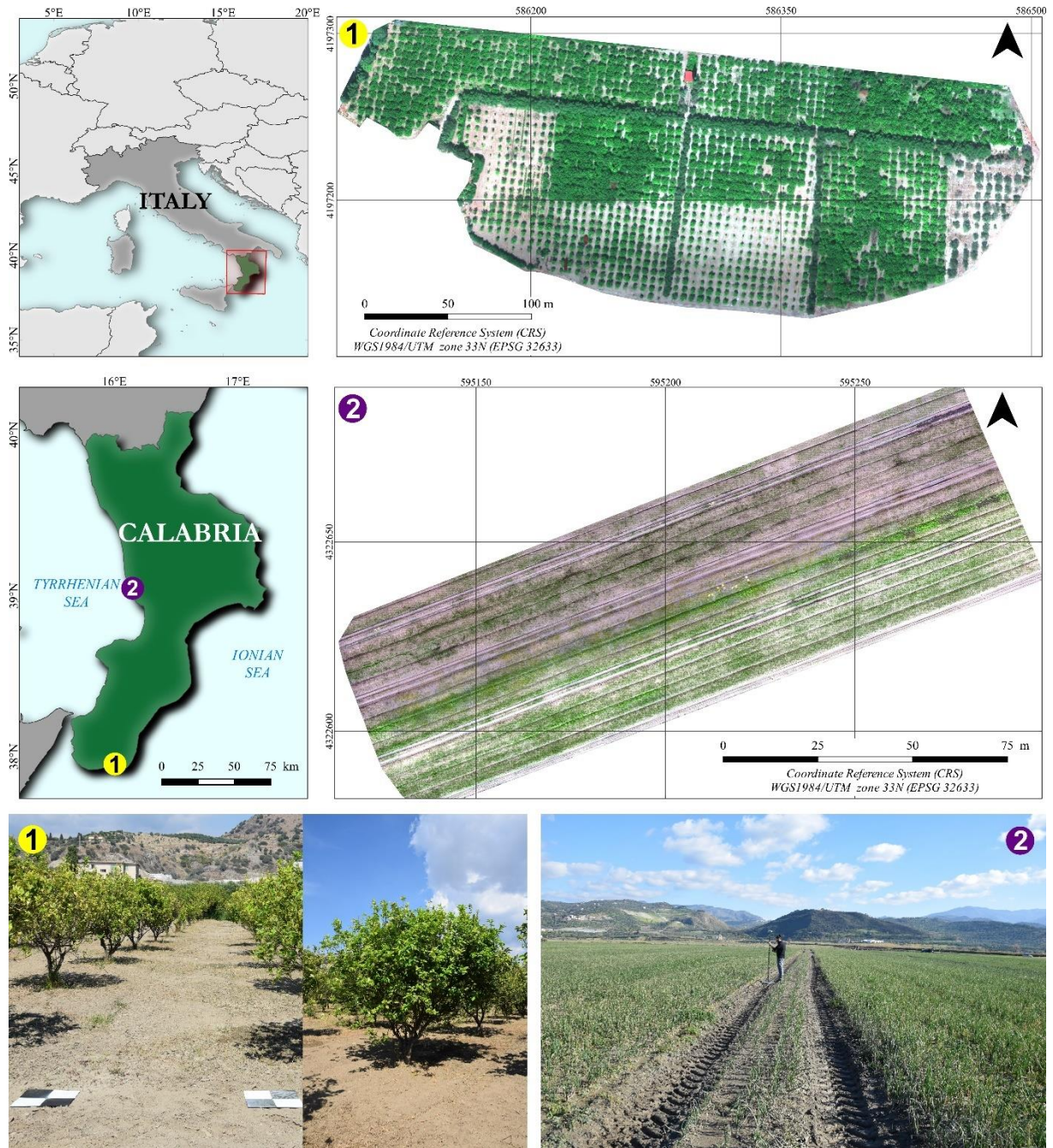


Figure 4.1 Geographical location of the two study sites, 1 (citrus orchard) and 2 (onion crop). Below, we provided two representative photos of them.

4.1.2 UAV surveys and data acquisition

The imagery of the two study sites was acquired using the Tetracam μ -MCA06 snap (Tetracam Inc. – Chatsworth, USA) mounted on board of a multirotor UAV (Multirotor G4 Surveying Robot – Service Drone GmbH) in planned waypoints mission mode. Flight missions were planned with the QGIS plugin “UAV Planner 3D” (www.altodrones.com, last access 30 April 2020) that uses morphology information of the study area as input to correct the altitude above ground level of

the UAV during the mission, following the altitude field variability. The μ -MCA06 snap is a six sensors narrow-band multispectral camera equipped with its own global navigation satellite system (GNSS). Each sensor shoots simultaneously, and all images are then synchronized via the master channel (Table 4.1).

Table 4.1 Tetracam μ -MCA06 snap (Global shutter) sensor characteristics bands specification (wavelength and bandwidth).

Geometry of lens	Sensors	Bands	Central band wavelength [nm]	Bandwidth [nm]
Focal Length (fixed lens) 9.6 mm Dimension 6.66mm x 5.32mm 1.3 Megapixel CMOS 4:3 format 1280 x 1024 pixels Pixel size 4.8 microns	Master (0)	Near-Infrared 1 (NIR1)	800	10
	1	Blue	490	10
	2	Green	550	10
	3	Red	680	10
	4	Red edge	720	10
	5	Near-Infrared 2 (NIR2)	900	20

Due to the different characteristics of the analyzed crops in the two study sites, we carried out surveys with different flight altitudes. Consequently, the GSD was 4.1 cm for study site 1 and 1.5 cm for study site 2 (Table 4.2).

In order to obtain a high quality geolocated output, the coordinate (WGS 84/ETRF 1989 UTM 33N) of a series of ground control points (GCPs - 50 cm x 50 cm black and white polypropylene panels) were acquired, before each flight mission, with Leica GS12 RTK GNSS (planimetric and altimetric accuracy of ± 2.5 cm and ± 5 cm, respectively).

Table 4.2 Flight and UAV dataset characteristics.

Study site	Date	Flight height [a.g.l.]	Take-off time [UTC+1]	Speed [m s ⁻¹]	N° of flights	Total duration [min]	Surveyed area [ha]	Photos [n°]	Sidelap and Overlap [%]	RMSE [m]		
										X	Y	Z
1	2018/09/17	80 m	11:00 am	2.5	2	49	7.9	2825	80	0.03	0.03	0.09
2	2019/11/21	30 m	12:00 am	2.5	1	19	1.0	1800	80	0.02	0.02	0.05

All the acquired images were first extracted from the camera and converted from the *.RAW format to 10-bit TIFF format using PixelWrench II (version 1.2.4, Tetracam Inc – Chatsworth, USA) and then aligned, stacked, and radiometrically corrected using Pix4Dmapper Pro (version 4.3 – Pix4D

SA, Switzerland). To enhance each band's radiometric calibration, the reflectance values of three calibration targets (50cm x 50 cm polypropylene panes in black, white, and gray respectively) were collected using the field spectroradiometer Apogee Ps-300. After this process, a reflectance orthomosaic was produced for each of the six bands of Tetracam μ -MCA06 snap and then stacked into a single multiband orthomosaic (Blue, Green, Red, Red edge, NIR1, and NIR2). Moreover, a Digital Surface Model (DSM) was created after a photogrammetric process.

4.1.3 Pre-processing and datasets

Before launching the GEOBIA workflow, GNDVI (Gitelson et al., 1996) was calculated for the two datasets to exploit it as an additional raster layer able to increase spectral information. Already several studies have shown that the vegetation indices enhanced spectral differences between vegetation/no-vegetation objects in UAV images (De Luca et al., 2019; Gašparović et al., 2020; López-Granados et al., 2016b; Solano et al., 2019; Torres-Sánchez et al., 2014; Villoslada et al., 2020). In this case GNDVI was used with the intention of exploiting its higher sensitivity to the chlorophyll concentration compared to NDVI (Candiago et al., 2015; Gitelson and Merzlyak, 1998). A linear band stretching (rescale) in a range of 8 bits [0, 255], was performed for all the six bands of the orthomosaic and for both GNDVI and DSM. The objective of the band stretching was to equalize the range of values of each input variable, minimizing the influence of differences in their magnitudes and the effect of potential outliers (Angelov and Gu, 2019; Immitzer et al., 2016). Subsequently, a layer stacking process was carried out by merging the six-bands with GNDVI and DSM. For each of the two datasets, eight layers were used: Blue, Green, Red, Red edge, Near-infrared 1 (NIR1), Near-infrared 2 (NIR2), GNDVI and DSM.

4.1.4 eCognition Multi-Resolution Segmentation (MRS)

In GEOBIA, image segmentation is the first process that fragmented a digital image into a set of spatially adjacent segments composed of a group of pixels presenting homogeneous radiometric and semantic features. Each segment on the image should represent a real object on the earth's surface (Blaschke, 2010; Blaschke et al., 2014; Pal and Pal, 1993).

The multiresolution (MRS) algorithm implemented in eCognition is a bottom-up region-merging strategy starting with one-pixel objects (Aguilar et al., 2016). MRS is a process of optimization which, starting from a given number of objects, minimizes their average heterogeneity and maximizes the homogeneity (Trimble Inc., 2019). As the first step, MRS identifies single objects of a pixel's size and then merges them with neighbor objects following a criterion of relative

homogeneity. This criterion allows analyzing the color and shape properties of the initial object and of that obtained by the merging process to measure the level of their homogeneity. Color homogeneity is assessed by the standard deviation of the spectral values, while the deviation from a compact (or smooth) shape allows measuring the shape homogeneity. The shape parameter deals with the influence of geometric form on the segmentation compared to the color, and its value ranges between 0 and 0.9. In contrast, the compactness parameter takes into account the combined influence of shape and smoothness. Concerning the scale parameter, several scholars showed its importance in determining the size and dimension of objects generated by the segmentation (Ma et al., 2017, 2015; Modica et al., 2020; Witharana and Civco, 2014; Yang et al., 2019). The higher the scale parameter values, the larger the obtained image objects, while, conversely, its low values resulting in smaller image objects.

4.1.5 Image Classification

For each of the two study sites, the following four classification algorithms were implemented: KNN, SVM, RF, and NB. The two study sites chosen, being different cultivations (i.e., an annual crop and a tree orchard), were considered suitable to compare four supervised classification algorithms' performance. The classification was implemented using five land cover (LC) classes for the study site 1 (i.e., "Bergamot", "Olive", "Grass", "Bare Soil", "Shadows") and three LC classes for the study site 2 (i.e., "Onion", "Weeds", "Bare soil"). After the segmentation process there is the choice of trainers which is one of the most important and critical steps affecting the final quality of the classification results (Ma et al., 2015). With the aim to train each of the four supervised algorithms, two samples of 800 and 500 points for study sites 1 and 2, respectively (Table 4.5). These points were randomly sampled in the QGIS environment. These points were then superimposed on each of the two segmentation output files obtained to select and extract the polygons within which each point fell. Polygons selected were then labeled with the corresponding LC class by visual interpretation (Figure 4.2). For each trainer polygon, some features' objects as mean and standard deviation were extracted.

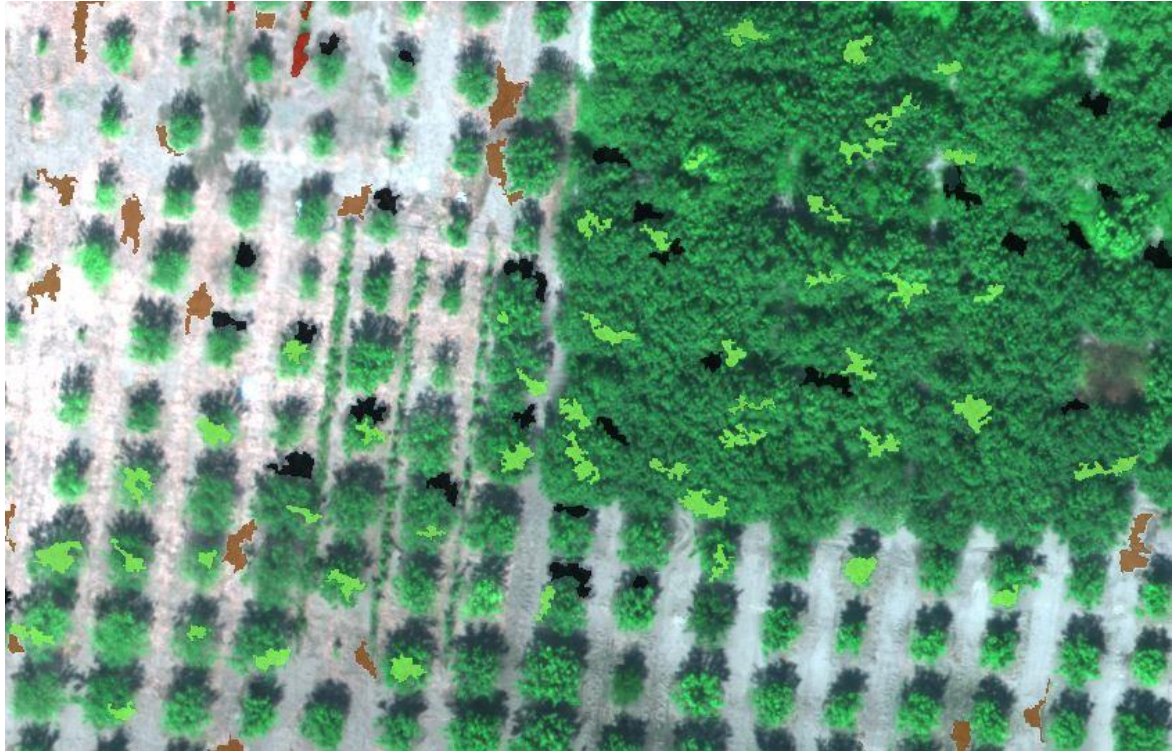


Figure 4.2 Training polygons of dataset 1: in green those belonging to the "bergamot" class; in brown those belonging to the "bare soil" class.

The KNN is a non-parametric classifier algorithm (Clarke et al., 1974) and is one of the more used classification methods in GEOBIA applications (Crabbe et al., 2020; Georganos et al., 2018; Griffith and Hay, 2018; Huang et al., 2016). It assigns an object to a given class based on the class to which the neighboring objects belong in an N-dimensional feature space. The KNN generally uses the Euclidean distance to select among the objects closest to each other (in terms of object features distance). The number of neighbors to be analyzed in the feature space is defined by parameter k 's value. k is the tuning parameter that determines the classifier's performance and is generally a small positive integer number (M. Li et al., 2016; Qian et al., 2015). For example, if $k = 2$, the object will be assigned to the nearest neighbor's class. Higher values reduce the effect of noise in classification, but there is less distinction between the boundaries of the different classes (Maxwell et al., 2018; Trimble Inc., 2019). In this case, k was equal to 1.

SVM is a supervised non-parametric classifier algorithm, which is based on the Statistical Learning Theory (Cortes and Vapnik, 1995; Vapnik, 1998) and on the kernel method, which has been introduced in the last years for the application of the image classification (Mountrakis et al., 2011). Originally, the SVM was introduced for linear binary classifications. However, it allows performing a multiclass classification. In a set of training examples belonging to each one to two classes, an SVM training algorithm creates a model that assigns new examples into one class or the

other (Trimble Inc., 2019). In particular, this algorithm learns the boundary between training samples belonging to different classes and so train the algorithm, projecting them into a multidimensional space and finding a hyperplane, or a set of hyperplanes that maximize the separation of the training dataset between the predefined number of classes (Huang et al., 2002; Mountrakis et al., 2011). SVM uses different kernels: linear, polynomial, sigmoid and radial basis function (RBF). In this study case, a linear kernel-type function with a C model-type was implemented. There is only one tuning parameter to set: the parameters of cost (C). The C parameter deals with the size of misclassification allowed for non-separable training data and regulates the training data's rigidity (Cortes and Vapnik, 1995; Vapnik, 1998). C value equal to 1 was used.

RF is an automatic learning algorithm proposed by Leo Breiman (2001) and improved by Cutler et al. (2007). The RF is a decisional tree's method that randomly creates a forest comprising many decision trees, every independent from each other (Li et al., 2016). Using an input feature vector, the algorithm classifies it accordingly with each tree in the forest and then outputs the class label that received the majority of "votes". All the trees are trained with the same features but on different training sets derived from the original training set. This happens utilizing bootstrap aggregation, namely, bagging, which permits the selection, for each training set, of the same number of vectors in order to create different formation subsets for producing a variety of trees, any one of which provides a classification result as in the original set (=N). The algorithm generates an internal and impartial estimation of the generalization error using "out-of-bag" (OOB) samples, which include observations that are in the original data and that not recur in the bootstrap sample (Cutler et al., 2007). The RF parameters were set as follows: the maximum depth of the tree was set on 10, the minimum number of samples per node was set on 10, and to the cluster possible values of a categorical variable into $K \leq \text{cat}$ clusters to find a suboptimal split was assigned a value of 16. The parameter which deals with the number of features in each split (or the number of features to build a random subset at each node) was set on the default value (0). About this parameter, many studies used the default value (Duro et al., 2012). Finally, the maximum number of trees was set on 300, while the OOB error was set on 0.01.

NB is a probabilistic classifier based on Bayes' theorem (from Bayesian statistics) (Qian et al., 2015). This algorithm is based on the concept that the presence (or absence) of a particular feature of a class is not correlated to the presence (or absence) of any other feature (Trimble Inc., 2019). It uses a training set to calculate the probability that an object belongs to a given class or not. NB first

estimates the mean vectors and covariance matrices of the training samples' selected features for each class, and through them, provides for a classification (Qian et al., 2015). This classifier does not need tuning parameters.

To have an objective comparison of the performance of the classification algorithms, their chosen parameters are the same in both study sites.

As far as the RF and SVM parameters, several parameters values were tested based on those recommended in De Luca et al. (2019). Furthermore, in selecting the values considered more effective of the algorithms' parameters, several research studies that dealt with this issue were taken into account (Li et al., 2016; Noi and Kappas, 2018; Qian et al., 2015; Rodriguez-Galiano et al., 2012; Sun et al., 2018). In Table 4.3, the values of the parameters set for each of the three classification algorithms were showed.

Table 4.3 Main parameters set for each of the implemented classification algorithms, K-Nearest Neighbour (KNN), Support Vector Machine (SVM) and Random Forest (RF).

Algorithm	Parameter	Values
KNN	k	5
SVM	C	1
RF	Number of trees	300
	Maximum tree depth	10
	Min. number of samples per node	1

*NB does not need tuning parameters

4.2 Accuracy Assessment

For the evaluation of the classification accuracy of the algorithms used, a sample of 500 random points was used for each of the two dataset scenes. Each point was labeled according to the LC classes defined by visual interpretation (ground truth). Then, for each of the four classifiers, all the polygons containing the sampling points were selected. The ground truths were compared with the classified LC class. The producer's accuracy, which represents the ratio between the correctly classified objects in a given class and the number of validation objects for that class, the user's accuracy which is the ratio between the correctly classified objects in a given class and all the classified objects in that class, and the overall accuracy (i.e., the total percentage of correct classification) were calculated (Congalton and Green, 2019; Lillesand et al., 2015). Subsequently,

from these measures, the F-score (Goutte and Gaussier, 2005; Ok et al., 2013; Shufelt, 1999; Sokolova et al., 2006) for every single class ($F\text{-score}_i$) (Equation 4.1) and the multi-class F-score ($F\text{-score}_M$) (Equation 4.2) (Sokolova and Lapalme, 2009) which represents the mean of all LC classes were calculated. The F-score is the harmonic mean of its components, *recall* (r), and *precision* (p). Having r and p the same meaning of producer's and user's accuracy, respectively, they were replaced in equations 4.3 and 4.4. The $F\text{-score}_i$ and the $F\text{-score}_M$ share the same formula (Equations 4.1 and 4.2).

$$F\text{score}_i = 2 \cdot \frac{\text{producer}'s_i \cdot \text{user}'s_i}{\text{producer}'s_i + \text{user}'s_i} \quad (4.1)$$

$$F\text{score}_M = 2 \cdot \frac{\text{producer}'s_M \cdot \text{user}'s_M}{\text{producer}'s_M + \text{user}'s_M} \quad (4.2)$$

$$\text{Producer}'s_M = \frac{\sum_{i=1}^n \text{producer}'s_i}{n} \quad (4.3)$$

$$\text{User}'s_M = \frac{\sum_{i=1}^n \text{user}'s_i}{n} \quad (4.4)$$

where i represents a single LC class and n is the total number of LC classes.

4.3 Results

4.3.1 Image Segmentation

To evaluate each dataset's segmentation performance, the two processes were timed, and the obtained segmentations were compared. Table 4.4 reports for the two study sites (1 and 2), the processing time, the number of obtained segments, and the following main characteristics: area and perimeter. For each of them, the mean and the standard deviation (StD) were reported. The processing time was calculated, not taking into account the time necessary for project preparation and setting up the parameters.

Table 4.4 The table shows the most important metrics of the obtained segmentations and the requested processing time in the study sites 1 and 2.

Study site	Processing time [min.]	n° of segments	Area [m ²]		Perimeter [m]	
			mean ± SE	StD	mean ± SE	StD
1	2	35,342	1.447 ± 0.005	0.972	10.843 ± 0.026	4.830
2	4	1,725,819	0.005 ± 0.00001	0.0035	0.450 ± 0.0001	0.181

*SE (standard error), StD (standard deviation).

Referring to both study sites, the processing time lasted, respectively, 2 and 4 minutes. The MRS algorithm produced 35,342 segments in the study site 1 and 1,725,819 in study site 2. This difference in the number of segments between the two study sites is clearly visible in Figures 4.3 and 4.4. The total number of segments and the mean area (in m²) with standard deviation provides a useful general measure of the relationship between size and number of image objects, which has a direct impact on the next classification steps (Ma et al., 2015; Torres-Sánchez et al., 2015). The mean segment size varies between 1.447 ± 0.005 (StD=0.972) m² and 0.005 ± 0.00001 (StD =0.0035) m² for study sites 1 and 2, respectively.

The mean perimeter length follows the trend of the mean segment size, varying from 10.843 ± 0.026 (StD =4.830) m and 0.450 ± 0.0001 (StD =0.181) m for study site 1 and 2, respectively.



Figure 4.3 Segmentation in study site 1.



Figure 4.4 Segmentation in study site 2.

4.3.2 Image Classification

In Table 4.5, the distribution of trainer points in all the defined land cover (LC) classes for the two study sites 1 and 2 was reported.

Table 4.5 Distribution of trainer points in land cover (LC) classes in the study sites sites.

Study site 1		Study site 2	
Number of trainers = 800		Number of trainers = 500	
Class	%	Class	%
Class 1 - Bergamot	28.21	Class 1 - Onion	57.00
Class 2 - Olive	17.53	Class 2 - Weeds	7.20
Class 3 - Grass	8.76	Class 3 – Bare soil	35.80
Class 4 – Bare soil	19.69		
Class 5 - Shadow	25.81		

In Figure 4.5, the histograms show the distribution of the number of classified segments (expressed as % of the total), according to the defined LC classes and to each classification algorithm, for study site 1. Figure 4.6 shows the same for study site 2. The graphs are compared with those that illustrate the area's distribution (in %) between each LC class and algorithm.

According to the study site 1, the classification results obtained from each of the implemented classification algorithms, the “Bergamot class” occupies the most extensive area with about 40%. The “Bare Soil” class follows, with a mean surface area of 25%, while the “Olive” class covers a surface ranging between 8% (NB) to 16% (KNN). The “Grass” class occupies the minor extension, ranging between 8% (KNN) to 18% (NB), while the surface occupied by the Shadow class occupies about 15%.

In study site 2, using SVM, RF and KNN, the distribution of area between LC classes was the most stable, resulting in a mean of 56%, 1.6%, and 42% for “Onion”, “Weeds” and “Bare Soil” classes respectively (on one hectare of a surface). In NB, the area occupied by onion is about 50%, while the area occupied by weeds and bare soil is 3% and 46%, respectively.

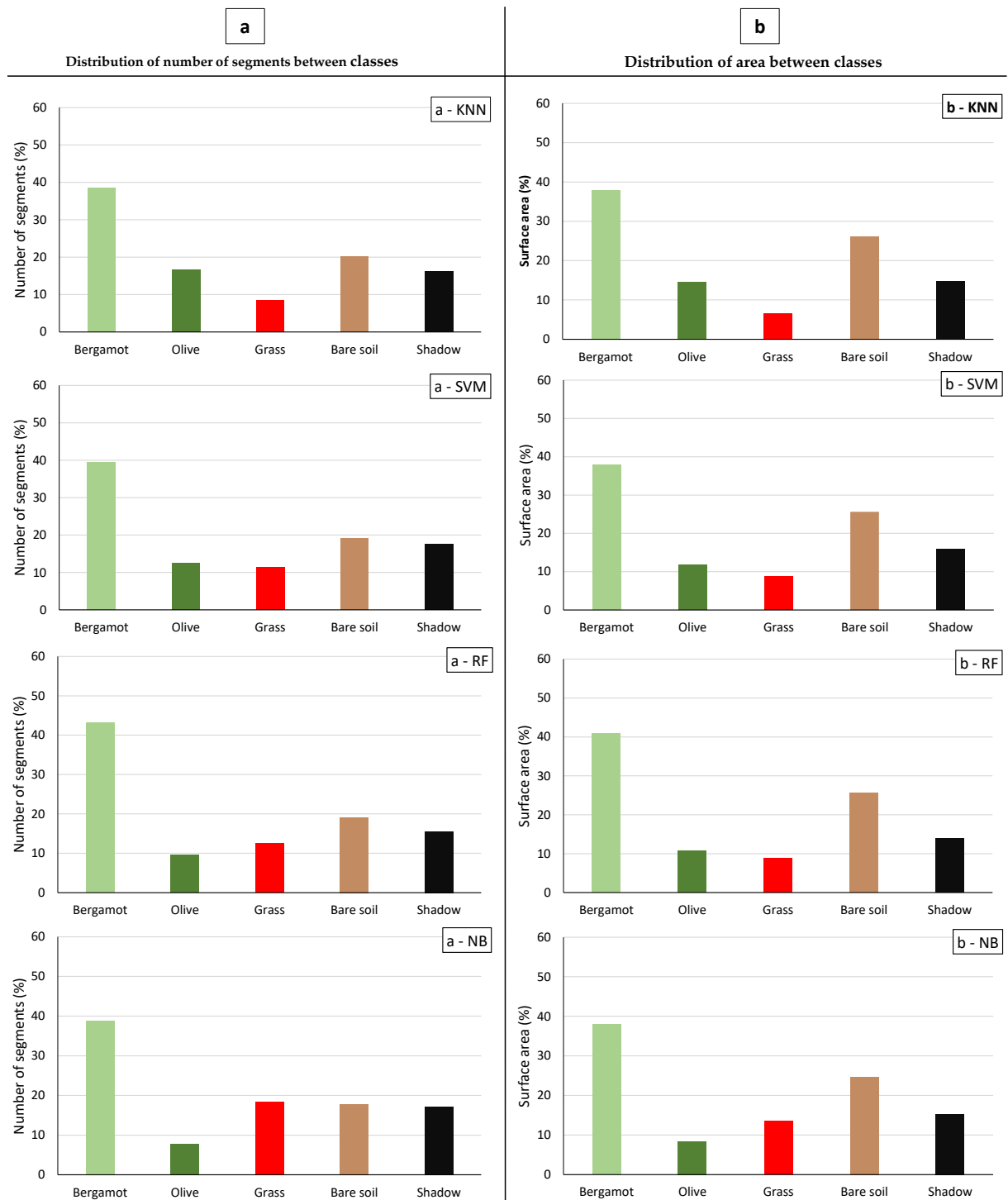


Figure 4.5 The main characteristics of the obtained classifications in the study site 1. On the left side (a), reported the distribution of the number of segments (in %) in each of the defined land use (LC) classes and according to each of the implemented classification algorithms were reported. On the right side (b), the distribution of the surface area of the obtained segments (in %) in each of the defined LC classes and according to each of the implemented classification algorithms were shown.

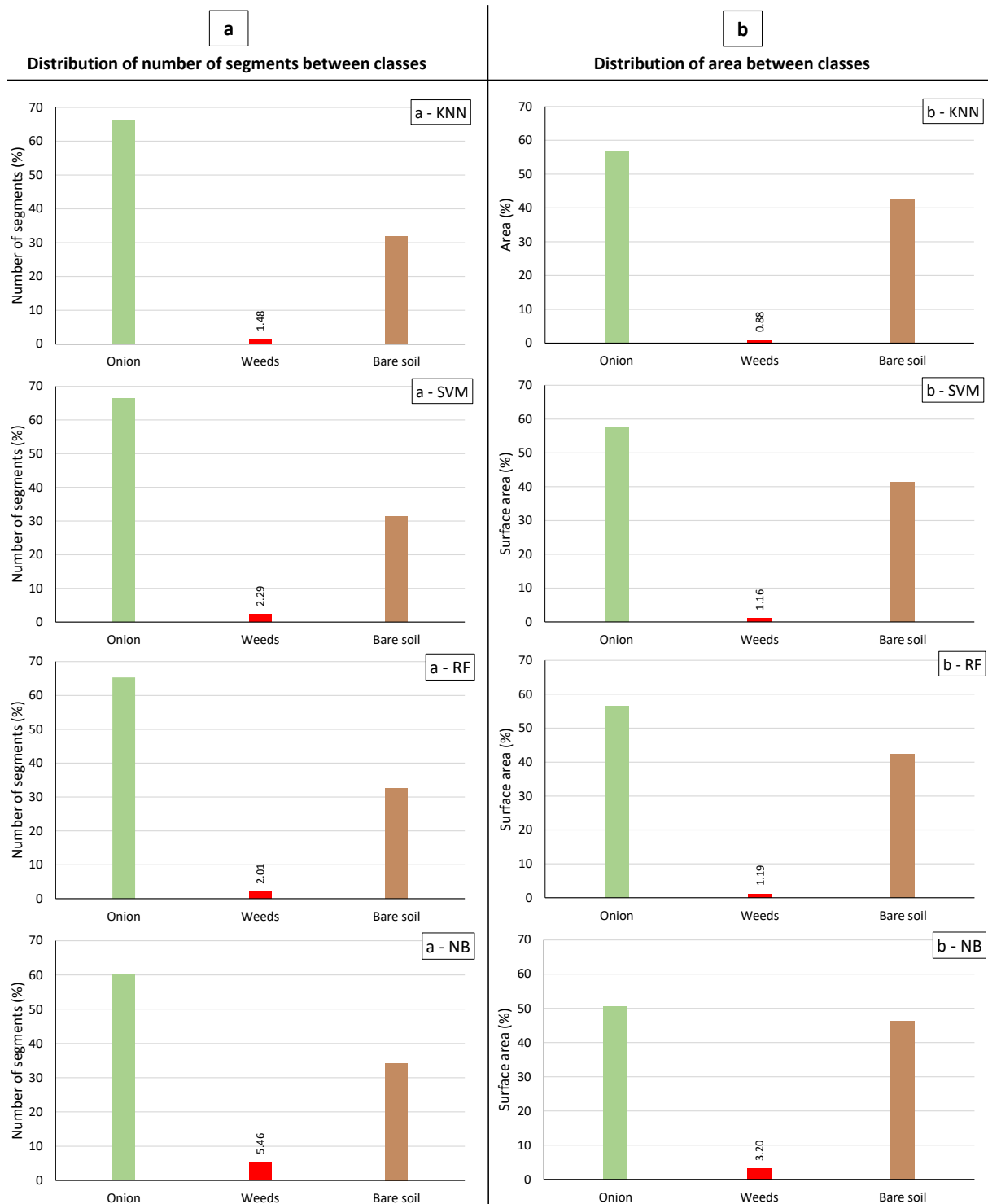


Figure 4.6 The figure shows the main characteristics of the obtained classifications of the study site 2. On the left side (a), the distribution of the number of segments (in %) in each of the defined land use (LC) classes and according to each of the implemented classification algorithms were reported. On the right side (b), we provided the distribution of the surface area of the obtained segments (in %) in each of the defined LC classes and, according to each of the implemented classification algorithms, were shown.

In Figures 4.7 and 4.8, a synoptic accuracy overview of the obtained results for all the four implemented classifiers was reported as overall, producer's and user's accuracy values, and $F\text{-score}_i$ (single-class) and $F\text{-score}_M$ (multi-class) values.

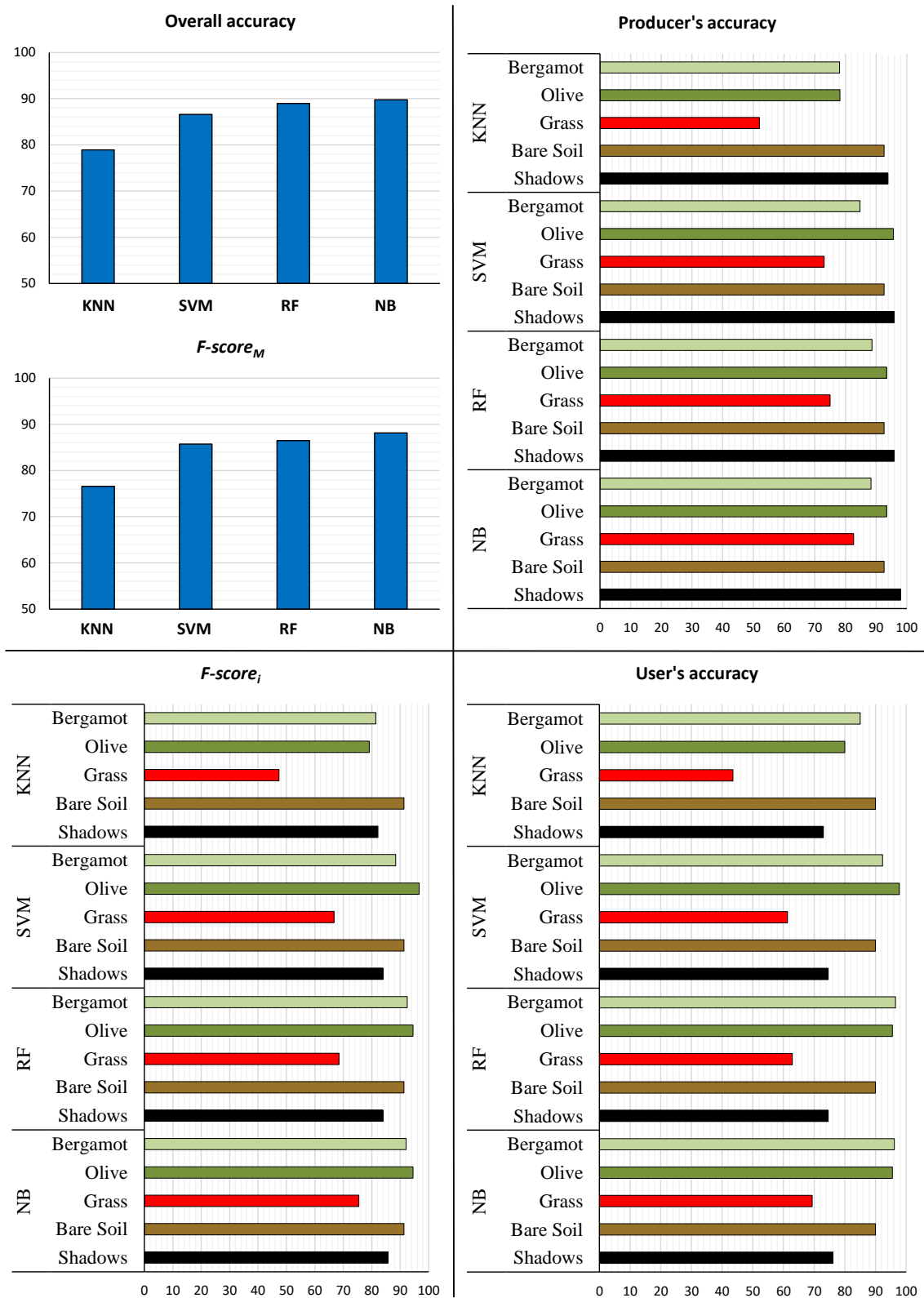


Figure 4.7 Study site 1. User's, Producer's and Overall accuracies, and $F\text{-score}_i$ (single-class) and $F\text{-score}_M$ (multi-class) values obtained for each algorithm.

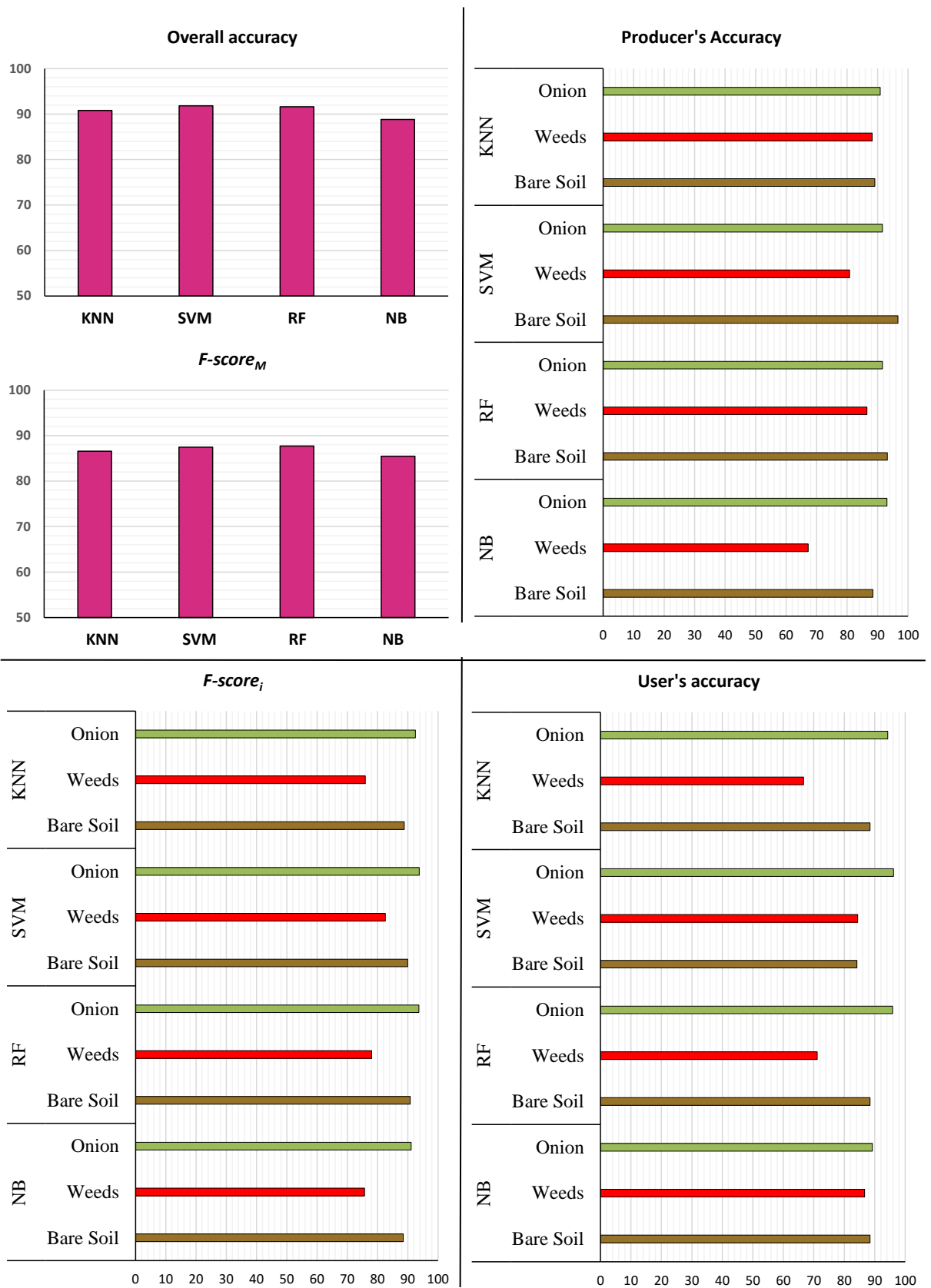


Figure 4.8 Study site 2. User's, Producer's and Overall accuracies, and $F\text{-score}_i$ (single-class) and $F\text{-score}_M$ (multi-class) values obtained for each algorithm.

In study site 1, the highest value of overall accuracy and $F\text{-score}_M$ were obtained using the NB algorithm, with 89.7 % and 88.1% ($F\text{-score}_M$). The RF and SVM algorithms follow at performance level with slightly lower overall accuracy values, 88.9% and 86.5%, respectively, while the lowest values were performed by KNN on with 78.9% and 76.5%, for overall and $F\text{-score}_M$, respectively.

In study site 2, the SVM had 91.8% of overall accuracy, followed by RF with 91.6% and KNN with 90.8%. On the other hand, the lowest performance was that of NB with 88.8% and 85.4% for overall accuracy and $F\text{-score}_M$, respectively.

Observing per-class accuracies (producer's, user's, and single-class $F\text{-score}_i$), in the Bergamot class, the highest $F\text{-score}_i$ value was found RF and NB algorithm with values higher than 92%, user's accuracy percentage was higher than 96% and the producer's accuracy corresponded to 88%. As for the Olive class, the highest values of accuracies were reached by SVM (97.7%, 95.6%, and 96.7% for user's, producer's and $F\text{-score}_i$ accuracies, respectively). In the Grass class, we found the lowest user's accuracy values, ranging from 43.54% (KNN) up to a maximum value reached by the NB classifier (69.3%). The $F\text{-score}_i$ follows the trend with the lowest value equal to 47.36% (KNN). As far as producer's accuracy percentage is concerned, the higher values were obtained with the NB classifier, 82.6%. The Bare Soil class maintains an accuracy value never lower than 90% (user's) and higher than 92% (producer's). Focusing on the "Shadows" class, the producer's accuracy never falling below 93.8% (KNN) reaching 97.9% using the NB algorithm. The users' accuracy has lower values but showed the same trend, as well as $F\text{-score}_i$, whose highest value is 85.7% (NB).

In the study site 2, as for the "Onion" class user's accuracy values, there are not many differences in the implemented algorithms' obtained results in the different software environments, maintaining averaged values around 94%. Only with the NB algorithm, the slightly lower value was obtained 89.2%. All the algorithms performed values of the producer's accuracy higher than 90%. The $F\text{-score}_i$ has values not lower than 91% (NB). As far as the "Weeds" class is concerned, the highest values of the user's accuracy were obtained using NB (86.6%) and SVM (84.44%). The lowest value was obtained by implementing KNN, which provided a value of 66.66%. Looking at the producer's accuracy values, the lowest performance was obtained with NB (67.2%), and the highest was 88.2% (KNN). Finally, considering "Bare Soil" class, the user's accuracy levels remained between 84.1% (SVM) and about 88% (KNN, RF and NB). The producer' accuracy reached 96.6% using SVM, while the lowest value is 88.4% with NB. Moreover, the $F\text{-score}_i$ values range between 88 and 91% using all the algorithms for this class.

For completeness, in Tables from 4.6 to 4.13, the confusion matrices obtained for each classifier in each study site were reported. In Figures 4.9 and 4.10, the classification resulting from the implementation of the four algorithms was showed.

Table 4.6 Confusion matrix obtained for the classifier K-Nearest Neighbour (KNN) in the study site 1.

eCognition - KNN		Ground Truth					
	Classes	1	2	3	4	5	Total
Classified	1	221	5	15	0	0	260
	2	29	36	8	0	2	45
	3	15	4	27	3	0	62
	4	3	0	2	63	1	70
	5	15	1	0	2	46	63
	Total	283	46	52	68	49	500

Table 4.7 Confusion matrix obtained for the classifier Random Forest (RF) in the study site 1.

eCognition - RF		Ground Truth					
	Classes	1	2	3	4	5	Total
Classified	1	251	0	4	0	0	260
	2	4	43	7	0	1	45
	3	14	1	39	3	0	62
	4	0	0	2	63	1	70
	5	14	2	0	2	47	63
	Total	283	46	52	68	49	500

Table 4.8 Confusion matrix obtained for the classifier Support Vector Machine (SVM) in the study site 1.

eCognition - SVM		Ground Truth					
	Classes	1	2	3	4	5	Total
Classified	1	240	0	4	0	1	260
	2	5	44	8	1	0	45
	3	20	1	38	2	0	62
	4	1	0	2	63	2	70
	5	17	1	0	2	47	63
	Total	283	46	52	68	49	500

Table 4.9 Confusion matrix obtained for the classifier Normal Bayes (NB) in the study site 1.

eCognition - NB		Ground Truth					
	Classes	1	2	3	4	5	Total
Classified	1	250	0	2	0	0	260
	2	1	43	5	0	0	45
	3	21	2	43	3	0	62
	4	0	0	2	63	1	70
	5	11	1	0	2	48	63
	Total	283	46	52	68	49	500

Table 4.10 Confusion matrix obtained for the classifier K-Nearest Neighbour (KNN) in the study site 2.

eCognition - KNN		Ground Truth			
	Classes	1	2	3	Total
Classified	1	298	4	14	316
	2	14	30	1	45
	3	16	0	123	139
Total		328	34	138	500

Table 4.11 Confusion matrix obtained for the classifier Random Forest (RF) in the study site 2.

eCognition - RF		Ground Truth			
	Classes	1	2	3	Total
Classified	1	303	5	8	316
	2	12	32	1	45
	3	16	0	123	139
Total		331	37	132	500

Table 4.12 Confusion matrix obtained for the classifier Support Vector Machine (SVM) in the study site 2.

eCognition - SVM		Ground Truth			
	Classes	1	2	3	Total
Classified	1	304	9	3	316
	2	6	38	1	45
	3	22	0	117	139
Total		332	47	121	500

Table 4.13 Confusion matrix obtained for the classifier Normal Bayes (NB) in the study site 2.

eCognition - NB		Ground Truth			
	Classes	1	2	3	Total
Classified	1	282	19	15	316
	2	5	39	1	45
	3	16	0	123	139
Total		303	58	139	500

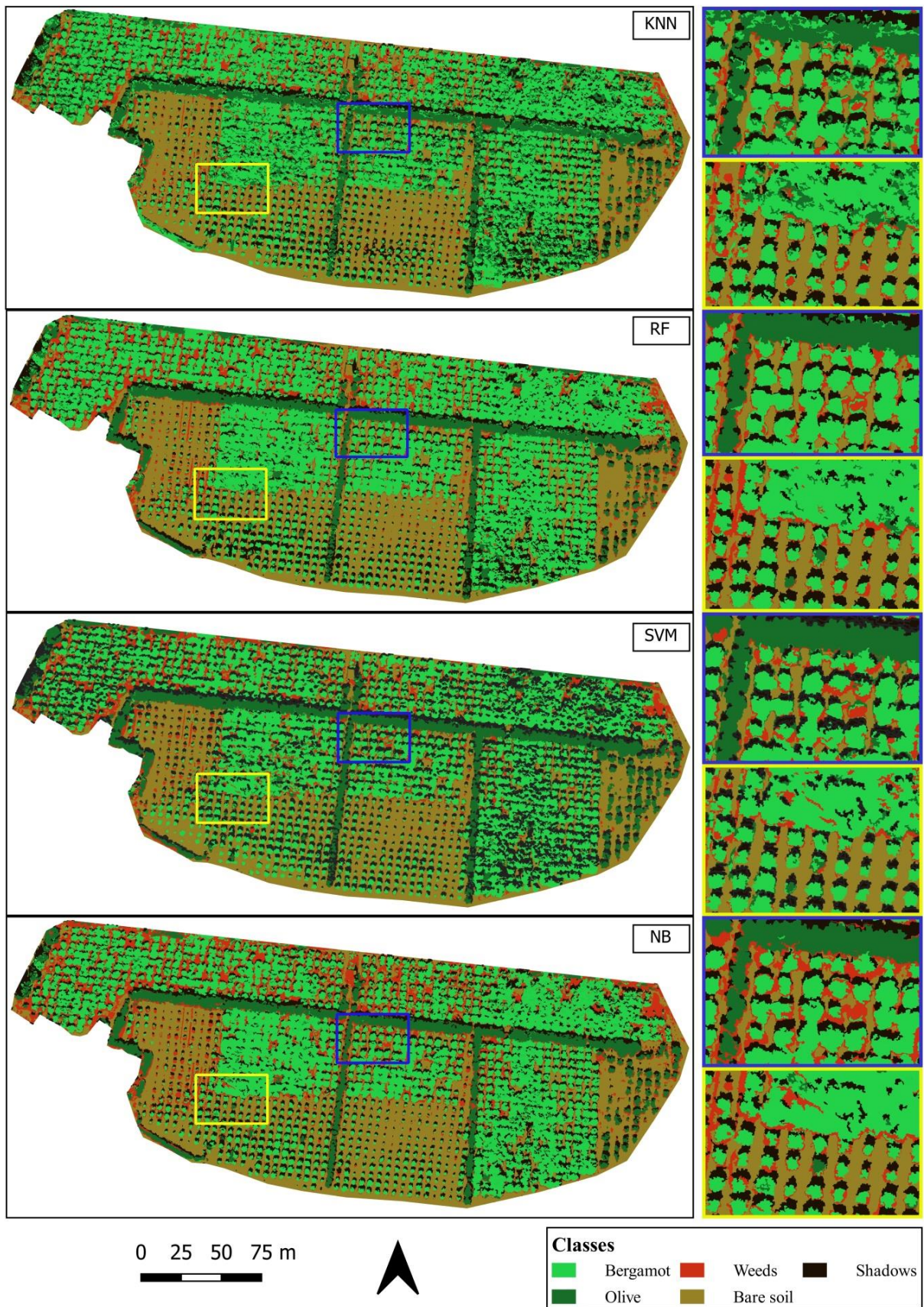
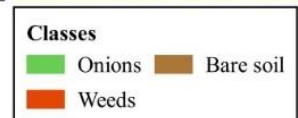
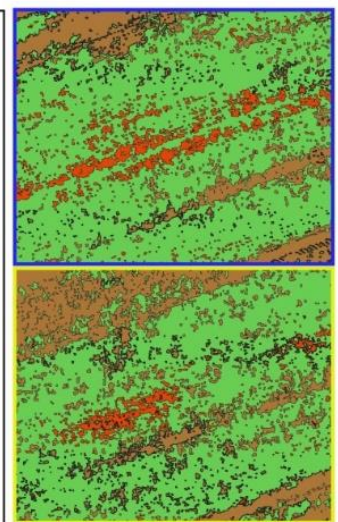
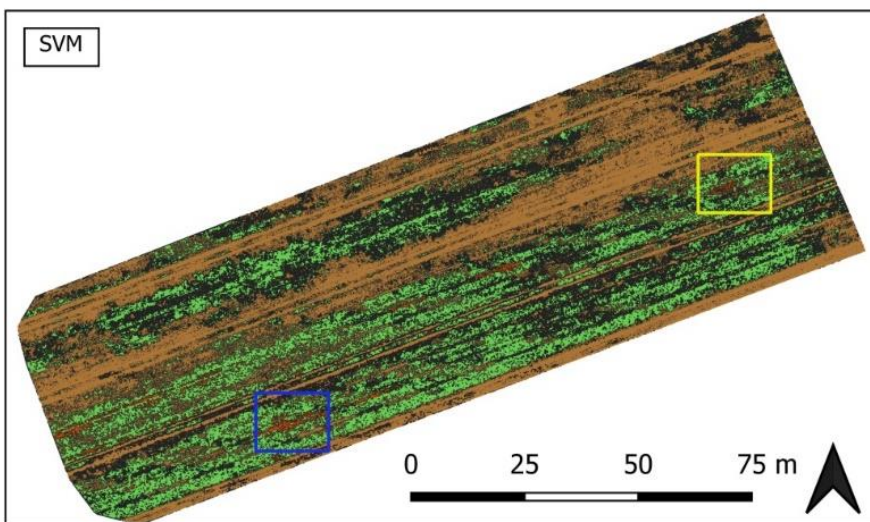
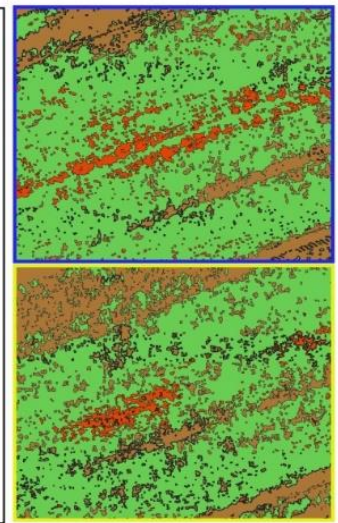
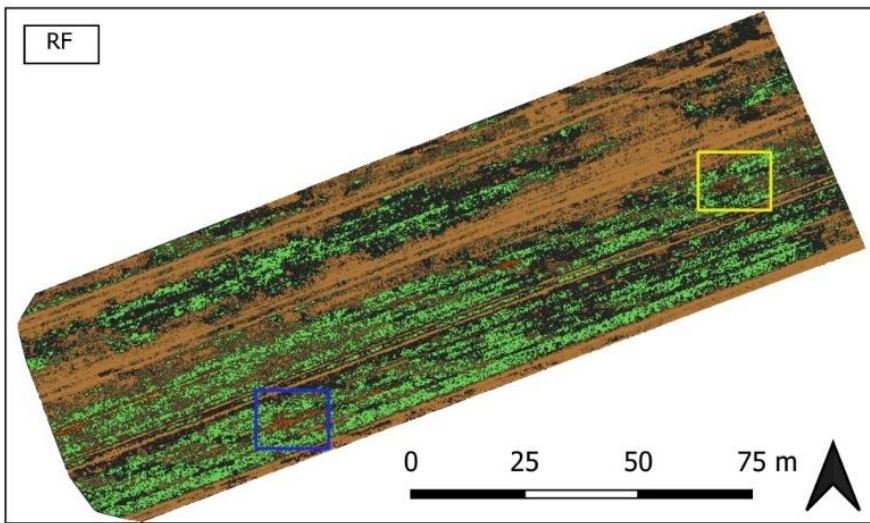
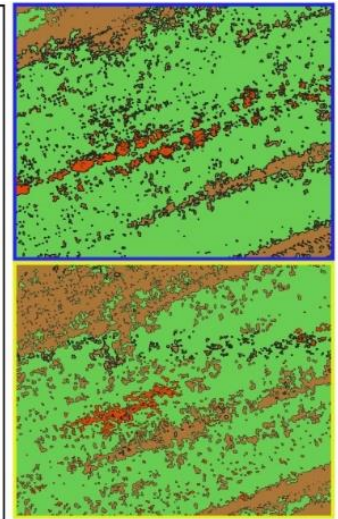
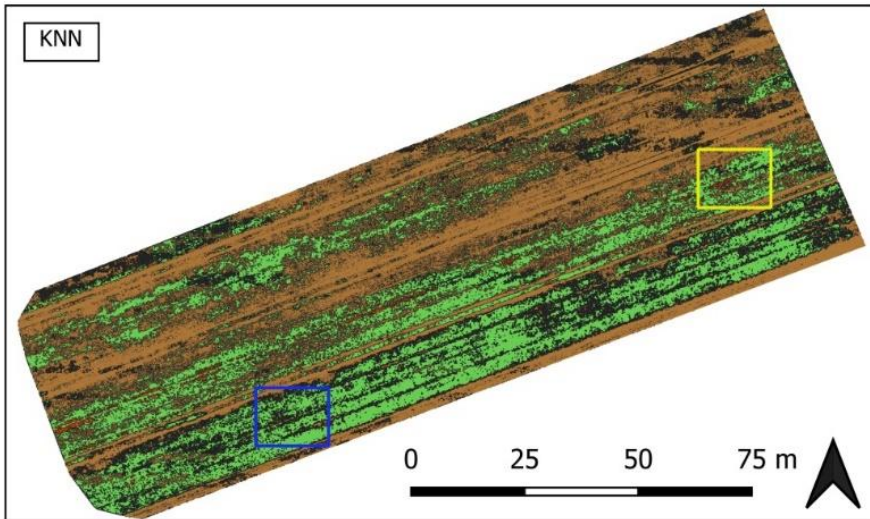


Figure 4.9 The classification of the study site 1 organized according to the four classification algorithms in order from top to bottom: K-Nearest Neighbour (KNN), Random Forest (RF), Support Vector Machine (SVM), and Normal Bayes (NB).



follow

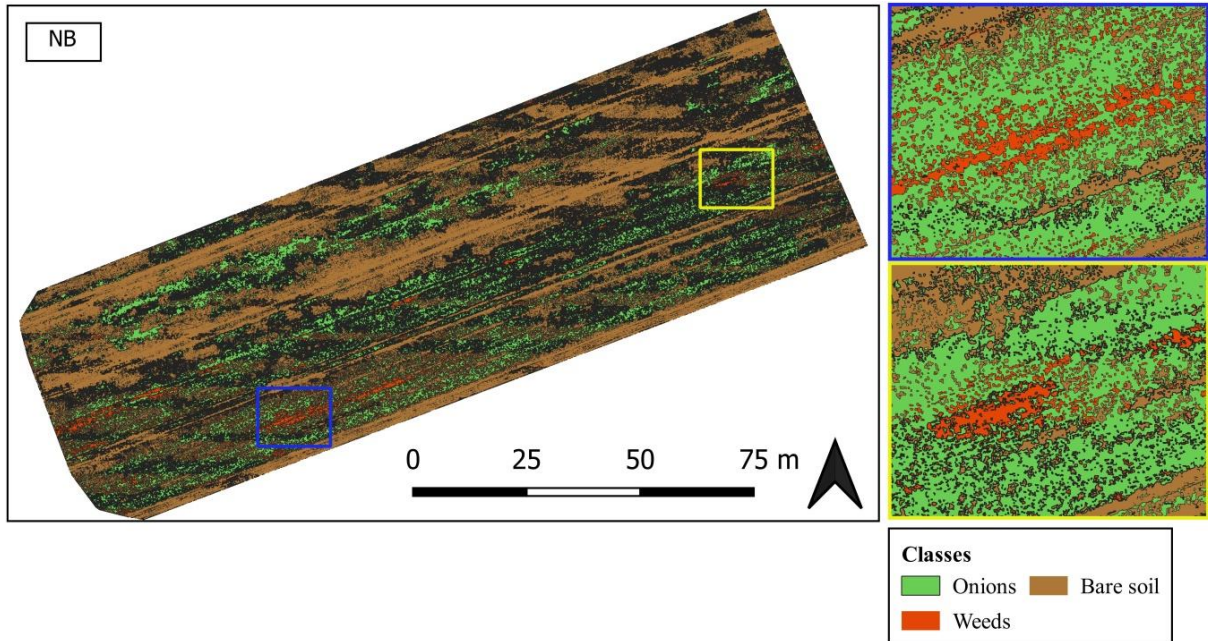


Figure 4.10 The classification of the study site 2 organized according to the four classification algorithms in order from top to bottom: K-Nearest Neighbour (KNN), Random Forest (RF), Support Vector Machine (SVM), and Normal Bayes (NB).

4.4 Discussion

4.4.1 Image Segmentation

In line with the results of Clewley et al. (2014), the MRS algorithm was very fast for both study sites, with a processing time ranging from 2 minutes (study site 1) to 4 minutes (study site 2).

In study site 1, the segmentation provided the highest number of segments, about fifty times the number of those on study site 2. Therefore, the differences in segment size between the study sites were particularly evident. As shown in Figure 4.3, segmentation provided in the study site 1 resulted in many segments whose vegetation LC classes represent the major part. However, at the same time, where the soil surface was continuous, larger segments were generated, and the same is true for the shadows.

This can be explained by the different behavior of the scene's features, as also shown in De Castro et al. (2018). The soil and shadows, having more similar spectral and geometrical characteristics than the vegetation (spectrally and structurally heterogeneous) were segmented differently from the latter. Indeed, this aspect is accentuated in VHR resolution images like those used, where it is expected that many segments are composed of heterogeneous regions (Hossain and Chen, 2019;

Torres-Sánchez et al., 2015). On the contrary, in the case of the bare soil, its homogeneous reflectance behavior of the bare soil could be due to its smoothed surface (low roughness). By considering the number and size of the segments of the different classes in the study site 1, the MRS algorithm produced many segments with similar size, which caused a light over-segmentation on the “Bare Soil” and “Shadow” classes and a light under-segmentation on the vegetation classes. This evidence is also confirmed by the final number, the mean size of segments, and a standard deviation of the mean area with similar values around 1.

In study site 2 the variation in segment size was not particularly evident, confirmed by the lower standard deviation. This was due to the homogeneous vegetation's size and structure of the crop surveyed if compared to the study site 1 (prevalence of tree species). Furthermore, it must be considered that the different age of the bergamot trees at the study site 1 leads to a greater diversification of the canopy size. As for the average object, size can be considered as a representation of the general segmentation scale (Torres-Sánchez et al., 2015).

Regarding study site 2, MRS algorithms show a minor scale with the mean area of segments 0.005 m^2 (± 0.00001). Generally, a smaller segmentation scale (producing smaller segments) is preferable for PA purposes, as far as vegetation monitoring is concerned, for early detection of a possible stress state of the plant (Meena, 2019). In particular, a smaller segmentation scale allows distinguishing plants, portions of the canopy of single trees, or weeds spaced in inter and intra rows. Typically, an inversely proportional correlation exists between the segmentation scale and the image resolution. Indeed the higher are the spatial resolution, the smaller the segmentation scales and vice-versa (M. Li et al., 2016; Ma et al., 2015). Besides, the scene's intrinsic characteristics and the objectives of the study must be taken into account and influenced the variability of the segmentation scale (M. Li et al., 2016; Ma et al., 2015). Therefore, an over-segmentation is preferred to an under-segmentation to prevent the correct discrimination of small vegetative characteristics.

4.4.2 Image Classification and Accuracy Assessment

The classification results were compared in terms of overall, user's and producer's accuracy and by single - and multi-class F-score. As shown by several scholars (M. Li et al., 2016; Ma et al., 2015; Mountrakis et al., 2011; Noi and Kappas, 2018; Yang et al., 2019), algorithms SVM, RF, and KNN are among the most used supervised classifiers in the literature, giving generally good results of accuracy on agriculture and land cover classification applications. These three ML algorithms

showed a similar classification performance in study site 1 (Figure 4.9). Instead, observing Figure 4.10 relating to the study site 2, it seems that the KNN underestimated weeds.

Looking at the overall accuracy, SVM and RF are the most stable classifiers, as in study site 2. It is confirmed by the overall accuracy values of 91.8% and 91.6%, respectively. For example, in the case of SVM Noi and Kappas (2018) and Qian et al. (2015) concord that it can be considered an algorithm with constant and high accuracy.

In study site 1, the NB algorithm provided the classification result with the highest overall accuracy (89.6%). This result does not differ much from the result given by SVM (86.5). This is in line with what was highlighted in Qian et al. (2015), where the accuracy of NB was similar to SVM accuracy and significantly high for more than 100 training samples for each class. In this case, the training samples were more than 100 for all LC classes except for "Grass" and "Weeds" (see Figure 4.10). The NB classifier is generally one of the most sensitive to sample size as, being a parametric algorithm, it uses training samples to estimate parameter values for the data distribution (Qian et al., 2015; Rehman et al., 2019) so, a greater number of samples can lead to an improvement in the estimated parameters (Qian et al., 2015).

On the contrary, SVM results to be least sensitive to the number of samples, and its classification accuracy is not influenced by an increase of this number because, rather than all the training samples, it uses the support vectors to define the separation hyperplane (Huang et al., 2002; Mountrakis et al., 2011; Qian et al., 2015). It is important to underline how the NB algorithm, not needing the setting of any parameter, proves to be the fastest way to classify, offering, among other things, good results. The other algorithms can instead be influenced by parameters set.

Overall accuracy provides total accuracy of the scene, while producer's and user's accuracies determine individual class accuracies. Observing in Figures 4.7 and 4.8 the results regarding crop species of each study site (bergamot and olive for study site 1 and onion for study site 2), it can be noted that the four classification algorithms provided high values of producer's and user's accuracy and *F-score*. The "Bergamot", "Olive", and "Onion" classes, seem to be better detected with values no lower than 85% in most cases. Regarding the "Bare soil" class, all the algorithms showed equally satisfactory for both user's and producer's accuracy. As already written, these results may be due to the spectral homogeneity of the bare soil surface.

Obviously, the total accuracy value mainly depends on the herbaceous vegetation classes. In study site 1, there was an overestimation of the grass present between trees in the bergamot orchard. On

the contrary, in study site 2, there was an underestimation of weeds, caused by a low distinction between weeds and onion crops. In study site 1, however, the algorithms classified with difficulty the class "Grass" due to the misidentification of grass with bergamot or olive and vice versa. This was probably due to the spectral similarity between grass/weeds and crops, which, as shown in Peña et al. (2013), often occurs in the early stage of vegetative growth. Many plant species that adapted to the thermo-pluviometric regimes typical of the Mediterranean environment (characterized by hot and dry summers), including the olive tree, adopted a typical phenological cycle in which, in addition to the main vernal budding phase, there is a second vegetative restart following a summer stasis which permits plants to limit evapotranspiration (Connor and Fereres, 2010; Fiorino, 2018; Iniesta et al., 2009; Palese et al., 2010).

Citrus trees also have more than one phase of vegetative growth in the Mediterranean environment, including the summer and autumn seasons (Primo-Millo and Agusti, 2020). As Pande-Chhetri et al. (2017) explained, the spectral features used during the training phase might not be enough to discriminate between different classes of vegetation. However, as highlighted in several studies (Gašparović et al., 2020; Solano et al., 2019; Villoslada et al., 2020), the use of VI, as in the case of GNDVI used in this work, can improve the spectral differences between vegetation and non-vegetation classes in VHR images. This resulted in good results in terms of accuracy, despite the similar spectral responses of vegetation coverings. Therefore DSM, as will be clarified subsequently, had a key role in this case.

Generally, the detection of herbaceous vegetation and weeds within crop represents still a common challenge in the framework of vegetation mapping (Gašparović et al., 2020; López-Granados et al., 2016b; Peña et al., 2015, 2013; Perez-Ortiz et al., 2017; Torres-Sánchez et al., 2015, 2013; Zisi et al., 2018). In other words, for example, to cope with this problem, combined ML approaches with different advanced semiautomatic techniques in which the characteristics relate to the position and structure of the weeds in-field were performed (De Castro et al., 2018; Gao et al., 2018; Peña et al., 2013; Perez-Ortiz et al., 2017; Pérez-Ortiz et al., 2016, 2015); in other cases more advanced deep learning techniques (Csillik et al., 2018; Huang et al., 2020).

The accuracy values obtained from this work do not differ much from those mentioned. Most of these mentioned works concern the monitoring of vegetation. However, this work was performed on two study sites characterized by different and more complicated conditions in agronomic and structural terms.

Being the DSM, resulting from the photogrammetric process, efficient for plant height detection (De Castro et al., 2018; Zisi et al., 2018), its use as an additional input layer increased the accuracy in the study site 1, which is characterized by greater variability in the height of the vegetation (trees and herbaceous). This was already proved in other works as in other works as (De Luca et al., 2019; Zisi et al., 2018). This aspect was necessary since the three vegetation classes' spectral signature was the same in study site 1. Instead, in study site 2, the DSM probably did not influence much the discrimination of onions from weeds since their height was very similar.

Besides the classification algorithm's choice, other parameters influenced the accuracy: as segmentation scale, characteristics of the trainers, sample scheme, object-features used, etc. (M. Li et al., 2016; Ma et al., 2017). The number of training also influenced the results. Indeed, a positive correlation there is between the number of the training sample and the classification accuracy and (M. Li et al., 2016; Ma et al., 2017, 2015; Noi and Kappas, 2018). This is also dependent by the method used for the choice of the training samples, which could significantly influence the final accuracy (Ma et al., 2015).

The results obtained do not define an algorithm better than all the others, although the NB in study site 1 and SVM in study 2 showed the higher classification efficiency. However, all the algorithms proved to be more suitable for crop recognition using GEOBIA and VHR UAV images. The observation of the user and producer accuracies showed how difficult it was to detect invasive species in the heterogeneous sites surveyed. This happened because of their position alongside crops and their very similar shape, size and spectral response. Furthermore, the images were taken in different seasons. This brings out the repeatability of the method and its capacity to manage the uncertainties caused by the heterogeneity present in the study sites surveyed.

4.5 Conclusions

This work's objective was to compare the applicability of four ML algorithms for classifying two different agricultural scenarios using UAV multispectral VHR imagery. The choice of using different combinations of classification algorithms allowed to evaluate what factors could have a significant impact on the mapping accuracy.

As regards segmentation, it is advisable to set the parameters with the aim obtain a lower scale, so having products more suitable for PA purposes, especially in the case in which herbaceous vegetation is present.

Regarding the classification algorithms used in this study, all the classifiers (KNN, SVM, RF, and NB) showed excellent performance. However, SVM resulted as the most stable classifier in terms of accuracy in study site 2, followed by NB in study site 1. The KNN gave the worst results in more cases. In fact, as also suggested by other studies (Ma et al., 2017), the use of KNN in GEOBIA applications should be reduced. The NB seems to be a good compromise for an easy and fast application of GEOBIA since it does not require the setting of parameters. Nevertheless, it produces satisfactory results.

Considering the importance of PA for practical business uses, this work arises from the need to evaluate a quick, solid, and repeatable approach for agricultural mapping in very heterogeneous agricultural contexts. The presented workflow can be applied to a wide range of vegetation types by also impractical or newbies operators. A future objective can be to increase the precision of the method by implementing and optimizing more advanced techniques to improve the classification accuracy of weeds.

5 Thermal UAV Remote Sensing in precision agriculture



Adapted from

Applications of UAV thermal imagery in precision agriculture: State of the art and future research outlook. Remote Sens. **2020**, *12*, doi:10.3390/RS12091491.



Review

Applications of UAV Thermal Imagery in Precision Agriculture: State of the Art and Future Research Outlook

Gaetano Messina  and Giuseppe Modica * 

Dipartimento di Agraria, Università degli Studi Mediterranea di Reggio Calabria, Località Feo di Vito, I-89122 Reggio Calabria, Italy; gaetano.messina@unirc.it

* Correspondence: giuseppe.modica@unirc.it; Tel.: +39-0965-1694261

Received: 16 March 2020; Accepted: 6 May 2020; Published: 8 May 2020



Abstract: Low-altitude remote sensing (RS) using unmanned aerial vehicles (UAVs) is a powerful tool in precision agriculture (PA). In that context, thermal RS has many potential uses. The surface temperature of plants changes rapidly under stress conditions, which makes thermal RS a useful tool for real-time detection of plant stress conditions. Current applications of UAV thermal RS include monitoring plant water stress, detecting plant diseases, assessing crop yield estimation, and plant phenotyping. However, the correct use and interpretation of thermal data are based on basic knowledge of the nature of thermal radiation. Therefore, aspects that are related to calibration and ground data collection, in which the use of reference panels is highly recommended, as well as data processing, must be carefully considered. This paper aims to review the state of the art of UAV thermal RS in agriculture, outlining an overview of the latest applications and providing a future research outlook.

Keywords: unmanned aerial vehicles (UAVs); remote sensing (RS); thermal UAV RS; thermal infrared (TIR); precision agriculture (PA); crop water stress monitoring; plant disease detection; yield estimation; vegetation status monitoring

In PA the thermal RS proved to be a very promising tool (Khanal et al., 2017). In recent years, taking into account improvements in sensor technology and cost reductions, thermal sensors have become more popular. Specifically, thermal sensors' measurement of surface temperature has proved to be a rapid response variable useful in monitoring plant growth and stress (Anderson et al., 2013; Khanal et al., 2017). Indeed, the temperature is a fundamental environmental variable that plays an essential role in plant physiological processes, such as transpiration, leaf water potential, and photosynthesis (Vasit Sagan et al., 2019).

The potentialities of the application of thermal UAV RS relate to mapping and monitoring issues such as yield estimation, plant phenotyping (Costa et al., 2013; Ludovisi et al., 2017) but also and above all to plant water stress detection (Gago et al., 2015; Radoglou-Grammatikis et al., 2020) and plant disease detection (Calderón et al., 2013). Focusing on the latter two applications by monitoring, using sensors mounted on UAVs, the state of health of the plants, identifying, if present, stress on the crops before they are irreparably damaged, could be a crucial goal.

In water stress monitoring, thermal images show a correlation between minor variations in water stress that cannot be detected, for example, by the NDVI (Baluja et al., 2012). In this respect, temperature-based indices represent a quick and practical way to evaluate and estimate crop water status, indicating plants' water content (Pádua et al., 2019). The crop water stress index (CWSI) (Idso et al., 1981) is the most widely used among the temperature-based indexes. CWSI has often been used to monitor the water status of plants and, consequently, for irrigation management (Alderfasi and Nielsen, 2001). The water stress indices have been applied to different tree and herbaceous species, including olives (Berni et al., 2009a), grapevines (Bellvert et al., 2014), sugar-beet (Quebrajo et al., 2018), maize (Romano et al., 2011), rice (Liu et al., 2018), and wheat and cotton (Sullivan et al., 2007).

The correct interpretation and use of a thermal image cannot be separated from a knowledge of the basic principles of thermal radiation's nature (Lillesand et al., 2015). Thermal images' quality can be influenced by several factors, such as the characteristics of the thermal camera, meteorological conditions, and several sources of emitted and reflected thermal radiation (Khanal et al., 2017). Therefore, the aspects related to calibration, ground data collection, the step in which the use of reference panels and the measurement of their temperature are recommended (Gómez-Candón et al., 2016), and data processing must be carried out carefully in order to obtain correct temperature data.

This chapter is partly devoted to the description of state of the art in PA applications. Particular attention has been devoted to various topics, based above all on the experience in the field and in the laboratory gained by the candidate during the Ph.D. course: description of the characteristics and functioning of thermal cameras; calibration; data collection and data processing. Finally, a case study was presented about the potentiality of coupling multispectral and thermal imagery acquired by UAVs in monitoring onion crops.

5.1 Thermal cameras types, structure and Unmanned Aerial Vehicles

Thermal cameras are equipped with a sensor that detects the infrared radiation emitted by a body, displaying its temperature in a digital radiometric image. Two types of thermal cameras are available: scanning devices that allow capturing a point or a line and those with a two-dimensional infrared focal plane array. The second type allows capturing all the elements of an image at once and is faster if combined with a better image resolution (Kaplan, 2009). It is the most commonly used (Gade and Moeslund, 2014). A further distinction concerns thermal and photon (or quantum) detectors. The latter works by converting directly absorbed EM into a variation in the distribution of electric energy in a semiconductor by changing the concentration of free charge carriers (Gade and Moeslund, 2014) and needs a cooling system. This is generally made using helium or liquid nitrogen at a temperature of $-196\text{ }^{\circ}\text{C}$ (Jensen, 2014). The cryocooler is used to lower the sensor's temperature, thus reducing the thermally induced noise to a lower level than the signal deriving from the image (FLIR, 2011). The higher the cooling system's efficiency, the more accurate the instrument's measurements, which makes the cooled thermal cameras more precise (Mesas-Carrascosa et al., 2018). The highest precision and accuracy allow detecting the slightest temperature differences in the image. The cooled thermal cameras usually work in the mid-wavelength infrared (MWIR) region ($3\text{--}8\text{ }\mu\text{m}$) in which the thermal contrast is high (Gade and Moeslund, 2014). An object/target's thermal radiation is easily detectable once it has been distinguished (upper or lower) from the background (FLIR, 2011). Unfortunately, the cooled sensors are large, expensive, higher energy consumption, and their higher weight is not suitable for UAVs (Jensen et al., 2014). Thermal detectors are less sensitive ($\pm 0.1\text{ }^{\circ}\text{C}$) and are slower than quantum detectors but have the advantage of not requiring cooling systems (Luhmann et al., 2013). Several types of uncooled detectors are currently available, and all of them are made of different and unconventional materials: the three most common types are composed of vanadium oxide (VOx), amorphous silicon ($\alpha\text{-Si}$) microbolometers, and ferroelectrics (Sizov, 2015). The operating

principle of thermal detectors is the conversion of absorbed EM radiation into thermal energy (Hyseni et al., 2010). Ferroelectric detectors work based on the ferroelectric phase transition, which can be detected in some dielectric materials. The microbolometer is a resistor organized in arrays—called focal plane arrays, made up of VO_x and α -Si—which is composed of a thermometer, integrated on a micro-bridge, and an adsorber. Temperature increases, caused by absorption of IR radiation, determine large fluctuations of its electrical resistance, which can be converted into electrical signals and processed to generate an image (Bhan et al., 2009; Bieszczad and Kastek, 2011; Fièque et al., 2007; FLIR, 2015; Gade and Moeslund, 2014), whose geometric resolution depends on the number of detectors. The low values of temperature differences equivalent to noise in uncooled thermal sensors, which reach 20 m°C, allows them to be used in applications where previously only cooled thermal sensors could be used (Mesas-Carrascosa et al., 2018). As a result of micro and nanotechnology's rapid development, microbolometers have become cheaper and more efficient (Budzier and Gerlach, 2015). The lenses reflect visible radiation and are made of germanium - a shiny semi-metal chosen for its transparency (Gade and Moeslund, 2014). Several parameters characterize a thermal camera. Among these, there is the temperature range measured, generally between -20 and +120 °C, and the thermal sensitivity, which determines the minimum value of temperature difference (ΔT) detectable in an image and usually ranges from 40 to 20 m°C for uncooled and cooled devices, respectively (Gade and Moeslund, 2014). Concerning the geometric resolution, currently, it is still very low compared to RGB cameras (to date, higher image resolutions range from 320 × 240 to 640 × 512 pixels). The spectral resolution generally ranges from 7 to 14 μm (Gago et al., 2015).

Regarding the price of thermal cameras, their cost can vary from € 1,000 to more than € 10,000, depending on both the sensor resolution and radiometric calibration accuracy (Kelly et al., 2019; Manfreda et al., 2018).

Cooled thermal infrared cameras are widely used in satellite and aerial RS, due to their thermal sensitivity and accuracy (Sheng et al., 2010); moreover, these sensors are larger and more expensive, even in energy consumption, than uncooled ones (Ribeiro-Gomes et al., 2017). Instead, uncooled thermal cameras can generally be mounted on UAVs (Figure 5.1a,b,c) because they are smaller, lighter, and lower consuming (Gallo et al., 1993).



Figure 5.1 DJI Phantom 4 Pro (a), (b) DJI Inspire 1, both equipped with a FLIR Vue Pro R 640 uncooled thermal camera (c) (*sources* (Messina and Modica, 2020b) and flir.it).

The limited payload and the limited battery life, which influence the duration of the flight, are maybe the main limits of UAVs, For example, in cases where large areas need to be covered several flights are required, and is not at all improbable that 45 minutes or more elapse between the first and the final image of the dataset (Maes et al., 2017).

Payload integration considerably changes between cooled and uncooled thermal cameras, where different ventilation modes are a key factor in image quality; thus, generally, an uncooled microbolometer is preferred for its weight benefits (Stark et al., 2014).

5.2 Camera calibration and data collection

Low-cost thermal cameras generally are not radiometrically calibrated and can only provide information about relative temperature differences (Kelly et al., 2019). The data provided by these instruments are represented in the form of raw digital numbers (DNs) expressing radiance. Using radiometrically calibrated UAV cameras, it is not easy to derive accurate and precise surface temperature measurements, due to their low accuracy affected by the presence of uncooled

microbolometers (Kelly et al., 2019). The sensitivity, and therefore the accuracy of a microbolometer, is influenced both by the temperature of the focal plane array (Olbrycht et al., 2012) and by the temperature of the other components of the thermal camera, among which the body and lenses, and is higher in the presence of a weak signal-to-noise ratio. (Budzier and Gerlach, 2015).

In addition to this, several other causes make it necessary to calibrate a thermal camera, as shown in Budzier and Gerlach (2015) and Ribeiro-Gomes et al. (2017). The atmosphere affects the quality of the thermal image as it absorbs and emits IR. In the case of UAVs, piloted at low altitudes, atmospheric effects can be considered negligible compared to aerial or satellite measurements (Kuenzer et al., 2013).

The effects of relative humidity, air density, and altitude can be avoided only by taking measurements within about 10 m or less of the object/target's surface (FLIR, 2012); obviously, under different conditions, these effects must be taken into account. Since meteorological conditions can have an indirect effect on the temperature measurements of uncooled thermal cameras (Maes et al., 2017), in order to reduce these effects, it is advisable to follow some recommendations during field surveys; the critical factors for data acquisition are the time of day, weather and the knowledge of the surrounding environment (Stark et al., 2014). Considering the applications in PA, midday has been generally identified as the best time for flying in terms of thermal accuracy (Alchanatis et al., 2010) and reduction of background effects (Sepulcre-Cantó et al., 2006).

Regarding the weather, UAV thermal surveys should always be done in the absence of clouds, dust, smoke, rain, snow, or any other darkening agents because all of these reduce atmospheric transition and also change the temperature of the background (FLIR, 2012). It would be useful if before the flight, after switching on, the camera sensor's temperature-stabilized for a time ranging from 20 minutes (Gómez-Candón et al., 2016) up to 1 hour (Berni et al., 2009b). Besides, it would also be advisable to perform a test flight to allow the thermal camera to acclimatize to local weather conditions, as well as to wrap the thermal camera in a casing (to reduce the effects of air temperature on the sensor) when mounted on a quadcopter UAV (Kelly et al., 2018).

Field temperature calibration is also a key aspect. The presumed coldest and hottest temperature and objects within the area of image acquisition should be measured for ground truth calibration (Kuenzer et al., 2013). Field calibration should be performed using the temperature measurements of target surfaces taken during the flight (Bellvert et al., 2014; Dupin et al., 2011). The temperature

of the targets placed in the study area could be measured using thermocouples (Maes et al., 2017) or infrared thermo-radiometers (Gómez-Candón et al., 2016), perhaps combined with data-loggers capable of recording the temperature throughout the flight. The temperature reference targets can be made using black and white polypropylene panels, representing the thermal extremes of the study site, and whose size is such as representing homogeneous pixels in the thermal image (Gómez-Candón et al., 2016).

In this experience, as is the case in Messina et al.'s (2019) work, dry and wet reference surfaces were used during the thermal UAV survey by taking images of them before and after every flight, as indicated by Maes (2017). Reference surfaces were placed close to UAV take-off and landing points, and their temperature was measured through a handheld infrared thermometer (FLIR E6) (Figure 5.4b).

In particular, the temperature was measured at three moments of the flight: at take-off, during, and end of each flight. Four reference surfaces were used: three dry panels (each entirely colored in black, grey, and white) and one made delimiting a square piece of the ground using circular targets covered with aluminum (Figure 5.2).

Portions of dry and wet soil can also represent suitable targets, as described in the next paragraph. In addition to these, as in the case of multispectral surveys, there are ground control points (GCP)s— i.e., points marked on the ground which have a known geographical position. The use of GCPs is important as it improves the positioning and accuracy of the mapping outputs.

To render GCPs more visible in thermal images, they should have a low emissivity compared to the nearby vegetation and other objects (Boesch, 2017).



Figure 5.2 The temperature reference targets used during thermal unmanned aerial vehicle (UAV) surveys carried out in an onion crop field in Calabria (Italy) (*source*, Messina and Modica, 2020b).

In the case of thermal surveys, GCPs are made of aluminum, exploiting the low emissivity, which makes it appear as a cold object in the thermal images (Park et al., 2017) (Figure 5.3b). Our proposed GCPs were made using 50 cm × 50 cm white polypropylene panels and covering two quadrants using aluminum sheets, as shown in Figure 5.3a. Black cardboard was used to partially cover the two quadrants to locate the point and make the GCP clearly visible and usable in multispectral surveys (Figure 5.3c). Figure 5.3 shows the detectability of the proposed target in thermal and multispectral images.

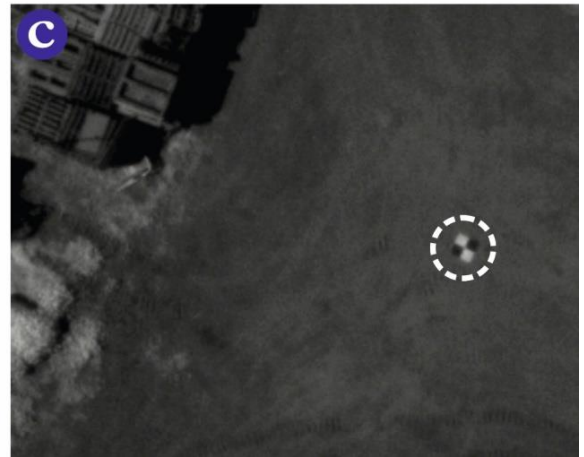
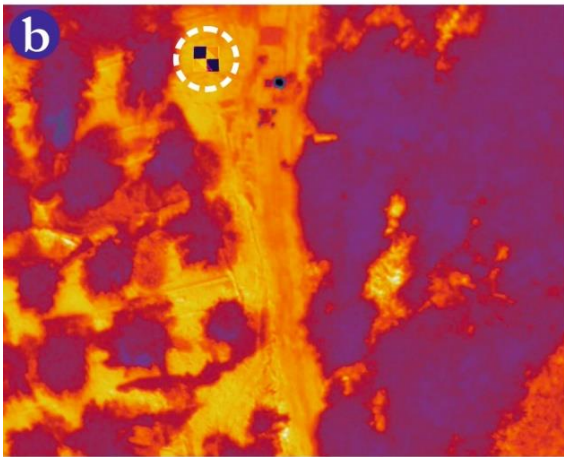
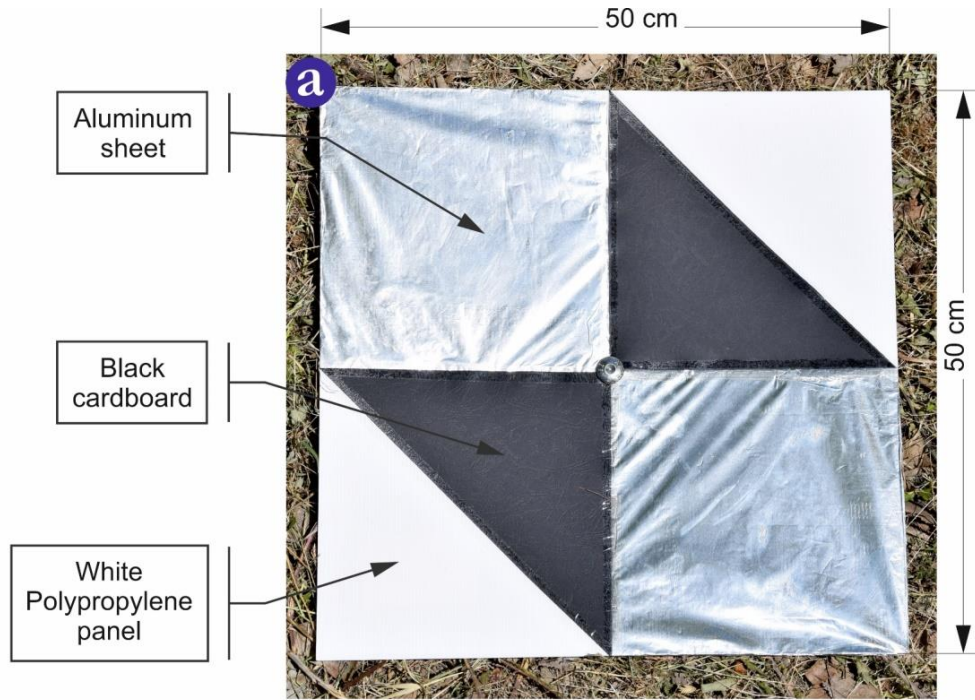


Figure 5.3 Photo of the homemade target for ground control points (GCPs) designed to be easily detected in both thermal and multispectral UAV surveys. (a). The GCP target (white dashed circle) as it appears in thermal (b) and in near-infrared (NIR) multispectral images (c) (source, Messina and Modica, 2020b).

A further effect of the weather conditions to be considered is that of attenuating the thermal radiance by the atmosphere (Maes et al., 2017). The sensor registers, for every pixel, an at-sensor radiance ($L_{\text{at-sensor}}$), expressed in Wm^{-2} , and determined by the following formula (Equation 5.1) (W. H. Maes et al., 2011):

$$L_{\text{at-sensor}} = \tau L_{\text{surf}} + L_{\text{atm}} \quad (5.1)$$

In Equation (5.1), τ is the atmospheric transmittance, while L_{atm} , measured in Wm^{-2} , represents the upwelling thermal radiation, created as a result of particles in the atmosphere, both depending on

the distance of the sensor from the object and the water content in the atmosphere (Maes et al., 2017). Parameters τ and L_{atm} can be derived by exploiting one of the theoretical atmospheric models, such as MODTRAN (Berk et al., 1999), which are generally and widely used for thermal data acquired from satellites (Khanal et al., 2017). MODTRAN allows the estimation of atmospheric emission, thermal scattering, and solar scattering by incorporating the effects of molecular absorbers and scatterers, aerosols and clouds, taking into account the wavelengths from the ultraviolet region to the far-infrared (Campbell e Wynne, 2017).

An example of MODTRAN application in on UAV data is described by Berni et al., (2009b), which shows that it allows obtaining the surface temperature by applying atmospheric correction methods based on entering the model as input data, i.e., data related to local atmospheric conditions. In the application on UAV data using this model, it is important to use local measurements of temperature, relative humidity, and atmospheric pressure acquired from a nearby meteorological station (Fig. 5.4a) placed in the field (Chen, 2015; FLIR, 2011; Gade and Moeslund, 2014; Kaplan, 2009; López et al., 2012).



Figure 5.4 (a) The weather station used during the thermal surveys carried on an onion field and (b) the handheld infrared thermometer (model FLIR E6) used to measure the temperature of reference surfaces (*source*, Messina and Modica, 2020b).

5.3 Data processing

Several steps are required to acquire geo-referenced UAV images, starting with flight planning which generates a navigation file necessary to guide the UAV into automatic image capture with the required overlaps and geometric resolution. Thermal imagery can be processed with structure-from-motion (SfM) algorithm, which, however, does not always work correctly (Maes et al., 2017), as reported in (Hoffmann et al., 2016; Pech et al., 2013). SfM can be unable to align properly thermal imagery, making it necessary to mosaic each separate image and geo-reference them manually using GCPs. These issues are due to the reduced information contained in the thermal image, which complicates the identification of the common features needed for bundle adjustment (Maes et al., 2017). Compared to other imagery types such as RGB, thermal imagery has lower geometric resolution and contrast and is characterized by a stronger optical distortion (Boesch, 2017). Increasing vertical and horizontal overlaps could help and the presence of an incorporated multispectral (or RGB) camera, characterized by a higher geometric resolution, which could also help the alignment of the images in the photogrammetric process. In Turner et al.'s (2014) research, a framework to process thermal imagery is shown. In detail, firstly, image pre-processing provided the removal of blurry imagery and then the subsequent conversion of images to a 16-bit file format. So, all images have the same dynamic scale, and a specific temperature value corresponds to the same digital number (DN) in all images. Secondly, image alignment was executed using GPS log files and the imagery's time stamps. As a final step, the spatial image was co-registered to RGB images. Several improvements of this framework were provided in Maes et al., (2017) to optimize the alignment and processing of thermal images by exploiting the increased information contained in the RGB data. Recent UAV models have been supplied with real-time kinematic global satellite navigation systems (RTK - GNSS) capable of achieving centimetric planimetric precision and high positioning accuracy. However, the placement of GCP within the surveyed site is generally expected and recommended. The images must be geometrically aligned (orthorectification), calibrated and corrected, considering the atmospheric effects before final orthomosaics are obtained (Khanal et al., 2017).

5.4 Thermal UAV imagery applications in precision agriculture

5.4.1 Crop water stress monitoring

Several detection systems have been developed for the production of special crops worldwide thanks to technological advances (Lee et al., 2010). The collection of accurate information concerning the spatial variability of fields is important in this context. Several factors affected the field's variability, including crop yield and water content, and sensors that can be used to detect these factors include thermal cameras.

Plant water stress is one of the main critical factors of abiotic stress because it limits the growth of crops (Gautam and Pagay, 2020; Gerhards et al., 2016). Therefore, among the applications of thermal UAV RS in agriculture, the identification of water stress from plant temperature data is of great importance, with irrigation resource management being a key issue for PA. The use of UAVs in the detection of plant water status requires measurements of stem water potential (ψ_s) and stomatal conductance (g_s). These water stress indicators are the most commonly used to determine crop water status (Ballester et al., 2017; Baluja et al., 2012; Turner et al., 2014; Zarco-Tejada et al., 2013). ψ_s and g_s can be measured in the field using a pressure chamber and porometers, respectively, although the interpolation of such local observations is not easy.

The use of thermal images permits detecting a plant's water stress conditions. At the foliar level, stomata closure reduces transpiration and evaporative cooling, which results in an increased temperature of the leaves (Gerhards et al., 2019; Hsiao, 1973). Thermal cameras can detect this increased temperature; so thermal images can provide spatially continuous information regarding the plants' water status in a broader area than that obtained by local measurements (Jackson et al., 1981; Lapidot et al., 2019). The temperature of the plant is regulated by the water supply and the micrometeorological conditions (Gerhards et al., 2018). In this regard, considering the climatic factors, atmospheric humidity plays a crucial role, and in environments with humid climates, cloudiness also becomes a critical factor (Jones, 2018). Several indices were developed in the past decades to compensate for the variation determined by these conditions (Gerhards et al., 2018).

The CWSI was developed for that purpose. Jackson and colleagues conceived the CWSI while using portable IR thermometers on herbaceous crops (Cohen et al., 2005; Jackson et al., 1981), formulating a normalized index to overcome environmental effects that may affect the relationship between plant temperature and water stress. CWSI can assume values ranging between 0 and 1

and results in being directly proportional to the water stress level of many species of interest. The CWSI is based on the normalization of the canopy–air temperature difference with evaporative demand through the vapor pressure deficit (VPD) of the air (Calderón et al., 2013). CWSI's formula is as follows, according to the methodology proposed by Idso et al. (1981) (Equation 5.2):

$$CWSI = \frac{(T_c - T_a) - (T_c - T_a)_{LL}}{(T_c - T_a)_{UL} - (T_c - T_a)_{LL}} \quad (5.2)$$

where $T_c - T_a$ represents the canopy–air temperature difference, while LL refers to the $T_c - T_a$ values for the lower limit and UL for the upper limit. The normalization related to the VPD considers the $T_c - T_a$ difference of a canopy under two boundary conditions: (a) a lower limit when it transpires at its potential rate (i.e., under well-watered conditions), and (b) an upper limit under no transpiration. The lower limit is described by linear regression between $T_c - T_a$ and the VPD, which is known as the non-water-stressed baseline (NWSB). The NWSB is derived empirically by measuring the leaf–air temperature difference for a well-watered crop in the experimental environment and provides the lowest temperature difference likely in that environment. Once the NWSB, $(T_c - T_a)_{LL}$ can be calculated by solving the baseline equation for the current VPD. The upper limit $(T_c - T_a)_{UL}$, which is a constant, is obtained by solving the same NWSB equation for a hypothetical slightly negative VPD. It represents the vapor pressure difference generated by the temperature differential $(T_c - T_a)$ when VPD is 0 (Idso et al., 1981). The upper limit value is close to the NWSB interception a (depending on temperature) and corresponds to a only when a is equal to 0 (Testi et al., 2008). This proposed method is site-dependent. Another approach for obtaining the upper and lower limits of $(T_c - T_a)$ is theoretical and foresees the combination of energy balance and diffusion equations. This second method requires knowledge of difficult to obtain variables such as net radiation and aerodynamic resistance (Berni et al., 2009a; Testi et al., 2008). A third approach, defined statistical, was used with good results (Alchanatis et al., 2010; Baluja et al., 2012; Gonzalez-Dugo et al., 2013; Rud et al., 2014). Briefly, it foresees the use of the average temperature of the coolest 5–10% of the canopy pixels as the wet reference to calculate the lower limit (Cohen et al., 2017).

Another method proposed to obtain the two limits foresees the use of direct measurements over wet or dry reference surfaces, natural or artificial. The reference dry targets, as suggested by Jones (Jones, 1999; Maes and Steppe, 2012), can be achieved, impeding leaf transpiration, by covering the leaf surface (on one or both sides) with petroleum jelly. The upper limit reference temperature results from the measurement of the leaf temperature carried out about 30 minutes after the

application of the gelatin layer. The wet targets can be obtained by spraying a thin layer of water on one or both leaf sides before taking the thermal image. This is valid on a single plant scale (Maes and Steppe, 2012). The advantage of this method is that stress levels are normalized to the actual response of the plants, but the need to repeat the measurement for each test site after each flight of the UAV can be an obstacle to its applicability. Another problem concerns the difficulty of identifying the leaves covered by petroleum jelly (Jones et al., 2009; W.H. Maes et al., 2011). Maes (2016) proposed an example of a wet artificial target made using a cloth and a steel wireframe. The target thus made, with an appearance, shape and size similar to grapevines and kiwi leaves, was kept wet for days simply by keeping the lower part of the cloth immersed inside a bottle filled with water. Artificial targets were also used in Agam et al. (2013). This study provides an approach in which the reference temperature of the upper limit is set at 5 °C above the air temperature while that of the lower limit is derived from the artificial target's temperature. Berni et al. (2009a) proposed an approach to monitor relatively large areas using UAVs to detect water stress; in particular, the work focused on the control of water stress in an olive grove, is based on the use of physical models for the estimation of input variables of energy balance equations, without requiring use of reference surfaces.

Two problems prevented the widespread use of the CWSI: the first regards its use under changing atmospheric conditions, while the second concerns the problem of “mixed-pixel value”. The latter occurs when using lower resolution data from satellites or aircrafts platforms (compared to UAVs). Part of the temperature of the pixel derives from the background soil and not from the temperature of the pure canopy (Jones and Sirault, 2014). These effects reduce the quality of the data.

Regarding the first aspect, CWSI was found to work better in conditions of dry climate while it were demonstrated important limitations in wet climates and in environments characterized by a substantial climatic variability (Hipps et al., 1985). It is important to consider that the absolute in leaf-air temperature difference decreases as the atmospheric humidity deficit decreases and this also applies for sensitivity to any measurements made. Furthermore, while taking the latter aspect into account in calculating the CWSI, as the humidity (and temperature) deficit decreases, the signal-to-noise ratio is reduced (Jones and Vaughan, 2010). Furthermore, it must be considered that the canopy temperature depends in part on variations in the roughness of the canopy and also on wind speed and net radiation, which are subject to greater variability in humid climates (Jones, 2018).

As far as the problem of “mixed-pixel value” is concerned, being the resolution of satellite images limited, the sensors mounted on UAVs, thanks to their sub-meter spatial resolution, allows to recover the pure canopy temperature minimizing the thermal effects of the background soil (Berni et al., 2009b; Herwitz et al., 2004; Sugiura et al., 2005). Various approaches can be adopted as shown in Jones and Sirault (2014). One possible approach to extracting the temperatures of canopies' sunlit leaves is to distinguish between canopy pixels and background pixels based on an analysis of the temperature distribution among the pixel population and then segment the image into two distinct classes. This approach represents a good solution in case there is a clear difference between the average temperature of the canopy and that of the soil/background. A valid approach also includes the use of additional information derived from RGB, multispectral and hyperspectral images (when several sensors are used simultaneously), in order to identify plant's pixels (Jones and Sirault, 2014). In this case, the use of vegetation indices, such as NDVI, to separate plant pixels and soil pixels can be useful.

In addition to CWSI other normalized thermal indices were developed between the 1970s and 1980s. For example, there are the conductance index (IG) and the stomatal conductance index (I3), whose formulas (Equations 5.3 and 5.4) are the following:

$$IG = \frac{T_{dry} - T_c}{T_c - T_{wet}} \quad (5.3)$$

$$I3 = \frac{T_c - T_{wet}}{T_{dry} - T_c} \quad (5.4)$$

where T_c is the surface temperature of the canopy, while T_{dry} and T_{wet} are entirely dry or wet reference surfaces to simulate leaf temperature under conditions of minimum and maximum transpiration.

These two indices' main characteristics are that IG increases with stomatal conductance and I3 is positively correlated with stomatal resistance (Maes et al., 2011; Maes and Steppe, 2012). The indices CWSI, IG, and I3 need the knowledge of canopy temperature under both wet and dry conditions but, as the concept of the CWSI is best known, it remains the most widely used (Maes and Steppe, 2012).

Research carried out thus far has concerned the monitoring of water stress in both herbaceous and tree crops. In Sullivan et al.'s (2007) and Bian et al.'s (2019) research, thermal UAVs were exploited, respectively, to monitor *Gossypium hirsutum* L. crop residue management and the response to

different irrigation treatments, calculating the CWSI. Martinez et al. (2017) studied the monitoring of sugar beet's water stress by comparing thermal data, obtained using a conventional thermal camera, with data obtained using a low-cost infrared sensor.

Zhang et al. (2019) monitored maize water stress at the farm scale using RGB and thermal UAV sensors. The work of Crusiol et al. (2020) concerns the evaluation of the water status of soybean plants under different water conditions. Other research (Raeva et al., 2019; Sagan et al., 2019) dealt with the monitoring of herbaceous crops using different sensors (RGB, multispectral, and thermal) with the objective to produce orthomosaics and vigor maps.

The CWSI is widely used for perennial crops. Bellvert et al. (2016) calculated the CWSI in peach trees (*Prunus Persica*), mapping the orchard's internal spatial variability using thermal UAV and verifying the relationships between this index and the leaf water potential in different growing seasons. Gonzalez-Dugo et al. (2013) investigated the spatial variations in the water status of five different fruit tree species: almond (*Prunus dulcis*), apricot (*Prunus armeniaca*), peach (*Prunus persica*), lemon (*Citrus x limon*), and orange (*Citrus sinensis*). In this regard, it is important to remember that stomatal response to environmental conditions can differ between species (Ballester et al., 2013). For example, olive and citrus show relevant stomatal closure at midday (Gonzalez-Dugo et al., 2013; Testi et al., 2008), while in other species, such as almond trees, the stomatal behavior varies between the different cultivars (Gonzalez-Dugo et al., 2012).

Some studies concerned the application of thermal UAV RS on citrus orchards (orange, *Citrus sinensis*, and mandarin, *Citrus reticulata*) with the aim to extract the temperature of the crowns for water stress detection (Gonzalez-Dugo et al., 2014; Zarco-Tejada et al., 2012). Research was carried out on olive crops, a species of great importance socio-economic in the countries of the Mediterranean basin (Solano et al., 2019), to verify the plant's behavior in response to various irrigation treatments. Poblete-Echeverría et al. (2016) showed that the temperature difference between the canopy (T_c) and air (T_a) is correlated to the difference in water potential under different irrigation treatments when the plants are in water stress conditions. Berni et al. (2009a) used very high-resolution UAV thermal imagery to calculate and map the tree canopy conductance and the CWSI in a heterogeneous olive orchard. Egea et al. (2017) proved the usefulness of the CWSI for monitoring water stress in a dense olive orchard by verifying good relationships between the CWSI and water stress indicators: stomatal conductance, stem water potential, and leaf transpiration rate. Ortega-Farías et al. (2016), using thermal and multispectral cameras (mounted on UAV), estimated

the energy balance components on a drip irrigation in an olive orchard, using high-resolution images to evaluate intra-field spatial variability.

Several works have exploited thermal UAVs to calculate the CWSI in vineyards, such as that of Zarco-Tejada et al. (2013). In Baluja et al.'s (2012) work concerns the determination of the relationships between the temperatures or indices derived from thermal and multispectral imagery and stomatal conductance and water potential. In this case, air and leaf temperatures were recorded with a handheld thermometer, stomatal conductance was measured with a leaf gas exchange system, and stem water potential was measured using a Scholander pressure bomb; in addition, CWSI, IG, and I3 were calculated. Likewise, the work by Bellvert et al. (2014) related the CWSI with leaf water potential while that by Santesteban et al. (2017) related the CWSI with stem water potential and seasonal leaf stomatal conductance to estimate the variability of plant water status in a vineyard. Matese et al. (2018) and Pàdua et al. (2020, 2019) used different sensors (RGB, multispectral, and thermal) for several applications in precision viticulture: production of vigor maps, multi-temporal analysis of vigor maps, and water stress detection. Gómez-Candón et al. (2016), proposed a methodology for obtaining thermal orthomosaics, tested in an apple orchard, including a method for radiometric correction of UAV thermal images.

5.4.2 Plant disease detection, phenotyping, yield estimation, and vegetation status monitoring

An important and interesting example of application in the context of plant pathology of thermal UAV RS is shown by Calderón et al. (2013). In this research, the authors aimed to evaluate the use of thermal imagery and physiological indices derived from other types of sensors to detect the presence of infection caused by the soil-borne fungus *Verticillium dahliae*. The role of thermal RS in the diagnosis of the pathology causing desiccation is due to the water stress of plants, caused by the fungus *Verticillium*, or by the stomatal closure, which causes the reduction of the transpiration rate. The reduction of evaporative cooling determines an increase in leaf temperature. Thanks to field measurements, it was proved that the crown's temperature variations are higher and stomatal conductance lower as the severity level of the disease increased. Besides, crown temperature and the CWSI index were shown to be among the best indicators to detect *Verticillium dahliae* at the early stages of disease development.

Regarding the issue of yield estimation and related aspects, thermal UAV RS was exploited in research concerning cotton, soybean, and rice crops (Feng et al., 2020; Liu et al., 2018; Maimaitijiang

et al., 2020). Feng et al. (2020), for example, exploits three types of sensors (RGB, multispectral, and thermal) to analyze several features in order to see which one had the best performance for the yield prediction and at which stages of the crop cycle: four vegetation indices, canopy cover, plant height, temperature, and a cotton fiber index. The research of Maimaitijiang et al. (2017) concerned soybean and, in particular, testing the potentialities of using different sensors (including the thermal camera) in the context of multimodal data fusion and deep neural network. The objective was deriving useful information for a yield prediction model. Liu et al. (2018) investigated rice lodging using RGB and thermal sensor UAV images. The research aimed to measure the daily temperature differences between lodged and non-lodged rice crops and to detect the optimal time window. Regarding this last aspect, being differences in temperature between 10 a.m. and 4 p.m. were significant, the thermal camera allowed to identify lodged rice plants.

Several works have focused on monitoring vineyards and related landscape elements such as agricultural terraces (Filippo et al., 2017; Parisi et al., 2019; Sangha et al., 2020; Tucci et al., 2019). For example, Tucci et al. (Parisi et al., 2019; Tucci et al., 2019) used RGB and thermal cameras to investigate the thermal dynamics of a vineyard grown on the dry-stone wall terraced land. The dry-stone terraces are part of the UNESCO's Representative List of the Intangible Cultural Heritage of Humanity, and are typical and iconic characterizing features of the agricultural landscapes across Europe, including Italy (Modica et al., 2017). However, their importance for the landscape agricultural terraces are threatened by the risk of abandonment and degradation. This may result in the increase of hazards linked to geo-hydrological processes triggered by rainfall events. In this context, the use of thermal and RGB sensors mounted on UAVs represents an efficient and cost-effective monitoring approach, also considering the high resolution of the images and the reduced time for their acquisition. Tucci et al. (2019) verified the effectiveness of the used sensors in monitoring the terraced crops. They investigated the influence that dry-stone walls can have on the vineyard's microclimate and, consequently, on the quality of the obtained grapes. The results of this study showed differences in temperature between the plants of the external rows (higher temperatures) and internal rows (lower temperatures).

Phenotyping has a crucial role in crop science research. The acquisition of crop phenotypic information in different environments allows the association of genomic and phenotypic information crucial to increase yield (G. Yang et al., 2017). In this field of study, recently, the importance of the use of UAVs has increased as monitoring with this platform provides a rapid and non-destructive approach to phenotyping, allowing the use of high spatial resolution images

(Neely et al., 2016; G. Yang et al., 2017). The monitoring with UAVs has made it possible to overcome several limits linked to the use of traditional methods, such as the difficulty in carrying out simultaneous measurements on different plots (Sankaran et al., 2015). In this framework, some research was carried out involving thermal UAV RS, thus showing its effectiveness, as in Vasit Sagan et al. (2019). Natarajan et al. (2019) used different sensors (visible, multispectral, and thermal) for the phenotyping of indirect traits (including canopy temperature) for early-stage selection in sugarcane breeding. Gracia-Romero et al.'s (2019) work focused on the comparison of the performance of RGB, multispectral, and thermal data, derived from UAV and ground-based, with the objective to assess genotypic differences in durum wheat's yield under different growing conditions. The measurement of the canopies' temperature was showed an alternative valid to that of leaf stomatal conductance. Perich et al. (2020) exploited thermal UAV RS to measure canopy temperature in wheat. In this crop, canopy temperature has a strong association with water status and stomatal conductance (Amani et al., 1996; Berliner et al., 1984; Blum et al., 1989); specifically, it was demonstrated that the low temperature of the cap could have been associated with a 30% increase in yield, as well as an increase in water absorption by the deeper roots when measured during the grain filling phase (Lopes and Reynolds, 2010). Maimaitijiang et al.'s (2017) work, performed on soybean, proved that the fusion of thermal and multispectral data could provide the best estimate of crops' biochemical traits, as chlorophyll content and N concentration, and biophysics, as LAI, fresh and dry biomass.

Another field of application in which thermal UAV RS has proven to be very promising, as the less-expensive way, is the mapping of drainage systems. Subsurface tile drainage is of great importance in the Midwest of the United States (Pavelis, 1987). Subsoil drainage permits groundwater level to be lowered by removing excess water and reducing soil erosion, increasing the aeration (Fausey, 2005; Lal and Taylor, 1970) and infiltration capacity of water derived from precipitation. Precise knowledge of the arrangement of drainage nets, as well as bringing benefits for their better functionality, is useful for soil and water conservation practices (Freeland et al., 2019). Besides, other benefits include increases in soil productivity and the yield of the crops, the majority of which do not tolerate excess water (Cannell et al., 1979; Du et al., 2005; Freeland et al., 2019). The usefulness of UAV mounted thermal sensors lies in this: being the soil directly above a drainage line, it results drier than the soil between the drainage lines (Allred et al., 2020) so differences in emissivity between dry and wet soil surfaces can be detected using a thermal camera (Mira et al., 2007). Indeed, as demonstrated in several studies, thermal cameras mounted on UAVs,

even in combination with visible and multispectral cameras, provided significant performance and potentialities for their use in mapping agricultural drainage pipe systems (Allred et al., 2020, 2018; Freeland et al., 2019; Williamson et al., 2019; Woo et al., 2019).

5.5 Future Research Outlook

The use of UAV thermal RS is not as widespread as that of optical and multispectral RS, and this is certainly due to the characteristics of thermal cameras and of data that are derived from them. With regard to the first aspect, an important limitation is the low geometric resolution of the thermal cameras when compared, for example, to RGB sensors. Another aspect concerns the data derived from the sensor, i.e., the temperature, which was shown to be fundamental in detecting water stress in plants, considering the natural mechanisms that regulate the temperature of plants. Excluding, maybe, this application, in which thermal sensors are protagonists and advantageous over other sensors, especially for the capacity to detect water stress connections in advance, other applications that have provided the exclusive use of thermal cameras are few, especially if we consider, above all, the field of plant pathology. The real potential of UAV applications can be exploited with the maximum profit in terms of utility, focusing on the feature that makes UAVs unique: that of being able to mount and use several sensors at the same time (Maes and Steppe, 2019). In addition, the possibility of carrying out surveys with a submetric resolution of just a few centimeters using several sensors at the same time and with more affordable costs gives UAVs a further advantage over aerial platforms. For these reasons, thermal cameras used with RGB and multispectral sensors can increase UAVs' efficiency in PA and expand their possibilities in terms of use. For example, in plant pathology, in order to improve the ability to detect diseases or parasite attacks at an early stage, the use of different sensors, optical, multispectral and thermal, and the fusion/combination of their data should be considered (J. Zhang et al., 2019).

New developments are expected in thermal RS. In particular, the current trend towards increased user-friendliness for all types of users is expected to continue in thermal sensors' technological development. It is also desirable to achieve a higher level of automation in aspects related to the field data acquisition phase (preparation of the optimal flight plan, configuration and calibration of the sensors before and during flight) and those related to the data processing phase (e.g. reduction of the time required for data processing). These steps forward are considered necessary to implement the use of thermal UAV RS in agriculture. Progress to be made in the data acquisition

phase on the ground also remains an essential step. Specifically for thermal RS, a simpler and more easy and immediate combination of the data that were collected by weather stations with data derived from UAVs would be useful, including a simpler and more immediate combination of data collected by meteorological stations with data derived from UAVs together with easier mitigation of atmospheric effects, complex interactions between soil and plants (Khanal et al., 2017). This is especially true in the case of thermal RS, whose raw data before the processing steps are far from offering true and accurate temperature measurements. In this regard, in order to obtain a final quality product, knowledge of thermography is essential (Maes and Steppe, 2019).

Currently, the PA requires high-intensity procedures for the processing and use of the acquired images and therefore requires the presence of experienced and qualified personnel (Parisi et al., 2019), which means higher costs for companies. In this way, the use of advanced technology, including the use of UAVs, has remained limited to farmers with large agricultural areas and greater economic resources (Tsouros et al., 2019).

In the case of UAV thermal surveys whose operating costs per hectare are higher than those of multi-spectral surveys, this aspect is even more obvious (Borgogno Mondino and Gajetti, 2017).

5.6 A case study on monitoring onion crops using UAV multispectral and thermal imagery

Adapted from

Monitoring onion crops using UAV multispectral and thermal imagery

Conf. AIIA Mid-Term 2019 Biosyst. Eng. Sustain. Agric. For. food Prod. Matera 2019.

Monitoring Onion Crops Using UAV Multispectral and Thermal Imagery: Preliminary Results



Gaetano Messina, Salvatore Praticò, Biagio Siciliani, Antonio Curcio, Salvatore Di Fazio and Giuseppe Modica

Abstract Agriculture constitutes one of the most important fields where Remote Sensing is employed, particularly in the aspects related to precision agriculture (PA). PA means a management strategy that aims at carrying out agronomic interventions in compliance with the actual crop needs and the biochemical and physical characteristics of the soil. PA analyses and manages the spatial variability of the field to optimize profitability, sustainability, and protection of agro-ecological services. The present paper shows the potentiality of coupling multispectral and thermal imagery acquired by an unmanned aerial vehicle (UAV) in monitoring crops. A case study in onion crop (Cipolla rossa di Tropea IGP) is provided. Multitemporal surveys were carried out by means of a fixed-wing UAV, equipped with a multispectral camera Sequoia Parrot (R-G-RedEdge-NIR) and a quadcopter equipped with a thermal camera Flir Vue Pro 640 R. Prior to proceeding with UAV surveys, soil characteristics were analysed on the basis of systematic sampling. According to the characteristics of thermal cameras, aluminum is used as the material of control targets with their size identified clearly in the thermal images. UAV multispectral imagery was calibrated with a panel with known reflectance, and verified with a spectroradiometer (Apogee Ps-300) on bare soil and vegetation. With regard to thermal ground truths, wet and dry panels/surfaces have been used as references, measuring their temperature before and after UAV thermal flights by means of a handheld infrared thermometer.

Keywords Precision agriculture (PA) · Remote sensing (RS) · Unmanned aerial vehicle (UAV) · Thermal surveys · Multispectral surveys · Onion crop

5.6.1 Materials and methods

The study was performed in an onion crop located in Campora S. Giovanni, in the municipality of Amantea (Cosenza, Italy). Since 2008, the onions here produced are labeled with the European Protected Geographical Indication label “Cipolla Rossa di Tropea IGP.” The producer farms are part of a consortium with a crop surface of 500 hectares. The study site has an area of 2 hectares (Figure 5.5). The UAV surveys were carried out three times, precisely two months after the transplant of onions (Figure 5.5, b and c), which took place in early September, carrying out the first flight on 23 November 2018 and the two other flights on 19 December 2018 and 18 January 2019.

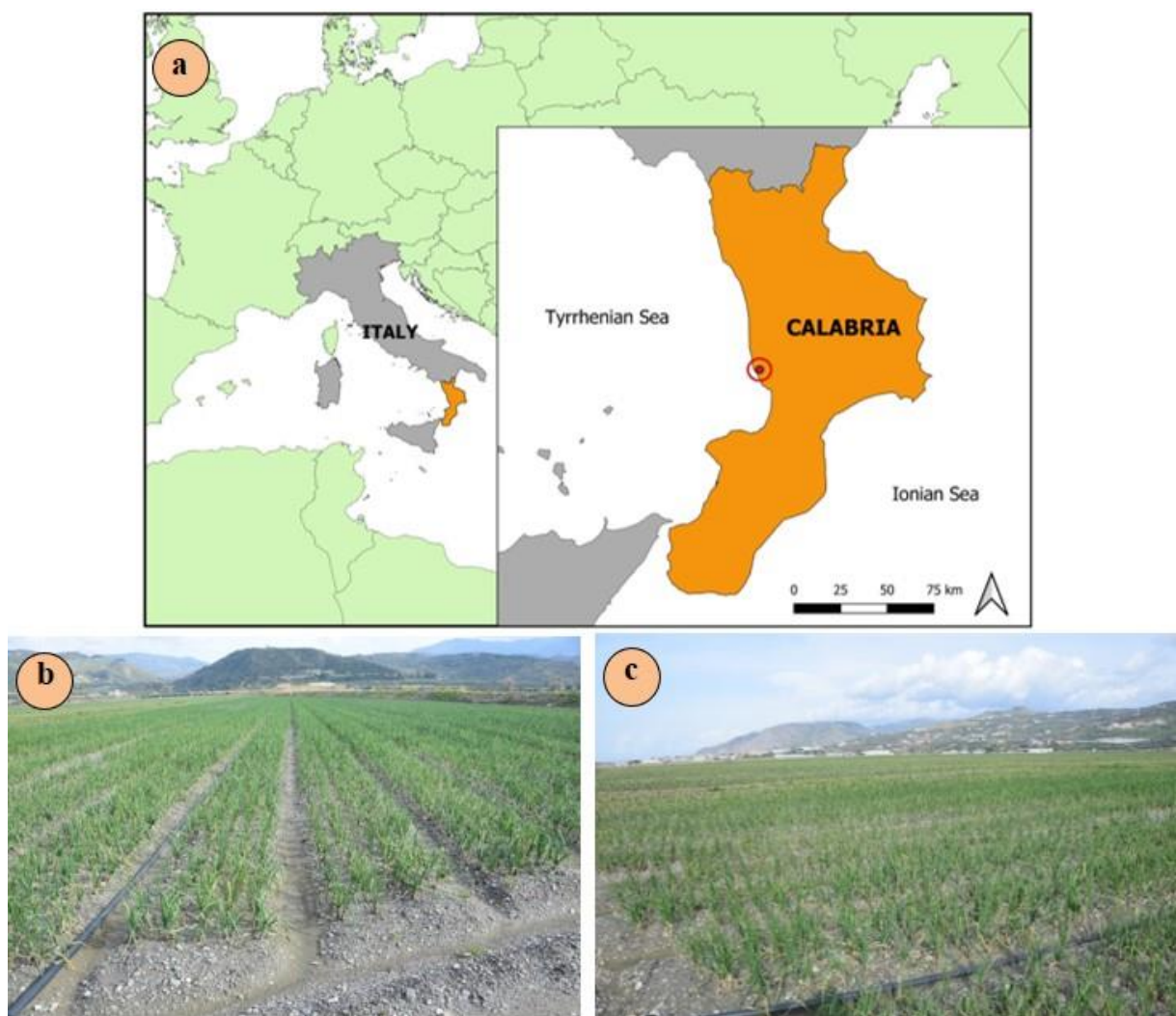


Figure 5.5 (a) The localisation of the study site (Campora S. Giovanni, CS – Italy). (b-c) The onion field where the experiments were carried out (*source*, Messina et al., 2019).

Multispectral (MS) surveys were performed at 50 m of flight height using the fixed-wing UAV Parrot Disco-Pro AG (Figure 5.6) equipped with a MS camera Sequoia Parrot (Figure 5.7a). The

Parrot Sequoia has four different channels, each with 1.2 Mpx of resolution: Green (530–570 nm), Red (640–680 nm), Red edge (730–740 nm) and Near-infrared (NIR) (770–810 nm). In addition, it is also equipped with an RGB composite sensor, and an external irradiance sensor with GPS and IMU placed on top of the UAV. The irradiance sensor captures sensor angle, sun angle, location, and irradiance for every image taken during the flight.

Thermal surveys were performed by means of quadcopter DJI Phantom 4 (Shenzhen, China) (Figure 5.6), equipped with a thermal camera FLIR Vue Pro R 640 (Figure 5.7b) (FLIR Systems, Inc., Wilsonville, Oregon, USA). This thermal camera captures temperature with a spectral range of 7.5–13.5 μm with a resolution of 640×512 pixels and a +/- 5°C thermal accuracy. The model used in these experiments was equipped with a 9 mm focal lens, providing a field of view (FOV) of 69°(H) × 56°(V). The thermal camera was set using a FLIR Vue Pro APP (Figure 5.8), which is the primary control interface available. The JPEG format selected has both the compressed 8-bit processed JPG image and 14-bit raw sensor data, which provide data about Scene, Palette, and Telemetry. Concerning radiometry settings, the humidity was set on medium value (45%), air temperature at 25°C and emissivity on 98%. The UAV equipped with a thermal camera was used two times during the day on 23 November between 12:28 and 12:50 (local time). The flight height was 40 m, and the interval timer shooting was 2 s.



Figure 5.6 The quadcopter DJI Phantom 4 equipped with the thermal camera FLIR Vue Pro R 640 (on the left) and the fixed-wing Parrot Disco-Pro AG equipped with the multispectral camera Parrot Sequoia (on the right) (*source*, Messina et al., 2019).



Figure 5.7 (a) Multispectral camera Parrot Sequoia and (b) thermal camera FLIR Vue Pro 640 R as used to carry out surveys.



Figure 5.8 FLIR Vue Pro APP used to set the thermal camera FLIR Vue Pro.

In the field, 9 ground GCP were placed and geo-referenced using a Leica RTK GNSS with a planimetric accuracy of 0.03 m. For each GCP, two types of targets were used, i.e., for multispectral and thermal surveys (Figure 5.9b). GCPs were made using 50 cm × 50 cm white polypropylene panels and covering two quadrants by respectively black cardboard and aluminum sheets in MS and thermal GCPs in order to locate the control point. Based on thermal cameras' characteristics, aluminum is used as the GCP material, with their size identified clearly in the thermal images. Being aluminum a material with low emissivity, the control target can be seen clearly as a cold object in thermal imagery.

Moreover, typically having thermal cameras mounted on UAVs uncooled microbolometer sensors, the thermal signal can be highly affected by the sensor, body, and lens temperature. Therefore wet

and dry reference panels/surfaces with known temperatures were used by taking images of them before and after each flight. Reference surfaces (Figure 5.9a) were placed near the UAV take-off and landing point. Then, their temperature was measured three times using a handheld infrared thermometer (FLIR E6): at take-off, during, and at the end of every flight. Temperature measurements can be used afterward to compensate for changes in sensor temperature. For this reason, four reference surfaces were used.

Three surfaces were dry: three panels of polypropylene (white, grey, and black). The fourth reference surface was made delimiting with circular targets, covered with aluminum, a square piece of ground keeping it constantly wet for the flight duration. Instead, the temperature of the dry soil near the targets was measured using a probe thermometer.

UAV MS imagery was calibrated using a panel with known reflectance and a spectroradiometer for ground truth measurements (Apogee Ps-300) on bare soil, vegetation and using Parrot Sequoia calibration target (Figure 5.9c).



Figure 5.9 (a) Temperature reference targets used during thermal surveys. (b) Thermal (above) and multispectral (below) targets are used as ground control points (GCPs) in the onion field. c The Parrot Sequoia calibration target (*source*, Messina et al., 2019).

All consecutive images were processed via aerial image triangulation with the geo-tagged flight log and the GCPs using the software Pix4D. The digital elevation model (DEM) was generated based on the point cloud, which is a set of matching points between overlapping images. The DEM has a 5 cm/pixel resolution and a mean geolocation accuracy of 0.37 for X/Y axes and 0.43 for Z axis. Finally, a georeferenced orthomosaic was built using the DEM as the surface reference.

5.6.2 Results

Orthomosaics obtained from both thermal and MS and characterized by 8.5 and 5 cm of ground sample distance (GSD), respectively, showed a clear difference in both temperature and vegetative state of the crop in at least two distinct areas of the analyzed experimental field (Figure 5.10 b-c).

Furthermore, a geographical object-based image classification (GEOBIA) procedure for the identification and classification of onions and weeds was performed. GEOBIA was implemented through eCognition Developer 9.1 (Trimble GeoSpatial, Munich, Germany). The classification was developed starting from images in the bands Green, NIR, Red, Red edge using only the vegetation's spectral response in the different bands. The images were segmented into uniform multi-pixel objects using the multiresolution segmentation algorithm (Baatz and Schäpe, 2000) and setting the following parameters: 1, 0.1, and 0.5 for scale, shape, and compactness, respectively. After segmentation, onions were classified according to Green Normalized Vegetation Index (GNDVI) (Equation 5.5) values (Figure 5.10a). In particular, onions objects were attributed to $GNDVI \geq -0.15$.

$$GNDVI = \frac{(\rho_{NIR} - \rho_{Green})}{(\rho_{NIR} + \rho_{Green})} \quad (5.5)$$

Given these results, a monitoring plan was prepared to detect the presence of any diseases that often cause damage to the production of the farm (for example, the *Onion Yellow Dwarf Virus-OYDV* and the fungus *Sclerotinia Cepivorum*) and other causes and concauses that determine conditions of vegetative stress of a part of the crop as can be seen. The plan provides for the monitoring of the crop from the transplantation phase to harvesting. The first step involves a systematic sampling of soil. Sampling will consist of collecting soil samples distributed according to a grid pattern. For each sample, the corresponding position will be stored using GNSS.

Following the soil analysis, constant UAV surveys (weekly or fortnightly) will be carried out until the harvesting to verify the state of growth and the crop's phytosanitary status.

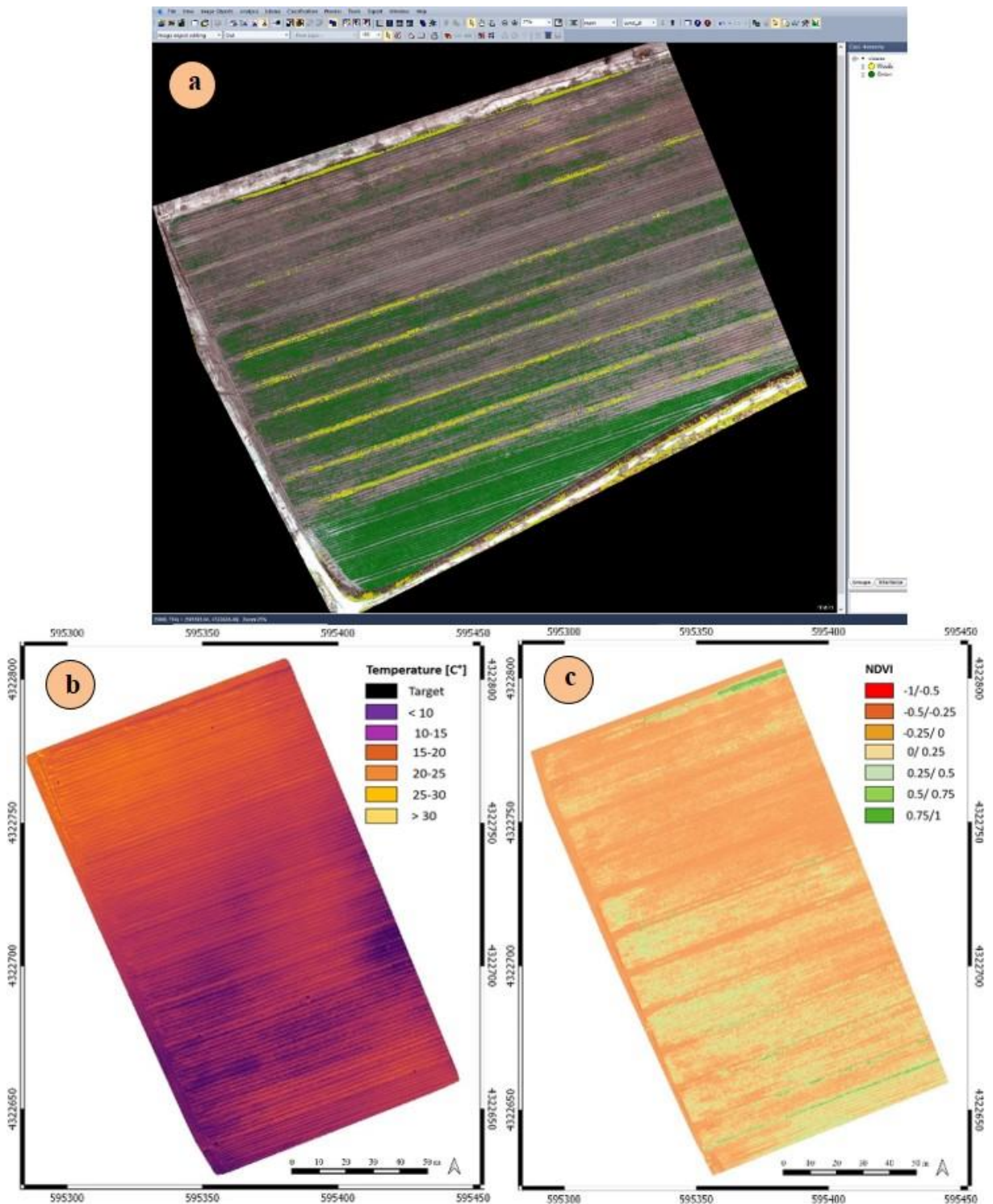


Figure 5.10 (a) Above, a map showing the image-object classification of weeds (yellow) and onions (green) performed in the eCognition suite. Below, the two obtained orthomosaics from the UAV surveys carried out on 23 November 2018. (b) Map of the temperatures [°C]. (c) Map of the Normalized Difference Vegetation Index (NDVI) (*source*, Messina et al., 2019).

The proposed methodology, especially in the presence of an area with homogeneous soil characteristics, could be a useful tool in studying the response of various crops to phytosanitary and fertilizer treatments in different areas.

6 Comparison of UAV and satellites multispectral imagery: a case study in monitoring onion “Cipolla Rossa di Tropea”

Adapted from

A comparison of UAV and satellites multispectral imagery in monitoring onion crop.

An application in the ‘Cipolla Rossa di Tropea’ (Italy). Remote Sensing. 2020, 12,

doi:10.3390/rs12203424



Article

A Comparison of UAV and Satellites Multispectral Imagery in Monitoring Onion Crop. An Application in the ‘Cipolla Rossa di Tropea’ (Italy)

Gaetano Messina ¹, Jose M. Peña ², Marco Vizzari ³ and Giuseppe Modica ^{1,*}

¹ Dipartimento di Agraria, Università degli Studi Mediterranea di Reggio Calabria, Località Feo di Vito, I-89122 Reggio Calabria, Italy; gaetano.messina@unirc.it

² Plant Protection Department, Institute of Agricultural Sciences (ICA), Spanish National Research Council (CSIC), 28006 Madrid, Spain; jmpena@ica.csic.es

³ Department of Agricultural, Food, and Environmental Sciences, University of Perugia, 06121 Perugia, Italy; marco.vizzari@unipg.it

* Correspondence: giuseppe.modica@unirc.it; Tel.: +39-0965-1694261

Received: 21 September 2020; Accepted: 16 October 2020; Published: 18 October 2020



Abstract: Precision agriculture (PA) is a management strategy that analyzes the spatial and temporal variability of agricultural fields using information and communication technologies with the aim to optimize profitability, sustainability, and protection of agro-ecological services. In the context of PA, this research evaluated the reliability of multispectral (MS) imagery collected at different spatial resolutions by an unmanned aerial vehicle (UAV) and PlanetScope and Sentinel-2 satellite platforms in monitoring onion crops over three different dates. The soil adjusted vegetation index (SAVI) was used for monitoring the vigor of the study field. Next, the vigor maps from the two satellite platforms with those derived from UAV were compared by statistical analysis in order to evaluate the contribution made by each platform for monitoring onion crops. Besides, the two coverage’s classes of the field, bare soil and onions, were spatially identified using geographical object-based image classification (GEOBIA), and their spectral contribution was analyzed comparing the SAVI calculated considering only crop pixels (i.e., SAVI onions) and that calculated considering only bare soil pixels (i.e., SAVI soil) with the SAVI from the three platforms. The results showed that satellite imagery, coherent and correlated with UAV images, could be useful to assess the general conditions of the field while UAV permits to discriminate localized circumscribed areas that the lowest resolution of satellites missed, where there are conditions of inhomogeneity in the field, determined by abiotic or biotic stresses.

Keywords: spatial resolution; mixed pixels; vegetation indices (VIs); soil adjusted vegetation index (SAVI); geographical object-based image classification (GEOBIA); correlation analysis; onion crops; bare soil

The agricultural sector is one of the most significant areas of application of geographic information systems (GISs), remote sensing (RS) methods, and data (Solano et al., 2019). The remote platforms and their associated imaging systems are distinguished based on platform altitude, spatial, and temporal resolution. The spatial resolution determines the area of the smallest pixel that can be identified. Thus, as the spatial resolution increases, the pixel area decreases, and soil or crop characteristics' homogeneity inside the pixel increases (Mulla, 2013).

The temporal resolution is essential for the evaluation of time patterns in plant and soil characteristics. However, the availability of RS images from satellite and aerial platforms is limited by cloud cover (Moran et al., 2000; Vasisht Sagan et al., 2019). Landsat platforms, among the most used satellites, have spectral resolutions of the order of 30 m in the visible and near-infrared (NIR) and have a temporal resolution close to 17 days (McCabe et al., 2016). For many precision agriculture (PA) applications, this temporal resolution is not suitable, even considering cloud cover problems that increase the time interval in which images without coverage are available. The same applies to spatial resolution, which may not be suitable for determining variability within the field. The launch of satellites by government space agencies and commercial earth-observing companies has provided a significant improvement in revisiting time and multispectral (MS) detection capability. In this respect, two examples are given by Sentinel-2 and PlanetScope satellites. Sentinel-2 satellites are equipped with sensors capable of exploiting as many as 13 spectral bands ranging from the visible to NIR and short wave infrared region, with spatial resolutions between 10 to 60 meters (earth.esa.int/web/sentinel/missions/sentinel-2/instrument-payload/resolution-and-swath, last access 2 April 2020) and a temporal resolution of about 5 days at the European latitudes (Modica et al., 2019; Vizzari et al., 2019). PlanetScope constellation composed by a large number of small nano-satellites equipped with RGB and NIR camera provides a 3-5 m ground sampling resolution with a one-day revisiting time (Houborg and McCabe, 2016).

While satellite observation has guided many information-based advances in agricultural management and practice (McCabe et al., 2016), critical technological developments and steep rise have affected unmanned aerial vehicles (UAVs), in the last decade, which represent a potential game-changer in PA applications (Colomina and Molina, 2014). In comparison with other RS platforms, UAVs are generally more independent of climatic variables.

Being able to provide data with higher temporal and spatial resolution, today represent a significant source of RS imagery in PA (Zhang and Kovacs, 2012) considering also that, as highlighted by scholars in PA applications, the knowledge of the within-field spatial variation of

edaphic factors and the state of crops constitute an essential prerequisite (Maes and Steppe, 2019). Among the sensors mounted on UAVs employed in agriculture, MS cameras are the most common (Khanal et al., 2017).

Thanks to UAVs and high-resolution MS images, managers and specialists in agriculture can use new tools and have more information to optimize management decisions and formulate precision farming solutions (He and Weng, 2018). In particular, this technology can be used to determine the amount number of agricultural inputs, including agrochemicals and fertilizers, based on non-invasive monitoring of crop growth status (Jeong et al., 2014). The ability to better control the use of agrochemicals and fertilizers brings benefits, in addition to the enhanced quality and quantity of production, reducing the environmental risks arising from the excessive use of inputs, increasing the use efficiency, and also reducing them, using variable management practices (Benincasa et al., 2017; Tang and Turner, 1999).

Many MS UAV cameras, in particular, permit to obtain spectral information in the Red, Red edge, and NIR band for vegetation applications with a very high spatial resolution (Yao and Qin, 2019). Based on the combination of these three bands, most of the indices (i.e., vegetation indices, VIs) were developed with the aim to monitor, analyze, and map temporal and spatial variations of vegetation in both field and tree crops (Yao and Qin, 2019). In the framework of PA applications, among the techniques capable of extracting reliable and reusable information, the geographic object-based image classification (GEOBIA) techniques have demonstrated their effectiveness (Solano et al., 2019).

GEOBIA is a typology of a digital RS image analysis and classification approach that studies geographical entities through the definition and analysis of object-based instead of single pixels (Blaschke, 2010; Blaschke et al., 2014). Image objects are objects that can be distinguished in the scene. They are formed by groups (or clusters) of neighboring pixels that share a common meaning, such as, for example, in a farm context, pixels that join together to form trees' canopies of an orchard or crops in a field (Chen et al., 2018). In the literature applications of GEOBIA, starting from satellite or UAV data, have concerned both herbaceous and tree crops (Belgiu and Csillik, 2018; Csillik et al., 2018; De Castro et al., 2018, 2017; López-Granados et al., 2016a; Ok and Ozdarici-Ok, 2018; Ozdarici-Ok, 2015; Peña-Barragán et al., 2012; Torres-Sánchez et al., 2015).

Onion (*Allium cepa* L.) is a vegetable bulb crop widely cultivated and known to most cultures (Ballesteros et al., 2018; Córcoles et al., 2013). For economic importance among vegetables, the onion ranks second after the tomato (Aboukhadrah et al., 2017; Mallor et al., 2011). This plant

belongs to Amaryllidaceae's family and is biannual or perennial (depending on the cultivar). The plant has shallow adventitious, fibrous roots (Ranjitkar, 2003), which grow, usually in the first 20-25 cm of soil. The umbrella-shaped inflorescence develops from an apical ring meristem and is formed by the aggregation of small single flowers (from 200 to 600).

The bulb has variable shapes (flat to globular to oblong) and colors (red, white, or yellow). The bulb, the edible part, comes from the enlargement of the basal part of the inserted leaves, superimposed on a central cauline axis. The bulb's thick outer leaves lose moisture and become scaly until harvest, while the inner leaves thicken as the bulb develops (Pareek et al., 2017).

In this framework, this study is aimed at comparing data acquired by fixed-wing UAV and the PlanetScope and Sentinel-2 satellites in onion crop monitoring. RS techniques applied to onion crops could help to monitor the crop growth, guide localized fertilization, phytosanitary treatments, and harvest and, in general, support PA techniques implementation. At our best knowledge, very few studies have dealt with onion crop monitoring using UAV and Satellite data in the PA framework (Ballesteros et al., 2018; Belgiu and Csillik, 2018; Córcoles et al., 2013; Jeong et al., 2014; Zhao et al., 2019).

Considering these research objectives, the study site was located in a very relevant onion production area of Southern Italy. The comparison is performed to achieve the following objectives: a) evaluate the similarities and the informative content of the vegetation index at different spatial resolutions; b) evaluate the contribution made by each platform for monitoring the vegetative status of the onion crop and in guiding fertilization and phytosanitary treatments.

This chapter is structured as follows. In Section 6.1, information about the study site, data acquisition and processing, and data analysis are reported. Section 6.2 is devoted to presenting and discussing the results. Section 6.3 deals with conclusions and future research perspectives.

6.1 Materials and methods

6.1.1 Study site

The onion field is located in Campora S. Giovanni, in the municipality of Amantea (Cosenza, Italy, 39°02' 55" N, 16°05' 59" E, 5 m a.s.l) (Figure 6.1a).

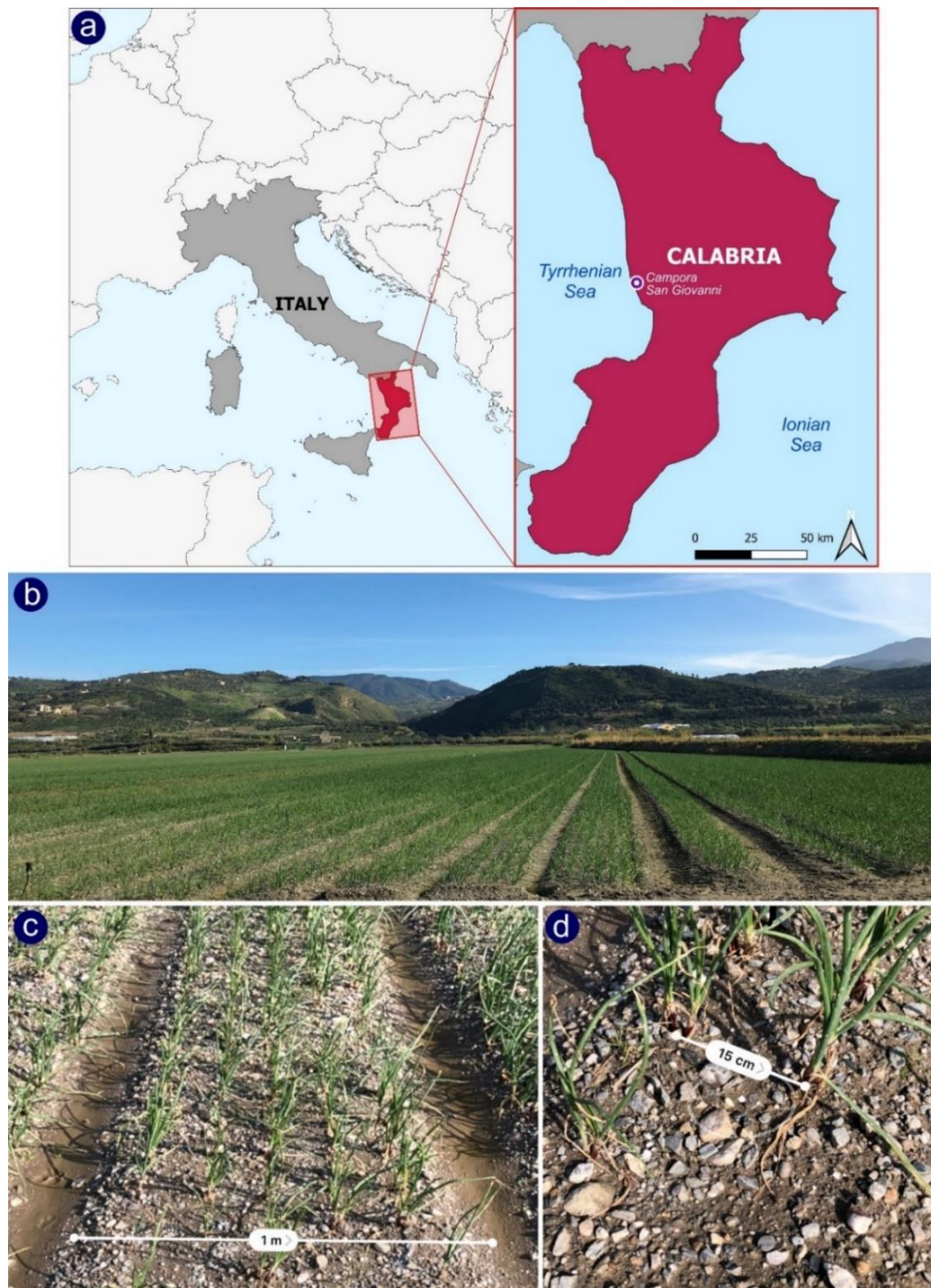


Figure 6.1 (a) The location of the study site. (b - c - d) The onion field in which the surveys were carried out (Campora S. Giovanni, CS – Italy) (source, Messina et al., 2020c).

The onions produced here are an essential local crop that, as a typical product, plays a crucial role in the economic and rural development of this territory (Bernardi et al., 2013). This particular pink-red colored onion type, since 2008, is labeled with the European Protected Geographical Indication “Cipolla Rossa di Tropea IGP”. It is well-known worldwide for its sweet flavor and for its high content of nutraceuticals that make it an upcoming “functional food” (Tiberini et al., 2019).

These unique characteristics have given the product a reputation at the national level and in markets outside Italy. The producing farms are organized in a consortium whose cultivated area is over 500 hectares (www.consorziocipollatropeaigp.com, last access 30 April 2020). The study area covers a surface of 4 hectares. The field is crossed by 10 paths, 2.5 m wide, used for the passage of agricultural vehicles necessary for phytosanitary treatments and fertilization. The plants are placed at a distance of 15 cm from each other, on baulature, 1 m wide, as shown in Figure 6.1 (b - c - d). The transplant took place between mid-August (end of the summer) and mid-September (early autumn). In particular, in a portion of the field, about 0.47 ha, transplantation took place 3 weeks later.

6.1.2 Platforms and data acquisition

UAV images

The UAV surveys were carried out between the middle (November) and the end of the cultivation cycle (January). Onion crop was, in this time frame, in the principal stage 4 (development of harvestable vegetative plant parts) (Figure 6.2) of the BBCH (Biologische Bundesanstalt, Bundessortenamt and Chemical Industry) extended scale (Meier, 2001). Surveys were carried out at 50 m of flight height using a very light fixed-wing UAV Parrot Disco-Pro AG made with foam and a weight of only 780 g (Figure 6.3). The UAV was equipped with an MS camera Parrot Sequoia, a light-weight camera employed in several pieces of research related to PA, on herbaceous crops, monitoring wheat (Bukowiecki et al., 2020), maize, and poppy crops (Iqbal et al., 2018), phenotyping of soybean (Maimaitijiang et al., 2017), and on tree crops proving useful in identifying citrus trees (Csillik et al., 2018), mapping irrigation inhomogeneities in an olive grove (Jorge et al., 2019) and the vigor in vineyards (Pádua et al., 2019). The Parrot Sequoia MS has four different channels, each with 1.2 Mp of resolution: Green (530–570 nm), Red (640–680 nm), Red edge (730–740 nm) and NIR (770–810 nm). Furthermore, it is also equipped with an RGB composite sensor, an external irradiance sensor with a global navigation satellite system (GNSS), and an inertial measurement unit (IMU) modules placed on top of the UAV. The irradiance sensor, which

measures the sky down-welling irradiance, is placed on top of the UAV and continuously captures the sky irradiance at the same spectral bands as the MS camera (Cubero-Castan et al., 2018; Deng et al., 2018). The IMU allows capturing sensor angle, sun angle, location, and irradiance for every image taken during the flight. This data was mainly used for image calibration. The UAV flights were carried out three times as follows: 23 November 2018, the second on 19 December 2018, and the last on 18 January 2019. As shown in Figure 6.2, the first two dates concern the phase of the crop cycle of the full development of harvestable vegetative plant parts. In this phase, crucial operations are carried out, such as a large part of the fertilization and phytosanitary treatments. Instead, on the last date of monitoring, in January, onions are close to harvesting.

The procedure performed for field surveys is similar to the one shown in Messina et al. (2020a, 2020d). In the field were placed 9 ground control points (GCPs) whose position was geo-referenced using a Leica RTK GNSS with a planimetric accuracy of 0.03 m. In particular, GCPs were made using 50 cm × 50 cm white polypropylene panels and covering two quadrants using black cardboard to locate the point. MS imagery was calibrated using a panel with known reflectance, the Parrot Sequoia calibration target. In particular, photos of the target were taken before and after the flight and it is assumed that the raw sensor data was transformed into percentage reflectance in combination with the data provided by the solar radiation sensor. All consecutive images were processed via aerial image triangulation with the geo-tagged flight log and the geographic tags through the software Pix4D mapper (Pix4D S.A., Switzerland). Following the recommended Sequoia image correction procedure, corrections were applied to the raw data generating four single reflectances calibrated GEOTIFFs.

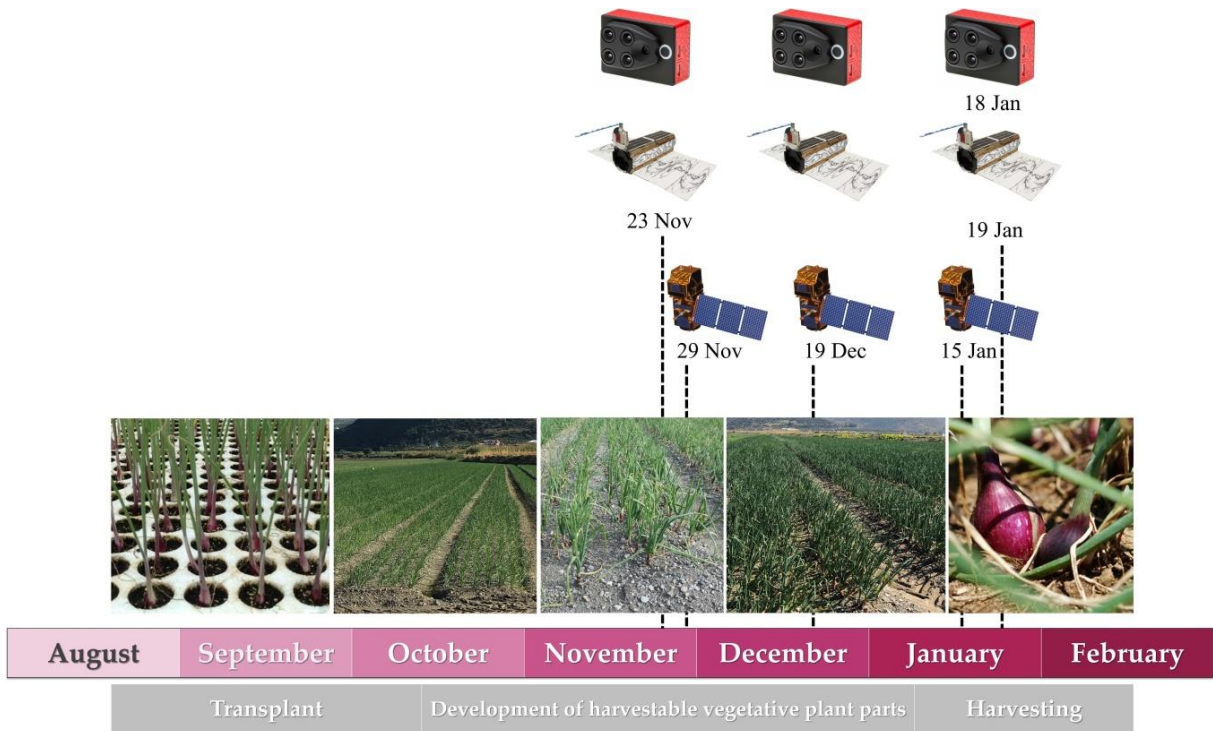


Figure 6.2 Crop cycle of the onion, dates of the unmanned aerial vehicles (UAVs) surveys and of imagery acquisition (*source*, Messina et al., 2020c).





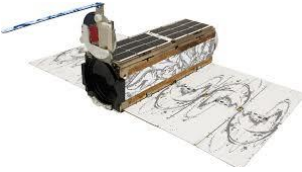
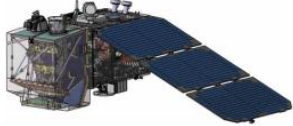
Figure 6.3 The Parrot Disco-Pro AG fixed-wing unmanned aerial vehicle (UAV) during the pre-flight calibration using the Parrot Sequoia calibration target (*source*, Messina et al., 2020c).

Satellites images

Sentinel-2 is managed through the Copernicus Program proposed by the European Union (EU) and the European Space Agency (ESA). The first satellite was launched in 2015 (Bartsch et al., 2020).

Sentinel-2 consists of two twin satellites, Sentinel-2A and Sentinel-2B, both operating on a single orbit plane but phased at 180° with a temporal resolution of 5 days with this bi-satellite system (Spoto et al., 2012; X. Yang et al., 2017). The Sentinel-2 data consists of 13 bands in the visible, NIR, and short-wavelength infrared (SWIR) spectral range (Rapinel et al., 2019; X. Yang et al., 2017) with a spatial resolution of 10 m, 20 m or 60 m depending on the band. Sentinel-2 images used in this work are the four spectral bands at 10 m spatial resolution in Blue, Green, Red, and NIR spectra showed in Table 6.1. Data were downloaded from the Copernicus Open Access Hub (scihub.copernicus.eu) in level 2A, which provides Bottom Of Atmosphere (BOA) reflectance images ortho-rectified in UTM/WGS84 projection.

Table 6.1 Characteristics of the multispectral camera and of the satellites whose images were used in this research.

Platform	UAV	SATELLITE	
	Parrot Disco-Pro AG	Planet Scope	Sentinel-2
  Camera Parrot Sequoia		 3U Cubesat	
Number of channels used	4	4	4
Spectral wavebands (nm)	Green 550 (width 40) Red 660 (width 40) Red edge 690 (width 10) NIR 790 (width 40)	Blue 464-517 Green 547-585 Red 650-682 NIR 846-888	Blue 426-558 (width 66) Green 523-595 (width 36) Red 633-695 (width 31) NIR 726-938 (width 106)
Radiometric resolution	10 bit	16 bit	16 bit
Dimension	59 mm x41 mm x 28 mm	100 mm x100 mm x300 mm	3.4 x1.8 x2.35 m
Weight	72 g	4 kg	1000 kg
FOV	HFOV: 62° VFOV: 49°	HFOV: 24.6 km VFOV: 16.4 km	HFOV: 290 km
Flight quote AGL	50 m	475 km	786 km
Ground resolution distance (GSD)	5 cm	3.7 m	10 m
Number of images	>1000	1	1

PlanetScope's imagery was acquired from the PlanetScope archive (Planet Labs Inc., 2020), which manages the largest satellite constellation consisting of more than 150 satellites orbiting the Earth. PlanetScope satellites follow two different orbital configurations (Ghuffar, 2018). Some satellites are in International Space Station Orbit (ISS), and they are at a 52° inclination at about 420 km of altitude. Other satellites are in the Sun Synchronous Orbit (SSO) with an altitude of 475 km (at 98° inclination) and have equatorial crossing between 9:30 and 11:30. These sensors called 3U CubeSats (Table 6.1), also called "Doves", have small dimensions (10 cm ×10 cm ×30 cm and a weight of 4 kg) and provide daily sun-synchronous coverage images of the whole Earth landmass (Ghuffar, 2018).

Dove satellites' CCD array sensor (6600×4400 pixel) allows capturing images using three bands RGB or four (in addition, there is NIR) (Kääb et al., 2017). PlanetScope imagery has a scene footprint of about 24.4 km × 8.1 km and a ground sample distance of 3.7 m. PlanetScope imagery available used are Ortho Scene (Level 3B), i.e., imagery processed to remove distortions caused by terrain. Imagery is radiometrically, sensor, and geometrically corrected (Planet Labs Inc., 2020). Furthermore, imagery was atmospherically corrected by Planet Labs using the 6S radiative transfer model with ancillary data from MODIS (Moderate-resolution imaging spectroradiometer) (Planet Labs Inc., 2020).

6.1.3 Vegetation indices

In view of comparing satellite data with UAV data, three satellite images from each satellite platform were collected. Images were selected among those available without cloud cover in the days closest to those of the UAV surveys, as follows: 1) 29 November 2018, 19 December 2018 and 15 January 2019 from Sentinel-2, and 2) 23 November 2018, 19 December 2018 and 19 January 2019 from PlanetScope (Figure 6.4). As one of the objectives of this work is to select a proper VI to perform the subsequent comparison between the three platforms, using UAV images, four VIs were calculated and compared in their capabilities to analyze the vegetative vigor of onion cultivation. To this aim, four VI were selected: Normalized Difference Vegetation Index (NDVI), Normalized Difference Red edge Vegetation Index (NDRE), Green Normalized Difference Vegetation Index (GNDVI), Soil-Adjusted Vegetation Index (SAVI) (Table 6.2). NDVI is one of the most used indices derived from the MS information and is calculated by the normalized ratio between the NIR and Red bands (Karnieli et al., 2010). It can assume values between -1 and 1 and measure healthy vegetation exploiting the highest chlorophyll absorption and reflectance regions

(Xue and Su, 2017). NDRE has a range of values and formula similar to that of NDVI but takes advantage of the sensitivity of the vegetation to the Red edge wavelengths by replacing the Red band. GNDVI (Gitelson et al., 1996) was developed to estimate leaf chlorophyll concentration and uses a Green band rather than a Red band as in the classic NDVI.

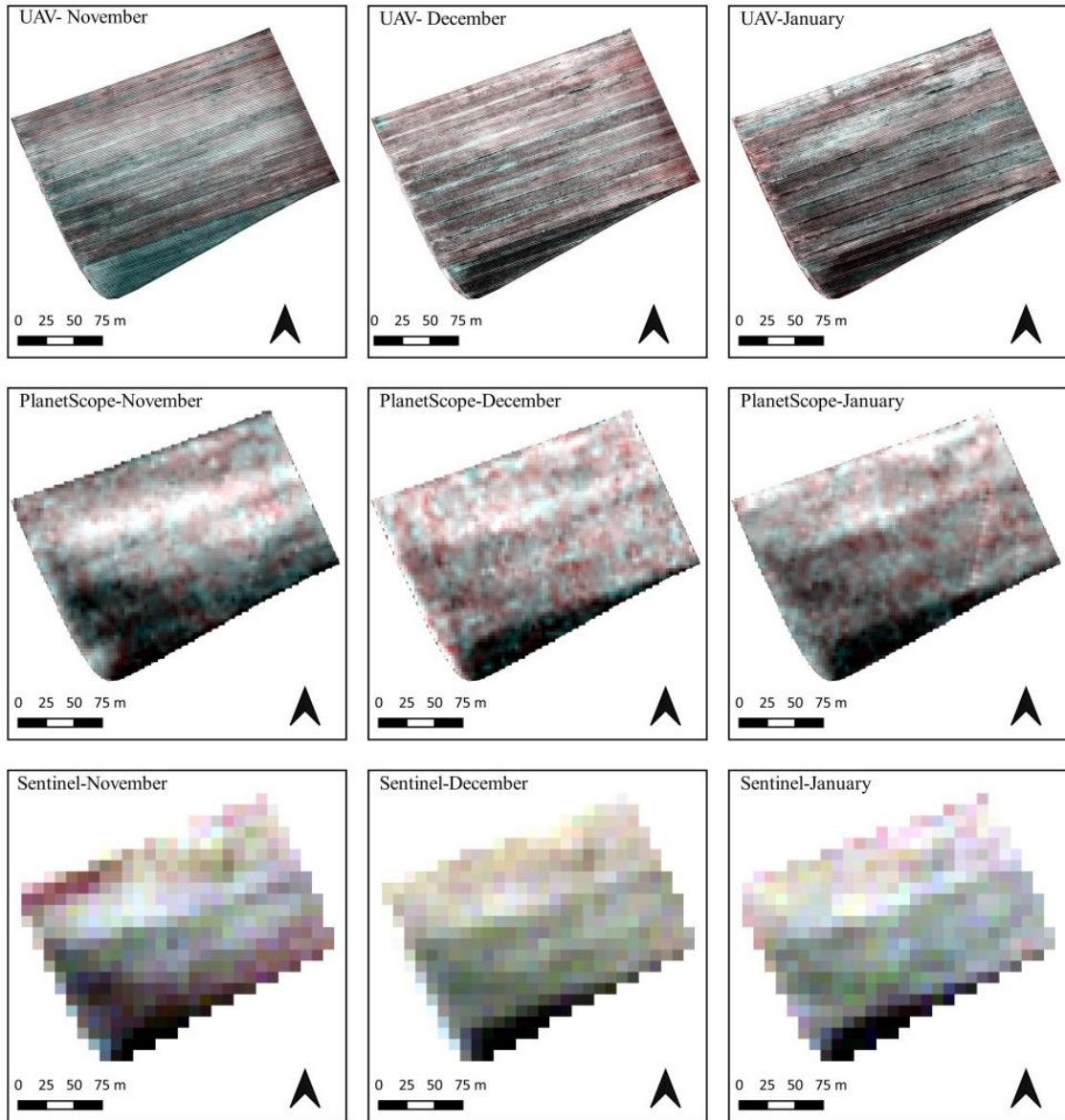


Figure 6.4 RGB orthomosaics of the three datasets (November-December and January) derived from the platforms UAV (top), satellite PlanetScope (center), and Satellite Sentinel-2 (bottom).

Table 6.2 Formulation of the four vegetation indices (VIs) used in the present research.

Index denomination	Index formula	References
Normalized Difference Vegetation Index (NDVI)	$\frac{(\rho_{NIR} - \rho_{Red})}{(\rho_{NIR} + \rho_{Red})}$	(Rouse et al., 1974)
Normalized Difference Red edge Vegetation Index (NDRE)	$\frac{(\rho_{NIR} - \rho_{RedEdge})}{(\rho_{NIR} + \rho_{RedEdge})}$	(Barnes et al., 2000)
Green Normalized Difference Vegetation Index (GNDVI)	$\frac{(\rho_{NIR} - \rho_{Green})}{(\rho_{NIR} + \rho_{Green})}$	(Gitelson et al., 1996)
Soil-Adjusted Vegetation Index (SAVI)	$\frac{(\rho_{NIR} - \rho_{Red})}{(\rho_{NIR} + \rho_{Red} + L)}(1 + L)$	(Huete, 1988)

Since NDVI is very sensitive to background factors, SAVI was developed by Huete (1988) to minimize the effects of soil background on the vegetation signal by inserting in the NDVI formula a constant soil adjustment factor L (Taylor and Silleos, 2006), the value of which can assume values between 0 and 1 depending on the level of vegetation cover. To better understand the behavior of the selected VIs, compared to each MS band, and to choose the most VI suitable for the subsequent comparison, a correlation analysis between them was implemented using Python. The implementation of the scatter plots, and the final correlation matrix was performed using *seaborn* libraries.

6.1.4 Comparison of vegetation indices (VIs) from the three platforms

A preliminary correlation analysis between a set of indices, including the four UAV bands and four commonly used VIs - NDVI, NDRE, GNDVI, and SAVI, was performed. Then, SAVI was calculated at the native MS band's resolution of each sensor (5 cm for UAV, 3 m for PlanetScope, and 10 m for Sentinel-2).

The SAVI was chosen to analyze the vegetative vigor of onion cultivation. SAVI was developed by Huete (1988) to minimize the effects of soil background on the vegetation signal by inserting in the NDVI formula a constant soil adjustment factor L (Taylor and Silleos, 2006), according to the following formula (Equation 6.1):

$$SAVI = \frac{(\rho_{NIR} - \rho_{Red})}{(\rho_{NIR} + \rho_{Red} + L)}(1 + L) \quad (6.1)$$

Where L is the constant soil adjustment factor, and which can assume values between 0 and 1, depending on the level of vegetation cover, and ρ is the reflectance at the given wavelength.

The various SAVI maps were used to describe and assess the variability within the onion field, as also shown in (Khaliq et al., 2019). Descriptive statistics and histograms, calculated with R software, were used for a preliminary comparison of image data with native image resolutions. The degree of correlation between pairs of SAVI maps was then investigated using Pearson's correlation coefficients. Initially, three comparisons were made taking into account the three dates investigated: a correlation between UAV (images resampled at 3 m resolution) and PlanetScope, a correlation between PlanetScope (images resampled at 10 m resolution) and Sentinel-2 and finally a correlation between UAV (images resampled at 10 m resolution) and Sentinel-2. Then, to investigate the relationships between crop and soil cover, further correlation analyzes were performed between the UAV SAVIs, including only onions and only soil and the SAVIs from the two satellite platforms.

6.1.5 Image Segmentation and Classification

A GEOBIA process was developed to explore the potentiality of UAV images in discriminating soil coverage types and in producing other UAV SAVI maps for the subsequent comparison. Considering the type of crop and the structure of the field, which imply the presence of portions of soil, clearly visible from above, both among the plants and in the paths used for the passage of agricultural vehicles, classification was performed to separate crop and soil. Firstly, to extract the onion crop, the GEOBIA image classification procedure was performed. The classification was developed considering only the spectral response of the vegetation in the different bands. The first step performed in the GEOBIA procedure is the segmentation of the image. It is a fundamental prerequisite for classification/feature extraction (Drăguț et al., 2014). It foresees the image's segmentation into separate, non-overlapping regions (Aguilar et al., 2016), then extracted in the form of vectorial objects.

Segmentation, which consists of dividing objects into smaller ones and creating new ones, altering the previously existing ones' morphology, takes place according to precise rules. Segmentation's algorithm used is the multiresolution segmentation (MRS) algorithm (Baatz and Schäpe, 2000). This algorithm operates by identifying single objects, having a pixel size, and merging them with the nearby objects following a criterion of relative homogeneity while minimizing the average heterogeneity (Trimble Inc., 2019). The homogeneity criterion is linked to the combination of the spectral and shape properties of the original image's objects and of those of "new" objects obtained by the merging process. Two parameters regulate homogeneity criteria by two parameters: shape

and compactness. The setting of the shape parameter concerns the importance/weight given by the segmentation process to the shape of objects with respect to color. The shape parameter can assume a value between 0 and 0.9. Color homogeneity derives from the standard deviation of spectral color. Indeed, shape homogeneity results from the deviation of a compact (or smooth). Color and shape are linked, and the user's value or weight to the shape parameter determines different results of the segmentation. In particular, the higher is the chosen value (between 0 and 0.9) the higher the influence of shape, respect to the color, in the segmentation, and vice versa (Drăguț et al., 2010). Compactness is the second adjustable parameter and determines the importance of shape with respect to smoothness. It results in the product of width and length calculated on numbers of pixels (El-naggar, 2018). The third parameter is the scale. The scale parameter determines the final size and dimension of the objects resulting from segmentation (Drăguț et al., 2014; Ma et al., 2017). Attributing higher values or smaller values of scale parameter generates larger and smaller objects, respectively. Since the objects' size depends on this parameter, it indirectly defines the maximum allowed heterogeneity for the obtained image objects. In addition, different weights can be attributed to the several input data (i.e., band layers). To perform the segmentation, the following parameters were chosen: 0.1 for shape, 0.5 for compactness, 0.3 for scale parameter, and weight 1 assigned to layers that correspond to the bands provided by Parrot Sequoia: Green, Red, Red edge, and NIR. Before choosing these parameters, some trial-and-error tests were performed, attributing different values to the segmentation parameters until the segmentation considered better (based on visual interpretation) was obtained. In this case, it was essential to obtain segments that would allow the single plants to be distinguished.

After completing the segmentation phase, the onion crops were classified based only on a SAVI threshold value ≥ 0.25 . The value was chosen as a result of some trial-and-error tests, and judged better based on visual interpretation of its ability to detect plants, following the methodology used in Modica et al. (2020). The data obtained concerning the vegetation coverage of the field was used to create a mask (and a second for the soil) to be applied to the map. The masks obtained by exporting a vector file containing only the class "onions", were applied to the UAV images at their native resolution with the aim to obtain only parts of orthomosaics concerning the onion crop.

In order to evaluate the presence of pure and mixed pixels of the vegetation class in Sentinel-2 and PlanetScope images, a spatial analysis procedure was developed in eCognition. First of all, shapefiles containing vector grids matching the Sentinel-2 and PlanetScope images' pixel size were prepared on eCognition using a chessboard segmentation.

These grids were then superimposed on the classified UAV images at an upper level of the hierarchy. Several levels of segmentation constitute a hierarchical structure in the GEOBIA paradigm (Peña et al., 2013), and in our case, the super-objects (the grids) belong to the upper level and include as a sub-object the vegetation class present in the lower level. Following this procedure, the area percentage occupied by the class “onion” within each pixel at Sentinel-2 and PlaneScope resolutions was calculated.

6.2 Results and discussions

The scatter plot of the November dataset (Figure 6.5) shows a high correlation between Red edge and NIR ($r = 0.96$) bands. Regarding the correlations between vegetation indices, NDVI and SAVI have quite the same behavior ($r = 0.95$). Analogous consideration can be made for the comparison between NDVI and GNDVI ($r = 0.95$) and between GNDVI and SAVI ($r = 0.94$). Also, in the case of the December dataset (Figure 6.6), the scatter plot matrix shows a high correlation between Red edge and NIR ($r = 0.94$).

The correlation between NDVI and SAVI indices shows that they coincide ($r = 1$). The same can be observed between NDVI and GNDVI ($r = 0.99$) and between GNDVI and SAVI ($r = 0.99$). In January’s dataset (Figure 6.7), the scatter plot shows data similar to the previous two. In particular, there is a high correlation between bands Red edge and NIR ($r = 0.98$), NDVI and SAVI ($r = 0.98$), NDVI, and GNDVI ($r = 0.99$), GNDVI and SAVI ($r = 0.98$).

The SAVI, belonging to the family of soil-corrected vegetation indices (Huete et al., 1985), is suitable to further reduce the background contribution reflectance by facilitating the identification of plants and their discrimination from the soil.

Therefore, also considering the high correlations with the other VIs, we choose to analyze the crop vegetative vigor using only the SAVI that limits the soil effect. In this case study, the species monitored, onions, have thin and small leaves, especially in the early and middle stages of growth (mid-August-October, Figure 6.2) and in monitoring their growth, it is difficult to effectively extract the images from the background (Jeong et al., 2014).

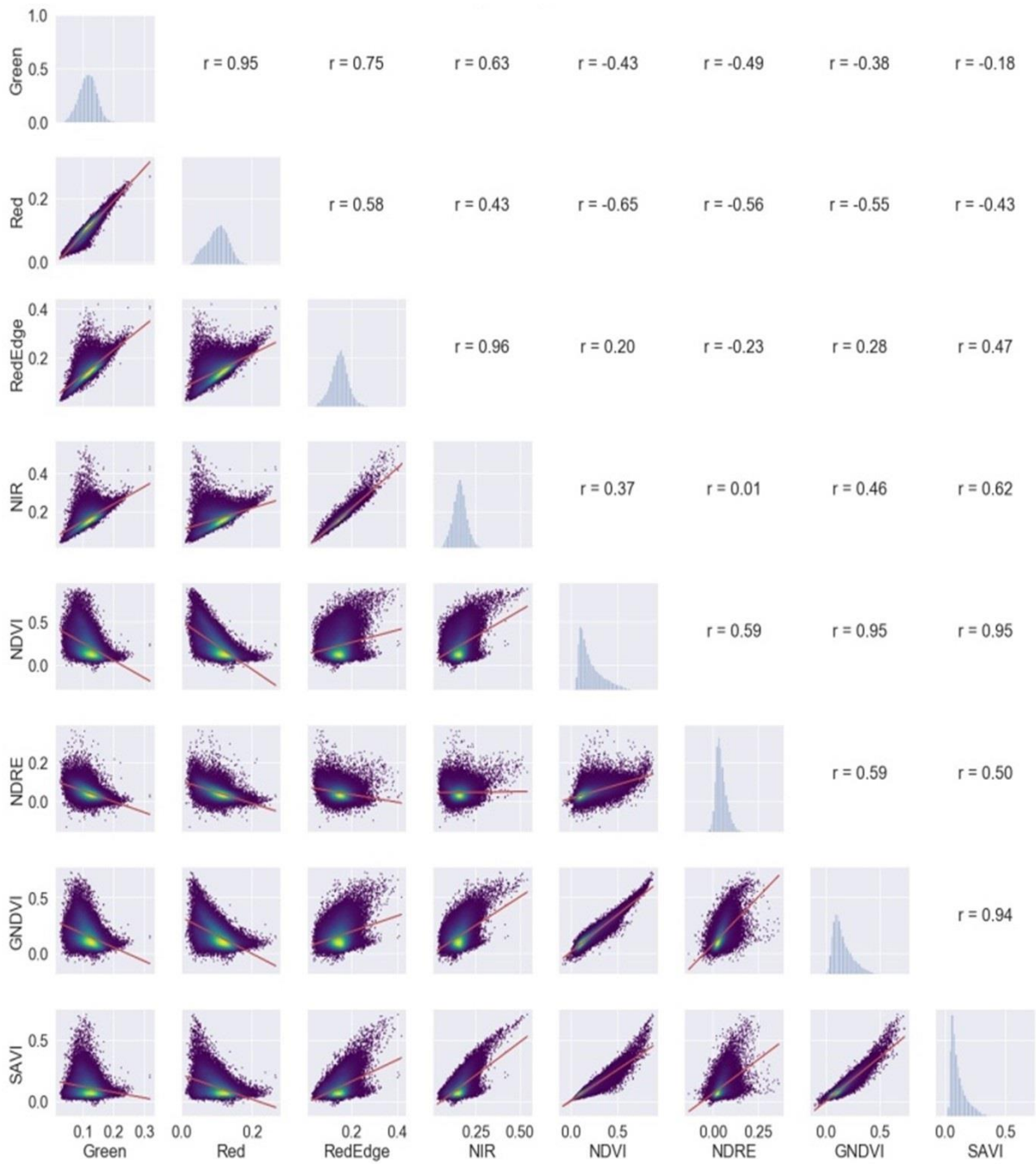


Figure 6.5 Scatter plots matrix showing the correlation between the four bands (Green, Red, Red edge, and NIR) and the four vegetation indices (VIs) analyzed (NDVI, NDRE, GNDVI, and SAVI). Dataset of 23 November 2018.

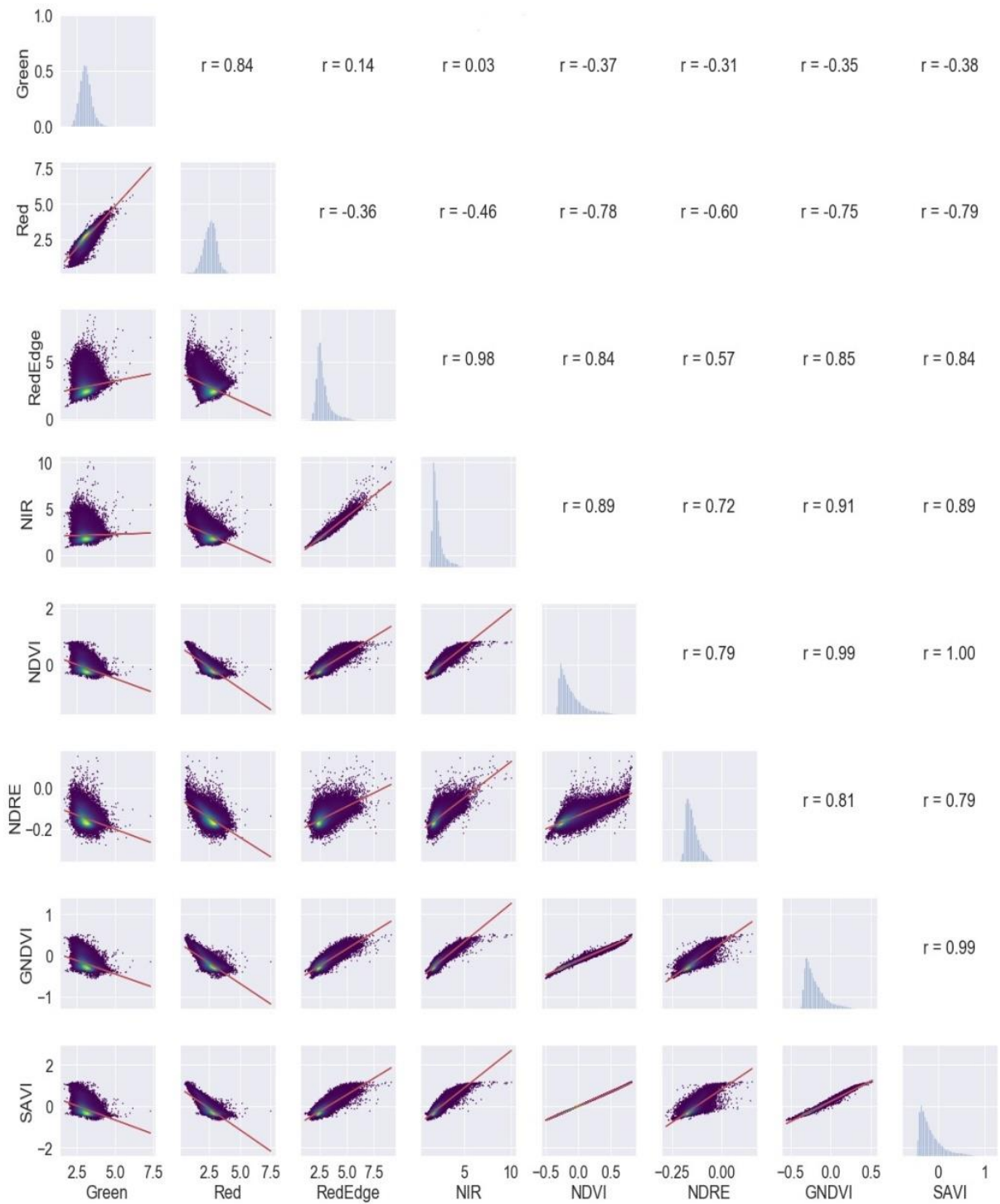


Figure 6.6 Scatter plots matrix showing the correlation between the four bands (Green, Red, Red edge, NIR) and the four vegetation indices (VIs) analyzed (NDVI, NDRE, GNDVI, and SAVI). Dataset of 19 December 2018.

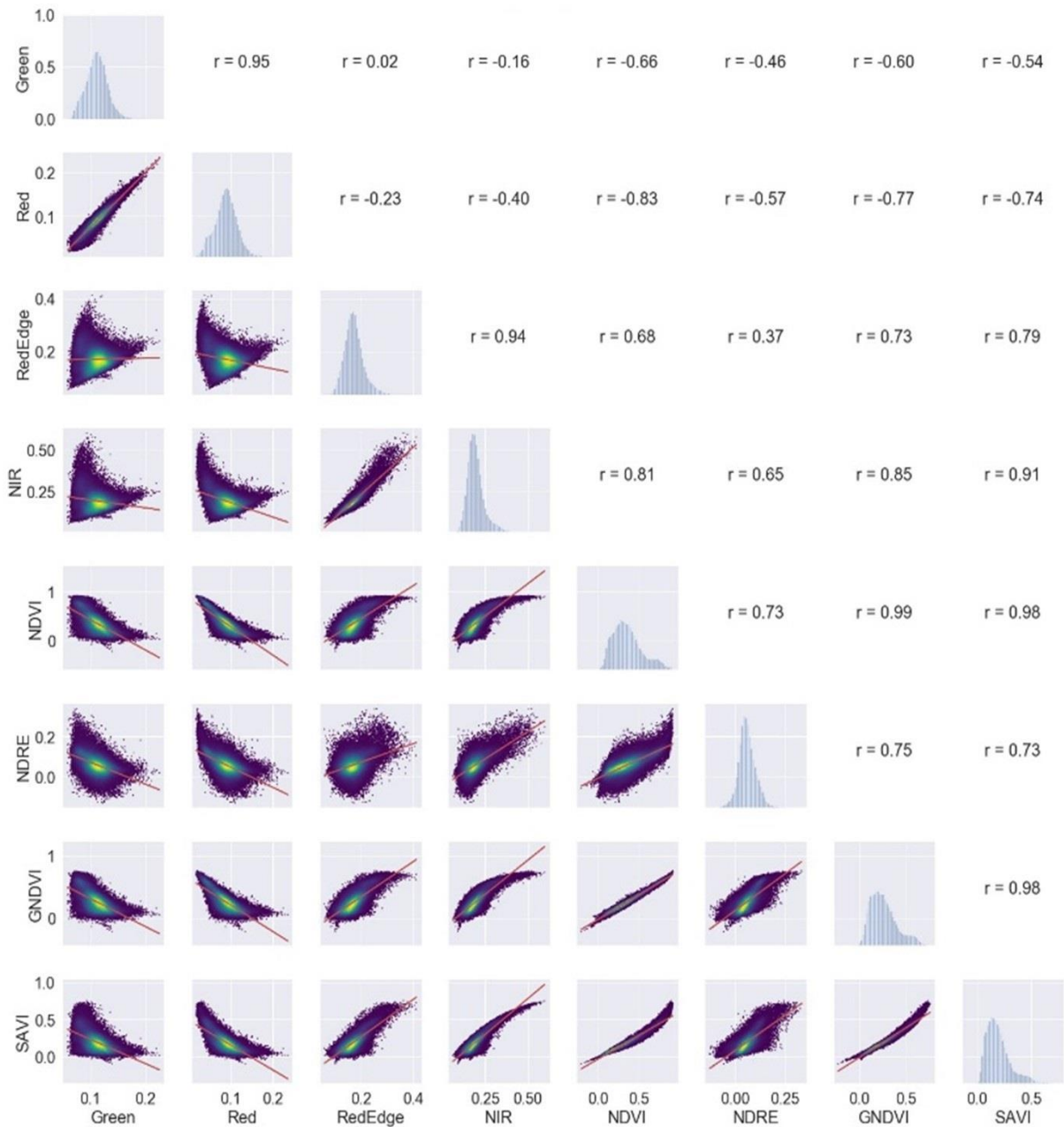


Figure 6.7 Scatter plots matrix showing the correlation between the four bands (Green, Red, Red edge, NIR) and the four vegetation indices (VIs) analyzed (NDVI, NDRE, GNDVI, and SAVI). Dataset of 18 January 2019.

SAVI calculated at the native MS band's resolution of each sensor is shown in Figure 6.8. Considering the imagery of November, UAV SAVI's value range from 0 to 0.4, PlanetScope SAVI's value range from 0.15 to 0.5, while Sentinel-2 SAVI's value range from 0.15 to 0.8. In December, UAV SAVI's value range from 0 to 0.7, PlanetScope SAVI's value range from 0.3 to 0.9, and Sentinel-2 SAVI's value range between 0.15 and 1. Lastly, in January, as far as the UAV is concerned, the range is similar to that of the previous month, while SAVI's value range between 0.15 and 0.8 and from 0.3 to 1 in PlanetScope and Sentinel-2, respectively.

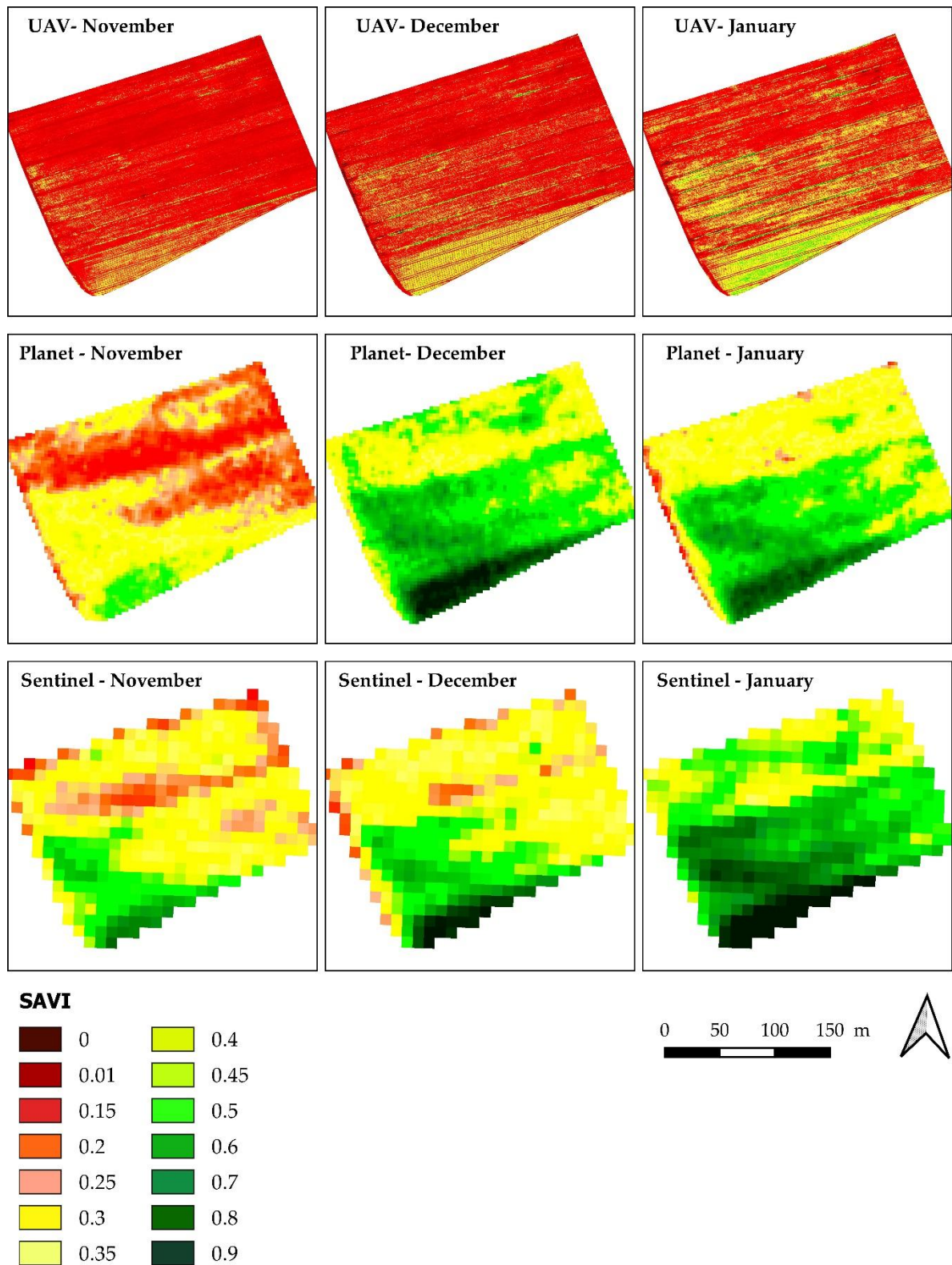


Figure 6.8 SAVI maps showing onion crop, derived from the platforms UAV (top), satellite PlanetScope (center), and Satellite Sentinel-2 (bottom) at their native resolutions (5 cm for UAV, 3 m for PlanetScope, and 10 m for Sentinel-2) (source, Messina et al., 2020c).

The histograms reported in Figure 6.9 show the frequency distribution of SAVI values as a percentage of the total values and the native resolution of each imagery. The histograms show interesting differences between the three platforms used and differences between the same platforms' datasets. In general, histograms showed a reduced range of UAV images compared to the broader ranges of PlanetScope and especially Sentinel-2.

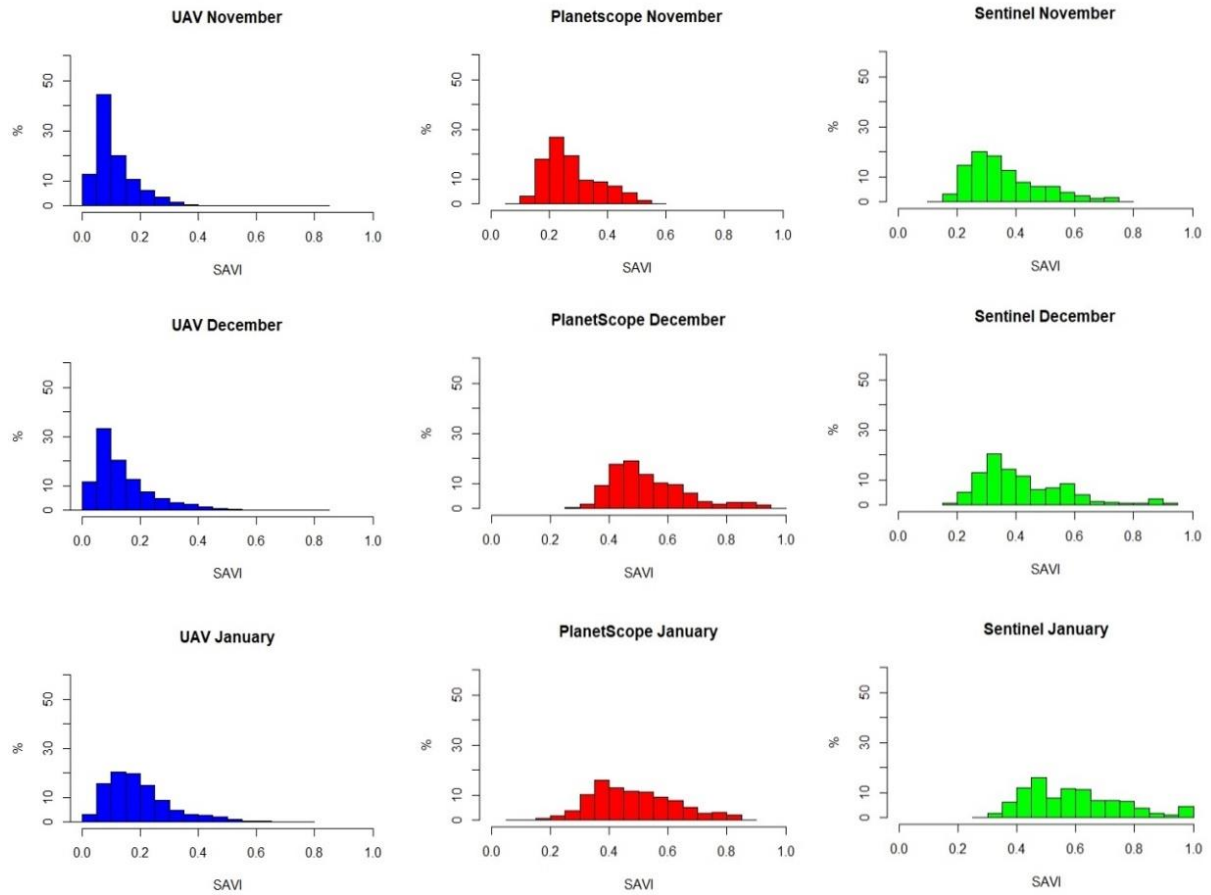


Figure 6.9 Histograms showing the distribution of SAVI values as a percentage of total values. The imagery of UAV is represented in blue, PlanetScope in red, and Sentinel-2 in green (*source*, Messina et al., 2020c).

UAV SAVI average has values of 0.11, 0.14, and 0.19 in November, December, and January, respectively (Table 6.3). As for PlanetScope images, the mean value of the SAVI is 0.27, 0.53, and 0.48 in November, December, and January, respectively. In Sentinel-2 images, the SAVI index's mean value is 0.36 in November, 0.42 in December, and 0.59 in January.

SAVI varied among different platforms, increasing its value from imagery with a higher resolution (UAV) to those with the lowest (Sentinel-2). However, even though the satellite and the UAV maps have different index ranges, it is possible to see some similarities in the distribution of vigor in the onion field. The SAVI values of UAV and PlanetScope showed a high correlation, with values

between 0.82 and 0.86 (Figure 6.10). Similar correlations resulted from the comparisons with Sentinel-2 imagery. This was highlighted by similarities in the localization of some areas of greater or lesser vigor of the field.

This is evident by imagining to divide the image into two parts: in the upper part, there are areas of less vigor, while in the lower part, there are areas of the field with high vigor. Therefore the satellites show that they are capable of assessing the general conditions of the field.

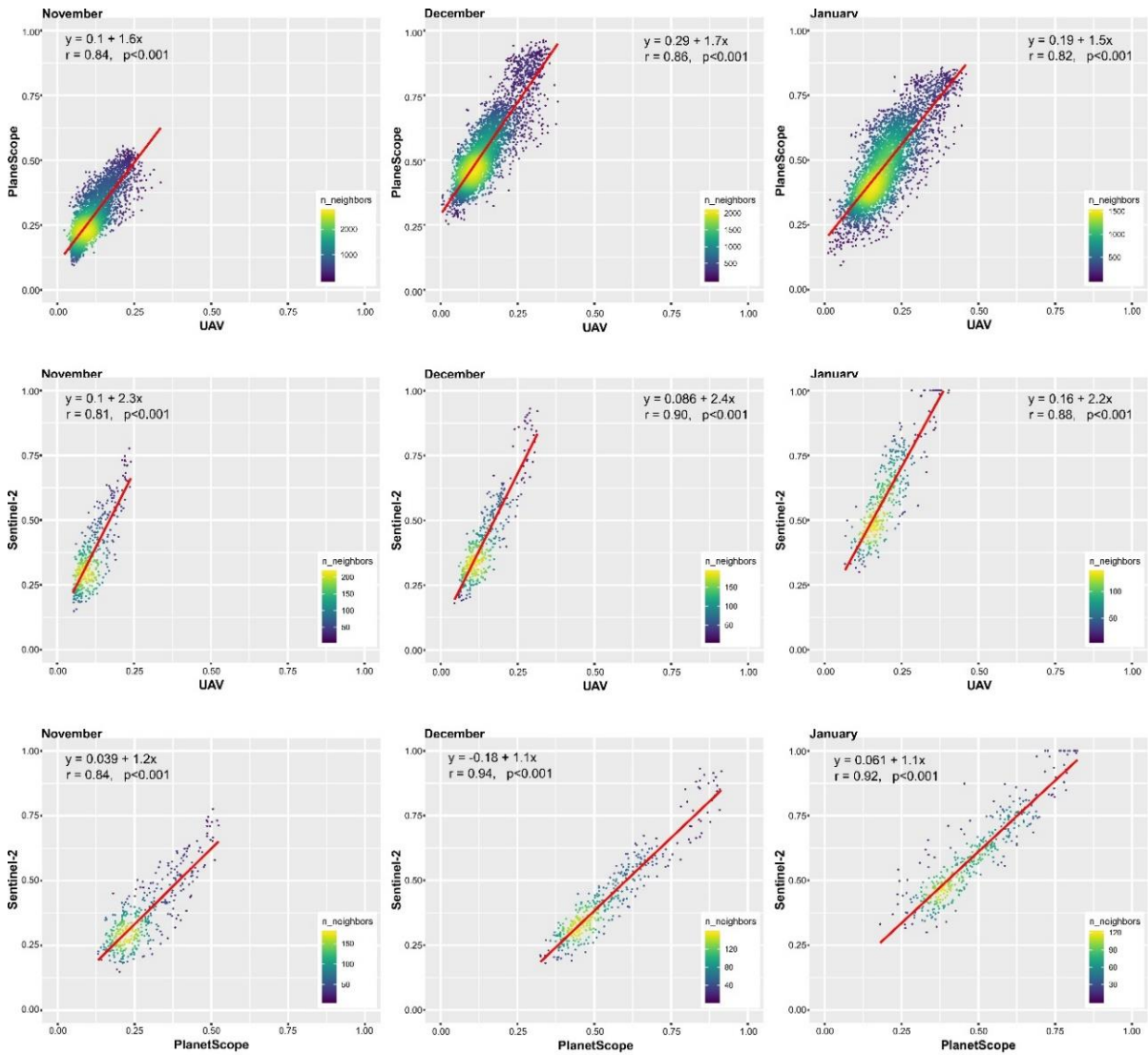


Figure 6.10 Scatter plots of SAVI values from the UAV, PlanetScope and Sentinel-2 (S2) map in three months surveyed (source, Messina et al., 2020c).

However, it is essential to remember that the heterogeneity of the surfaces analyzed in terms of land cover (rows, inter-rows, and paths) and the spatial resolution of Sentinel-2 imagery implies that a single pixel is made up for the most part of rows, inter-rows, and paths used for the passage of agricultural machines (Malacarne et al., 2018). Evaluating the three platforms' spectral

resolution, taking into account the coefficient of variation (CV), there is a clear difference between the CV of UAV images and that of satellites, as shown in Table 6.3. Considering the UAV imagery, CV has a value of 62% in November, 70% in December, and 55% in January, while the CV in satellite imagery ranges between 24% and 35% in the three months/datasets. In general, there is an increase of CV low (satellite) to high resolution (UAV) imagery. However, the increase in CV is not accompanied by a greater range of SAVI values in UAV images than those of the satellites. Higher standard deviation values also confirm this in satellite imagery than those of the UAV.

Table 6.3 Basic statistics considering images of the three platforms (UAV, PlanetScope, and Sentinel-2) at their original resolution.

Date	Platform	Number of pixels	SAVI mean	SAVI Standard deviation	SAVI CV (%)
November 2018	UAV	28,132,559	0.112	0.07	62.5
	PlanetScope	8,118	0.276	0.09	32.6
	Sentinel-2	696	0.360	0.12	33.3
December 2018	UAV	28,132,559	0.142	0.10	70.4
	PlanetScope	8,118	0.536	0.13	24.2
	Sentinel-2	696	0.420	0.15	35.7
January 2019	UAV	28,132,559	0.199	0.11	55.2
	PlanetScope	8,118	0.484	0.14	28.9
	Sentinel-2	696	0.590	0.16	27.1

The onion crop surveyed is a highly heterogeneous crop characterized by the alternation of plants (higher values), inter-rows and bare soil of background (lower values). The 5-cm very high-resolution of UAV images detected the oscillation of these values allowing a distinction between plants and soil. On the other hand, the discontinuity between plants and bare soil was not detected by the lower satellites' resolution that averages plants and bare soil reflectance values, therefore resulting in a narrow distribution.

Regarding the degree of correlation between pairs of SAVI maps based on Pearson's correlation coefficients, observing the coherence between SAVI maps of the UAV (resampled at 3 m) and PlanetScope satellite platforms (Figure 6.10), high correlations emerge in the three months with r index values of 0.84 in November, 0.86 in December, and 0.82 in January. A similar correlation was found when comparing Sentinel-2 and UAV in November (0.81). Higher values are that of December and January, 0.9 and 0.88, respectively. Comparing PlanetScope images with those of Sentinel-2 can be observed the highest correlation values each month, compared to previous

correlations with 0.84, 0.94, and 0.92 in November, December, and January, respectively. Indeed, even comparing visually at their respective resolutions (Figure 6.8), this was highlighted by similarities in the localization of some areas of greater or lesser vigor of the field.

The results obtained from the correlations of the UAV images resampled first at 3 m and then at 10 m, seem to indicate a certain coherence between the three platforms' information.

With the aim of obtaining a more comprehensive picture of the analyzed crop, the SAVI index was also calculated by classifying the onion crop and the soil separately, using the UAV imagery as reference. Therefore, on the one hand, we obtained crop pixels (i.e., SAVI onions) and, on the other hand, bare soil pixels observed in the inter-rows and the paths (i.e., SAVI soil). This allows taking into account the presence of mixed spectral pixels, dependent on the spatial resolution (Chuvieco, 2016) and more evident, considering the size of the pixels compared to the object of study, in PlanetScope and Sentinel-2 images.

Then, further correlation analyzes were performed to analyze platforms' ability to provide information on crop and soil. Observing the correlation between SAVI onions and PlaneScope (Figure 6.11), values are 0.61 in November, 0.84 in December, and 0.7 in January. The analysis of the correlation between SAVI onions and Sentinel-2 (Figure 6.11) showed the following values 0.63, 0.83, 0.77 in November, December, and January, respectively. The lower correlation in November values found with both satellites could be explained by a lower crop coverage compared to the soil, unlike December, where there is an increase in coverage.

Observing the correlation between SAVI soil and PlaneScope (Figure 6.12), values are 0.56 in November, 0.24 in December, and 0.28 in January. The analysis of the correlation between SAVI soil and Sentinel-2 (Figure 6.12) showed similar following values 0.55, 0.31, 0.25 in November, December, and January, respectively. The correlation values in December and January are quite similar, while the highest value was found in November. This probably confirms what was said before, considering that in November, the bare soil is prevalent within the scene compared to the crop. The results obtained confirm what was shown in Khaliq et al. (2019). In particular, satellite imagery shows some limitations indirectly providing reliable information concerning the status of the crops where the crop radiometric information can be altered by the presence of other sources like the soil, in this case, which in November is predominant. In the following months, lower correlation values are due to a smaller presence of bare soil, compared to parts of the field completely covered or sporadically covered by the crop.

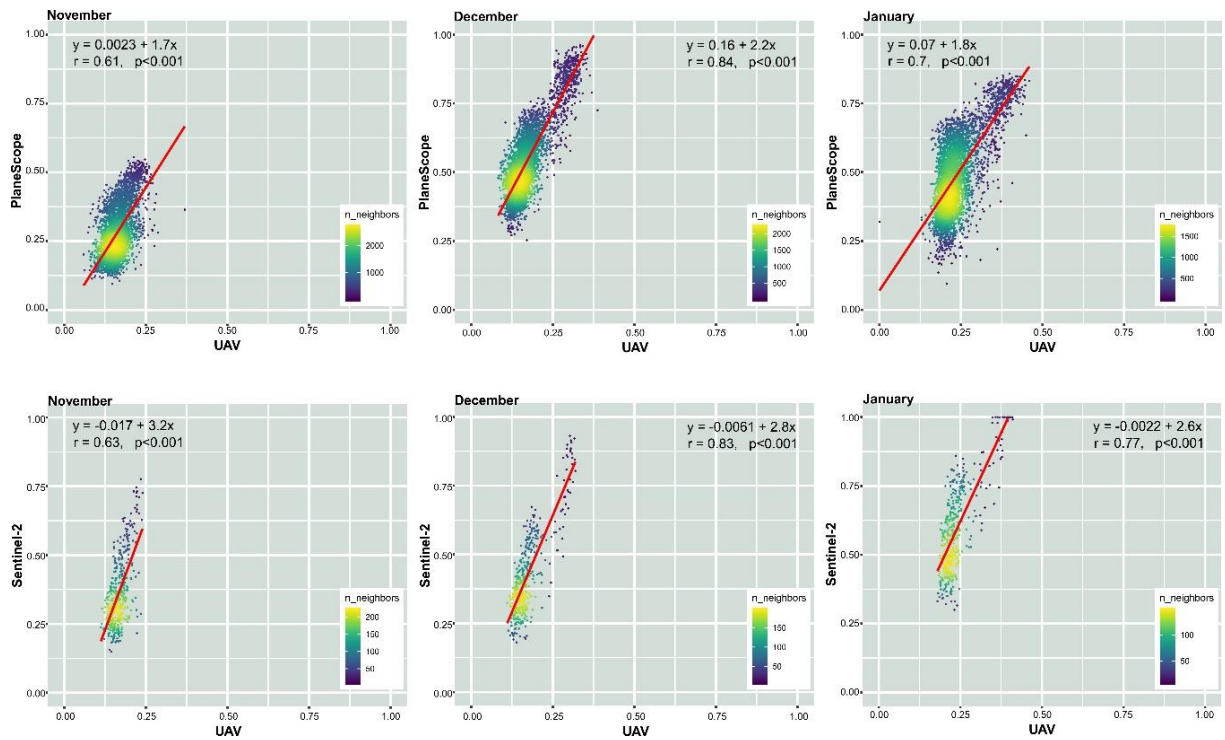


Figure 6.11 Scatter plots of SAVI values from UAV onions mask (SAVI onions) (x-axis), PlanetScope and Sentinel-2 maps in the three months surveyed (*source*, Messina et al., 2020c).

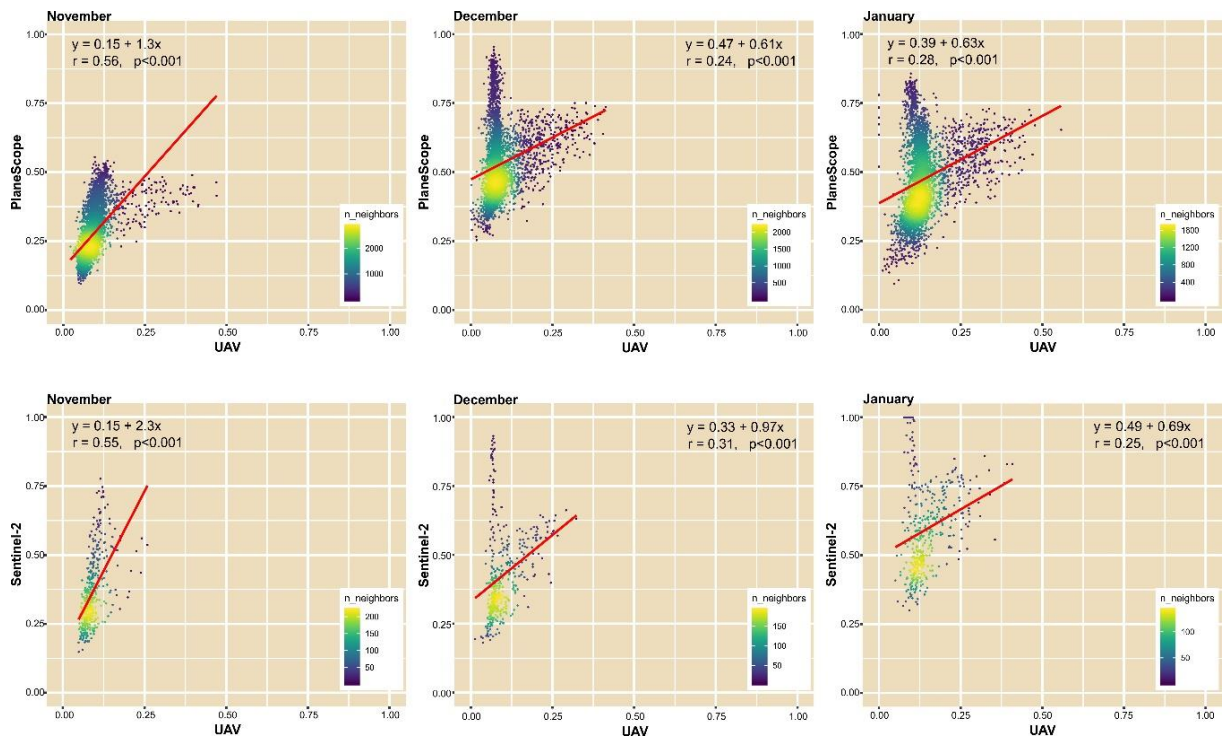


Figure 6.12 Scatter plots of SAVI values from UAV considering only soil pixels (SAVI soil) (x-axis), PlanetScope and Sentinel-2 maps in the three months surveyed (*source*, Messina et al., 2020c).

The aspect of the influence exerted by the different types of coverage on the pixel signal is related to spectral mixing pixels. This is a problem that concerns lower resolution images, i.e., those of PlanetScope and Sentinel-2.

Using the onion class mask extracted from the UAV images, the percentage of area occupied by vegetation (onion) within the PlanetScope and Sentinel-2 pixels was calculated and showed in Figure 6.13. Pixels in orange contain a percentage of the pixel area occupied by vegetation between 0 and 10% and can be assimilated to bare soil's pure pixels. On the other hand, pixels in dark green can be assimilated, with a percentage of the pixel area occupied by vegetation between 90 and 100%, to pure vegetation pixels. The remaining pixels, colored with different shades of green, are mixed pixels. A preponderant presence of orange pixels and, therefore, bare soil is easily visible in PlanetScope and Sentinel-2's maps of November.

On the other hand, pure pixels of vegetation are mostly present in the maps of the following months, as a natural consequence of the cultivation cycle course. During these months, where the crop is regularly growing and the underlying soil cover capacity is improved, there are many pure vegetation pixels. This happens especially in PlanetScope images, whose pixels cover an area of 9 m² each. After all, the smaller the pixel size, the less likely it is that a pixel contains more coverage types. Fewer pure pixels are present in Sentinel-2 images whose pixels have a size of 10 m x 10 m.

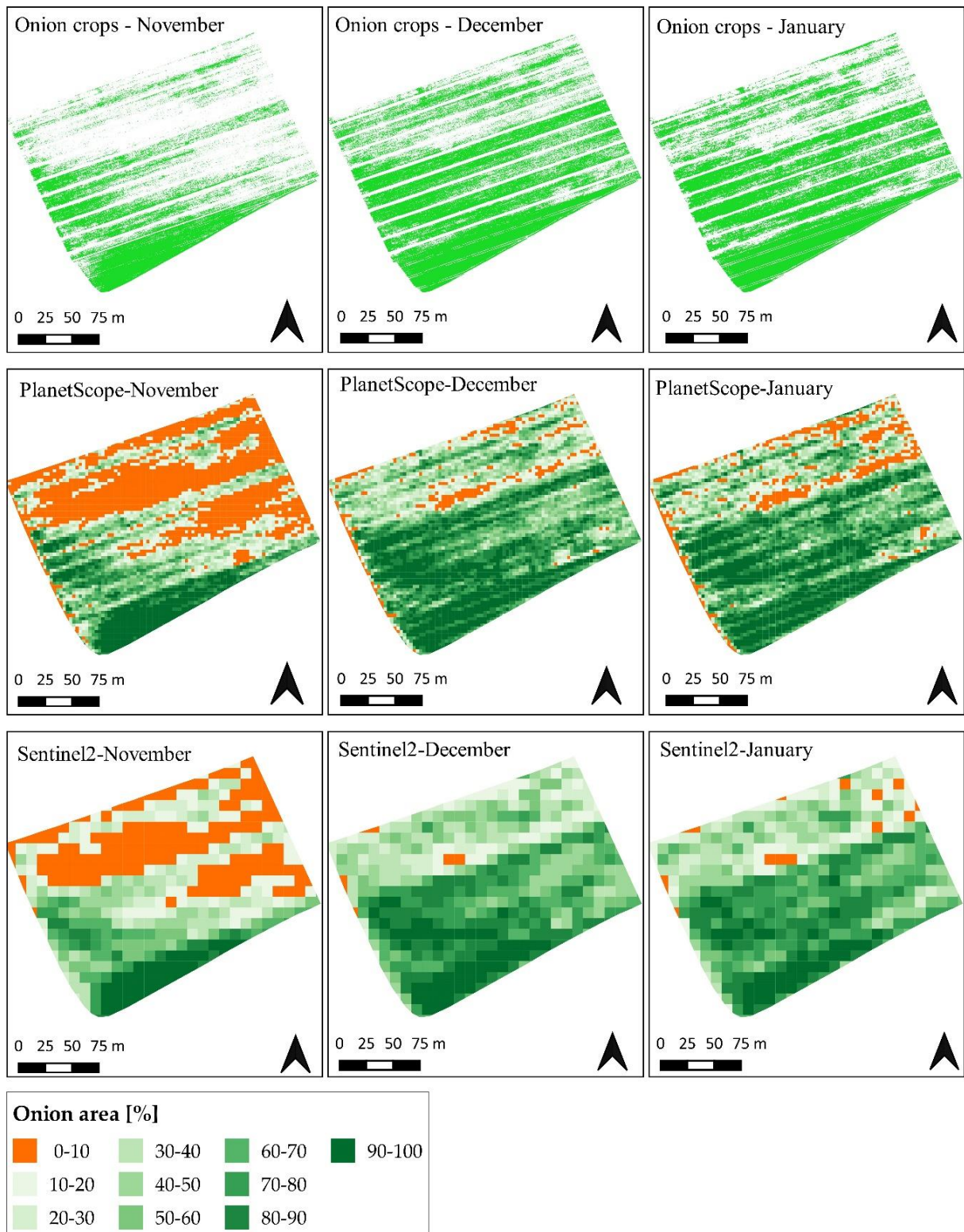


Figure 6.13 Maps showing onion crop area, derived from the UAV imagery (top), and the percentage of area covered by onion crop within PlanetScope's (center), and Sentinel-2's (bottom) pixels at their native resolutions (3 m for PlanetScope, and 10 m for Sentinel-2) (*source*, Messina et al., 2020c).

A correlation analysis between SAVI values and the percentage of area covered by onion crop within PlanetScope's, and Sentinel-2's pixels was performed in order to deepen the aspect related to the presence of mixed pixels (Figure 6.14). Regarding PlanetScope images, the highest value was that of November with 0.86, probably explained by a predominant presence of bare soil's pure pixels. In the following months, the value obtained is 0.7; fewer bare soil pixels are present, but the pure pixels of vegetation increase. This trend is similar in the correlation between Sentinel-2 images, but the values are lower: 0.74 in November, 0.6 in December, and 0.59 in January. In these images, the problem of mixed pixels is more pronounced.

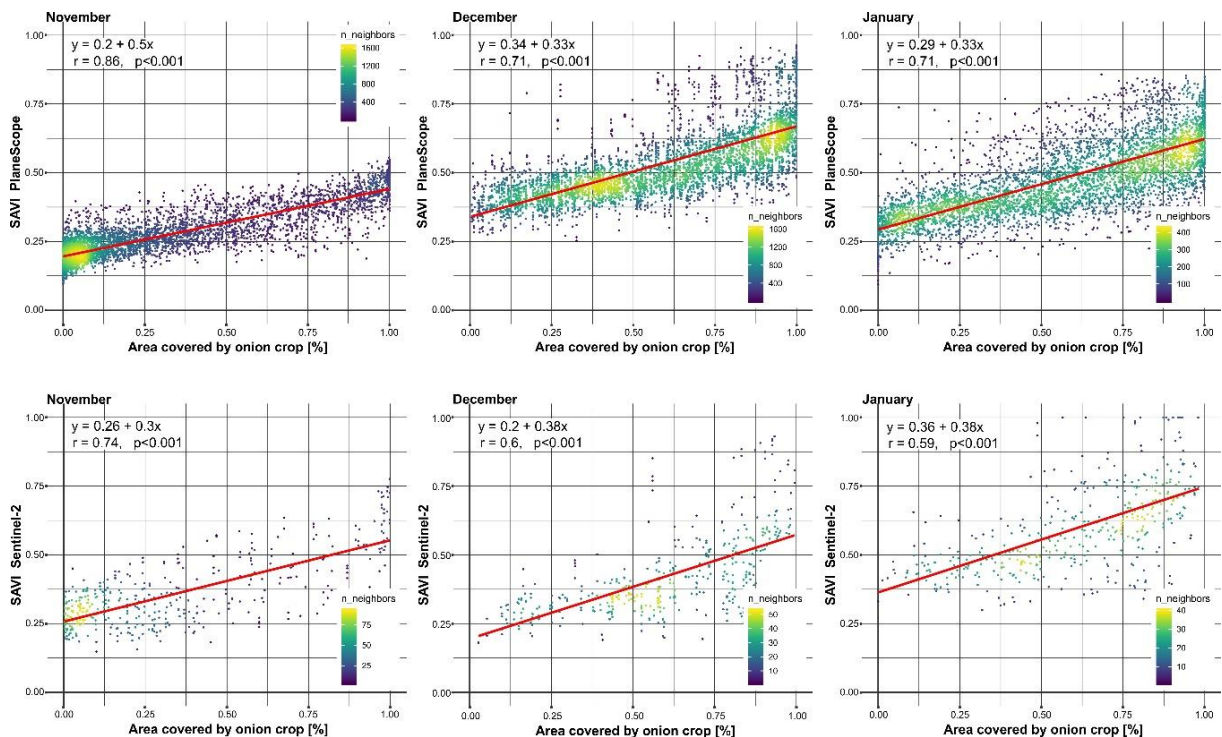


Figure 6.14 Scatter plots showing the correlation between SAVI values from satellites and the area covered by onion crop (x-axis) in the three months surveyed (source, Messina et al., 2020c).

Finally, we produced the SAVI maps using the images surveyed of the three months and all the three platforms (Figure 6.15). With this aim, the UAV and PlanetScope maps were resampled at Sentinel-2's 10 m geometrical resolution.

Looking at the map, the main effect of resampling UAV images is evident: the impossibility of distinguishing the details, which permit to discriminate among the crop, the soil, and the inter-rows. The resampling of the UAV images to a coarser spatial resolution, resulting in fewer pixels, has as its main visible consequence the loss of information related to the different SAVI values of rows, inter-rows, and paths. Indeed, the upscaling of spatial resolution has the consequence of erasing the original data's details (Jones and Vaughan, 2010). Increasing pixel size determines the

decreasing of spatial variability of a vegetation index, as shown in Tarnavsky et al. (2008). Besides, radiometric resolution influence VIs' dynamic range. Indeed, observing SAVI in Figure 6.15, differences between platforms in the range of the index values appear immediately evident. What is evident at first glance is the difference between the SAVI values of the UAV images compared to the images of the two satellites, resulting from lower spectral variability in UAV images.

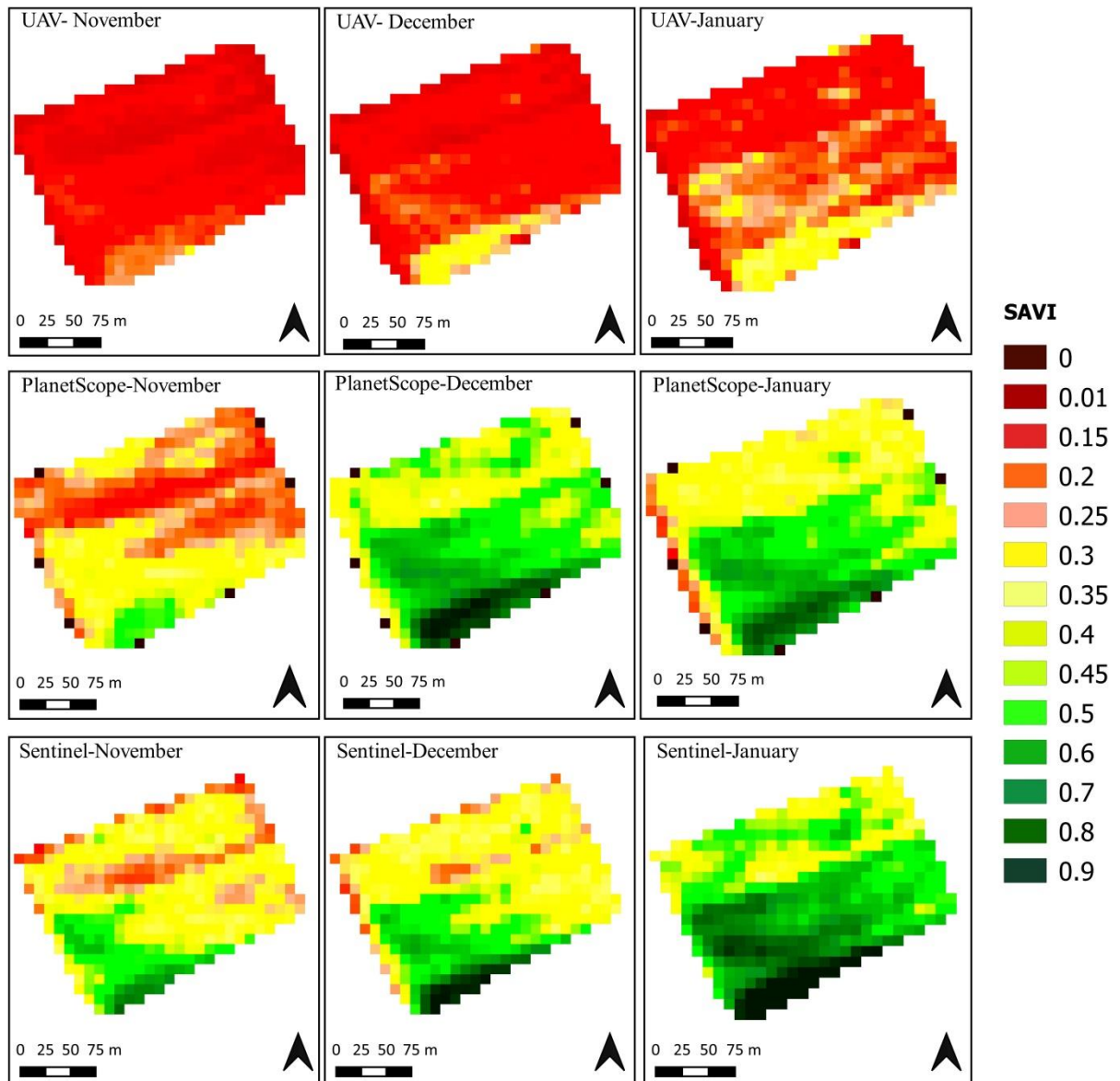


Figure 6.15 SAVI maps showing onion crop with 10 m resolution, derived from the platforms UAV (top), satellite PlanetScope (center), and Satellite Sentinel-2 (bottom) (*source*, Messina et al., 2020c).

As far as UAV images are concerned, the lowest values are close to 0, while the highest values are 0.3 in November and December and 0.4 in January. Looking at the PlanetScope images instead, the highest values reached by the SAVI are 0.5, 0.9, and 0.8 in November, December, and January,

respectively. In the Sentinel-2 images, there are minimum values higher than those of the other platforms, between 0.2 (from November) and 0.3 (in January). The maximum values reached by the SAVI are 0.7, 0.9, and 1 in November, December, and January, respectively. One important aspect must be stressed. The SAVI trend, proceeding from November, two months after the transplantation, until January, the period close to the onion harvest, is the same regardless of the platform used. The same trend was confirmed by comparing the bands of the SAVI highlighted in trend was confirmed by comparing the bands of the SAVI highlighted in the spectral signatures derived from pure pixels of onion in the three periods (Figure 6.16). The SAVI increased progressively from November to December and January.

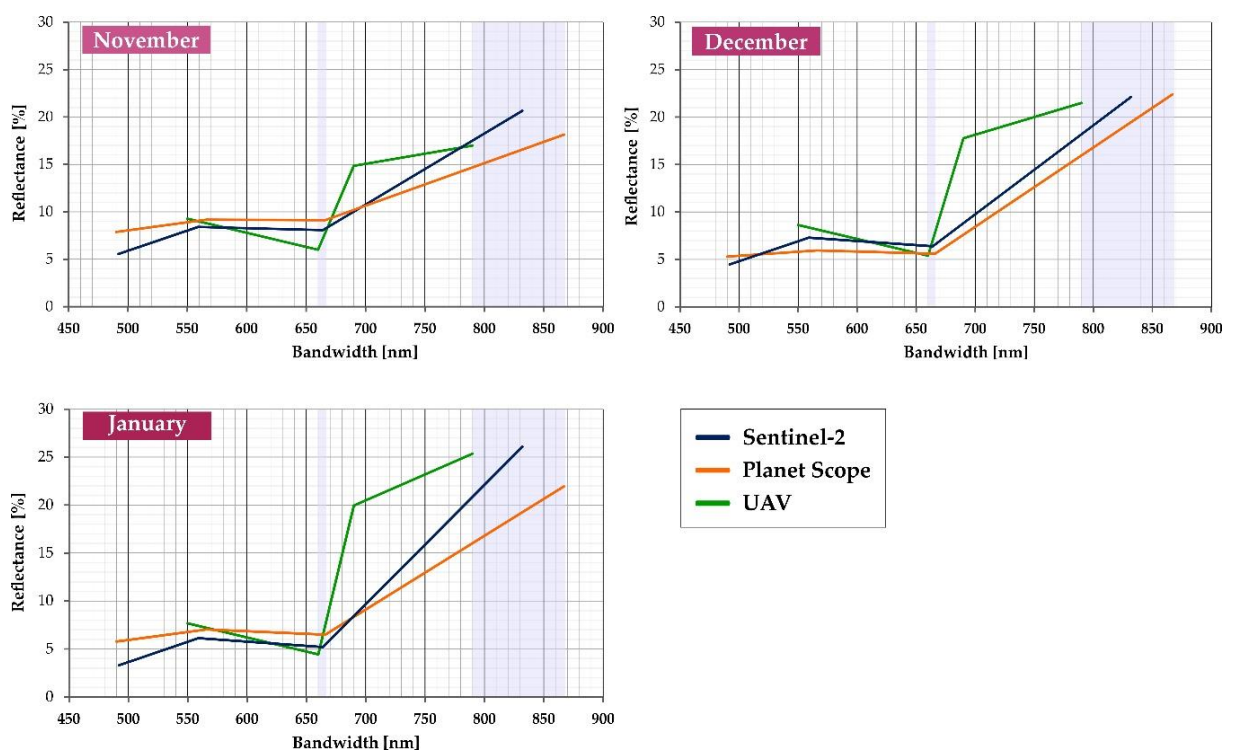


Figure 6.16 The spectral signature of onion crop derived from the reflectance data of pure onion pixels for the three platforms in the three periods surveyed (November, December, and January). The shaded light violet indicates the region of the two bands used for the soil adjusted vegetation index (SAVI) calculation (red and near-infrared, NIR) (*source*, Messina et al., 2020c).

This aspect appears less apparent when looking at the UAV images resampled due to the loss of information. However, the SAVI calculated on the satellites' lower resolution images has higher values, from the dominant green color of the relevant vigor maps. While it is not clear how differences in spatial resolution affect VIs values under field conditions, some studies demonstrated this effect by comparing different satellites (Abuzar, 2014; Anderson et al., 2011; Goward et al., 2003; Psomiadis et al., 2016; Soudani et al., 2006; Xu and Zhang, 2010) showing that

VIs values are higher in coarser spatial resolution images. Factors responsible for inter-sensor VIs variations can be several (Abuzar, 2014). Firstly, is the calibration procedure that may cause inter-sensor SAVI variations. Calibration provides precision and correctness to the data derived from a sensor so that all the datasets obtained from the same sensor can be compared. For calibration, including those useful for radiometric correction, algorithms are different between one sensor and another. These uncertainties remain when VIs produced by different sensors are compared (Miura et al., 2008; Yin et al., 2012). However, as far as the calibration aspect is concerned, Sentinel-2's images are better than PlanetScope (Li et al., 2020). Obviously, the technological differences between the UAVs' sensors and those present on the satellites cannot be ignored. Other variation can be due to the lack of bandwidth correspondence, as shown in Gallo and Daughtry (1987) and Teillet et al. (1997). Besides, the differences in the spatial and radiometric resolution of the several sensors must also be taken into account (Abuzar, 2014). Therefore, since several factors are responsible for the differences between the sensors concerning the values of the vegetation indexes, it must be taken into account that these differences are not necessarily attributable to a single factor. It is rather prudent to consider all the cumulative effects of factors on VIs (Abuzar, 2014).

In addition to the maps with 10 m resolution, another was made, including the SAVI computed only on the onion crop. This was done in order to evaluate the contribution made by the UAV images. As shown, the UAV images proved useful for a separation between vegetation and soil, where, due to obvious limitations (related to the size of individual plants) due to the satellites' spatial resolution. The maps were produced using the masks produced on eCognition, already shown in Figure 6.17. In particular, the masks obtained by exporting a vector file containing only the class "onions", were applied to the UAV images at their native resolution with the aim to obtain only parts of orthomosaics concerning onion crop. As a result, parts of the scene occupied by soil are excluded from the onion's map.

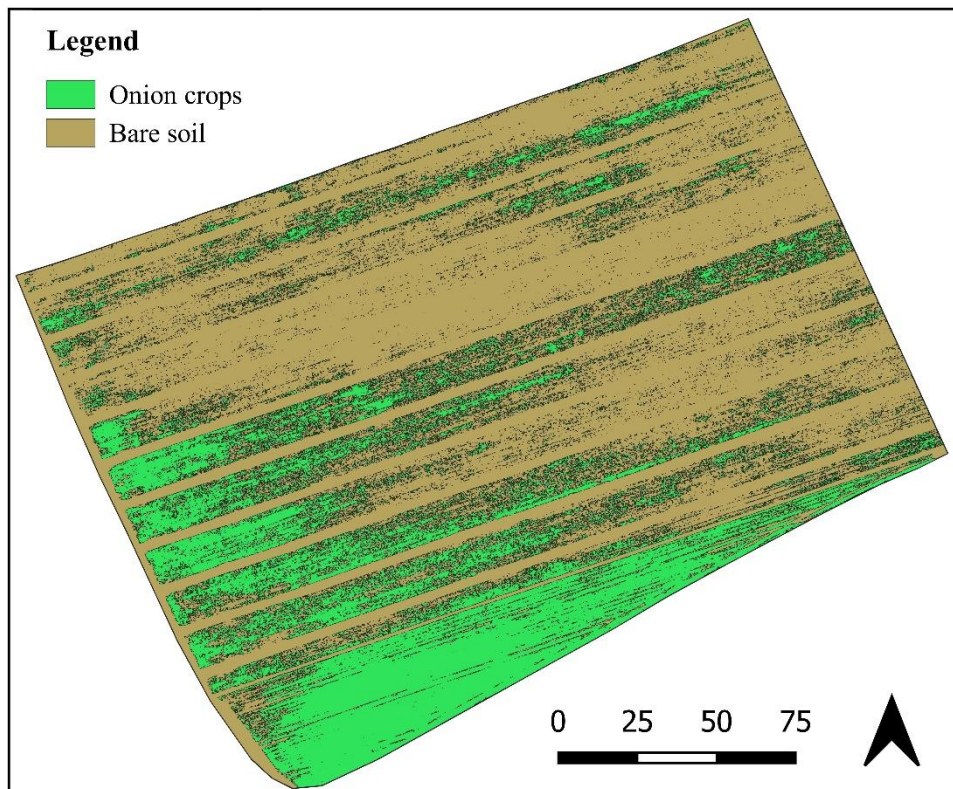


Figure 6.17 A map showing the image-object classification of bare soil (in brown) and onions (in green) performed using eCognition Developer. Dataset of 23 November 2018 (*source*, Messina et al., 2020c).

Observing SAVI maps (Figure 6.18), applied to UAV images, considering only the part of the imagery occupied by onion crop, the index for three months surveyed is between 0 and 0.9. The values for November are the lowest. This could be since the crop is still in the early stages of the cultivation cycle. Besides, during the segmentation phase, the software could not correctly separate the vegetation from the background. It is conceivable that the lower values in the map can be traced back to the underlying terrain. Considering the map of December, the values are higher than the previous month. In the portion of the field where the transplant took place in mid-September, the index values are lower and are between 0.15 and 0.45. There are also evident areas where vegetation is challenging to grow, as shown in Messina et al. (2020a). In the portion of the field in an advanced stage of cultivation, the values are higher. In particular, the values are between 0.45 and 0.9. The contrast of colors between the two areas of the field with different transplanting times is evident. The January map shows an increase in SAVI values where the crop is at a near harvest stage.

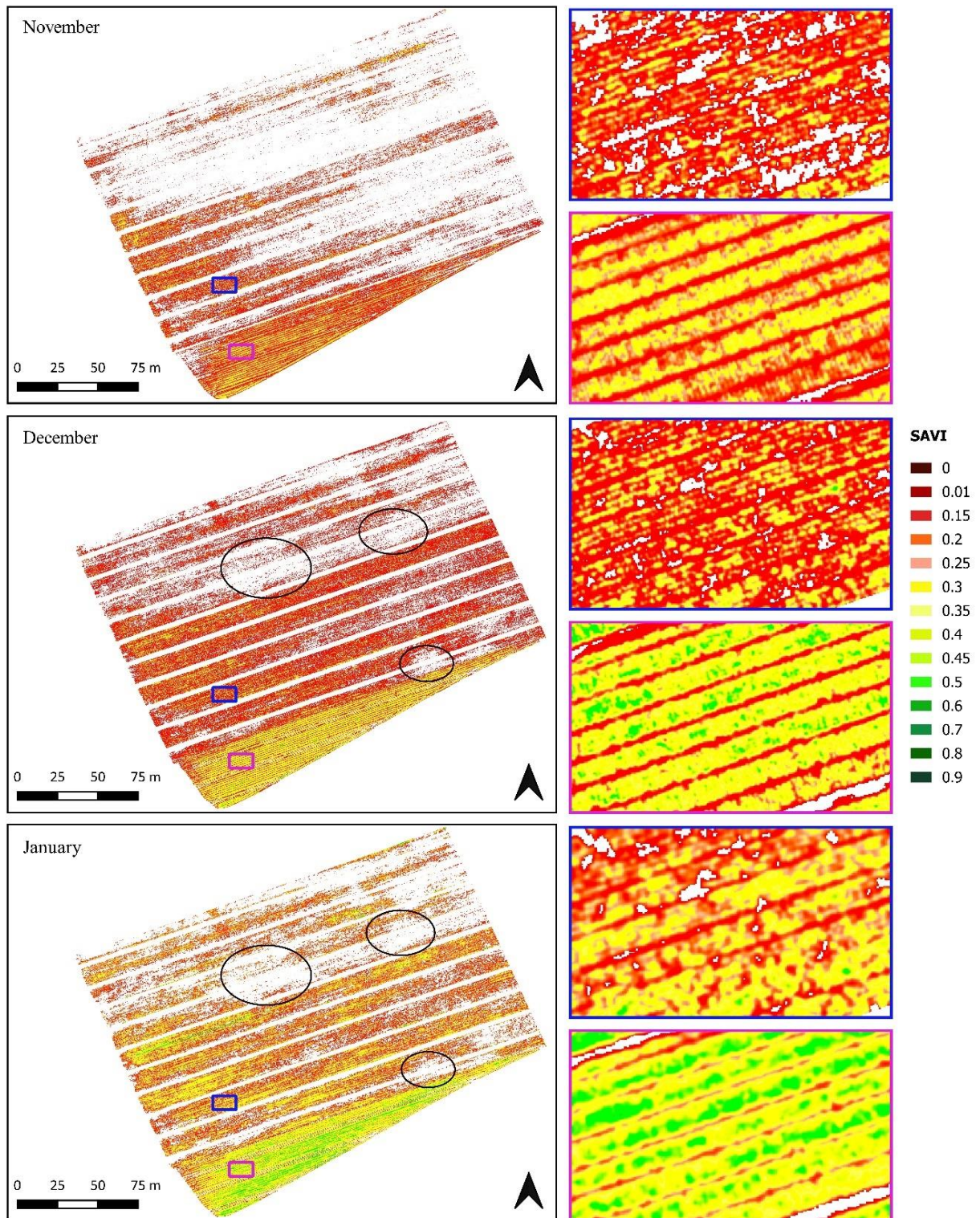


Figure 6.18 SAVI maps from November 2018 (top) to January 2019 (bottom). Next to each dataset's image, blue and magenta rectangles magnify the details of onion crops' vegetative vigor in two different parts of the field and where the transplanting took place three weeks apart. The ellipses highlight areas of the field where the onion crops are absent or have had difficulty growing (*source*, Messina et al., 2020c).

Vigor maps produced are useful to investigate areas of the field where the crop is struggling to grow, providing the farmer with potentially helpful information. Indeed, as shown in Figure 6.18, we can well distinguish areas (white, in the absence of data) where the crop seems not to be present. In November, this area is higher than in the following months. Being in the month of November at the initial stages of growth, many plants, probably still too small, were not identified by the classification software and also given the structure of the epigeal part of the onion, especially in this phase would have required a resolution equal to or higher than 4 cm. In fact, in December, many of the voids present in November were filled. However, some areas of the field where the crop is absent remain circled in black. These voids persist in January and probably indicate a problem of stunted growth due to several possible causes. These causes may be attributable to the action of abiotic agents such as water stagnation, nutrient deficiency, or maybe the presence of a disease. In essence, beyond the values assumed by the index, the UAV has risen usefully and is able to identify the individual plants. Where this has not happened, we find voids. These voids can be explained either by the complete absence of the plants or by poorly cultivated plants or have had difficulty growing. So these vigor maps indirectly provide an indication to the farmer. This information could be used, for example, for localized fertilization or the grubbing up of diseased plants.

When comparing the strength maps of the different platforms, the satellites, considering the altitude in which they are located, provide images characterized by a coarser resolution but applicable for monitoring large areas and still able to recognize the variation in vegetation growth and health crop status (Huete et al., 1997). Besides, as shown in this study, they are often characterized by a higher spectral variability and greater temporal and spatial reliability in the range of values assumed by the index, also taking into account a consolidated (in the case of Sentinel-2) calibration method. In addition, the SWIR band with which Sentinel-2 is equipped allows the calculation of other indices useful for monitoring, such as the Normalized Difference Moisture Index (NDMI) (Wilson and Sader, 2002).

On the other hand, low altitude RS by using UAV is confirmed to be a useful tool in PA. In PA, considering agricultural monitoring, repeatable and timely information on variability within the field has a specific utility (Moran et al., 2000; Zhang et al., 2002) as it allows to optimize production efficiency through sustainable and spatially explicit management practices (Gebbers and Adamchuk, 2010; Robert, 2002). In the present case study, some details of Figure 6.18 were made evident only by the UAV images' vigor map. This is evident given the inability of satellites to

discriminate against specific details of the field, such as inter-row paths, as also shown in (Khaliq et al., 2019; Matese et al., 2015; Pádua et al., 2019), which implies that the value of a VI within a pixel is necessarily derived from the average of the crop and inter-row information. It is also necessary to consider the limits due to their spatial resolution, which prevents satellites from highlighting problems located in areas whose area is less than the minimum identifiable by them.

6.3 Conclusions

This chapter dealt with a comparison between images of onion crops derived from three different platforms, a UAV and two satellites, one free medium resolution platform, and the other low-cost, high resolution. The comparison was mainly based on the analysis of the spatial resolution differences and the effects they may have on data quality in a PA context. For this reason, vigor maps were generated, using the SAVI index, and resampled at the lowest resolution of the satellite Sentinel-2.

Regarding the comparison between UAVs and satellites, the introduction of relatively new platforms, including nano-satellites, equipped with sensors that provide high or ultra-high resolution images, less than 3 m and 1 m respectively, makes satellites increasingly competitive with UAVs in PA applications. The feature that makes the latter unique is that they can mount several types of sensors simultaneously (Maes and Steppe, 2019). Otherwise, considering all the platforms available, there is probably not yet one that can provide high spectral, spatial, and temporal resolution images (J. Zhang et al., 2019). Currently, simultaneous requirements for ultra-high spatial resolution images (<10 m) with almost daily time resolution can only be met by targeted acquisition via commercial programmable multi-sensor systems such as WorldView with an MS resolution of about 1 m. Simultaneously, Sentinel-2 is currently the finest resolution MS imaging mission in open source image data. In the case study, taking into account the crop characteristics, a resolution of less than or equal to one meter is preferable for more accurate data collection.

This case study confirms the results of other studies that have highlighted the role of high-resolution satellites in crop monitoring on a large scale. On the other hand, some limitations and uncertainties emerged in this case study where there is a need to discriminate localized conditions of inhomogeneity in the field, determined by abiotic or biotic stresses. This can be important in order to plan remedial interventions such as localized application of pesticides, herbicides, and

fertilizers. In this case, the images provided by UAVs make the difference proving to be useful in guiding agronomic localized operations such as fertilization and phytosanitary treatments. In the present case study, the monitoring regarded a crop such as onion, characterized mainly in the early stages of the crop cycle by the small size and a non-homogeneous soil cover capacity. It is necessary to specify that better monitoring with UAVs could be obtained with higher resolution images than the one used, below 4 cm. As for a more accurate comparison of the quality of the data provided on the vegetation index values, it would be interesting to make a further comparison, in the same context, by including higher-priced cameras. Considering the overall results of the comparison carried out, it emerges that the contribution made by each platform must be regarded as complementary to that made by the other and not sufficient by itself in accurate monitoring of the crop under study. This is true in light of the limitations shown by each platform.

Considering contexts similar to the one presented, the frequent use of the UAV for weekly monitoring could be uncomfortable and expensive if executed in several fields, perhaps not too large and spaced out from each other. In this regard, in these cases, it would be easier to use satellite images to check the general conditions of the field, interspersed with the use of more detailed UAV images at critical moments in the crop cycle. The advisable solution is not the use and preference of one platform over another. Therefore, combining different platforms, taking into account the level of information quality that each one can give, is desirable when the proper technical knowledge is available. To overcome the limitations of all the platforms described above, it would be desirable to combine UAV images (preferable with higher than 4 cm of resolution) with high-resolution satellite images to improve the overall quality of the final products. To be able to deepen the aspect related to the comparison between the different platforms, it would also be interesting to test the proposed approach on other crops.

7 General conclusions

In the present Ph.D. thesis, several case studies were collected, which involved the application of remote sensing (RS) techniques to monitor herbaceous and tree crops of primary interest in the Calabria region (Italy). In particular, several RS platforms were used, including UAVs, in monitoring the investigated study sites. The use of the UAV platform, mounting several types of sensors, demonstrated flexibility and reliability in photogrammetric reconstruction at the farming scale, using ultra-high-resolution images to obtain a reasonable reconstruction of the orchards and monitoring of the crop conditions. Obviously, for obtaining good results, good quality of UAV field surveys is a pre-condition. Therefore, during the individual surveys' execution, the correct UAV flight planning had a crucial role in obtaining satisfactory results. The same can be said about the field measures, such as the GCP laying (i.e., their number and correct distribution).

Semi-automatic workflows involved the use of unsupervised and supervised classification techniques applied on crops characterized by different dimension, spatial pattern, density, and crop management. Specifically, some workflows allowed to produce vigor maps by extracting the whole field as in the case of onions or only the parts of interest as in the case of olive, bergamot and clementine tree crowns. The results obtained showed several important commonalities and strengths despite the differences in approaches and cases addressed. The first strength and novelty of the proposed procedures relies on their replicability, reliability, speed and simplicity of the approaches. The second strength concerns the ability of implemented approaches to prove effective in different datasets characterized by heterogeneous agricultural contexts. The heterogeneity concerned several crop species, tree plantation distances and composition, different crop management, and different tree age, height, and crown diameters in the surveyed orchards, thus resulting in the scene's high spatial variability. Therefore, the heterogeneity within the analysed scenarios also concerned in some cases the different arrangement of crops, not always regular, combined, in some cases, with problems of overlap (between tree crowns), and the spectral similarity between the species of interest and or between them and weeds.

The promising results despite all the aspects and difficulties mentioned, proved that the proposed approaches could be applied to a wide range of vegetation types.

On the other hand, compared to traditional satellites, the introduction of other platforms, including nanosatellites, and equipped with sensors capable of offering very-high-resolution images of less than 3 m or the ultra-high resolution of fewer than 1 m, makes satellites increasingly competitive

concerning the use of UAVs in PA applications. For this purpose, a comparison has been made between images of onion crops derived from three different platforms, a UAV and two satellites, one free medium resolution platform, and the other low-cost, high resolution. The study was focused on the analysis of the spatial resolution differences and the effects they may have on data quality in a PA context. The results confirms the role of high-resolution satellites in crop monitoring on a large scale. However, some limitations and uncertainties emerged where there is a need to discriminate localized conditions of inhomogeneity in the field, thus proving UAVs make the difference in guiding agronomic localized operations.

As things stand and taking into account the results, when considering the different platforms and sensors of RS, no one is probably able to offer a high resolution in all spatial, spectral, and temporal dimensions. Therefore, it would be desirable to synergize UAV images with high-resolution satellite images to improve the quality of the final products to overcome these limits taking into account the level of information quality of each platform.

Concerning the time, the implemented workflows needed one or two working days of two good skilled operators in geomatics, starting from the on-field data collection to obtaining vigor maps. These characteristics are in line with the need of the PA to provide information, in a short time, useful to guide farmers' decisions. Considering the importance of PA for practical business uses, this work arises from the need to evaluate a quick, reliable, and repeatable approach for agricultural mapping. The results obtained in the case studies showed the potential of the approaches adopted in providing useful information to manage farm operations and guide farmers' decisions in PA. This was proved with promising results even in small and medium-sized farms, not necessarily characterized by crop parcels of very large dimensions. Notwithstanding this aspect, an increasing use of RS tools, techniques and data, even if limited and aimed at monitoring and carrying out certain crop operations, brings undoubted benefits to the farm and is a fundamental step towards the agriculture of the future.

Acknowledgements

At the end of this course of study, first of all I thank Prof. Giuseppe Modica for guiding me in the realization of this thesis.

I thank José Peña for his teachings during my time abroad in Madrid.

Thanks to the members of the Rural group (Rural Architecture and Landscape) of the Department of Agriculture of the Mediterranea University of Reggio Calabria, Giandomenico De Luca and Salvatore Praticò, for their contribution.

I also want to thank Prof. Salvatore Di Fazio for the valuable advice he gave me during my PhD experience.

8 LIST OF FIGURES

Figure 1.1 Olive orchard.

Figure 1.2 Total area and production in Italy and Calabria and related percentages.

Figure 1.3 Total area and production in Italy and Calabria's provinces expressed in percentage.

Figure 1.4 Bergamot orchard (top) and fruits at different degrees of ripeness (below).

Figure 1.5 Trees and clementine fruits.

Figure 1.6 Total area and production in Italy and Calabria and related percentages.

Figure 1.7 Map of Calabria with the municipalities belonging to the production area of "Clementine di Calabria IGP" highlighted in yellow.

Figure 1.8 Total area and production in Italy and Calabria's provinces expressed in percentage.

Figure 1.9 Onions on the field (left) and onions "Cipolla Rossa di Tropea" (right).

Figure 1.10 Map of Calabria with the municipalities belonging to the production area of "Cipolla di Tropea IGP" highlighted in orange..

Figure 1.11 Total area and production in Italy and Calabria's provinces expressed in percentage.

Figure 2.1 The electromagnetic spectrum. In evidence, the visible region, in which the three bands blue, green and red ($0.4 - 0.7 \mu\text{m}$) are further detailed.

Figure 2.2 The electromagnetic radiation's components according to the wave theory of light.

Figure 2.3 The electromagnetic spectrum. In evidence, the infrared region (IR), in which the reflected-IR ($0.7-3.0 \mu\text{m}$) and the emitted-IR ($3.0-100 \mu\text{m}$) are further detailed (Messina and Modica, 2020b).

Figure 2.4 Atmospheric transmittance in the thermal region with typical absorption bands induced by gases and water (*source* (Messina and Modica, 2020b) modified from (Richter and Schlapfer, 2019)).

Figure 2.5 Typical spectral signatures of a healthy and stressed plant (micasense.com).

Figure 2.6 Interaction of electromagnetic energy in the different leaf layers.

Figure 2.7 Typical spectral signature of different types of soil (Jones and Vaughan, 2010).

Figure 2.8 Types of surface reflection.

Figure 2.9 UAV quadcopter DJI Phantom 4 Pro.

Figure 2.10 An example of multispectral UAV, the Parrot Sequoia, capable of taking pictures in 4 different bands: Green, Red, Red edge and NIR.

Figure 3.1 Geographic location and photographic description of the study sites A1 (Clementine), A2 (Olive), and B (Bergamot and olive) orchard (*source*, Modica et al., 2020).

Figure 3.2 Workflow followed for the vegetation monitoring using UAV multispectral imagery in heterogeneous citrus and olive orchards (*source*, Modica et al., 2020).

Figure 3.3 Top left (1), the UAV Multirotor G4 Surveying-Robot (Service Drone GmbH) equipped with Tetracam μ -MCA06 snap multispectral camera; top right (2), camera mounted on UAV gimbal and ready to capture images. Bottom left (3), a graphical scheme shows how the UAV takes into account the 3D morphology of the surveyed area, guaranteeing a constant height of flight and (4) a 3D view of a flight plan (*source*, Modica et al., 2020).

Figure 3.4 Ground control point (GCP) made by attaching two black cards to a polypropylene panel.

Figure 3.5 Segmentation in the study site A1.

Figure 3.6 Segmentation in the study site A2.

Figure 3.7 Segmentation in the study site B.

Figure 3.8 Map showing the study site B with, highlighted in red, the ten parcels identified according to the irrigation scheme (*source*, Modica et al., 2020).

Figure 3.9 Correlation matrix between the six selected vegetation indices (VIs) implemented on the whole image of the study site A1.

Figure 3.10 Study site A1. Scatter plot matrix showing all bivariate relationships between the input layer bands. For each scatterplot, implemented using the 2D kernel density estimate (KDE) with a Gaussian function, the correlation line (in red), was provided. The main diagonal reports the histograms showing the frequency distribution of pixel values. In the upper half-matrix, Pearson's correlation (R) coefficients for all pairwise combinations of variables, are reported (*source*, Modica et al., 2020).

Figure 3.11 Correlation matrix between the six selected vegetation indices (VIs) implemented on the whole image of the study site A2.

Figure 3.12 Study site A2. Scatter plot matrix showing all bivariate relationships between the input layer bands. For each scatterplot, implemented using the 2D kernel density estimate (KDE) with a Gaussian function, the correlation line (in red), was reported. The main diagonal reports the histograms showing

the frequency distribution of pixel values. In the upper half-matrix, Pearson's correlation (R) coefficients for all pairwise combinations of variables, are reported (*source*, Modica et al., 2020).

Figure 3.13 Correlation matrix between the six selected vegetation indices (VIs) implemented on the whole image of the study site B.

Figure 3.14 Study site B. Scatter plot matrix showing all bivariate relationships between the input layer bands. For each scatterplot, implemented using the 2D kernel density estimate (KDE) with a Gaussian function, the correlation line (in red), was reported. The main diagonal reports the histograms showing the frequency distribution of pixel values. In the upper half-matrix, Pearson's correlation (R) coefficients for all pairwise combinations of variables, are reported (*source*, Modica et al., 2020).

Figure 3.15 Land use maps of the three study sites obtained applying the implemented image object classification workflow: A1(Clementine), A2 (Olive), and B (Bergamot and Olive) (*source*, Modica et al., 2020).

Figure 3.16 Maps showing a visual picture of the obtained accuracy in the analyzed three study sites [A1 (Clementine), A2 (Olive) and B (Bergamot and Olive)], using the onscreen digitized canopy boundaries as reference data. Reference crowns (Rc) are in blue, true positives (TP) are in green, false negatives (FN) in red, and false positives (FP) in yellow (*source*, Modica et al., 2020).

Figure 3.17 Correlation matrix between the six selected vegetation indices (VIs) implemented only using the class of trees (bergamot, clementine, and olive) as input data (*source*, Modica et al., 2020).

Figure 3.18 Vegetative vigor maps of the three analyzed study site [A1 (Clementine), A2 (Olive) and B (Bergamot and Olive)] based on the Normalized Difference Vegetation Index (NDVI) values (*source*, Modica et al., 2020).

Figure 3.19 Vegetative vigor maps of the three analyzed study site [A1 (Clementine), A2 (Olive) and B (Bergamot and Olive)] based on the Normalized Difference Red edge Vegetation Index (NDRE) values (*source*, Modica et al., 2020).

Figure 4.1 Geographical location of the two study sites, 1 (citrus orchard) and 2 (onion crop). Below, we provided two representative photos of them.

Figure 4.2 Training polygons of dataset 1: in green those belonging to the "bergamot" class; in brown those belonging to the "bare soil" class.

Figure 4.3 Segmentation in the study site 1.

Figure 4.4 Segmentation in the study site 2.

Figure 4.5 The main characteristics of the obtained classifications in the study site 1. On the left side (a), reported the distribution of the number of segments (in %) in each of the defined land use (LC) classes and according to each of the implemented classification algorithms were reported. On the right side (b), the distribution of the surface area of the obtained segments (in %) in each of the defined LC classes and according to each of the implemented classification algorithms were showed.

Figure 4.6 The figure shows the main characteristics of the obtained classifications of the study site 2. On the left side (a), the distribution of the number of segments (in %) in each of the defined land use (LC) classes and according to each of the implemented classification algorithms were reported. On the right side (b), we provided the distribution of the surface area of the obtained segments (in %) in each of the defined LC classes and according to each of the implemented classification algorithms were showed.

Figure 4.7 Study site 1. User's, Producer's and Overall accuracies, and $F\text{-score}_i$ (single-class) and $F\text{-score}_M$ (multi-class) values obtained for each algorithm.

Figure 4.8 Study site 2. User's, Producer's and Overall accuracies, and $F\text{-score}_i$ (single-class) and $F\text{-score}_M$ (multi-class) values obtained for each algorithm.

Figure 4.9 The classification of the study site 1 organized according to the four classification algorithms in order from top to bottom: K-Nearest Neighbour (KNN), Random Forest (RF), Support Vector Machine (SVM), and Normal Bayes (NB).

Figure 4.10 The classification of the study site 2 organized according to the four classification algorithms in order from top to bottom: K-Nearest Neighbour (KNN), Random Forest (RF), Support Vector Machine (SVM), and Normal Bayes (NB).

Figure 5.1 DJI Phantom 4 Pro (a), (b) DJI Inspire 1, both equipped with a FLIR Vue Pro R 640 uncooled thermal camera (c) (*sources* (Messina and Modica, 2020b) and flir.it).

Figure 5.2 The temperature reference targets used during thermal unmanned aerial vehicle (UAV) surveys carried out in an onion crop field in Calabria (Italy) (*source*, Messina and Modica, 2020b).

Figure 5.3 Photo of the homemade target for ground control points (GCPs) designed to be easily detected in both thermal and multispectral UAV surveys. (a). The GCP target (white dashed circle) as it appears in thermal (b) and in near-infrared (NIR) multispectral images (c) (*source*, Messina and Modica, 2020b).

Figure 5.4 (a) The weather station used during the thermal surveys carried on an onion field and **(b)** the handheld infrared thermometer used to measure the temperature of reference surfaces (*source*, Messina and Modica, 2020b).

Figure 5.5 (a) The localisation of the study site (Campora S. Giovanni, CS – Italy). **(b-c)** The onion field where the experiments were carried out (*source*, Messina et al., 2019).

Figure 5.6 The quadcopter DJI Phantom 4 equipped with the thermal camera Flir Vue Pro R 640 (on the left) and the fixed-wing Parrot Disco-Pro AG equipped with the multispectral camera Parrot Sequoia (on the right) (*source*, Messina et al., 2019).

Figure 5.7 (a) Multispectral camera Parrot Sequoia and **(b)** thermal camera FLIR Vue Pro 640 R as used to carry out surveys.

Figure 5.8 FLIR Vue Pro APP used to set the thermal camera FLIR Vue Pro.

Figure 5.8 (a) Temperature reference targets used during thermal surveys. **(b)** Thermal (above) and multispectral (below) targets used as ground control points (GCPs) in the onion field. **c** The Parrot Sequoia calibration target (*source*, Messina et al., 2019).

Figure 5.9 (a) Above, a map showing the image-object classification of weeds (yellow) and onions (green) performed in eCognition suite. Below, the two obtained orthomosaics from the UAV surveys carried out on 23 November 2018. **(b)** Map of the temperatures [°C]. **(c)** Map of the normalized difference vegetation index (NDVI) (*source*, Messina et al., 2019).

Figure 6.2 (a) The location of the study site. **(b - c- d)** The onion field in which the surveys were carried out (Campora S. Giovanni, CS – Italy) (*source*, Messina et al., 2020c).

Figure 6.2 Crop cycle of the onion, dates of the unmanned aerial vehicles (UAVs) surveys and of imagery acquisition (*source*, Messina et al., 2020c).

Figure 6.3 The Parrot Disco-Pro AG fixed wing unmanned aerial vehicle (UAV) during the pre-flight calibration using the Parrot Sequoia calibration target (*source*, Messina et al., 2020c).

Figure 6.4 RGB orthomosaics of the three datasets (November-December and January) derived from the platforms UAV (top), satellite PlanetScope (center), and Satellite Sentinel-2 (bottom).

Figure 6.5 Scatter plots matrix showing the correlation between the four bands (Green, Red, Red edge, and NIR) and the four vegetation indices (VIs) analyzed (NDVI, NDRE, GNDVI, and SAVI). Dataset of 23 November 2018.

Figure 6.6 Scatter plots matrix showing the correlation between the four bands (Green, Red, Red edge, NIR) and the four vegetation indices (VIs) analyzed (NDVI, NDRE, GNDVI, and SAVI). Dataset of 19 December 2018.

Figure 6.7 Scatter plots matrix showing the correlation between the four bands (Green, Red, Red edge, NIR) and the four vegetation indices (VIs) analyzed (NDVI, NDRE, GNDVI, and SAVI). Dataset of 18 January 2019.

Figure 6.8 SAVI maps showing onion crop, derived from the platforms UAV (top), satellite PlanetScope (center), and Satellite Sentinel-2 (bottom) at their native resolutions (5 cm for UAV, 3 m for PlanetScope, and 10 m for Sentinel-2) (*source*, Messina et al., 2020c).

Figure 6.9 Histograms showing the distribution of SAVI values as a percentage of total values. The imagery of UAV is represented in blue, PlanetScope in red, and Sentinel-2 in green (*source*, Messina et al., 2020c).

Figure 6.10 Scatter plots of SAVI values from the UAV, PlanetScope and Sentinel-2 (S2) map in three months surveyed (*source*, Messina et al., 2020c).

Figure 6.11 Scatter plots of SAVI values from UAV onions mask (SAVI onions) (x-axis), PlanetScope and Sentinel-2 maps in the three months surveyed (*source*, Messina et al., 2020c).

Figure 6.12 Scatter plots of SAVI values from UAV considering only soil pixels (SAVI soil) (x-axis), PlanetScope and Sentinel-2 maps in the three months surveyed (*source*, Messina et al., 2020c).

Figure 6.13 Maps showing onion crop area, derived from the UAV imagery (top), and the percentage of area covered by onion crop within PlanetScope's (center), and Sentinel-2's (bottom) pixels at their native resolutions (3 m for PlanetScope, and 10 m for Sentinel-2) (*source* Messina et al., 2020c).

Figure 6.14 Scatter plots showing the correlation between SAVI values from satellites and the area covered by onion crop (x-axis) in the three months surveyed (*source*, Messina et al., 2020c).

Figure 6.15 SAVI maps showing onion crop with 10 m resolution, derived from the platforms UAV (top), satellite PlanetScope (center), and Satellite Sentinel-2 (bottom) (*source*, Messina et al., 2020c).

Figure 6.16 The spectral signature of onion crop derived from the reflectance data of pure onion pixels for the three platforms in the three periods surveyed (November, December, and January). The shaded light violet indicates the region of the two bands used for the soil adjusted vegetation index (SAVI) calculation (red and near-infrared, NIR) (*source*, Messina et al., 2020c).

Figure 6.17 A map showing the image-object classification of bare soil (in brown) and onions (in green) performed in the eCognition Developer suite. Dataset of 23 November 2018 (*source*, Messina et al., 2020c).

Figure 6.18 SAVI maps from November 2018 (top) to January 2019 (bottom). Next to the image of each dataset, blue and magenta rectangles magnify the details of the vegetative vigor of onion crops in two different parts of the field and where the transplanting took place with three weeks apart. The ellipses highlight areas of the field where the onion crops are absent or have had difficulty growing (*source*, Messina et al., 2020c).

9 LIST OF TABLES

Table 1.1 Total area cultivated and total production (quintals of olives) in Italy and Calabria.

Table 1.2 Total area cultivated and total production in Calabria's provinces.

Table 1.3 Total area cultivated and total production (quintals) in Italy and Calabria.

Table 1.4 Total area cultivated and total production (quintals) in Calabria's provinces.

Table 1.5 Total area cultivated and total production (quintals) in Calabria's provinces.

Table 2.1 The emissivity of different surfaces over the range of 8–14 μm (Campbell e Wynne, 2017; Lillesand et al., 2015).

Table 3.1. Tetracam μ -MCA06 snap (Global shutter) sensor characteristics bands specification (wavelength and bandwidth).

Table 3.2 Flight and UAV dataset characteristics.

Table 3.3 Formulation of the six vegetation indices (VIs) used in the present work.

Table 3.4 Results and accuracy indicators of the trees' crowns extraction (TP, true positives; FP, false positives; FN, false negatives; r, recall; p, precision; branching factor, BF).

Table 4.2 Tetracam μ -MCA06 snap (Global shutter) sensor characteristics bands specification (wavelength and bandwidth).

Table 4.2 Flight and UAV dataset characteristics.

Table 4.3 Main parameters set for each of the implemented classification algorithms, K-Nearest Neighbour (KNN), Support Vector Machine (SVM) and Random Forest (RF).

Table 4.4 The table shows the most significant metrics of the obtained segmentations and the requested processing time for each algorithm in the study sites 1 and 2.

Table 4.5 Distribution of trainer points in land cover (LC) classes in the study sites sites.

Table 4.6 Confusion matrix obtained for the classifier K-Nearest Neighbour (KNN) in the study site 1.

Table 4.7 Confusion matrix obtained for the classifier Random Forest (RF) in the study site 1.

Table 4.8 Confusion matrix obtained for the classifier Support Vector Machine (SVM) in the study site 1.

Table 4.9 Confusion matrix obtained for the classifier Normal Bayes (NB) in the study site 1.

Table 4.10 Confusion matrix obtained for the classifier K-Nearest Neighbour (KNN) in the study site 2.

Table 4.11 Confusion matrix obtained for the classifier Random Forest (RF) in the study site 2.

Table 4.12 Confusion matrix obtained for the classifier Support Vector Machine (SVM) in the study site 2.

Table 4.13 Confusion matrix obtained for the classifier Normal Bayes (NB) in the study site 2.

Table 6.1 Characteristics of the multispectral camera and of the satellites whose images were used in this research.

Table 6.2 Formulation of the four vegetation indices (VIs) used in the present research.

Table 6.3 Basic statistics considering images of the three platforms (UAV, PlanetScope, and Sentinel-2) at their original resolution.

10 ACRONYMS

CHM = canopy height model

CVI = Chlorophyll Vegetation Index

DSM = digital surface model

DTM = digital terrain model

EM = electromagnetic

GEOBIA = geographic object-based image analysis

GNDVI = Green Normalized Difference Vegetation Index

GNSS = global navigation satellite system

GRNDVI = Green and Red Normalized Difference Vegetation Index

GCP = Ground Control Point

GSD = ground sample distance

KNN = k-nearest neighbour

LAI = leaf area index

LC = land cover

ML = machine learning

MRS = multiresolution segmentation

MS = multispectral

NB = normal bayes

NDRE = Normalized Difference Red edge Index

NDVI = Normalized Difference Vegetation Index

NIR = Near-infrared

p = precision

PA = precision agriculture

PDO = protected designation of origin

PGI = protected geographical indication

r = recall

RF = random forest

RS = remote sensing

SAVI = Soil-Adjusted Vegetation Index

SE = standard error

SR = simple ratio

SVM = support vector machine

TIR = thermal infrared

VHR = very high resolution

UAV = unmanned aerial vehicle

VI = vegetation index

VIS = visible

11 References

- Abdulridha, J., Batuman, O., Ampatzidis, Y., 2019a. UAV-Based Remote Sensing Technique to Detect Citrus Canker Disease Utilizing Hyperspectral Imaging and Machine Learning. *Remote Sens.* 11, 1373. <https://doi.org/10.3390/rs11111373>
- Abdulridha, J., Ehsani, R., Abd-Elrahman, A., Ampatzidis, Y., 2019b. A remote sensing technique for detecting laurel wilt disease in avocado in presence of other biotic and abiotic stresses. *Comput. Electron. Agric.* 156, 549–557. <https://doi.org/10.1016/J.COMPAG.2018.12.018>
- Aboukhadrah, S.H., El - Alsayed, A.W.A.H., Sobhy, L., Abdelmasieh, W., 2017. Response of Onion Yield and Quality To Different Planting Date, Methods and Density. *Egypt. J. Agron.* 39, 203–219. <https://doi.org/10.21608/agro.2017.1203.1065>
- Abuzar, M., 2014. Comparing Inter-Sensor NDVI for the Analysis of Horticulture Crops in South-Eastern Australia. *Am. J. Remote Sens.* 2, 1. <https://doi.org/10.11648/j.ajrs.20140201.11>
- Agam, N., Cohen, Y., Berni, J.A.J., Alchanatis, V., Kool, D., Dag, A., Yermiyahu, U., Ben-Gal, A., 2013. An insight to the performance of crop water stress index for olive trees. *Agric. Water Manag.* 118, 79–86. <https://doi.org/10.1016/j.agwat.2012.12.004>
- Aguilar, M.A., Aguilar, F.J., García Lorca, A., Guirado, E., Betlej, M., Cichon, P., Nemmaoui, A., Vallario, A., Parente, C., 2016. Assessment of multiresolution segmentation for extracting greenhouses from WorldView-2 imagery. *Int. Arch. Photogramm. Remote Sens. Spat. Inf. Sci. - ISPRS Arch.* 41, 145–152. <https://doi.org/10.5194/isprsarchives-XLI-B7-145-2016>
- Albetis, J., Jacquin, A., Goulard, M., Poilvé, H., Rousseau, J., Clenet, H., Dedieu, G., Duthoit, S., 2018. On the Potentiality of UAV Multispectral Imagery to Detect Flavescence dorée and Grapevine Trunk Diseases. *Remote Sens.* 11, 23. <https://doi.org/10.3390/rs11010023>
- Alchanatis, V., Cohen, Y., Cohen, S., Moller, M., Sprinstin, M., Meron, M., Tsipris, J., Saranga, Y., Sela, E., 2010. Evaluation of different approaches for estimating and mapping crop water status in cotton with thermal imaging. *Precis. Agric.* 11, 27–41. <https://doi.org/10.1007/s11119-009-9111-7>
- Alderfasi, A.A., Nielsen, D.C., 2001. Use of crop water stress index for monitoring water status and scheduling irrigation in wheat. *Agric. Water Manag.* 47, 69–75. [https://doi.org/10.1016/S0378-3774\(00\)00096-2](https://doi.org/10.1016/S0378-3774(00)00096-2)
- Allred, B., Eash, N., Freeland, R., Martinez, L., Wishart, D.B., 2018. Effective and efficient agricultural drainage pipe mapping with UAS thermal infrared imagery: A case study. *Agric. Water Manag.* 197, 132–137. <https://doi.org/10.1016/j.agwat.2017.11.011>
- Allred, B., Martinez, L., Fessehazion, M.K., Rouse, G., Williamson, T.N., Wishart, D.B., Koganti, T., Freeland, R., Eash, N., Batschelet, A., Featheringill, R., 2020. Overall results and key findings on the use of UAV visible-color, multispectral, and thermal infrared imagery to map agricultural drainage pipes. *Agric. Water Manag.* 232, 106036. <https://doi.org/10.1016/j.agwat.2020.106036>
- Amani, I., Fischer, R.A., Reynolds, M.P., 1996. Canopy temperature depression association with yield of irrigated spring wheat cultivars in a hot climate. *J. Agron. Crop Sci.* 176, 119–129. <https://doi.org/10.1111/j.1439-037X.1996.tb00454.x>
- Ampatzidis, Y., Partel, V., 2019. UAV-Based High Throughput Phenotyping in Citrus Utilizing Multispectral Imaging and Artificial Intelligence. *Remote Sens.* 11, 410. <https://doi.org/10.3390/rs11040410>

- Anderson, J.H., Weber, K.T., Gokhale, B., Chen, F., 2011. Intercalibration and Evaluation of ResourceSat-1 and Landsat-5 NDVI. *Can. J. Remote Sens.* 37, 213–219. <https://doi.org/10.5589/m11-032>
- Anderson, M.C., Hain, C., Otkin, J., Zhan, X., Mo, K., Svoboda, M., Wardlow, B., Pimstein, A., 2013. An Intercomparison of Drought Indicators Based on Thermal Remote Sensing and NLDAS-2 Simulations with U.S. Drought Monitor Classifications. *J. Hydrometeorol.* 14, 1035–1056. <https://doi.org/10.1175/JHM-D-12-0140.1>
- Angelov, P., Gu, X., 2019. Empirical Approach to Machine Learning, *IEEE Transactions on Cybernetics*. Springer International Publishing. <https://doi.org/10.1109/TCYB.2017.2753880>
- Aplin, P., 2006. On scales and dynamics in observing the environment. *Int. J. Remote Sens.* 27, 2123–2140. <https://doi.org/10.1080/01431160500396477>
- Asrar, G., Myneni, R.B., Choudhury, B.J., 1992. Spatial heterogeneity in vegetation canopies and remote sensing of absorbed photosynthetically active radiation: A modeling study. *Remote Sens. Environ.* 41, 85–103. [https://doi.org/10.1016/0034-4257\(92\)90070-Z](https://doi.org/10.1016/0034-4257(92)90070-Z)
- Baatz, M., Schape, A., 2000. Multi-resolution segmentation: An optimization approach for high quality multi-scale. *Beiträge zum, Agit XII Symp. Salsburg*, 12–23. https://doi.org/10.1207/s15326888chc1304_3
- Ballester, C., Jiménez-Bello, M.A., Castel, J.R., Intrigliolo, D.S., 2013. Usefulness of thermography for plant water stress detection in citrus and persimmon trees. *Agric. For. Meteorol.* 168, 120–129. <https://doi.org/10.1016/j.agrformet.2012.08.005>
- Ballester, C., Zarco-Tejada, P.J., Nicolás, E., Alarcón, J.J., Fereres, E., Intrigliolo, D.S., Gonzalez-Dugo, V., 2017. Evaluating the performance of xanthophyll, chlorophyll and structure-sensitive spectral indices to detect water stress in five fruit tree species. *Precis. Agric.* 1–16. <https://doi.org/10.1007/s11119-017-9512-y>
- Ballesteros, R., Ortega, J.F., Hernandez, D., Moreno, M.A., 2018. Onion biomass monitoring using UAV-based RGB imaging. *Precis. Agric.* 1–18. <https://doi.org/10.1007/s11119-018-9560-y>
- Baluja, J., Diago, M.P., Balda, P., Zorer, R., Meggio, F., Morales, F., Tardaguila, J., 2012. Assessment of vineyard water status variability by thermal and multispectral imagery using an unmanned aerial vehicle (UAV). *Irrig. Sci.* 30, 511–522. <https://doi.org/10.1007/s00271-012-0382-9>
- Barnes, E.M., Clarke, T.R., Richards, S.E., Colaizzi, P.D., Haberland, J., Kostrzewski, M., Waller, P., Choi, C., R.E., Thompson, T., Lascano, R.J., Li, H., Moran, M.S., 2000. Coincident detection of crop water stress, nitrogen status and canopy density using ground based multispectral data, in: *Proc. 5th Int. Conf. Precis Agric.*
- Bartsch, A., Widhalm, B., Leibman, M., Ermokhina, K., Kumpula, T., Skarin, A., Wilcox, E.J., Jones, B.M., Frost, G. V., Höfler, A., Pointner, G., 2020. Feasibility of tundra vegetation height retrieval from Sentinel-1 and Sentinel-2 data. *Remote Sens. Environ.* 237, 111515. <https://doi.org/10.1016/j.rse.2019.111515>
- Belgiu, M., Csillik, O., 2018. Sentinel-2 cropland mapping using pixel-based and object-based time-weighted dynamic time warping analysis. *Remote Sens. Environ.* 204, 509–523. <https://doi.org/10.1016/j.rse.2017.10.005>
- Bellvert, J., Marsal, J., Girona, J., Gonzalez-Dugo, V., Fereres, E., Ustin, S.L., Zarco-Tejada, P.J., 2016. Airborne thermal imagery to detect the seasonal evolution of crop water status in peach, nectarine and Saturn peach orchards. *Remote Sens.* 8, 1–17. <https://doi.org/10.3390/rs8010039>

- Bellvert, J., Zarco-Tejada, P.J., Girona, J., Fereres, E., 2014. Mapping crop water stress index in a “Pinot-noir” vineyard: Comparing ground measurements with thermal remote sensing imagery from an unmanned aerial vehicle. *Precis. Agric.* 15, 361–376. <https://doi.org/10.1007/s11119-013-9334-5>
- Ben-Dor, E., 2002. Quantitative remote sensing of soil properties. *Adv. Agron.* [https://doi.org/10.1016/s0065-2113\(02\)75005-0](https://doi.org/10.1016/s0065-2113(02)75005-0)
- Benabdelkamel, H., Di Donna, L., Mazzotti, F., Naccarato, A., Sindona, G., Tagarelli, A., Taverna, D., 2012. Authenticity of PGI “clementine of Calabria” by multielement fingerprint. *J. Agric. Food Chem.* 60, 3717–3726. <https://doi.org/10.1021/jf2050075>
- Bendig, J.V., 2015. Unmanned aerial vehicles (UAVs) for multi-temporal crop surface modelling. A new method plant Height biomass Estim. based RGB-imaging 156.
- Benincasa, P., Antognelli, S., Brunetti, L., Fabbri, C.A., Natale, A., Sartoretti, V., Modeo, G., Guiducci, M., Tei, F., Vizzari, M., 2017. Reliability of Ndvi Derived By High Resolution Satellite and Uav Compared To in-Field Methods for the Evaluation of Early Crop N Status and Grain Yield in Wheat. *Exp. Agric.* 54, 1–19. <https://doi.org/10.1017/S0014479717000278>
- Berk, A., Anderson, G.P., Acharya, P.K., Chetwynd, J.H., Bernstein, L.S., Shettle, E.P., Matthew, M.W., Adler-Golden, S., 1999. MODTRAN4 User’s manual. Hanscom AFB, MA Air Force Res. Lab.,
- Berliner, P., Oosterhuis, D.M., Green, G.C., 1984. Evaluation of the infrared thermometer as a crop stress detector. *Agric. For. Meteorol.* 31, 219–230. [https://doi.org/10.1016/0168-1923\(84\)90036-4](https://doi.org/10.1016/0168-1923(84)90036-4)
- Bernardi, B., Zimbalatti, G., Proto, A.R., Benalia, S., Fazari, A., Callea, P., 2013. Mechanical grading in PGI Tropea red onion post harvest operations. *J. Agric. Eng.* 44, 317–322. [https://doi.org/10.4081/jae.2013.\(s1\):e63](https://doi.org/10.4081/jae.2013.(s1):e63)
- Berni, J., Zarco-Tejada, P.J., Sepulcre-Cantó, G., Fereres, E., Villalobos, F., 2009a. Mapping canopy conductance and CWSI in olive orchards using high resolution thermal remote sensing imagery. *Remote Sens. Environ.* 113, 2380–2388. <https://doi.org/10.1016/j.rse.2009.06.018>
- Berni, J., Zarco-Tejada, P.J., Suarez, L., Fereres, E., 2009b. Thermal and Narrowband Multispectral Remote Sensing for Vegetation Monitoring From an Unmanned Aerial Vehicle. *IEEE Trans. Geosci. Remote Sens.* 47, 722–738. <https://doi.org/10.1109/TGRS.2008.2010457>
- Bhan, R.K., Saxena, R.S., Jalwania, C.R., Lomash, S.K., 2009. Uncooled infrared microbolometer arrays and their characterisation techniques. *Def. Sci. J.* 59, 580–589. <https://doi.org/10.14429/dsj.59.1562>
- Bian, J., Zhang, Z., Chen, J., Chen, H., Cui, C., Li, X., Chen, S., Fu, Q., 2019. Simplified Evaluation of Cotton Water Stress Using High Resolution Unmanned Aerial Vehicle Thermal Imagery. *Remote Sens.* 11, 267. <https://doi.org/10.3390/rs11030267>
- Bieszczad, G., Kastek, M., 2011. Measurement of thermal behavior of detector array surface with the use of microscopic thermal camera. *Metrol. Meas. Syst.* 18, 679–690. <https://doi.org/10.2478/v10178-011-0064-6>
- Blaschke, T., 2010. Object based image analysis for remote sensing. *ISPRS J. Photogramm. Remote Sens.* 65, 2–16. <https://doi.org/10.1016/j.isprsjprs.2009.06.004>
- Blaschke, T., Hay, G.J., Kelly, M., Lang, S., Hofmann, P., Addink, E., Queiroz Feitosa, R., van der Meer, F., van der Werff, H., van Coillie, F., Tiede, D., 2014. Geographic Object-Based Image Analysis - Towards a new paradigm. *ISPRS J. Photogramm. Remote Sens.* 87, 180–191. <https://doi.org/10.1016/j.isprsjprs.2013.09.014>

- Blum, A., Shpiler, L., Golan, G., Mayer, J., 1989. Yield stability and canopy temperature of wheat genotypes under drought-stress. *F. Crop. Res.* 22, 289–296. [https://doi.org/10.1016/0378-4290\(89\)90028-2](https://doi.org/10.1016/0378-4290(89)90028-2)
- Boesch, R., 2017. Thermal remote sensing with UAV-based workflows. *Int. Arch. Photogramm. Remote Sens. Spat. Inf. Sci. - ISPRS Arch.* 42, 41–46. <https://doi.org/10.5194/isprs-archives-XLII-2-W6-41-2017>
- Borgogno Mondino, E., Gajetti, M., 2017. Preliminary considerations about costs and potential market of remote sensing from UAV in the Italian viticulture context. *Eur. J. Remote Sens.* 50, 310–319. <https://doi.org/10.1080/22797254.2017.1328269>
- Breiman, L., 2001. Random forests. *Mach. Learn.* 45, 5–32. <https://doi.org/10.1023/A:1010933404324>
- Brocks, S., Bareth, G., 2018. Estimating barley biomass with crop surface models from oblique RGB imagery. *Remote Sens.* 10. <https://doi.org/10.3390/rs10020268>
- Budzier, H., Gerlach, G., 2015. Calibration of uncooled thermal infrared cameras. *J. Sensors Sens. Syst.* 4, 187–197. <https://doi.org/10.5194/jsss-4-187-2015>
- Bukowiecki, J., Rose, T., Ehlers, R., Kage, H., 2020. High-Throughput Prediction of Whole Season Green Area Index in Winter Wheat With an Airborne Multispectral Sensor. *Front. Plant Sci.* 10, 1. <https://doi.org/10.3389/fpls.2019.01798>
- Calderón, R., Navas-Cortés, J.A., Lucena, C., Zarco-Tejada, P.J., 2013. High-resolution airborne hyperspectral and thermal imagery for early detection of Verticillium wilt of olive using fluorescence, temperature and narrow-band spectral indices. *Remote Sens. Environ.* 139, 231–245. <https://doi.org/10.1016/j.rse.2013.07.031>
- Campbell e Wynne, 2017. Introduction to remote sensing. The Guilford Press, New York, NY, USA.
- Candiago, S., Remondino, F., De Giglio, M., Dubbini, M., Gattelli, M., 2015. Evaluating multispectral images and vegetation indices for precision farming applications from UAV images. *Remote Sens.* 7, 4026–4047. <https://doi.org/10.3390/rs70404026>
- Cannell, R.Q., Gales, K., Snaydon, R.W., Suhail, B.A., 1979. Effects of short-term waterlogging on the growth and yield of peas (*Pisum sativum*). *Ann. Appl. Biol.* 93, 327–335. <https://doi.org/10.1111/j.1744-7348.1979.tb06549.x>
- Caruso, G., Zarco-Tejada, P.J., González-Dugo, V., Moriondo, M., Tozzini, L., Palai, G., Rallo, G., Hornero, A., Primicerio, J., Gucci, R., 2019. High-resolution imagery acquired from an unmanned platform to estimate biophysical and geometrical parameters of olive trees under different irrigation regimes. *PLoS One* 14, e0210804. <https://doi.org/10.1371/journal.pone.0210804>
- Chen, C., 2015. Determining the leaf emissivity of three crops by infrared thermometry. *Sensors (Switzerland)* 15, 11387–11401. <https://doi.org/10.3390/s150511387>
- Chen, G., Weng, Q., Hay, G.J., He, Y., 2018. Geographic object-based image analysis (GEOBIA): emerging trends and future opportunities. *GIScience Remote Sens.* 55, 159–182. <https://doi.org/10.1080/15481603.2018.1426092>
- Chuvieco, E., 2016. Fundamentals of Satellite Remote Sensing, Second ed. CRC Press, Boca Raton, United States.
- Clarke, M.R.B., Duda, R.O., Hart, P.E., 1974. Pattern Classification and Scene Analysis. *J. R. Stat. Soc. Ser. A* 137, 442. <https://doi.org/10.2307/2344977>

- Clewley, D., Bunting, P., Shepherd, J., Gillingham, S., Flood, N., Dymond, J., Lucas, R., Armston, J., Moghaddam, M., 2014. A python-based open source system for Geographic Object-Based Image Analysis (GEOBIA) utilizing raster attribute tables. *Remote Sens.* 6, 6111–6135. <https://doi.org/10.3390/rs6076111>
- Cohen, Y., Alchanatis, V., Meron, M., Saranga, Y., Tsipris, J., 2005. Estimation of leaf water potential by thermal imagery and spatial analysis. *J. Exp. Bot.* 56, 1843–1852. <https://doi.org/10.1093/jxb/eri174>
- Cohen, Y., Alchanatis, V., Saranga, Y., Rosenberg, O., Sela, E., Bosak, A., 2017. Mapping water status based on aerial thermal imagery: comparison of methodologies for upscaling from a single leaf to commercial fields. *Precis. Agric.* 18, 801–822. <https://doi.org/10.1007/s11119-016-9484-3>
- Collins, W., 1978. Remote Sensing of crop type and maturity. *Photogramm. Eng. Remote Sensing* 44, 42–55.
- Colomina, I., Molina, P., 2014. Unmanned aerial systems for photogrammetry and remote sensing: A review. *ISPRS J. Photogramm. Remote Sens.* 92, 79–97. <https://doi.org/10.1016/j.isprsjprs.2014.02.013>
- Congalton, R.G., Green, K., 2019. Assessing the Accuracy of Remotely Sensed Data, *Assessing the Accuracy of Remotely Sensed Data*. <https://doi.org/10.1201/9780429052729>
- Connor, D.J., Fereres, E., 2010. The Physiology of Adaptation and Yield Expression in Olive, in: *Horticultural Reviews*. <https://doi.org/10.1002/9780470650882.ch4>
- Córcoles, J.I., Ortega, J.F., Hernández, D., Moreno, M.A., 2013. Estimation of leaf area index in onion (*Allium cepa* L.) using an unmanned aerial vehicle. *Biosyst. Eng.* 115, 31–42. <https://doi.org/10.1016/j.biosystemseng.2013.02.002>
- Cortes, C., Vapnik, V., 1995. Support-Vector Networks Editor. *Mach. Learn.* 20, 273–297. <https://doi.org/10.1023/A:1022627411411>
- Costa, J.M., Grant, O.M., Chaves, M.M., 2013. Thermography to explore plant-environment interactions. *J. Exp. Bot.* 64, 3937–3949. <https://doi.org/10.1093/jxb/ert029>
- Crabbe, R.A., Lamb, D., Edwards, C., 2020. Int J Appl Earth Obs Geoinformation Discrimination of species composition types of a grazed pasture landscape using Sentinel-1 and Sentinel-2 data. *Int J Appl Earth Obs Geoinf.* 84, 101978. <https://doi.org/10.1016/j.jag.2019.101978>
- Crusiol, L.G.T., Nanni, M.R., Furlanetto, R.H., Sibaldelli, R.N.R., Cezar, E., Mertz-Henning, L.M., Nepomuceno, A.L., Neumaier, N., Farias, J.R.B., 2020. UAV-based thermal imaging in the assessment of water status of soybean plants. *Int. J. Remote Sens.* 41, 3243–3265. <https://doi.org/10.1080/01431161.2019.1673914>
- Csillik, O., Cherbini, J., Johnson, R., Lyons, A., Kelly, M., 2018. Identification of Citrus Trees from Unmanned Aerial Vehicle Imagery Using Convolutional Neural Networks. *Drones* 2, 39. <https://doi.org/10.3390/drones2040039>
- Cubero-Castan, M., Schneider-Zapp, K., Bellomo, M., Shi, D., Rehak, M., Strecha, C., 2018. Assessment Of The Radiometric Accuracy In A Target Less Work Flow Using Pix4D Software, in: *2018 9th Workshop on Hyperspectral Image and Signal Processing: Evolution in Remote Sensing (WHISPERS)*. IEEE, pp. 1–4. <https://doi.org/10.1109/WHISPERS.2018.8746910>
- Cutler, D.R., Edwards, T.C., Beard, K.H., Cutler, A., Hess, K.T., Gibson, J., Lawler, J.J., 2007. Random forests for classification in ecology. *Ecology* 88, 2783–2792. <https://doi.org/10.1890/07-0539.1>

- Da Pozzo, E., De Leo, M., Faraone, I., Milella, L., Cavallini, C., Piragine, E., Testai, L., Calderone, V., Pistelli, L., Braca, A., Martini, C., 2018. Antioxidant and antisenescence effects of bergamot juice. *Oxid. Med. Cell. Longev.* 2018. <https://doi.org/10.1155/2018/9395804>
- De Castro, A.I., Ehsani, R., Ploetz, R., Crane, J.H., Abdulridha, J., 2015. Optimum spectral and geometric parameters for early detection of laurel wilt disease in avocado. *Remote Sens. Environ.* 171, 33–44. <https://doi.org/10.1016/j.rse.2015.09.011>
- De Castro, A.I., Peña, J.M., Torres-Sánchez, J., Jiménez-Brenes, F., López-Granados, F., 2017. Mapping *Cynodon dactylon* in vineyards using UAV images for site-specific weed control. *Adv. Anim. Biosci.* 8, 267–271. <https://doi.org/10.1017/s2040470017000826>
- De Castro, A.I., Torres-Sánchez, J., Peña, J.M., Jiménez-Brenes, F.M., Csillik, O., López-Granados, F., 2018. An automatic random forest-OBIA algorithm for early weed mapping between and within crop rows using UAV imagery. *Remote Sens.* 10, 1–21. <https://doi.org/10.3390/rs10020285>
- De Luca, G., N. Silva, J.M., Cerasoli, S., Araújo, J., Campos, J., Di Fazio, S., Modica, G., 2019. Object-Based Land Cover Classification of Cork Oak Woodlands using UAV Imagery and Orfeo ToolBox. *Remote Sens.* 11, 1238. <https://doi.org/10.3390/rs11101238>
- De Montis, A., Modica, G., Arcidiacono, C., 2019. Encyclopedia of Big Data. *Encycl. Big Data.* <https://doi.org/10.1007/978-3-319-32001-4>
- Deng, L., Mao, Z., Li, X., Hu, Z., Duan, F., Yan, Y., 2018. UAV-based multispectral remote sensing for precision agriculture: A comparison between different cameras. *ISPRS J. Photogramm. Remote Sens.* 146, 124–136. <https://doi.org/10.1016/j.isprsjprs.2018.09.008>
- Díaz-Varela, R.A., de la Rosa, R., León, L., Zarco-Tejada, P.J., 2015. High-resolution airborne UAV imagery to assess olive tree crown parameters using 3D photo reconstruction: Application in breeding trials. *Remote Sens.* 7, 4213–4232. <https://doi.org/10.3390/rs70404213>
- Drăguț, L., Csillik, O., Eisank, C., Tiede, D., 2014. Automated parameterisation for multi-scale image segmentation on multiple layers. *ISPRS J. Photogramm. Remote Sens.* 88, 119–127. <https://doi.org/10.1016/j.isprsjprs.2013.11.018>
- Drăguț, L., Tiede, D., Levick, S.R., 2010. ESP: a tool to estimate scale parameter for multiresolution image segmentation of remotely sensed data. *Int. J. Geogr. Inf. Sci.* 24, 859–871. <https://doi.org/10.1080/13658810903174803>
- Du, B., Arnold, J.G., Saleh, A., Jaynes, D.B., 2005. Development and application of SWAT to landscapes with tiles and potholes. *Trans. Am. Soc. Agric. Eng.* 48, 1121–1133. <https://doi.org/10.13031/2013.18522>
- Dupin, S., Gobrecht, A., B.Tisseyre, 2011. Airborne Thermography of Vines Canopy: Effect of the Atmosphere and Mixed Pixels on Observed Canopy Temperature. 8^{ème} Conférence Eur. sur l’Agriculture Précision 1, 1–9.
- Duro, D.C., Franklin, S.E., Dubé, M.G., 2012. Multi-scale object-based image analysis and feature selection of multi-sensor earth observation imagery using random forests. *Int. J. Remote Sens.* 33, 4502–4526. <https://doi.org/10.1080/01431161.2011.649864>
- earth.esa.int/web/sentinel/missions/sentinel-2/instrument-payload/resolution-and-swath, (last access 2 April 2020) [WWW Document].
- Egea, G., Padilla-Díaz, C.M., Martínez-Guanter, J., Fernández, J.E., Pérez-Ruiz, M., 2017. Assessing a crop water stress index derived from aerial thermal imaging and infrared thermometry in super-

- high density olive orchards. *Agric. Water Manag.* 187, 210–221. <https://doi.org/10.1016/j.agwat.2017.03.030>
- El-naggar, A.M., 2018. Determination of optimum segmentation parameter values for extracting building from remote sensing images. *Alexandria Eng. J.* 57, 3089–3097. <https://doi.org/10.1016/j.aej.2018.10.001>
- Eshel, G., Levy, G.J., Singer, M.J., 2004. Spectral Reflectance Properties of Crusted Soils under Solar Illumination. *Soil Sci. Soc. Am. J.* 68, 1982–1991. <https://doi.org/10.2136/sssaj2004.1982>
- Falcone, G., Stillitano, T., De Luca, A.I., Di Vita, G., Iofrida, N., Strano, A., Gulisano, G., Pecorino, B., D'Amico, M., 2020. Energetic and Economic Analyzes for Agricultural Management Models: The Calabria PGI Clementine Case Study. *Energies* 1289. <https://doi.org/10.3390/en13051289>
- Fausey, N.R., 2005. Drainage management for humid regions. *Int. Agric. Eng. J.* 14, 209–214.
- Feng, A., Zhou, J., Vories, E.D., Sudduth, K.A., Zhang, M., 2020. Yield estimation in cotton using UAV-based multi-sensor imagery. *Biosyst. Eng.* 193, 101–114. <https://doi.org/10.1016/j.biosystemseng.2020.02.014>
- Fièque, B., Tissot, J.L., Trouilleau, C., Crastes, A., Legras, O., 2007. Uncooled microbolometer detector: Recent developments at Ulis. *Infrared Phys. Technol.* 49, 187–191. <https://doi.org/10.1016/j.infrared.2006.06.030>
- Filippo, S., Gennaro, D., Matese, A., Gioli, B., Toscano, P., Zaldei, A., Palliotti, A., Genesio, L., 2017. Multisensor approach to assess vineyard thermal dynamics combining high-resolution unmanned aerial vehicle (UAV) remote sensing and wireless sensor network (WSN) proximal sensing. *Sci. Hortic. (Amsterdam)*. 221, 83–87. <https://doi.org/10.1016/j.scienta.2017.04.024>
- Fiorino, P., 2018. *Olea. Trattato di Olivicoltura*. Edagricole - Edizioni Agricole di New Business Media srl, Bologna.
- FLIR, 2015. *Uncooled Detectors for Thermal Imaging Cameras 6*.
- FLIR, 2012. *Tech Note:Radiometric Temperature Measurements Surface characteristics and atmospheric compensation*.
- FLIR, 2011. *Cooled versus uncooled cameras for long range surveillance*.
- Freeland, R., Allred, B., Eash, N., Martinez, L., Wishart, D.B., 2019. Agricultural drainage tile surveying using an unmanned aircraft vehicle paired with Real-Time Kinematic positioning—A case study. *Comput. Electron. Agric.* 165, 104946. <https://doi.org/10.1016/j.compag.2019.104946>
- Gade, R., Moeslund, T.B., 2014. Thermal cameras and applications: a survey. *Mach. Vis. Appl.* 25, 245–262. <https://doi.org/10.1007/s00138-013-0570-5>
- Gago, J., Douthe, C., Coopman, R.E., Gallego, P.P., Ribas-Carbo, M., Flexas, J., Escalona, J., Medrano, H., 2015. UAVs challenge to assess water stress for sustainable agriculture. *Agric. Water Manag.* 153, 9–19. <https://doi.org/10.1016/j.agwat.2015.01.020>
- Gallo, K.P., Daughtry, C.S.T., 1987. Differences in vegetation indices for simulated Landsat-5 MSS and TM, NOAA-9 AVHRR, and SPOT-1 sensor systems. *Remote Sens. Environ.* 23, 439–452. [https://doi.org/10.1016/0034-4257\(87\)90100-3](https://doi.org/10.1016/0034-4257(87)90100-3)
- Gallo, M.A., Willits, D.S., Lubke, R.A., Thiede, E.C., 1993. Low-cost uncooled IR sensor for battlefield surveillance, in: Andresen, B.F., Shepherd, F.D. (Eds.), *In Proceedings of the SPIE*. p. 351. <https://doi.org/10.1117/12.160556>

- Gamon, J.A., Surfus, J.S., 1999. Assessing leaf pigment content and activity with a reflectometer. *New Phytol.* 143, 105–117. <https://doi.org/10.1046/j.1469-8137.1999.00424.x>
- Gao, J., Liao, W., Nuyttens, D., Lootens, P., Vangeyte, J., Pižurica, A., He, Y., Pieters, J.G., 2018. Fusion of pixel and object-based features for weed mapping using unmanned aerial vehicle imagery. *Int. J. Appl. Earth Obs. Geoinf.* 67, 43–53. <https://doi.org/10.1016/j.jag.2017.12.012>
- Gašparović, M., Zrinjski, M., Barković, Đ., Radočaj, D., 2020. An automatic method for weed mapping in oat fields based on UAV imagery. *Comput. Electron. Agric.* 173, 105385. <https://doi.org/10.1016/j.compag.2020.105385>
- Gautam, D., Pagay, V., 2020. A review of current and potential applications of remote sensing to study the water status of horticultural crops. *Agronomy* 10. <https://doi.org/10.3390/agronomy10010140>
- Gebbers, R., Adamchuk, V.I., 2010. Precision agriculture and food security. *Science* (80-.). <https://doi.org/10.1126/science.1183899>
- Georganos, S., Grippa, T., Vanhuysse, S., Lennert, M., Shimoni, M., Kalogirou, S., Wolff, E., 2018. Less is more: optimizing classification performance through feature selection in a very-high-resolution remote sensing object-based urban application. *GIScience Remote Sens.* <https://doi.org/10.1080/15481603.2017.1408892>
- Gerhards, M., Rock, G., Schlerf, M., Udelhoven, T., 2016. Water stress detection in potato plants using leaf temperature, emissivity, and reflectance. *Int. J. Appl. Earth Obs. Geoinf.* 53, 27–39. <https://doi.org/10.1016/j.jag.2016.08.004>
- Gerhards, M., Schlerf, M., Mallick, K., Udelhoven, T., 2019. Challenges and future perspectives of multi-/Hyperspectral thermal infrared remote sensing for crop water-stress detection: A review. *Remote Sens.* 11. <https://doi.org/10.3390/rs11101240>
- Gerhards, M., Schlerf, M., Rascher, U., Udelhoven, T., Juszczak, R., Alberti, G., Miglietta, F., Inoue, Y., 2018. Analysis of airborne optical and thermal imagery for detection of water stress symptoms. *Remote Sens.* 10. <https://doi.org/10.3390/rs10071139>
- Ghuffar, S., 2018. DEM generation from multi satellite PlanetScope imagery. *Remote Sens.* 10, 1–22. <https://doi.org/10.3390/rs10091462>
- Gitelson, A.A., Kaufman, Y.J., Merzlyak, M.N., 1996. Use of a green channel in remote sensing of global vegetation from EOS- MODIS. *Remote Sens. Environ.* 58, 289–298. [https://doi.org/10.1016/S0034-4257\(96\)00072-7](https://doi.org/10.1016/S0034-4257(96)00072-7)
- Gitelson, A.A., Merzlyak, M.N., 1998. Remote sensing of chlorophyll concentration in higher plant leaves. *Adv. Sp. Res.* 22, 689–692. [https://doi.org/10.1016/S0273-1177\(97\)01133-2](https://doi.org/10.1016/S0273-1177(97)01133-2)
- Giuffrè, A.M., 2019. Bergamot (*Citrus bergamia*, Risso): The effects of cultivar and harvest date on functional properties of juice and cloudy juice. *Antioxidants* 8. <https://doi.org/10.3390/antiox8070221>
- Gómez-Candón, D., Virlet, N., Labbé, S., Jolivot, A., Regnard, J.L., 2016. Field phenotyping of water stress at tree scale by UAV-sensed imagery: new insights for thermal acquisition and calibration. *Precis. Agric.* 17, 786–800. <https://doi.org/10.1007/s11119-016-9449-6>
- Gonzalez-Dugo, V., Zarco-Tejada, P., Berni, J.A.J., Suárez, L., Goldhamer, D., Fereres, E., 2012. Almond tree canopy temperature reveals intra-crown variability that is water stress-dependent. *Agric. For. Meteorol.* 154–155, 156. <https://doi.org/10.1016/j.agrformet.2011.11.004>

- Gonzalez-Dugo, V., Zarco-Tejada, P., Nicolás, E., Nortes, P.A., Alarcón, J.J., Intrigliolo, D.S., Fereres, E., 2013. Using high resolution UAV thermal imagery to assess the variability in the water status of five fruit tree species within a commercial orchard. *Precis. Agric.* 14, 660–678. <https://doi.org/10.1007/s11119-013-9322-9>
- Gonzalez-Dugo, V., Zarco-Tejada, P.J., Fereres, E., 2014. Applicability and limitations of using the crop water stress index as an indicator of water deficits in citrus orchards. *Agric. For. Meteorol.* 198–199, 94–104. <https://doi.org/10.1016/j.agrformet.2014.08.003>
- Goutte, C., Gaussier, E., 2005. A Probabilistic Interpretation of Precision, Recall and F-Score, with Implication for Evaluation. *Lect. Notes Comput. Sci.* 3408, 345–359. https://doi.org/10.1007/978-3-540-31865-1_25
- Goward, S.N., Davis, P.E., Fleming, D., Miller, L., Townshend, J.R., 2003. Empirical comparison of Landsat 7 and IKONOS multispectral measurements for selected Earth Observation System (EOS) validation sites. *Remote Sens. Environ.* 88, 80–99. <https://doi.org/10.1016/j.rse.2003.07.009>
- Gracia-Romero, A.; Kefauver, S.C.; Fernandez-Gallego, J.A.; Vergara-Díaz, O.; Nieto-Taladriz, M.T.; Araus, J.L. UAV and ground image-based phenotyping: A proof of concept with durum wheat. *Remote Sens.* 2019, 11, doi:10.3390/rs11101244
- Griffith, D.C., Hay, G.J., 2018. Integrating GEOBIA , Machine Learning , and Volunteered Geographic Information to Map Vegetation over Rooftops. <https://doi.org/10.3390/ijgi7120462>
- Hay, G.J., Castilla, G., 2008. Geographic object-based image analysis (GEOBIA): A new name for a new discipline. *Lect. Notes Geoinf. Cartogr.* 75–89. https://doi.org/10.1007/978-3-540-77058-9_4
- Hay, G.J., Castilla, G., 2006. Object-based image analysis: Strengths, weaknesses, opportunities and threats (SWOT), in: *The International Archives of the Photogrammetry, Remote Sensing and Spatial Information Sciences*. pp. 4–5.
- He, Y., Weng, Q., 2018. High spatial resolution remote sensing. *Data, Analysis, and Applications, Computer Applications in Sustainable Forest Management*.
- Herwitz, S.R., Johnson, L.F., Dunagan, S.E., Higgins, R.G., Sullivan, D. V., Zheng, J., Lobitz, B.M., Leung, J.G., Gallmeyer, B.A., Aoyagi, M., Slye, R.E., Brass, J.A., 2004. Imaging from an unmanned aerial vehicle: Agricultural surveillance and decision support. *Comput. Electron. Agric.* 44, 49–61. <https://doi.org/10.1016/j.compag.2004.02.006>
- Hipps, L.E., Asrar, G., Kanemasu, E.T., 1985. A theoretically-based normalization of environmental effects on foliage temperature. *Agric. For. Meteorol.* 35, 113–122. [https://doi.org/10.1016/0168-1923\(85\)90078-4](https://doi.org/10.1016/0168-1923(85)90078-4)
- Hoffmann, H., Nieto, H., Jensen, R., Guzinski, R., Zarco-Tejada, P., Friborg, T., 2016. Estimating evaporation with thermal UAV data and two-source energy balance models. *Hydrol. Earth Syst. Sci.* 20, 697–713. <https://doi.org/10.5194/hess-20-697-2016>
- Hofmann, P., Blaschke, T., Strobl, J., 2011. Quantifying the robustness of fuzzy rule sets in object-based image analysis. *Int. J. Remote Sens.* 32, 7359–7381. <https://doi.org/10.1080/01431161.2010.523727>
- Hossain, M.D., Chen, D., 2019. Segmentation for Object-Based Image Analysis (OBIA): A review of algorithms and challenges from remote sensing perspective. *ISPRS J. Photogramm. Remote Sens.* 150, 115–134. <https://doi.org/10.1016/j.isprsjprs.2019.02.009>
- Houborg, R., McCabe, M.F., 2016. High-Resolution NDVI from planet’s constellation of earth observing nano-satellites: A new data source for precision agriculture. *Remote Sens.* 8.

<https://doi.org/10.3390/rs8090768>

- Hsiao, T.C., 1973. Plants response to water stress. *Ann Rev. Plant Physiol.* 24, 519–570.
- Huang, C., Davis, L.S., Townshend, J.R.G., 2002. An assessment of support vector machines for land cover classification. *Int. J. Remote Sens.* 23, 725–749. <https://doi.org/10.1080/01431160110040323>
- Huang, H., Lan, Y., Yang, A., Zhang, Y., Wen, S., Deng, J., 2020. Deep learning versus Object-based Image Analysis (OBIA) in weed mapping of UAV imagery. *Int. J. Remote Sens.* 41, 3446–3479. <https://doi.org/10.1080/01431161.2019.1706112>
- Huang, K., Li, S., Kang, X., Fang, L., 2016. Spectral–Spatial Hyperspectral Image Classification Based on KNN. *Sens. Imaging* 17, 1–13. <https://doi.org/10.1007/s11220-015-0126-z>
- Huete, A., Didan, K., Miura, T., Rodriguez, E.P., Gao, X., Ferreira, L.G., 2002. Overview of the radiometric and biophysical performance of the MODIS vegetation indices. *Remote Sens. Environ.* 83, 195–213. [https://doi.org/10.1016/S0034-4257\(02\)00096-2](https://doi.org/10.1016/S0034-4257(02)00096-2)
- Huete, A., Justice, C., Liu, H., 1994. Development of vegetation and soil indices for MODIS-EOS. *Remote Sens. Environ.* 49, 224–234. [https://doi.org/10.1016/0034-4257\(94\)90018-3](https://doi.org/10.1016/0034-4257(94)90018-3)
- Huete, A.R., 1988. A soil-adjusted vegetation index (SAVI). *Remote Sens. Environ.* 25, 295–309. [https://doi.org/10.1016/0034-4257\(88\)90106X](https://doi.org/10.1016/0034-4257(88)90106X)
- Huete, A.R., Jackson, R.D., Post, D.F., 1985. Spectral response of a plant canopy with different soil backgrounds. *Remote Sens. Environ.* 17, 37–53. [https://doi.org/10.1016/0034-4257\(85\)90111-7](https://doi.org/10.1016/0034-4257(85)90111-7)
- Huete, A.R., Liu, H.Q., Batchily, K., Van Leeuwen, W., 1997. A comparison of vegetation indices over a global set of TM images for EOS-MODIS. *Remote Sens. Environ.* 59, 440–451. [https://doi.org/10.1016/S0034-4257\(96\)00112-5](https://doi.org/10.1016/S0034-4257(96)00112-5)
- Hyseni, G., Caka, N., Hyseni, K., 2010. Infrared thermal detectors parameters: Semiconductor bolometers versus pyroelectrics. *WSEAS Trans. Circuits Syst.* 9, 238–247.
- Idso, S.B., Jackson, R.D., Pinter, P.J., Reginato, R.J., Hatfield, J.L., 1981. Normalizing the stress-degree-day parameter for environmental variability. *Agric. Meteorol.* 24, 45–55. [https://doi.org/10.1016/0002-1571\(81\)90032-7](https://doi.org/10.1016/0002-1571(81)90032-7)
- Immitzer, M., Vuolo, F., Atzberger, C., 2016. First experience with Sentinel-2 data for crop and tree species classifications in central Europe. *Remote Sens.* 8. <https://doi.org/10.3390/rs8030166>
- Iniesta, F., Testi, L., Orgaz, F., Villalobos, F.J., 2009. The effects of regulated and continuous deficit irrigation on the water use, growth and yield of olive trees. *Eur. J. Agron.* 30, 258–265. <https://doi.org/10.1016/j.eja.2008.12.004>
- Iqbal, F., Lucieer, A., Barry, K., 2018. Poppy crop capsule volume estimation using UAS remote sensing and random forest regression. *Int. J. Appl. Earth Obs. Geoinf.* 73, 362–373. <https://doi.org/10.1016/j.jag.2018.06.008>
- ISPAG, 2019. ISPAG, 2019. Precision Agriculture definition [WWW Document]. URL <https://www.springer.com/journal/11119/updates/17240272> (accessed 4.18.20).
- Jackson, R.D., Idso, S.B., Reginato, R.J., Pinter, J.P.J., 1981. Canopy temperature as a crop water stress indicator. *Water Resour. Res.* 17, 1133–1138. <https://doi.org/10.1029/WR017i004p01133>
- Jacob, F., Petitcolin, F., Schmutge, T., Vermote, É., French, A., Ogawa, K., 2004. Comparison of land surface emissivity and radiometric temperature derived from MODIS and ASTER sensors. *Remote*

Sens. Environ. 90, 137–152. <https://doi.org/10.1016/j.rse.2003.11.015>

- Jensen, A.M., McKee, M., Chen, Y., 2014. Procedures for processing thermal images using low-cost microbolometer cameras for small unmanned aerial systems. *Int. Geosci. Remote Sens. Symp.* 2629–2632. <https://doi.org/10.1109/IGARSS.2014.6947013>
- Jensen, J.R., 2014. *Remote sensing of the environment: an earth resource perspective second edition*, Pearson Education Limited, Harlow, England.
- Jeong, S., Kim, D., Yun, H., Cho, W., Kwon, Y., Kim, H., 2014. Monitoring the growth status variability in Onion (*Allium cepa*) and Garlic (*Allium sativum*) with RGB and multi-spectral UAV remote sensing imagery 1–6.
- Jiménez-Brenes, F.M., López-Granados, F., De Castro, A.I., Torres-Sánchez, J., Serrano, N., Peña, J.M., 2017. Quantifying pruning impacts on olive tree architecture and annual canopy growth by using UAV-based 3D modelling. *Plant Methods* 13, 55. <https://doi.org/10.1186/s13007-017-0205-3>
- Jones, H., Sirault, X., 2014. Scaling of Thermal Images at Different Spatial Resolution: The Mixed Pixel Problem. *Agronomy* 4, 380–396. <https://doi.org/10.3390/agronomy4030380>
- Jones, H.G., 2018. Thermal imaging and infrared sensing in plant ecophysiology. *Adv. Plant Ecophysiol. Tech.* 135–151. https://doi.org/10.1007/978-3-319-93233-0_8
- Jones, H.G., 1999. Use of infrared thermometry for estimation of stomatal conductance as a possible aid to irrigation scheduling. *Agric. For. Meteorol.* 95, 139–149. [https://doi.org/10.1016/S0168-1923\(99\)00030-1](https://doi.org/10.1016/S0168-1923(99)00030-1)
- Jones, H.G., Serraj, R., Loveys, B.R., Xiong, L., Wheaton, A., Price, A.H., 2009. Thermal infrared imaging of crop canopies for the remote diagnosis and quantification of plant responses to water stress in the field. *Funct. Plant Biol.* 36, 978–989. <https://doi.org/10.1071/FP09123>
- Jones, H.G., Vaughan, R.A., 2010. *Remote Sensing of Vegetation Principles, Techniques, and Applications*. Oxford University Press, Oxford, UK.
- Jorge, J., Vallbé, M., Soler, J.A., 2019. Detection of irrigation inhomogeneities in an olive grove using the NDRE vegetation index obtained from UAV images. *Eur. J. Remote Sens.* 52, 169–177. <https://doi.org/10.1080/22797254.2019.1572459>
- Kääb, A., Altena, B., Mascaro, J., 2017. Coseismic displacements of the 14 November 2016 Mw 7.8 Kaikoura, New Zealand, earthquake using the Planet optical cubesat constellation. *Nat. Hazards Earth Syst. Sci.* 17, 627–639. <https://doi.org/10.5194/nhess-17-627-2017>
- Kaplan, H., 2009. *Practical Applications of Infrared Thermal Sensing and Imaging Equipment, Third Edition*, Practical Applications of Infrared Thermal Sensing and Imaging Equipment, Third Edition. <https://doi.org/10.1117/3.725072>
- Karnieli, A., Agam, N., Pinker, R.T., Anderson, M., Imhoff, M.L., Gutman, G.G., Panov, N., Goldberg, A., 2010. Use of NDVI and land surface temperature for drought assessment: Merits and limitations. *J. Clim.* 23, 618–633. <https://doi.org/10.1175/2009JCLI2900.1>
- Kaufman, Y.J., Remer, L.A., 1994. Detection of Forests Using Mid-IR Reflectance: An Application for Aerosol Studies. *IEEE Trans. Geosci. Remote Sens.* 32, 672–683. <https://doi.org/10.1109/36.297984>
- Kelly, J., Eklundh, L., Kljun, N., 2018. Radiometric calibration of a UAV thermal camera 10.
- Kelly, J., Kljun, N., Olsson, P.O., Mihai, L., Liljeblad, B., Weslien, P., Klemedtsson, L., Eklundh, L., 2019. Challenges and best practices for deriving temperature data from an uncalibrated UAV thermal

- infrared camera. *Remote Sens.* 11. <https://doi.org/10.3390/rs11050567>
- Khaliq, A., Comba, L., Biglia, A., Ricauda Aimonino, D., Chiaberge, M., Gay, P., 2019. Comparison of satellite and UAV-based multispectral imagery for vineyard variability assessment. *Remote Sens.* 11. <https://doi.org/10.3390/rs11040436>
- Khanal, S., Fulton, J., Shearer, S., 2017. An overview of current and potential applications of thermal remote sensing in precision agriculture. *Comput. Electron. Agric.* 139, 22–32. <https://doi.org/10.1016/j.compag.2017.05.001>
- Koc-San, D., Selim, S., Aslan, N., San, B.T., 2018. Automatic citrus tree extraction from UAV images and digital surface models using circular Hough transform. *Comput. Electron. Agric.* 150, 289–301. <https://doi.org/10.1016/j.compag.2018.05.001>
- Kuenzer, C., Dech, S., Zhang, J., Jing, L., Huadong, G., 2013. Thermal infrared remote sensing: Sensors, Methods, Applications, in: *Remote Sensing and Digital Image Processing*. Springer: Heidelberg, Germany. https://doi.org/10.1007/978-94-007-6639-6_21
- Lal, R., Taylor, G.S., 1970. Drainage and Nutrient Effects in a Field Lysimeter Study: II. Mineral Uptake by Corn. *Soil Sci. Soc. Am. J.* 34, 245–248. <https://doi.org/10.2136/sssaj1970.03615995003400020020x>
- Laliberte, A.S., Rango, A., 2009. Texture and scale in object-based analysis of subdecimeter resolution unmanned aerial vehicle (UAV) imagery. *IEEE Trans. Geosci. Remote Sens.* 47, 1–10. <https://doi.org/10.1109/TGRS.2008.2009355>
- Lamb, D.W., Brown, R.B., 2001. PA – Precision Agriculture: Remote-Sensing and Mapping of Weeds in Crops. *J. Agric. Eng. Res.* <https://doi.org/10.1006/jaer.2000.0630>
- Lapidot, O., Ignat, T., Rud, R., Rog, I., Alchanatis, V., Klein, T., 2019. Use of thermal imaging to detect evaporative cooling in coniferous and broadleaved tree species of the Mediterranean maquis. *Agric. For. Meteorol.* 271, 285–294. <https://doi.org/10.1016/j.agrformet.2019.02.014>
- Larson, W.E., Robert, P.C., 1991. Farming by Soil, in: *Soil Management for Sustainability*. pp. 103–112.
- Lee, W.S., Alchanatis, V., Yang, C., Hirafuji, M., Moshou, D., Li, C., 2010. Sensing technologies for precision specialty crop production. *Comput. Electron. Agric.* 74, 2–33. <https://doi.org/10.1016/j.compag.2010.08.005>
- Li, M., Ma, L., Blaschke, T., Cheng, L., Tiede, D., 2016. A systematic comparison of different object-based classification techniques using high spatial resolution imagery in agricultural environments. *Int. J. Appl. Earth Obs. Geoinf.* 49, 87–98. <https://doi.org/10.1016/j.jag.2016.01.011>
- Li, W., Guo, Q., Jakubowski, M.K., Kelly, M., 2012. A New Method for Segmenting Individual Trees from the Lidar Point Cloud. *Photogramm. Eng. Remote Sens.* 78, 75–84. <https://doi.org/10.14358/PERS.78.1.75>
- Li, W., Niu, Z., Chen, H., Li, D., Wu, M., Zhao, W., 2016. Remote estimation of canopy height and aboveground biomass of maize using high-resolution stereo images from a low-cost unmanned aerial vehicle system. *Ecol. Indic.* 67, 637–648. <https://doi.org/10.1016/j.ecolind.2016.03.036>
- Li, Z., Zhang, H.K., Roy, D.P., Yan, L., Huang, H., 2020. Sharpening the Sentinel-2 10 and 20 m Bands to PlanetScope-0 3 m Resolution. *Remote Sens.* 12, 2406. <https://doi.org/10.3390/rs12152406>
- Liakos, K.G., Busato, P., Moshou, D., Pearson, S., Bochtis, D., 2018. Machine learning in agriculture: A review. *Sensors (Switzerland)* 18, 1–29. <https://doi.org/10.3390/s18082674>
- Lillesand, T., Kiefer, R.W., Chipman, J., 2015. *Remote sensing and image interpretation*, 7th ed. Wiley

and sons, New York.

- Liu, T., Li, R., Zhong, X., Jiang, M., Jin, X., Zhou, P., Liu, S., Sun, C., Guo, W., 2018. Estimates of rice lodging using indices derived from UAV visible and thermal infrared images. *Agric. For. Meteorol.* 252, 144–154. <https://doi.org/10.1016/j.agrformet.2018.01.021>
- Lopes, M.S., Reynolds, M.P., 2010. Partitioning of assimilates to deeper roots is associated with cooler canopies and increased yield under drought in wheat. *Funct. Plant Biol.* 37, 147–156. <https://doi.org/10.1071/FP09121>
- López-Granados, F., Torres-Sánchez, J., De Castro, A.I., Serrano-Pérez, A., Mesas-Carrascosa, F.J., Peña, J.M., 2016a. Object-based early monitoring of a grass weed in a grass crop using high resolution UAV imagery. *Agron. Sustain. Dev.* 36. <https://doi.org/10.1007/s13593-016-0405-7>
- López-Granados, F., Torres-Sánchez, J., Serrano-Pérez, A., De Castro, A.I., Mesas-Carrascosa, F.J., Peña, J.M., 2016b. Early season weed mapping in sunflower using UAV technology: variability of herbicide treatment maps against weed thresholds. *Precis. Agric.* 17, 183–199. <https://doi.org/10.1007/s11119-015-9415-8>
- López, A., Molina-Aiz, F.D., Valera, D.L., Peña, A., 2012. Determining the emissivity of the leaves of nine horticultural crops by means of infrared thermography. *Sci. Hortic. (Amsterdam)*. 137, 49–58. <https://doi.org/10.1016/j.scienta.2012.01.022>
- Ludovisi, R., Tauro, F., Salvati, R., Khoury, S., Mugnozza, G.S., Harfouche, A., 2017. Uav-based thermal imaging for high-throughput field phenotyping of black poplar response to drought. *Front. Plant Sci.* 8, 1–18. <https://doi.org/10.3389/fpls.2017.01681>
- Luhmann, T., Piechel, J., Roelfs, T., 2013. Geometric calibration of thermographic cameras. *Remote Sens. Digit. Image Process.* 17, 27–42. https://doi.org/10.1007/978-94-007-6639-6_2
- Ma, L., Cheng, L., Li, M., Liu, Y., Ma, X., 2015. Training set size, scale, and features in Geographic Object-Based Image Analysis of very high resolution unmanned aerial vehicle imagery. *ISPRS J. Photogramm. Remote Sens.* 102, 14–27. <https://doi.org/10.1016/j.isprsjprs.2014.12.026>
- Ma, L., Li, M., Ma, X., Cheng, L., Du, P., Liu, Y., 2017. A review of supervised object-based land-cover image classification. *ISPRS J. Photogramm. Remote Sens.* 130, 277–293. <https://doi.org/10.1016/j.isprsjprs.2017.06.001>
- Maes, W., Huete, A., Steppe, K., 2017. Optimizing the Processing of UAV-Based Thermal Imagery. *Remote Sens.* 9, 476. <https://doi.org/10.3390/rs9050476>
- Maes, W.H., Achten, W.M.J., Reubens, B., Muys, B., 2011. Monitoring stomatal conductance of *Jatropha curcas* seedlings under different levels of water shortage with infrared thermography. *Agric. For. Meteorol.* 151, 554–564. <https://doi.org/10.1016/j.agrformet.2010.12.011>
- Maes, W.H., Baert, A., Huete, A.R., Minchin, P.E.H., Snelgar, W.P., Steppe, K., 2016. A new wet reference target method for continuous infrared thermography of vegetations. *Agric. For. Meteorol.* 226–227, 119–131. <https://doi.org/10.1016/j.agrformet.2016.05.021>
- Maes, W.H., Pashuysen, T., Trabucco, A., Veroustraete, F., Muys, B., 2011. Does energy dissipation increase with ecosystem succession? Testing the ecosystem exergy theory combining theoretical simulations and thermal remote sensing observations. *Ecol. Modell.* 222, 3917–3941. <https://doi.org/10.1016/j.ecolmodel.2011.08.028>
- Maes, W.H., Steppe, K., 2019. Perspectives for Remote Sensing with Unmanned Aerial Vehicles in Precision Agriculture. *Trends Plant Sci.* 24, 152–164. <https://doi.org/10.1016/j.tplants.2018.11.007>

- Maes, W.H., Steppe, K., 2012. Estimating evapotranspiration and drought stress with ground-based thermal remote sensing in agriculture: a review. *J. Exp. Bot.* 63, 4671–4712. <https://doi.org/10.1093/jxb/ers165>
- Maimaitijiang, M., Ghulam, A., Sidike, P., Hartling, S., Maimaitiyiming, M., Peterson, K., Shavers, E., Fishman, J., Peterson, J., Kadam, S., Burken, J., Fritschi, F., 2017. Unmanned Aerial System (UAS)-based phenotyping of soybean using multi-sensor data fusion and extreme learning machine. *ISPRS J. Photogramm. Remote Sens.* 134, 43–58. <https://doi.org/10.1016/j.isprsjprs.2017.10.011>
- Maimaitijiang, M., Sagan, V., Sidike, P., Hartling, S., Esposito, F., Fritschi, F.B., 2020. Soybean yield prediction from UAV using multimodal data fusion and deep learning. *Remote Sens. Environ.* 237. <https://doi.org/10.1016/j.rse.2019.111599>
- Malacarne, D., Pappalardo, S.E., Codato, D., 2018. Sentinel-2 Data Analysis and Comparison with UAV Multispectral Images for Precision Viticulture. *GI_Forum* 105–116. https://doi.org/10.1553/giscience2018_01_s105
- Malambo, L., Popescu, S.C., Murray, S.C., Putman, E., Pugh, N.A., Horne, D.W., Richardson, G., Sheridan, R., Rooney, W.L., Avant, R., Vidrine, M., McCutchen, B., Baltensperger, D., Bishop, M., 2018. Multitemporal field-based plant height estimation using 3D point clouds generated from small unmanned aerial systems high-resolution imagery. *Int. J. Appl. Earth Obs. Geoinf.* 64, 31–42. <https://doi.org/10.1016/J.JAG.2017.08.014>
- Mallor, C., Balcells, M., Mallor, F., Sales, E., 2011. Genetic variation for bulb size, soluble solids content and pungency in the Spanish sweet onion variety Fuentes de Ebro. Response to selection for low pungency. *Plant Breed.* 130, 55–59. <https://doi.org/10.1111/j.1439-0523.2009.01737.x>
- Manfreda, S., McCabe, M.F., Miller, P.E., Lucas, R., Madrigal, V.P., Mallinis, G., Dor, E. Ben, Helman, D., Estes, L., Ciraolo, G., Müllerová, J., Tauro, F., de Lima, M.I., de Lima, J.L.M.P., Maltese, A., Frances, F., Caylor, K., Kohv, M., Perks, M., Ruiz-Pérez, G., Su, Z., Vico, G., Toth, B., 2018. On the use of unmanned aerial systems for environmental monitoring. *Remote Sens.* 10. <https://doi.org/10.3390/rs10040641>
- Martínez, J., Egea, G., Agüera, J., Pérez-Ruiz, M., 2017. A cost-effective canopy temperature measurement system for precision agriculture: a case study on sugar beet. *Precis. Agric.* 18, 95–110. <https://doi.org/10.1007/s11119-016-9470-9>
- Matese, A., Baraldi, R., Berton, A., Cesaraccio, C., Di Gennaro, S.F., Duce, P., Facini, O., Mameli, M.G., Piga, A., Zaldei, A., 2018. Estimation of Water Stress in grapevines using proximal and remote sensing methods. *Remote Sens.* 10, 1–16. <https://doi.org/10.3390/rs10010114>
- Matese, A., Toscano, P., Di Gennaro, S.F., Genesio, L., Vaccari, F.P., Primicerio, J., Belli, C., Zaldei, A., Bianconi, R., Gioli, B., 2015. Intercomparison of UAV, aircraft and satellite remote sensing platforms for precision viticulture. *Remote Sens.* 7, 2971–2990. <https://doi.org/10.3390/rs70302971>
- Maxwell, A.E., Warner, T.A., Fang, F., 2018. Implementation of machine-learning classification in remote sensing: An applied review. *Int. J. Remote Sens.* 39, 2784–2817. <https://doi.org/10.1080/01431161.2018.1433343>
- McCabe, M.F., Houborg, R., Lucieer, A., 2016. High-resolution sensing for precision agriculture: from Earth-observing satellites to unmanned aerial vehicles. *Remote Sens. Agric. Ecosyst. Hydrol.* XVIII 9998, 999811. <https://doi.org/10.1117/12.2241289>
- Meena, A.K., 2019. Use of Precision Agriculture for Sustainability and Environmental Protection.
- Meier, U., 2001. Growth stages of mono- and dicotyledonous plants, BBCH Monograph.

<https://doi.org/10.5073/bbch0515>

- Mesas-Carrascosa, F.-J., Pérez-Porras, F., Meroño de Larriva, J., Mena Frau, C., Agüera-Vega, F., Carvajal-Ramírez, F., Martínez-Carricondo, P., García-Ferrer, A., 2018. Drift Correction of Lightweight Microbolometer Thermal Sensors On-Board Unmanned Aerial Vehicles. *Remote Sens.* 10, 615. <https://doi.org/10.3390/rs10040615>
- Messina, G., Fiozzo, V., Praticò, S., Siciliani, B., Curcio, A., Di Fazio, S., Modica, G., 2020a. Monitoring Onion Crops Using Multispectral Imagery from Unmanned Aerial Vehicle (UAV), in: Bevilacqua, C., Francesco, C., Della Spina, L. (Eds.), "NEW METROPOLITAN PERSPECTIVES. Knowledge Dynamics and Innovation-Driven Policies Towards Urban and Regional Transition"(Vol.2). Springer, Reggio Calabria, Italy, pp. 1640–1649.
- Messina, G., Modica, G., 2020b. Applications of UAV thermal imagery in precision agriculture: State of the art and future research outlook. *Remote Sens.* 12. <https://doi.org/10.3390/RS12091491>
- Messina, G., Peña, J.M., Vizzari, M., Modica, G., 2020c. A Comparison of UAV and Satellites Multispectral Imagery in Monitoring Onion Crop. An Application in the "Cipolla Rossa di Tropea" (Italy). *Remote Sens.* 12, 3424. <https://doi.org/10.3390/rs12203424>
- Messina, G., Praticò, S., Siciliani, B., Curcio, A., Di Fazio, S., Modica, G., 2020d. Telerilevamento multispettrale da drone per il monitoraggio delle colture in agricoltura di precisione. Un'applicazione alla cipolla rossa di Tropea (Multispectral UAV remote sensing for crop monitoring in precision farming. An application to the Red onion of Tropea). *LaborEst* 21, <https://doi.org/10.19254/LaborEst.21.12>.
- Messina, G., Praticò, S., Siciliani, B., Curcio, A., Di Fazio, S., Modica, G., 2019. Monitoring onion crops using UAV multispectral and thermal imagery. *Conf. AIIA Mid-Term 2019 Biosyst. Eng. Sustain. Agric. For. food Prod. Matera*.
- Mira, M., Valor, E., Boluda, R., Caselles, V., Coll, C., 2007. Influence of soil water content on the thermal infrared emissivity of bare soils: Implication for land surface temperature determination. *J. Geophys. Res. Earth Surf.* 112, 1–11. <https://doi.org/10.1029/2007JF000749>
- Miura, T., Yoshioka, H., Fujiwara, K., Yamamoto, H., 2008. Inter-comparison of ASTER and MODIS surface reflectance and vegetation index products for synergistic applications to natural resource monitoring. *Sensors* 8, 2480–2499. <https://doi.org/10.3390/s8042480>
- Modica, G., Messina, G., De Luca, G., Fiozzo, V., Praticò, S., 2020. Monitoring the vegetation vigor in heterogeneous citrus and olive orchards. A multiscale object-based approach to extract trees' crowns from UAV multispectral imagery. *Comput. Electron. Agric.* 175, 105500. <https://doi.org/10.1016/j.compag.2020.105500>
- Modica, G., Pollino, M., Solano, F., 2019. Sentinel-2 Imagery for Mapping Cork Oak (*Quercus suber* L.) Distribution in Calabria (Italy): Capabilities and Quantitative Estimation, in: *New Metropolitan Perspectives. ISHT 2018. Smart Innovation, Systems and Technologies*, Calabrò, F.; Della Spina, L.; Bevilacqua, C., Eds.; Springer: Cham, pp. 60–67. <https://doi.org/10.1007/978-3-319-92099-3>
- Modica, G., Praticò, S., Di Fazio, S., 2017. Abandonment of traditional terraced landscape: A change detection approach (a case study in Costa Viola, Calabria, Italy). *L. Degrad. Dev.* 28, 2608–2622. <https://doi.org/10.1002/ldr.2824>
- Mohan, M., Silva, C.A., Klauberg, C., Jat, P., Catts, G., Cardil, A., Hudak, A.T., Dia, M., 2017. Individual tree detection from unmanned aerial vehicle (UAV) derived canopy height model in an open canopy mixed conifer forest. *Forests* 8. <https://doi.org/10.3390/f8090340>

- Moran, M.S., Inoue, Y., Barnes, E.M., 2000. Opportunities and Limitations for Image-Based Crop Management 319346.
- Mountrakis, G., Im, J., Ogole, C., 2011. Support vector machines in remote sensing: A review. *ISPRS J. Photogramm. Remote Sens.* 66, 247–259. <https://doi.org/10.1016/j.isprsjprs.2010.11.001>
- Mulla, D.J., 2013. Twenty five years of remote sensing in precision agriculture: Key advances and remaining knowledge gaps. *Biosyst. Eng.* 114, 358–371. <https://doi.org/10.1016/j.biosystemseng.2012.08.009>
- Natarajan, S., Basnayake, J., Wei, X., Lakshmanan, P., 2019. High-throughput phenotyping of indirect traits for early-stage selection in sugarcane breeding. *Remote Sens.* 11. <https://doi.org/10.3390/rs11242952>
- Neely, L., Rana, A., Bagavathiannan, M. V, Henrickson, J., Putman, E.B., Popescu, S., Burks, T., Cope, D., Ibrahim, A., 2016. Unmanned Aerial Vehicles for High- Throughput Phenotyping and Agronomic. *PLoS One* c, 1–26. <https://doi.org/10.5061/dryad.65m87>
- Nesci, F.S., Sapone, N., 2014. BERGAMOT - A Green and Multifunctional Asset Exclusive from the Province of Reggio Calabria. *Adv. Eng. Forum* 11, 376–379. <https://doi.org/10.4028/www.scientific.net/aef.11.376>
- Nex, F., Remondino, F., 2014. UAV for 3D mapping applications: A review. *Appl. Geomatics* 6, 1–15. <https://doi.org/10.1007/s12518-013-0120-x>
- Noi, P.T., Kappas, M., 2018. Comparison of random forest, k-nearest neighbor, and support vector machine classifiers for land cover classification using sentinel-2 imagery. *Sensors (Switzerland)* 18. <https://doi.org/10.3390/s18010018>
- Ok, A.O., Ozdarici-Ok, A., 2018. 2-D delineation of individual citrus trees from UAV-based dense photogrammetric surface models. *Int. J. Digit. Earth* 11, 583–608. <https://doi.org/10.1080/17538947.2017.1337820>
- Ok, A.O., Senaras, C., Yuksel, B., 2013. Automated Detection of Arbitrarily Shaped Buildings in Complex Environments From Monocular VHR Optical Satellite Imagery. *IEEE Trans. Geosci. Remote Sens.* 51, 1701–1717. <https://doi.org/10.1109/TGRS.2012.2207123>
- Olbrycht, R., Wiecek, B., De Mey, G., 2012. Thermal drift compensation method for microbolometer thermal cameras. *Appl. Opt.* 51, 1788–1794. <https://doi.org/10.1364/AO.51.001788>
- Ortega-Farías, S., Ortega-Salazar, S., Poblete, T., Kilic, A., Allen, R., Poblete-Echeverría, C., Ahumada-Orellana, L., Zuñiga, M., Sepúlveda, D., 2016. Estimation of Energy Balance Components over a Drip-Irrigated Olive Orchard Using Thermal and Multispectral Cameras Placed on a Helicopter-Based Unmanned Aerial Vehicle (UAV). *Remote Sens.* 8, 638. <https://doi.org/10.3390/rs8080638>
- Ozdarici-Ok, A., 2015. Automatic detection and delineation of citrus trees from VHR satellite imagery. *Int. J. Remote Sens.* 36, 4275–4296. <https://doi.org/10.1080/01431161.2015.1079663>
- Pádua, L., Adão, T., Sousa, A., Peres, E., Sousa, J.J., 2020. Individual Grapevine Analysis in a Multi-Temporal Context Using UAV-Based Multi-Sensor Imagery. *Remote Sens.* 12, 139. <https://doi.org/10.3390/rs12010139>
- Pádua, L., Marques, P., Adão, T., Guimarães, N., Sousa, A., Peres, E., Sousa, J.J., 2019. Vineyard variability analysis through UAV-based vigor maps to assess climate change impacts. *Agronomy* 9. <https://doi.org/10.3390/agronomy9100581>

- Pádua, L., Vanko, J., Hruška, J., Adão, T., Sousa, J.J., Peres, E., Morais, R., 2017. UAS, sensors, and data processing in agroforestry: a review towards practical applications. *Int. J. Remote Sens.* 38, 2349–2391. <https://doi.org/10.1080/01431161.2017.1297548>
- Pajares, G., 2015. Overview and Current Status of Remote Sensing Applications Based on Unmanned Aerial Vehicles (UAVs). *Photogramm. Eng. Remote Sens.* 81, 281–330. <https://doi.org/10.14358/PERS.81.4.281>
- Pal, N.R., Pal, S.K., 1993. A review on image segmentation techniques. *Pattern Recognit.* [https://doi.org/10.1016/0031-3203\(93\)90135-J](https://doi.org/10.1016/0031-3203(93)90135-J)
- Palese, A.M., Nuzzo, V., Favati, F., Pietrafesa, A., Celano, G., Xiloyannis, C., 2010. Effects of water deficit on the vegetative response, yield and oil quality of olive trees (*Olea europaea* L., cv Coratina) grown under intensive cultivation. *Sci. Hortic. (Amsterdam)*. 125, 222–229. <https://doi.org/10.1016/j.scienta.2010.03.025>
- Panagiotidis, D., Abdollahnejad, A., Surový, P., Chiteculo, V., 2017. Determining tree height and crown diameter from high-resolution UAV imagery. *Int. J. Remote Sens.* 38, 2392–2410. <https://doi.org/10.1080/01431161.2016.1264028>
- Pande-Chhetri, R., Abd-Elrahman, A., Liu, T., Morton, J., Wilhelm, V.L., 2017. Object-based classification of wetland vegetation using very high-resolution unmanned air system imagery. *Eur. J. Remote Sens.* 50, 564–576. <https://doi.org/10.1080/22797254.2017.1373602>
- Pareek, S., Sagar, N.A., Sharma, S., Kumar, V., 2017. Onion (*Allium cepa* L.), in: Yahia, E.M. (Ed.), *Fruit and Vegetable Phytochemicals: Chemistry and Human Health*. pp. 1145–1159. <https://doi.org/10.1002/9781119158042.ch58>
- Parisi, E.I., Suma, M., Güleç Korumaz, A., Rosina, E., Tucci, G., 2019. Aerial platforms (uav) surveys in the vis and tir range. Applications on archaeology and agriculture. *ISPRS Ann. Photogramm. Remote Sens. Spat. Inf. Sci.* 42, 945–952. <https://doi.org/10.5194/isprs-Archives-XLII-2-W11-945-2019>
- Park, S., Ryu, D., Fuentes, S., Chung, H., Hernández-Montes, E., O'Connell, M., 2017. Adaptive estimation of crop water stress in nectarine and peach orchards using high-resolution imagery from an unmanned aerial vehicle (UAV). *Remote Sens.* 9. <https://doi.org/10.3390/rs9080828>
- Pavelis, G.A., 1987. Economic Survey of Farm Drainage. Doc. RESUME CE 050 265 Pavelis, Georg. A., Ed. *Farm Drain. United States. Hist. Status, Prospect. Misc. Publ. Number 110.*
- Pech, K., Stelling, N., Karrasch, P., De, H.M., 2013. Generation of Multitemporal Thermal Orthophotos From UAV Data. *Int. Arch. Photogramm. Remote Sens.* XL, 4–6.
- Peña, J.M., Kelly, M., De Castro, A.I., López-Granados, F., 2012. Discrimination of crop rows using object-based approaches in UAV images for early site-specific weed management in maize fields. *Proc. 1st Int. Conf. Robot. Assoc. High Technol. Equip. Agric.* 249–254.
- Peña, J.M., Torres-Sánchez, J., De Castro, A.I., Kelly, M., López-Granados, F., 2013. Weed Mapping in Early-Season Maize Fields Using Object-Based Analysis of Unmanned Aerial Vehicle (UAV) Images. *PLoS One* 8. <https://doi.org/10.1371/journal.pone.0077151>
- Peña, J.M., Torres-Sánchez, J., Serrano-Pérez, A., De Castro, A., López-Granados, F., 2015. Quantifying Efficacy and Limits of Unmanned Aerial Vehicle (UAV) Technology for Weed Seedling Detection as Affected by Sensor Resolution. *Sensors* 15, 5609–5626. <https://doi.org/10.3390/s150305609>
- Peña Barragán, J.M., Kelly, M., Castro, A.I. de, López Granados, F., 2012. Object-based approach for

- crop row characterization in UAV images for site-specific weed management. Queiroz-Feitosa al., Ed. 4th Int. Conf. Geogr. Object-Based Image Anal. (GEOBIA 2012), Rio Janeiro, Brazil 426–430.
- Perez-Ortiz, M., Gutierrez, P.A., Pena, J.M., Torres-Sanchez, J., Lopez-Granados, F., Hervás-Martínez, C., 2017. Machine learning paradigms for weed mapping via unmanned aerial vehicles. 2016 IEEE Symp. Ser. Comput. Intell. SSCI 2016. <https://doi.org/10.1109/SSCI.2016.7849987>
- Pérez-Ortiz, M., Peña, J.M., Gutiérrez, P.A., Torres-Sánchez, J., Hervás-Martínez, C., López-Granados, F., 2016. Selecting patterns and features for between- and within- crop-row weed mapping using UAV-imagery. *Expert Syst. Appl.* 47, 85–94. <https://doi.org/10.1016/j.eswa.2015.10.043>
- Pérez-Ortiz, M., Peña, J.M., Gutiérrez, P.A., Torres-Sánchez, J., Hervás-Martínez, C., López-Granados, F., 2015. A semi-supervised system for weed mapping in sunflower crops using unmanned aerial vehicles and a crop row detection method. *Appl. Soft Comput.* 37, 533–544. <https://doi.org/10.1016/j.asoc.2015.08.027>
- Perich, G., Hund, A., Anderegg, J., Roth, L., Boer, M.P., Walter, A., Liebisch, F., Aasen, H., 2020. Assessment of Multi-Image Unmanned Aerial Vehicle Based High-Throughput Field Phenotyping of Canopy Temperature. *Front. Plant Sci.* 11, 1–17. <https://doi.org/10.3389/fpls.2020.00150>
- Pernice, R., Borriello, G., Ferracane, R., Borrelli, R.C., Cennamo, F., Ritieni, A., 2009. Bergamot: A source of natural antioxidants for functionalized fruit juices. *Food Chem.* 112, 545–550. <https://doi.org/10.1016/j.foodchem.2008.06.004>
- Planet Labs Inc., 2020. Planet Imagery and Archive. URL <https://www.planet.com/products/planet-imagery/> (accessed 4.30.20).
- Poblete-Echeverría, C., Sepulveda-Reyes, D., Ortega-Farias, S., Zuñiga, M., Fuentes, S., 2016. Plant water stress detection based on aerial and terrestrial infrared thermography: A study case from vineyard and olive orchard. *Acta Hort.* 1112, 141–146. <https://doi.org/10.17660/ActaHortic.2016.1112.20>
- Popescu, S.C., 2007. Estimating biomass of individual pine trees using airborne lidar. *Biomass and Bioenergy* 31, 646–655. <https://doi.org/10.1016/j.biombioe.2007.06.022>
- Prakash, A., 2000. Thermal Remote Sensing : concepts , issues and applications. *Int. Arch. Photogramm. Remote Sens XXXIII*, 239–243.
- Primicerio, J., Di Gennaro, S.F., Fiorillo, E., Genesio, L., Lugato, E., Matese, A., Vaccari, F.P., 2012. A flexible unmanned aerial vehicle for precision agriculture. *Precis. Agric.* 13, 517–523. <https://doi.org/10.1007/s11119-012-9257-6>
- Primo-Millo, E., Agusti, M., 2020. Chapter 10 - Vegetative growth, in: Woodhead Publishing (Ed.), *The Genus Citrus*. Woodhead Publishing, Sawston, Cambridge. <https://doi.org/10.1016/B978-0-12-812163-4.00010-3>
- Prošek, J., Šimová, P., 2019. UAV for mapping shrubland vegetation: Does fusion of spectral and vertical information derived from a single sensor increase the classification accuracy? *Int. J. Appl. Earth Obs. Geoinf.* 75, 151–162. <https://doi.org/10.1016/J.JAG.2018.10.009>
- Psomiadis, E., Dercas, N., Dalezios, N.R., Spyropoulos, N. V., 2016. The role of spatial and spectral resolution on the effectiveness of satellite-based vegetation indices. *Remote Sens. Agric. Ecosyst. Hydrol.* XVIII 9998, 99981L. <https://doi.org/10.1117/12.2241316>
- Qian, Y., Zhou, W., Yan, J., Li, W., Han, L., 2015. Comparing machine learning classifiers for object-based land cover classification using very high resolution imagery. *Remote Sens.* 7, 153–168. <https://doi.org/10.3390/rs70100153>

- Quebrajo, L., Perez-Ruiz, M., Pérez-Urrestarazu, L., Martínez, G., Egea, G., 2018. Linking thermal imaging and soil remote sensing to enhance irrigation management of sugar beet. *Biosyst. Eng.* 165, 77–87. <https://doi.org/10.1016/j.biosystemseng.2017.08.013>
- Radoglou-Grammatikis, P., Sarigiannidis, P., Lagkas, T., Moscholios, I., 2020. A compilation of UAV applications for precision agriculture. *Comput. Networks.* <https://doi.org/10.1016/j.comnet.2020.107148>
- Raeva, P.L., Šedina, J., Dlesk, A., 2019. Monitoring of crop fields using multispectral and thermal imagery from UAV. *Eur. J. Remote Sens.* 52, 192–201. <https://doi.org/10.1080/22797254.2018.1527661>
- Ranjitkar, H., 2003. *A Handbook of Practical Botany*. Kathmandu.
- Rapinel, S., Mony, C., Lecoq, L., Clément, B., Thomas, A., Hubert-Moy, L., 2019. Evaluation of Sentinel-2 time-series for mapping floodplain grassland plant communities. *Remote Sens. Environ.* 223, 115–129. <https://doi.org/10.1016/j.rse.2019.01.018>
- Rapisarda, A., Paula Germano, M., 2014. Citrus bergamia: Bergamot and its Derivatives, in: *Citrus Bergamia: Bergamot and Its Derivatives*. pp. 9–24.
- Rehman, T.U., Mahmud, M.S., Chang, Y.K., Jin, J., Shin, J., 2019. Current and future applications of statistical machine learning algorithms for agricultural machine vision systems. *Comput. Electron. Agric.* 156, 585–605. <https://doi.org/10.1016/j.compag.2018.12.006>
- Ribeiro-Gomes, K., Hernández-López, D., Ortega, J., Ballesteros, R., Poblete, T., Moreno, M., 2017. Uncooled Thermal Camera Calibration and Optimization of the Photogrammetry Process for UAV Applications in Agriculture. *Sensors* 17, 2173. <https://doi.org/10.3390/s17102173>
- Richter, R., Schlapfer, D., 2019. Atmospheric and Topographic Correction : Model ATCOR3. *Aerospace* 3, 1–144.
- Robert, P.C., 2002. Precision agriculture: A challenge for crop nutrition management. *Plant Soil.* <https://doi.org/10.1023/A:1021171514148>
- Rodriguez-Galiano, V.F., Ghimire, B., Rogan, J., Chica-olmo, M., Rigol-sanchez, J.P., 2012. An assessment of the effectiveness of a random forest classifier for land-cover classification. *ISPRS J. Photogramm. Remote Sens.* 67, 93–104. <https://doi.org/10.1016/j.isprsjprs.2011.11.002>
- Romano, G., Zia, S., Spreer, W., Sanchez, C., Cairns, J., Araus, J.L., Müller, J., 2011. Use of thermography for high throughput phenotyping of tropical maize adaptation in water stress. *Comput. Electron. Agric.* 79, 67–74. <https://doi.org/10.1016/j.compag.2011.08.011>
- Romero-Trigueros, C., Nortes, P.A., Alarcón, J.J., Hunink, J.E., Parra, M., Contreras, S., Droogers, P., Nicolás, E., 2017. Effects of saline reclaimed waters and deficit irrigation on Citrus physiology assessed by UAV remote sensing. *Agric. Water Manag.* 183, 60–69. <https://doi.org/10.1016/j.agwat.2016.09.014>
- Rondeaux, G., Steven, M., Baret, F., 1996. Optimization of soil-adjusted vegetation indices. *Remote Sens. Environ.* 55, 95–107. [https://doi.org/10.1016/0034-4257\(95\)00186-7](https://doi.org/10.1016/0034-4257(95)00186-7)
- Roth, L., Streit, B., 2018. Predicting cover crop biomass by lightweight UAS-based RGB and NIR photography: an applied photogrammetric approach. *Precis. Agric.* 19, 93–114. <https://doi.org/10.1007/s11119-017-9501-1>
- Rouse, W., Haas, R.H., Deering, D.W., 1974. Monitoring vegetation systems in the Great Plains with

ERTS, NASA SP-351. Third ERTS-1 Symp. Vol. 1.

- Rud, R., Cohen, Y., Alchanatis, V., Levi, A., Brikman, R., Shenderey, C., Heuer, B., Markovitch, T., Dar, Z., Rosen, C., Mulla, D., Nigon, T., 2014. Crop water stress index derived from multi-year ground and aerial thermal images as an indicator of potato water status. *Precis. Agric.* 15, 273–289. <https://doi.org/10.1007/s11119-014-9351-z>
- Rutzinger, M., Rutzinger, M., Rottensteiner, F., Rottensteiner, F., Pfeifer, N., 2009. A Comparison of Evaluation Techniques for Building Extraction from Airborne Laser Scanning. *IEEE J. Sel. Top. Appl. Earth Obs. Remote Sens.* 2, 11–20. <https://doi.org/10.1109/JSTARS.2009.2012488>
- Sabin, F., 1997. *Remote Sensing: Principles and Interpretation*, (Floyd F. Sabins), Waveland Press, Inc.
- Sagan, V., Maimaitijiang, M., Sidike, P., Eblimit, K., Peterson, K., Hartling, S., Esposito, F., Khanal, K., Newcomb, M., Pauli, D., Ward, R., Fritschi, F., Shakoob, N., Mockler, T., 2019. UAV-Based High Resolution Thermal Imaging for Vegetation Monitoring, and Plant Phenotyping Using ICI 8640 P, FLIR Vue Pro R 640, and thermoMap Cameras. *Remote Sens.* 11, 330. <https://doi.org/10.3390/rs11030330>
- Sagan, V., Maimaitiyiming, M., Sidike, P., Maimaitiyiming, M., Erkbol, H., Peterson, K.T., Peterson, J., Burken, J., Fritschi, F., 2019. UAV / Satellite Multiscale Data Fusion for Crop Monitoring and Early Stress Detection. *Int. Arch. Photogramm. Remote Sens. Spat. Inf. Sci.*
- Sangha, H.S., Sharda, A., Koch, L., Prabhakar, P., Wang, G., 2020. Impact of camera focal length and sUAS flying altitude on spatial crop canopy temperature evaluation. *Comput. Electron. Agric.* 172. <https://doi.org/10.1016/j.compag.2020.105344>
- Sankaran, S., Khot, L.R., Espinoza, C.Z., Jarolmasjed, S., Sathuvalli, V.R., Vandemark, G.J., Miklas, P.N., Carter, A.H., Pumphrey, M.O., Knowles, N.R., Pavek, M.J., 2015. Low-altitude, high-resolution aerial imaging systems for row and field crop phenotyping: A review. *Eur. J. Agron.* 70, 112–123. <https://doi.org/10.1016/j.eja.2015.07.004>
- Santesteban, L.G., Di Gennaro, S.F., Herrero-Langreo, A., Miranda, C., Royo, J.B., Matese, A., 2017. High-resolution UAV-based thermal imaging to estimate the instantaneous and seasonal variability of plant water status within a vineyard. *Agric. Water Manag.* 183, 49–59. <https://doi.org/10.1016/j.agwat.2016.08.026>
- Schirrmann, M., Giebel, A., Gleiniger, F., Pflanz, M., Lentschke, J., Dammer, K.H., 2016. Monitoring agronomic parameters of winter wheat crops with low-cost UAV imagery. *Remote Sens.* 8. <https://doi.org/10.3390/rs8090706>
- Schmugge, T., French, A., Ritchie, J.C., Rango, A., Pelgrum, H., 2002. Temperature and emissivity separation from multispectral thermal infrared observations. *Remote Sens. Environ.* 79, 189–198. [https://doi.org/10.1016/S0034-4257\(01\)00272-3](https://doi.org/10.1016/S0034-4257(01)00272-3)
- scihub.copernicus.eu, n.d. , (last access 15 April 2020) [WWW Document].
- Seelan, S.K., Laguetta, S., Casady, G.M., Seielstad, G.A., 2003. Remote sensing applications for precision agriculture: A learning community approach. *Remote Sens. Environ.* <https://doi.org/10.1016/j.rse.2003.04.007>
- Senthilnath, J., Kandukuri, M., Dokania, A., Ramesh, K.N., 2017. Application of UAV imaging platform for vegetation analysis based on spectral-spatial methods. *Comput. Electron. Agric.* 140, 8–24. <https://doi.org/10.1016/j.compag.2017.05.027>
- Sepulcre-Cantó, G., Zarco-Tejada, P.J., Jiménez-Muñoz, J.C., Sobrino, J.A., Miguel, E. De, Villalobos, F.J.,

2006. Detection of water stress in an olive orchard with thermal remote sensing imagery. *Agric. For. Meteorol.* 136, 31–44. <https://doi.org/10.1016/j.agrformet.2006.01.008>
- Sepulcre-Canto, G., Zarco-Tejada, P.J., Sobrino, J. a., Jimenez-Munoz, J.C., Villalobos, E., 2005. Spatial variability of crop water stress in an olive grove with high-spatial thermal remote sensing imagery. *Precis. Agric.* '05 2017, 267–272.
- Shakhatreh, H., Sawalmeh, A., Al-Fuqaha, A., Dou, Z., Almaita, E., Khalil, I., Othman, N.S., Khreishah, A., Guizani, M., 2018. Unmanned Aerial Vehicles: A Survey on Civil Applications and Key Research Challenges 1–58.
- Sheng, H., Chao, H., Coopmans, C., Han, J., McKee, M., Chen, Y., 2010. Low-cost UAV-based thermal infrared remote sensing: Platform, calibration and applications, in: *Proceedings of 2010 IEEE/ASME International Conference on Mechatronic and Embedded Systems and Applications*, Qingdao, China. IEEE, pp. 38–43. <https://doi.org/10.1109/MESA.2010.5552031>
- Shufelt, J.A., 1999. Performance evaluation and analysis of monocular building extraction from aerial imagery. *IEEE Trans. Pattern Anal. Mach. Intell.* 21, 311–326. <https://doi.org/10.1109/34.761262>
- Sizov, F.F., 2015. IR region challenges: Photon or thermal detectors? Outlook and means. *Semicond. Phys. Quantum Electron. Optoelectron.* 15, 193–199. <https://doi.org/10.15407/spqeo15.03.193>
- Sokolova, M., Japkowicz, N., Szpakowicz, S., 2006. Beyond Accuracy, F-Score and ROC: A Family of Discriminant Measures for Performance Evaluation. pp. 1015–1021. https://doi.org/10.1007/11941439_114
- Sokolova, M., Lapalme, G., 2009. A systematic analysis of performance measures for classification tasks. *Inf. Process. Manag.* 45, 427–437. <https://doi.org/10.1016/j.ipm.2009.03.002>
- Solano, F., Di Fazio, S., Modica, G., 2019. A methodology based on GEOBIA and WorldView-3 imagery to derive vegetation indices at tree crown detail in olive orchards. *Int. J. Appl. Earth Obs. Geoinf.* 83, 101912. <https://doi.org/10.1016/j.jag.2019.101912>
- Soudani, K., François, C., le Maire, G., Le Dantec, V., Dufrêne, E., 2006. Comparative analysis of IKONOS, SPOT, and ETM+ data for leaf area index estimation in temperate coniferous and deciduous forest stands. *Remote Sens. Environ.* 102, 161–175. <https://doi.org/10.1016/j.rse.2006.02.004>
- Spoto, F., Martimort, P., Drusch, M., 2012. Sentinel - 2: ESA's optical high-resolution mission for GMES operational services, European Space Agency, (Special Publication) ESA SP.
- Stafford, J. V., 2000. Implementing precision agriculture in the 21st century. *J. Agric. Eng. Res.* 76, 267–275. <https://doi.org/10.1006/jaer.2000.0577>
- Stark, B., Smith, B., Chen, Y., 2014. Survey of thermal infrared remote sensing for Unmanned Aerial Systems. 2014 Int. Conf. Unmanned Aircr. Syst. (ICUAS), Orlando, FL, USA 1294–1299. <https://doi.org/10.1109/ICUAS.2014.6842387>
- Sugiura, R., Noguchi, N., Ishii, K., 2005. Remote-sensing technology for vegetation monitoring using an unmanned helicopter. *Biosyst. Eng.* 90, 369–379. <https://doi.org/10.1016/j.biosystemseng.2004.12.011>
- Sullivan, D.G., Fulton, J.P., Shaw, J.N., Bland, G., 2007. Evaluating the sensitivity of an unmanned thermal infrared aerial system to detect water stress in a cotton canopy. *Trans. ASABE* 50, 1963–1969. <https://doi.org/10.13031/2013.24091>

- Sun, H., Wang, Q., Wang, G., Lin, H., Luo, P., Li, J., Zeng, S., Xu, X., Ren, L., 2018. Optimizing kNN for mapping vegetation cover of arid and semi-arid areas using landsat images. *Remote Sens.* 10. <https://doi.org/10.3390/rs10081248>
- Tang, C., Turner, N.C., 1999. The influence of alkalinity and water stress on the stomatal conductance, photosynthetic rate and growth of *Lupinus angustifolius* L. and *Lupinus pilosus* Murr. *Aust. J. Exp. Agric.* 39, 457–464. <https://doi.org/10.1071/EA98132>
- Tarnavsky, E., Garrigues, S., Brown, M.E., 2008. Multiscale geostatistical analysis of AVHRR, SPOT-VGT, and MODIS global NDVI products. *Remote Sens. Environ.* 112, 535–549. <https://doi.org/10.1016/j.rse.2007.05.008>
- Taylor, P., Silleos, N.G., 2006. Vegetation Indices: Advances Made in Biomass Estimation and Vegetation Monitoring in the Last 30 Years. *Vegetation Indices. Geocarto Int.* 37–41. <https://doi.org/10.1080/10106040608542399>
- Teillet, P.M., Staenz, K., Williams, D.J., 1997. Effects of spectral, spatial, and radiometric characteristics on remote sensing vegetation indices of forested regions. *Remote Sens. Environ.* 61, 139–149. [https://doi.org/10.1016/S0034-4257\(96\)00248-9](https://doi.org/10.1016/S0034-4257(96)00248-9)
- Teodoro, A.C., Araujo, R., 2016. Comparison of performance of object-based image analysis techniques available in open source software (Spring and Orfeo Toolbox/Monteverdi) considering very high spatial resolution data. *J. Appl. Remote Sens.* 10, 16011. <https://doi.org/10.1117/1.JRS.10.016011>
- Testi, L., Goldhamer, D.A., Iniesta, F., Salinas, M., 2008. Crop water stress index is a sensitive water stress indicator in pistachio trees. *Irrig. Sci.* 26, 395–405. <https://doi.org/10.1007/s00271-008-0104-5>
- Thenkabail, P., 2015. *Remote Sensing Handbook Volume 1 - Remotely sensed data characterization, classification, and accuracies.* CRC Press, Boca Raton, United States.
- Tiberini, A., Mangano, R., Micali, G., Leo, G., Mangli, A., Tomassoli, L., Albanese, G., 2019. Onion yellow dwarf virus $\Delta\Delta C_t$ -based relative quantification obtained by using real-time polymerase chain reaction in “Rossa di Tropea” onion. *Eur. J. Plant Pathol.* 153, 251–264. <https://doi.org/10.1007/s10658-018-1560-2>
- Torres-Sánchez, J., López-Granados, F., De Castro, A.I., Peña-Barragán, J.M., 2013. Configuration and Specifications of an Unmanned Aerial Vehicle (UAV) for Early Site Specific Weed Management. *PLoS One* 8. <https://doi.org/10.1371/journal.pone.0058210>
- Torres-Sánchez, J., López-Granados, F., Peña, J.M., 2015. An automatic object-based method for optimal thresholding in UAV images: Application for vegetation detection in herbaceous crops. *Comput. Electron. Agric.* 114, 43–52. <https://doi.org/10.1016/j.compag.2015.03.019>
- Torres-Sánchez, J., Peña, J.M., De Castro, A.I., López-Granados, F., 2014. Multi-temporal mapping of the vegetation fraction in early-season wheat fields using images from UAV. *Comput. Electron. Agric.* 103, 104–113. <https://doi.org/10.1016/j.compag.2014.02.009>
- Trimble Inc., 2019. eCognition® Developer 1–266.
- Tsouros, D.C., Bibi, S., Sarigiannidis, P.G., 2019. A review on UAV-based applications for precision agriculture. *Inf.* 10. <https://doi.org/10.3390/info10110349>
- Tucci, G., Parisi, E.I., Castelli, G., Errico, A., Corongiu, M., Sona, G., Viviani, E., Bresci, E., Preti, F., 2019. Multi-sensor UAV application for thermal analysis on a dry-stone terraced vineyard in rural Tuscany landscape. *ISPRS Int. J. Geo-Information* 8. <https://doi.org/10.3390/ijgi8020087>

- Turner, D., Lucieer, A., Malenovský, Z., King, D.H., Robinson, S.A., 2014. Spatial co-registration of ultra-high resolution visible, multispectral and thermal images acquired with a micro-UAV over antarctic moss beds. *Remote Sens.* 6, 4003–4024. <https://doi.org/10.3390/rs6054003>
- Vacante, V., Calabrese, F., 2009. *Citrus - Trattato di agrumicoltura*, 1st ed. Edagricole, Milano.
- Vapnik, V., 1998. *Statistical Learning Theory*. Wiley and sons, New York.
- Villoslada, M., Bergamo, T.F., Ward, R.D., Burnside, N.G., Joyce, C.B., Bunce, R.G.H., Sepp, K., 2020. Fine scale plant community assessment in coastal meadows using UAV based multispectral data. *Ecol. Indic.* 111, 105979. <https://doi.org/10.1016/j.ecolind.2019.105979>
- Vincini, M., Frazzi, E., D'Alessio, P., 2007. Comparison of narrow-band and broad-band vegetation indices for canopy chlorophyll density estimation in sugar beet, in: *Precision Agriculture 2007 - Papers Presented at the 6th European Conference on Precision Agriculture, ECPA 2007*. pp. 189–196.
- Vinet, L., Zhedanov, A., 2010. A “missing” family of classical orthogonal polynomials. *Geogr. J.* 146, 448. <https://doi.org/10.1088/1751-8113/44/8/085201>
- Vizzari, M., Santaga, F., Benincasa, P., 2019. Sentinel 2-based nitrogen VRT fertilization in wheat: Comparison between traditional and simple precision practices. *Agronomy* 9, 1–12. <https://doi.org/10.3390/agronomy9060278>
- Walker, J., Halliday, D., Resnick, R., 2015. *Fundamentals of physics*, 10th ed. New York.
- Wang, F., Huang, J., Tang, Y., Wang, X., 2007. New Vegetation Index and Its Application in Estimating Leaf Area Index of Rice. *Rice Sci.* 14, 195–203. [https://doi.org/10.1016/S1672-6308\(07\)60027-4](https://doi.org/10.1016/S1672-6308(07)60027-4)
- Wang, Q., Adiku, S., Tenhunen, J., Granier, A., 2005. On the relationship of NDVI with leaf area index in a deciduous forest site. *Remote Sens. Environ.* 94, 244–255. <https://doi.org/10.1016/j.rse.2004.10.006>
- Williamson, T.N., Dobrowolski, E.G., Meyer, S.M., Frey, J.W., Allred, B.J., 2019. Delineation of tile-drain networks using thermal and multispectral imagery – Implications for water quantity and quality differences from paired edge-of-field sites. *J. Soil Water Conserv.* 74, 1–11. <https://doi.org/10.2489/jswc.74.1.1>
- Wilson, E.H., Sader, S.A., 2002. Detection of forest harvest type using multiple dates of Landsat TM imagery. *Remote Sens. Environ.* 80, 385–396. [https://doi.org/10.1016/S0034-4257\(01\)00318-2](https://doi.org/10.1016/S0034-4257(01)00318-2)
- Witharana, C., Civco, D.L., 2014. Optimizing multi-resolution segmentation scale using empirical methods: Exploring the sensitivity of the supervised discrepancy measure Euclidean distance 2 (ED2). *ISPRS J. Photogramm. Remote Sens.* 87, 108–121. <https://doi.org/10.1016/j.isprsjprs.2013.11.006>
- Wójtowicz, M., Wójtowicz, A., Piekarczyk, J., 2016. Application of remote sensing methods in agriculture. *Commun. Biometry Crop Sci.* 11, 31–50.
- Woo, D.K., Song, H., Kumar, P., 2019. Mapping subsurface tile drainage systems with thermal images. *Agric. Water Manag.* 218, 94–101. <https://doi.org/10.1016/j.agwat.2019.01.031>
- www.altodrones.com, (last access 30 April 2020).
- www.consorziocipollatroppeaigp.com, (last access 30 April 2020).
- www.ispag.org/about/definition, (last access 15 May 2020).

- Xu, H., Zhang, T., 2010. Comparison of Landsat-7 ETM+ and ASTER NDVI measurements, in: Remote Sensing of the Environment: The 17th China Conference on Remote Sensing. p. 82030K. <https://doi.org/10.1117/12.910397>
- Xue, J., Su, B., 2017. Significant remote sensing vegetation indices: a review of developments and applications. *J. sensors* Vol.2017, 17p. <https://doi.org/10.1155/2017/1353691>
- Yang, G., Liu, J., Zhao, C., Li, Z., Huang, Y., Yu, H., Xu, B., Yang, X., Zhu, D., Zhang, X., Zhang, R., Feng, H., Zhao, X., Li, Z., Li, H., Yang, H., 2017. Unmanned Aerial Vehicle Remote Sensing for Field-Based Crop Phenotyping: Current Status and Perspectives. *Front. Plant Sci.* 8. <https://doi.org/10.3389/fpls.2017.01111>
- Yang, L., Mansaray, L.R., Huang, J., Wang, L., 2019. Optimal segmentation scale parameter, feature subset and classification algorithm for geographic object-based crop recognition using multisource satellite imagery. *Remote Sens.* 11. <https://doi.org/10.3390/rs11050514>
- Yang, X., Zhao, S., Qin, X., Zhao, N., Liang, L., 2017. Mapping of urban surface water bodies from sentinel-2 MSI imagery at 10 m resolution via NDWI-based image sharpening. *Remote Sens.* 9, 1–19. <https://doi.org/10.3390/rs9060596>
- Yao, H., Qin, R., 2019. Unmanned Aerial Vehicle for Remote Sensing Applications — A Review 1–22.
- Yin, H., Udelhoven, T., Fensholt, R., Pflugmacher, D., Hostert, P., 2012. How Normalized Difference Vegetation Index (NDVI) Trends from Advanced Very High Resolution Radiometer (AVHRR) and Système Probatoire d’Observation de la Terre VEGETATION (SPOT VGT) Time Series Differ in Agricultural Areas: An Inner Mongolian Case Study. *Remote Sens.* 4, 3364–3389. <https://doi.org/10.3390/rs4113364>
- Zarco-Tejada, P.J., Diaz-Varela, R., Angileri, V., Loudjani, P., 2014. Tree height quantification using very high resolution imagery acquired from an unmanned aerial vehicle (UAV) and automatic 3D photo-reconstruction methods. *Eur. J. Agron.* 55, 89–99. <https://doi.org/10.1016/j.eja.2014.01.004>
- Zarco-Tejada, P.J., González-Dugo, V., Berni, J.A.J., 2012. Fluorescence, temperature and narrow-band indices acquired from a UAV platform for water stress detection using a micro-hyperspectral imager and a thermal camera. *Remote Sens. Environ.* 117, 322–337. <https://doi.org/10.1016/j.rse.2011.10.007>
- Zarco-Tejada, P.J., González-Dugo, V., Williams, L.E., Suárez, L., Berni, J.A.J., Goldammer, D., Fereres, E., 2013. A PRI-based water stress index combining structural and chlorophyll effects: Assessment using diurnal narrow-band airborne imagery and the CWSI thermal index. *Remote Sens. Environ.* 138, 38–50. <https://doi.org/10.1016/j.rse.2013.07.024>
- Zhang, C., Kovacs, J.M., 2012. The application of small unmanned aerial systems for precision agriculture: A review. *Precis. Agric.* 13, 693–712. <https://doi.org/10.1007/s11119-012-9274-5>
- Zhang, J., Huang, Y., Pu, R., Gonzalez-Moreno, P., Yuan, L., Wu, K., Huang, W., 2019. Monitoring plant diseases and pests through remote sensing technology: A review. *Comput. Electron. Agric.* 165. <https://doi.org/10.1016/j.compag.2019.104943>
- Zhang, L., Niu, Y., Zhang, H., Han, W., Li, G., Tang, J., Peng, X., 2019. Maize Canopy Temperature Extracted From UAV Thermal and RGB Imagery and Its Application in Water Stress Monitoring. *Front. Plant Sci.* 10, 1–18. <https://doi.org/10.3389/fpls.2019.01270>

- Zhang, N., Wang, M., Wang, N., 2002. Precision agriculture - A worldwide overview, in: *Computers and Electronics in Agriculture*. pp. 113–132. [https://doi.org/10.1016/S0168-1699\(02\)00096-0](https://doi.org/10.1016/S0168-1699(02)00096-0)
- Zhao, L., Shi, Y., Liu, B., Hovis, C., Duan, Y., Shi, Z., 2019. Finer Classification of Crops by Fusing UAV Images and Sentinel-2A Data.
- Zisi, T., Alexandridis, T.K., Kaplanis, S., Navrozidis, I., Tamouridou, A.A., Lagopodi, A., Moshou, D., Polychronos, V., 2018. Incorporating surface elevation information in UAV multispectral images for mapping weed patches. *J. Imaging* 4. <https://doi.org/10.3390/jimaging4110132>
- Zohary, D., Hopf, M., Weiss, E., 2015. Domestication of Plants in the Old World, Domestication of Plants in the Old World. <https://doi.org/10.1093/acprof:osobl/9780199549061.001.0001>